1.6-2.5 μm long wavelength quantum dash based lasers for gas sensing

Konstantinos Papatryfonos

THESE DE DOCTORAT DE TELECOM SUDPARIS

en co-accréditation avec

L'UNIVERSITE PIERRE ET MARIE CURIE - PARIS 6

Spécialité : Physique

Ecole doctorale EDITE de Paris

Présentée par

Konstantinos PAPATRYFONOS

Pour obtenir le grade de docteur délivré par

TÉLÉCOM SUDPARIS

Sujet de la thèse :

Lasers à bâtonnets quantiques InAs/InP émettant dans la gamme 1.6-2.5 µm pour la détection de gaz

Soutenue le 11 Juin 2015
devant le jury composé de :

Prof. Aurore VICET	HDR Institut d'électronique Université de Montpellier 2	Rapporteur
Prof. Alain LE CORRE	Professeur, INSA Rennes	Rapporteur
Prof. Anthony KRIER	Professeur, Université de Lancaster	Examinateur
Prof. Aziz BENLARBI-DELAI	Professeur, Université Paris 6	Examinateur
Prof. Abderrahim RAMDANE	Directeur de recherche, CNRS-LPN Professeur, TELECOM SudParis	Directeur de thèse
Dr. Anthony MARTINEZ	Chargé de recherche, CNRS-LPN	Co-encadrant

Thèse n^{o} : 2015TELE0011

Contents

Résumé

Introduction

Les boîtes quantiques semiconductrices (BQs) ont fait l'objet d'une attention considérable ces dernières décennies en raison de leurs propriétés remarquables provenant du confinement des porteurs dans les trois dimensions de l'espace [1,2]. Ce confinement leur confère un spectre en énergie discret qui peut être ajusté en modifiant leur composition, leur forme ou encore leur taille au cours de leur fabrication par croissance épitaxiale. Les BQs ont fait l'objet d'un intérêt tout particulier dans le domaine des lasers où leur utilisation donne lieu à des densités de courant de seuil faibles et une grande insensibilité en température, comme cela a été démontré dans le système de matériaux InAs/GaAs couvrant la bande O des télécommunications à 1.3 μm [3,4]. Pour la bande C à 1.55 μm, ainsi que pour d'autres applications comme la spectroscopie d'absorption haute résolution pour la détection de gaz à 2 μm, c'est le système de matériaux basé sur l'InP qui doit être utilisé [5,6]. Alors que le désaccord de maille entre InAs et GaAs est d'environ 7%, ce qui conduit à la formation de boîtes quantiques pour une couche InAs au-delà de l'épaisseur critique, cette valeur est deux fois moins grande dans le cas InAs/InP. Les différences dans les conditions de croissance résultent en la formation d'îlots allongés lorsque le substrat est de l'InP orienté [001], de telles structures étant souvent appelées bâtonnets quantiques (Qdashes) [7]. Ces nanostructures ont une section dans la direction (1-10) similaire à celle d'une boîte quantique peu profonde, de l'ordre de 3-4 nm par 10-20 nm, tandis que leur longueur dans la direction [1-10] est de l'ordre de 200 à 300 nm. Il a été démontré que ces bâtonnets quantiques ont des caractéristiques laser compatibles avec des applications pratiques [8] ainsi que de meilleurs performances en termes de blocage de modes [9]. De plus, leur impact sur la dynamique laser a été étudiée théoriquement de façon détaillée [10-12]. La croissance de BQs en InAs sur substrat InP est difficile [10] quoique possible sous certaines conditions de croissance bien précises comme cela a été démontré à quelques reprises [13-15]. Dans ce travail, nous nous sommes cependant focalisés sur les Qdashes parce ces derniers ont systématiquement permis jusqu'ici de réaliser des dispositifs aux performances meilleures que ceux basés sur des BQs dans cette gamme de longueurs d'onde.

Dans le présent travail, des nanostructures de type Qdash ont été étudiées expérimentalement, tout d'abord d'un point de vue de leurs propriétés fondamentales afin d'avoir une meilleure connaissance de leur structure électronique et deuxièmement, au travers de l'évaluation des performances de dispositifs lasers dans lesquels les Qdash forment le milieu actif, ceci dans le but d'exploiter leurs atouts pour des applications spécifiques et plus particulièrement la détection de gaz.

Dans la première partie de notre travail, de la microscopie et de la spectroscopie basse température STM en section transverse (X-STM/STS) ont été effectuées sur des Qdashes InAs(P)/InGaAsP/InP(001) inclus dans une structure de diode laser. La région active lasante

n'est pas dopée et consiste en neuf couches de Qdash séparées par des barrières d'alliage quaternaire. L'étude comporte à la fois des mesures à grande échelle, à travers toute la région active ainsi que des mesures à haute résolution d'énergie sur des Qdash individuels après s'être focalisé sur une région plus petite. Sur les mesures spectroscopiques à grande échelle, l'effet du potentiel «built-in» de la jonction p-i-n sur la structure de bande a été mis en évidence et quantifié. En comparant les canaux de courant tunnel de seuil dans des couches successives de Qdash ou de barrières, un décalage systématique en énergie a été mesuré à chaque fois, que ce soit pour le niveau fondamental d'énergie des Qdashes ou pour le bord de la bande de conduction des barrières. Les valeurs extraites sont en très bon accord quantitatif avec les calculs théoriques de structure de bande, ce qui démontre la grande sensibilité de cette technique de mesure spectroscopique pour sonder la structure électronique de nanostructures individuelles, en ce qui concerne la résolution spatiale de variations de potentiel local. De plus, il est montré qu'en tirant parti de la courbure de bande induite par dopage dans des études de dimensionnalité, un comportement hypothétique 0D peut être exclu. Pour obtenir des preuves supplémentaires et pour répondre à la question ouverte concernant la dimensionnalité des Qdashes, nous nous sommes focalisé sur des Qdash individuels se prêtant à des mesures de haute résolution d'énergie. L'étude de la densité locale d'états indique clairement une nature 1D de type fil quantique pour ces nanostructures dont le carré des fonctions d'ondes électroniques a ensuite été imagé par cartographie de conductivité différentielle. Ce type de mesures a un intérêt fondamental double, puisqu'en plus d'une caractérisation expérimentale complète des Qdash, l'imagerie X-STM/STS de fonctions d'ondes obtenue à partir de mesures de cartographie de conductance haute stabilité à basse température (T=5K) peut être étendue à des dispositifs pratiques ayant des surfaces faiblement dopées, ce qui permet une compréhension accrue du comportement des nanostructures semiconductrices.

Dans la seconde partie, nous avons développé des diodes laser à Qdash émettant aux grandes longueurs d'ondes compatibles avec la spectroscopie d'absorption haute résolution pour la détection de gaz. Ce travail a fait partie d'une collaboration étroite entre le groupe PHOTDEV au LPN et le III-V lab d'Alcatel-Thalès. Au LPN, nous avons effectué la fabrication du laser, la caractérisation de base et le design matériau pour les campagnes de croissance ultérieures tandis que le III-V lab était en charge de la croissance des matériaux. L'ensemble du projet faisait partie du réseau Initial Marie Curie Training Network (ITN) PROPHET, au sein duquel des caractérisations plus poussées des lasers ont été effectuées lorsque cela s'avérait nécessaire, en collaboration avec nos partenaires académiques le Tyndal National Institue à Cork, en Irlande, et l'université de Lancaster au Royaume-Uni. Au démarrage du projet, le groupe PHOTEV et le III-V lab avaient tous deux une expertise poussée de la fabrication de lasers Qdash émettant à 1.55 μm, lesquels avaient déjà été très bien étudiés et utilisés avec succès pour des applications en télécommunication. Dans ce projet, la cible principale a été de repousser la longueur d'onde d'émission vers des longueurs d'ondes plus grandes tout en maintenant de bonnes performances. La motivation principale de cet effort est de pouvoir utiliser de tels lasers pour la détection de gaz en tirant parti du fait qu'un grand nombre de gaz polluants ont de très fortes raies d'absorption à 2 μm ou à des longueurs d'onde plus grandes. Si l'on combine à cela le fait que l'eau a une très faible

absorption dans cette gamme de longueur d'onde, ces lasers permettraient ainsi une spectroscopie d'absorption haute résolution pour la détection de gaz. La composition nominale des Qdashes était de l'InAs binaire alors que dans cette partie du projet, la composition de la barrière a été variée en fonction de la longueur d'onde d'émission ciblée suivant une procédure d'optimisation qui sera expliquée en détail au chapitre 2. Toutes nos expériences et fabrications de dispositifs ont été effectuées sur substrat InP(001) dopé S. La longueur d'onde d'émission a été contrôlée par l'augmentation de la taille des Qdashes, la hauteur de ceux-ci étant le paramètre dominant qui détermine cette valeur. Un processus cyclique a été mis en œuvre, dans lequel la longueur d'onde d'émission (la taille des Qdashes) est déplacée d'une certaine valeur, après quoi l'ensemble du dispositif est optimisé pour cette nouvelle longueur d'onde puis l'on recommence une nouvelle itération. Après plusieurs campagnes de croissance de matériau, de fabrication et de caractérisation, nous avons réussi à obtenir des performances satisfaisantes pour des longueurs d'onde d'émission allant jusqu'à 2 μm. Combinés à des simulations additionnelles, nos résultats laissent espérer qu'il sera possible d'atteindre des longueurs d'ondes encore plus éloignées avec le même système de matériaux à l'avenir. Une description des principales étapes de la procédure d'optimisation des matériaux sera fournie dans ce manuscrit.

Après avoir atteint la longueur d'onde d'émission appropriée par rapport aux résonances des gaz, il devenait désirable d'avoir des lasers monomodes pour faire de la détection de gaz haute résolution. C'est pourquoi, l'un des autres buts de ce projet a été de fabriquer des lasers DFB (distributed feedback) ou DBR (distributed Bragg reflector) à partir de nos wafers épitaxies. D'après nos collaborateurs industriels du réseau PROPHET, il importe d'avoir deux paramètres à l'esprit pour être compétitif par rapport aux technologies concurrentes lorsque l'on conçoit des diodes laser pour des applications industrielles de détection de gaz : le coût de fabrication et le courant de seuil, qui doivent être minimisés par rapport aux alternatives existantes.

Pour tenter d'atteindre ces buts, nous avons proposé une nouvelle architecture pour un laser DFB couplée latéralement au réseau de Bragg avec un rapport cyclique élevée, et nous avons développé le procédé de fabrication en salle blanche conséquent. Le design à couplage latéral permet de satisfaire l'exigence de réduction des coûts en s'affranchissant des étapes extrêmement délicates de recroissance, ce qui simplifie considérablement le processus de fabrication ; les réseaux gravés permettent de diminuer le courant de seuil et d'augmenter la puissance de sortie en se substituant aux réseaux de Bragg métalliques très absorbants ; enfin, le rapport cyclique élevé permet de maintenir un coefficient de couplage suffisant entre le réseau et le mode guidé, ce qui n'était pas le cas dans tous les autres lasers LC-DFB à réseaux gravés qui ont été introduits jusqu'ici. En utilisant cette procédure, nous avons réussi à faire la démonstration de lasers LC-DFB monomodes avec un « side mode suppression ratio » (SMSR) élevé, de l'ordre de 40 dB, et un courant de seuil et une puissance de sortie similaires à ceux de laser Fabry-Pérot (FP) obtenus avec le même wafer. De plus, nous montrons que le coefficient de couplage de ces lasers est de l'ordre de 40 cm^{-1}, ce qui est assez pour fabriquer des lasers DBR à couplage latéral (LC-DBR) ayant des sections de réseaux suffisamment petites (~ 300 - 400 μm) à l'aide de la même technologie mais en configuration double ou

triple section. De plus, cette technologie est complètement générale et peut être utilisée avec n'importe quel système de matériau du moment que des recettes de gravure permettant la fabrication de réseaux de grande qualité sont développées. Tous les détails concernant la conception basée sur simulations, les étapes d'optimisation et de fabrication et les résultats finals seront donnés dans ce manuscrit.

Microscopie à effet tunnel sur la tranche et spectroscopie de Quantum Dash uniques

Les Qdashes sont des nanostructures qui possèdent un diamètre similaire à des boîtes quantiques dans une direction, et un diamètre de l'ordre de 200 à 300nm dans la direction [1-10]. Des telles nanostructures ont des applications pratiques comme matériau actif dans des lasers et amplificateurs optiques à semi-conducteurs, composants qui tirent profit de leurs propriétés avantageuses [8]. L'effet des Qdashes sur la dynamique des lasers a déjà été étudié du point de vue théorique [10-12]. De plus, la structure atomique des Qdashes en InAs obtenues dans un système de matériaux similaire, ainsi que celle des Qdashes obtenues par décomposition d'une matrice InGaAsP ont été récemment décrites et analysées à l'aide de la microscopie à effet tunnel sur la tranche (X-STM) [16,17]. Bien que ces études aient apporté un certain de nombre de réponse quant aux propriétés structurales des Qdashes, les propriétés physiques fondamentales, telles que la densité d'états éléctroniques, de ces nano-structures restent encore méconnues. En particulier, il manque à ce jour une étude expérimentale approfondie des effets de la dimensionnalité des Qdashes. De ce fait, il n'y a pas à ce jour de distinction claire entre Qdashes et boîtes quantiques, et les deux termes sont utilisés invariablement dans la littérature pour décrire ces nano-structures de basse dimensionnalité. Les méthodes communément employées pour prédire si une nano-structure se comporte comme un boîte quantique, telles que celles qui consistent à comparer les dimensions physiques des nano-structures à celle de l'exciton de Bohr, ne peuvent être appliquées dans le cas des Qdashes, en raison de la forte anisotropie des ces dernières. Les Qdashes sont des nano-structures uniques et distinctes des nano-fils et des boîtes quantiques, en raison de leur rapports longueur à largeur et largeur à hauteur (de l'ordre de 10). De plus, leur forme peut fluctuer pour localement s'élargir ou présenter de courbures similaires à des zig-zags. Un exemple de fluctuations de la forme des Qdashes est observé dans la micrographie MET en vue plane de la Figure 0.1. Dans cette micrographie, des fortes variations de la longueur caractéristique des Qdashes peuvent être observées. Comme décrit dans la Réf. [10], de telles fluctuations sont susceptibles de provoquer une localisation des porteurs et potentiellement aboutir à une densité éléctronique zéro-dimensionnelle pour une partie ou la totalité des Qdashes. Des travaux ultérieurs ont aussi montré que les zig-zags [18], ainsi que des inhomogeneités de composition ou une distribution non-uniforme de la contrainte [19] dans ces nano-structures peuvent aussi produire de centres de localisation des porteurs. Certaines études ont postulé une densité d'état unidimensionnelle, similaire à celle des nano-fils, dans leur analyse du gain d'ensemble de Qdash, montrant un bon accord entre les performances théoriques et expérimentales de leurs composants [10, 11, 20, 21]. D'autres études ont quant à elles considéré les Qdashes comme des boîtes quantiques [8, 22-24], ou ont montré que les Qdashes possèdent les propriétés d'un objet de dimensionnalité zéro [25-27]. D'un autre côté, des dashes avec un diamètre plus grand, montraient un confinement bidimensionnel

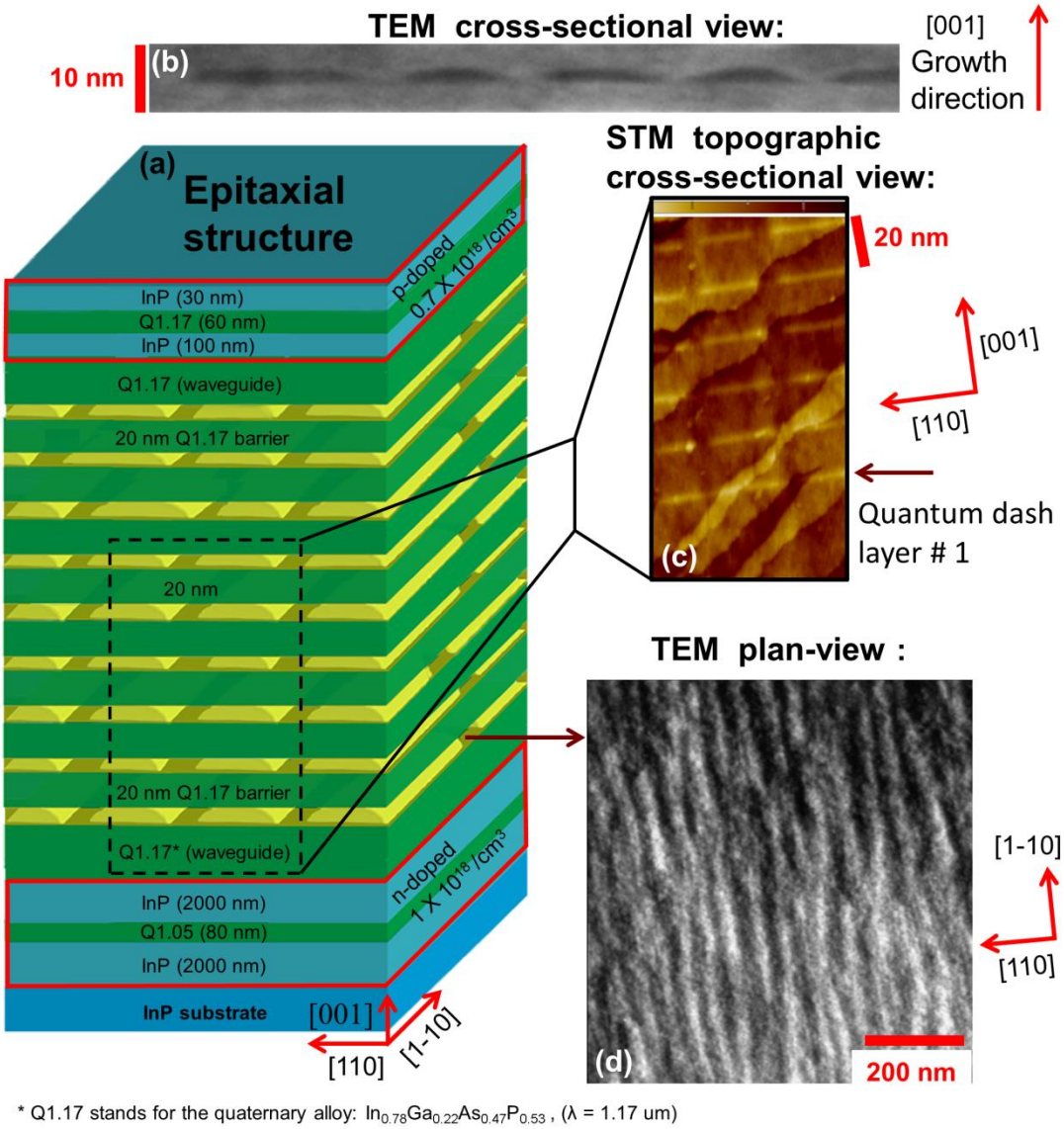

Figure 0.1 – (a) Schéma de la structure épitaxiée, (b) micrographie TEM d'une tranche de la structure, (c) image topographique d'une section de la structure observée en STM et (d) micrographie TEM en vue plane de l'échantillon étudié. La structure a eté épitaxiée sur un substrat InP dopé S. La région active non-dopée comporte neuf couches de QDashes, séparées par des barrières de 20nm d'un quaternaire InGaAsP (λ_{PL} =1.17 µm). La région active est entourée des deux couches guidantes en quaternaire, elles-mêmes entre un buffer dopé n (en bas) et un buffer dopé p (en haut). Cet échantillon ne possède pas de cladding supérieur, ni de couches de contacts utilisées pour la fabrication d'un laser, couches qui n'impactent pas les propriétés étudiées ici en STM/SMS.

seulement des porteurs, le confinement se limitant à seule la hauteur des dashes selon la direction de croissance. En raison des inhomogénéités dans la taille et la forme de Qdashes que l'on peut observer lors d'une croissance auto-assemblée, les Qdashes individuelles d'un même échantillon peuvent avoir des propriétés électroniques très différentes de celles des Qdashes environnantes. Cela peut potentiellement dégrader les performances d'un composant optoélectronique. Comprendre les propriétés électroniques des Qdashes individuelles devient

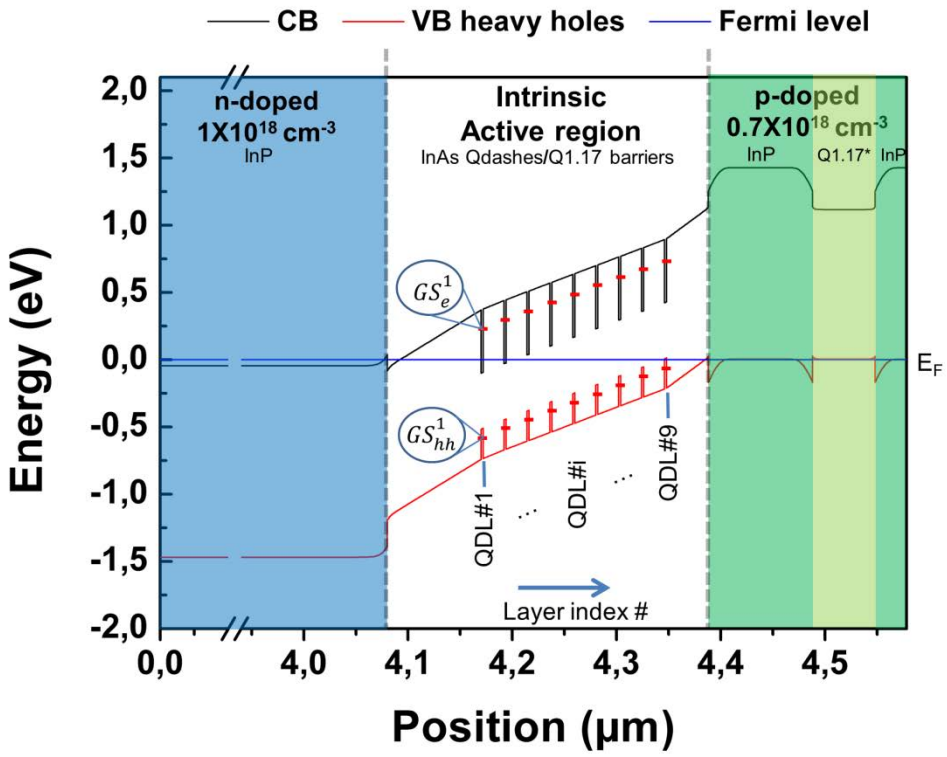

Figure 0.2 – Profils de la bande de conduction et de la partie trous-lourds de la bande de valence de l'échantillon étudié. Les couches de bâtonnets quantiques sont labellisées QDL#i, en comptant (i=1 à 9) à partir des couches tampons InP de type n. Seuls les états fondamentaux des électrons et trous lourds sont montrés pour chaque bâtonnet quantique. La ligne bleue représente le niveau de Fermi.

donc très important et intéressant, d'un point de vue tant scientifique que pratique. Les avancées récentes en microscopie et spectroscopie par effet tunnel (X-STM/STS), associées aux techniques de clivage sous vide, ont permis d'avoir accès à la densité d'états locale (LDOS) de nanostructures enterrées, grâce à la mesure de spectres de conductance différentielle dI/dV (V) en des sites spécifiques [28,29]. D'autre part la possibilité d'acquérir des cartes de conductivité différentielle résolue en énergie et dans l'espace dI/dV (V,x,y), permet d'établir la distribution énergie-espace de la densité d'états locale (LDOS) à travers une section transversale et ainsi déduire le carré de la fonction d'onde [30]. La technique X-STM/STS est ainsi une technique très adaptée pour l'imagerie des fonctions d'onde. L'échantillon à bâtonnets quantiques étudié a été élaboré par épitaxie par jets moléculaires à sources gazeuses (GSMBE) sur un substrat InP(001) dopé n. Les parties a-d de la figure 0.1 montrent respectivement une vue schématique de la structure, une image transverse TEM, une vue topographique transverse obtenue par STM (1-10), et des vues planaires TEM des couches à bâtonnets quantiques. La figure 0.2 montre le schéma de la structure de bandes de cet échantillon, calculée en résolvant de façon auto-consistante les équations de Schrödinger-Poisson à T=5K, à l'aide du logiciel NEXTNANO [31]. Dans ce travail nous présentons les mesures X-STM/STS effectuées sous ultra-vide (UHV) et à basse température (T = 5K) sur des bâtonnets quantiques InAs clivées (1-10). Ces bâtonnets sont incorporés dans la zone intrinsèque d'une diode p-i-n, préalablement optimisée comme zone active d'un laser. Ce travail d'optimisation a porté sur les conditions de croissance, le choix du matériau (hauteur

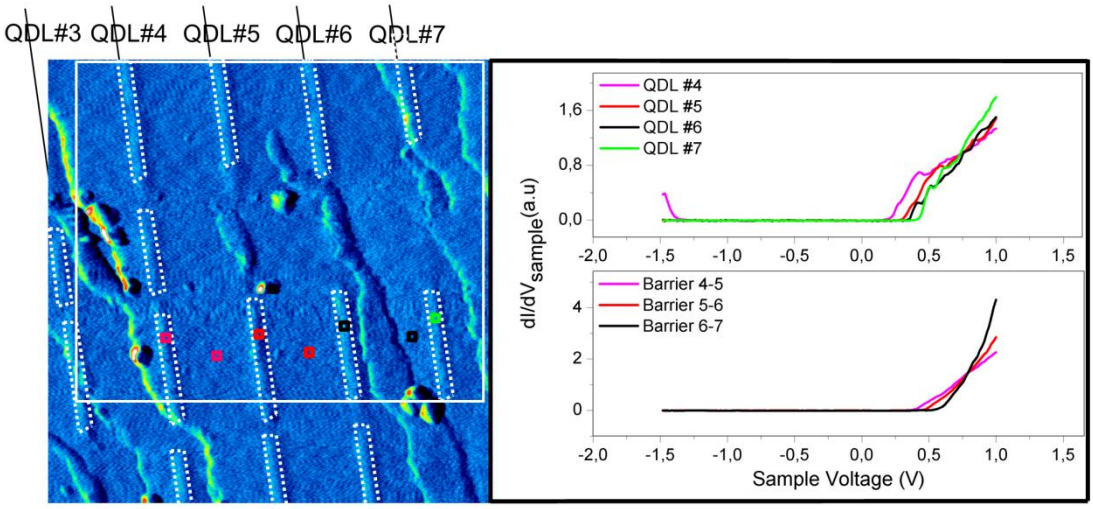

Figure 0.3 – Gauche : Image STM à grande échelle d'une surface 100 nm x 100 nm montrant 5 couches de bâtonnets quantiques InAs, référencées de QDL#3 à QDL#7, et séparées par des barrières en quaternaire InGaAsP (λ_{PL} = 1.17 µm) ; (T = 5K, I_t = 100 pA, V_t = +1 V). Les contours à points blancs sont dessinés pour identifier les bâtonnets quantiques alors que les lignes obliques noires montrent les couches successives. Le rectangle blanc montre la zone où les cartes de conductivité différentielle (voir Fig. 1.4) ont été acquises. Droite : Spectres individuels dI/dV obtenus pour des couches et barrières successives de bâtonnets quantiques. Les positions exactes sont marquées par les carrés correspondants colorés dans l'image STM.

des barrières de bandes) et le profil de dopage de la structure, en tenant compte des mesures de PL et des résultats de composants, après plusieurs essais de croissance et de fabrication de lasers. Dans notre étude nous avons alors utilisé un échantillon de la structure finale, avec une qualité de matériau la plus élevée.

Etude de la structure électronique des bâtonnets quantiques en fonction des variations locales du potentiel

La figure 0.3 sur le panneau de gauche, montre une image topographique à grande échelle (100 nm x 100 nm de surface, $V_{échantillon}$ = 1.0 V et I_{tunnel} = 100 pA) pour cinq couches de bâtonnets quantiques (#3 - # 7, le comptage commence de gauche à droite le long de l'axe de croissance), séparées par des barrières d'épaisseur 20 nm. Sur le panneau de droite est montrée une série de spectres individuels dI/dV (V) mesurés sur ces bâtonnets quantiques et sur les barrières intermédiaires. Chaque courbe colorée a été mesurée à un endroit spécifique indiqué par le carré de même couleur sur l'image topographique. Ces courbes illustrent le décalage en énergie du bord de la bande de conduction à différentes positions dans la structure, induit par le potentiel auto-installé dans la région d'appauvrissement de la jonction p-i-n. Les figures 0.4 a-d montrent les cartes de conductivité différentielle pour des tensions d'échantillon V = 288 meV, 356 meV, 410 meV et 475 meV respectivement, pour la zone sélectionnée (95 nm x 80 nm) marquée par le rectangle blanc dans l'image STM de la figure 0.3. Nous avons observé pour cette séquence de densités d'états locales (LDOS (x,y,V)) des contrastes importants de lumière sur les couches successives de bâtonnets quantiques de gauche à droite quand on augmente la tension sur l'échantillon. Chaque incrément de tension

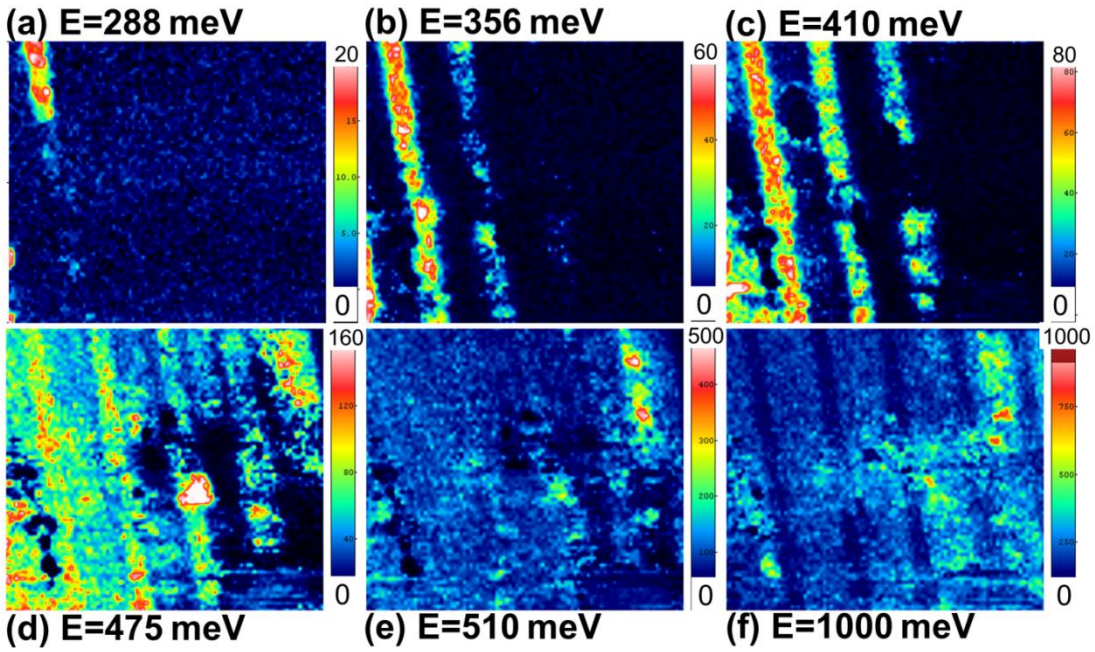

Figure 0.4 – Conductance différentielle dI(V,x,y)/dV obtenue pour les couches de QDash #4 to #8 (l'aire sélectionnée est de 95 nm x 80 nm encadrée par un rectangle blanc dans l'image STM de la figure 0.3). (a) – (d) une cartographie STS est présentée aux énergies de bord de bande respectives correspondant à une densité local d'états en marche d'escaliers, V= 288 meV; 356 meV; 410 meV ; 475 meV pour les couches successives. Pour chaque image STS, la couleur de dI/dV est adaptée à la variation de la densité locale d'états en fonction de la tension aux bornes de l'échantillon (du bleu: faible LDOS au rouge: haute LDOS). Cartographie (e) et (f) sont acquises à des tensions relatives à des conditions spécifiques pour lesquelles aucun contraste n'est observé à V = 510 mV ou un contraste noir est observé sur des QDashes à V = 1000 mV.

élève le niveau d'énergie des électrons tunnel en face des n_i à n_{i+1} couches successives, ouvrant ainsi un nouveau canal de conduction pour les électrons injectés de la pointe vers les niveaux quantifiés des bâtonnets. Le décalage de l'état fondamental des différentes couches de bâtonnets en fonction de leur position précise dans la jonction p-i-n apparaît clairement sur ces cartes. Ce décalage est une manifestation directe de la forme du potentiel en pente (voir Figure 0.2). Il est bien connu que la pointe induit des effets de distorsion de bandes (TIBB) à l'origine de la distorsion de niveaux énergétiques qui dépend de la géométrie de la pointe, du niveau de dopage et de la tension appliquée [32,33]. Le décalage énergétique mesuré entre des couches adjacentes, $\Delta E = E_{000}^{(i+1)} - E_{000}^{(i)}$, (ou décalage de la bande de conduction entre des barrières adjacentes, ΔE_c) est en bon accord avec la pente de la courbure de bande (gradient de potentiel) obtenue par résolution auto-consistante des équations de Schrödinger et de Poisson pour notre système. La valeur calculée pour le décalage énergétique du potentiel en fonction de la distance à partir des couches n est de 3 meV/nm , correspondant à ΔE = 60 meV pour des couches adjacentes de bâtonnets quantiques. Les figures 0.4 e, f montrent des cartes obtenues à des tensions particulières pour lesquelles soit aucun contraste n'est observé à V = 510 mV (compensation complexe de la distance pointe-surface, déformation des bandes et densité d'états électroniques), soit un contraste 'sombre'

est observé à V = 1000 mV (lié à un effet tunnel plus important dans le continuum des couches barrières).

Nature de la dimensionnalité des bâtonnets quantiques et imagerie de la fonction d'ondes

Une autre caractéristique qui mérite attention sur figure Fig. 0.4a,b concerne la nature de la dimensionnalité des bâtonnets quantiques, puisque l'hypothèse d'une dimensionnalité 0-D peut déjà être exclue. La raison tient au fait que dans l'hypothèse d'un spectre de niveaux d'énergie discret, pour la nature 0-D, la densité d'état de la couche de bâtonnets # 4 devrait disparaître à partir des Figures 0.4a et b, dans lesquelles la couche de bâtonnets # 5 est en résonance (Le même argument peut être appliqué en comparant les Figures 0.4b-c et ainsi de suite). Au contraire, nos mesures montrent que la couche de bâtonnets # 4 présente

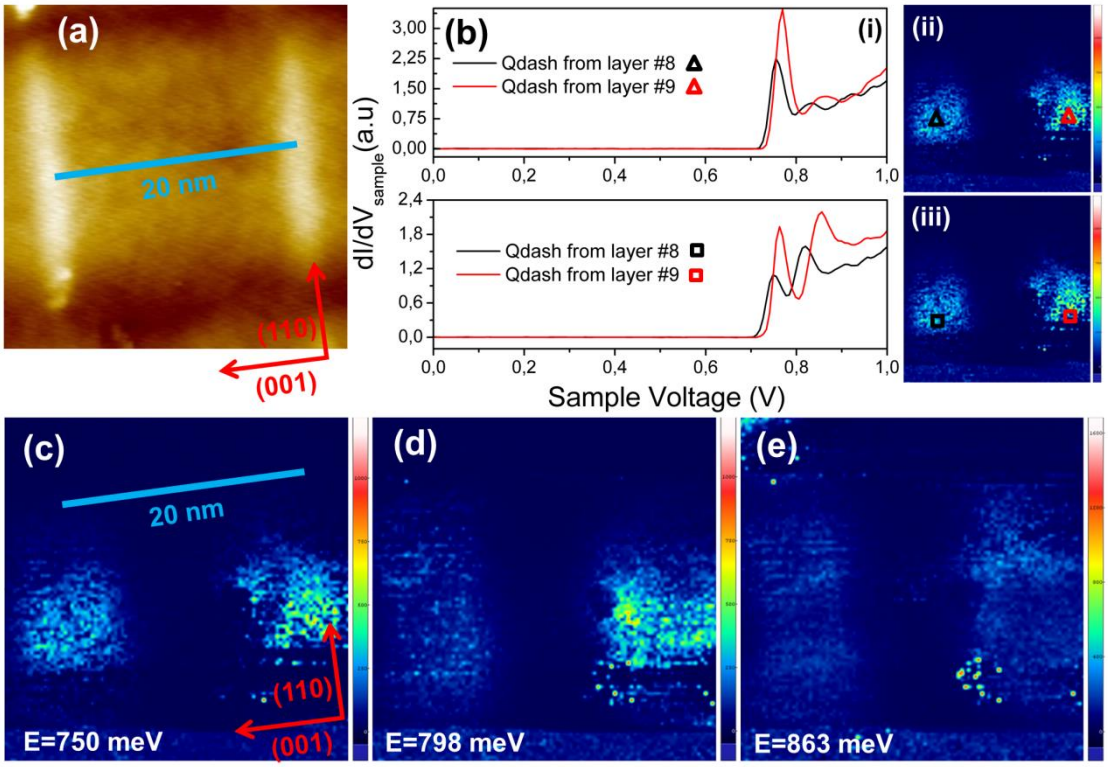

Figure 0.5- (a) Images X-STM de topographie à courant constant (Vsample=1.0 V et Itunnel=100 pA) s'intéressant à deux QDashes. (b) Spectres individuels dI/dV pris sur les Qdashes à partir des couches #8 and #9 aux positions indiquées par les triangles colorés respectifs et les carrés dans la cartographie de la conductance différentielle présentée sur les images 5b(ii) and (iii). (c-e) Cartographie de la conductance différentielle à différentes tensions, révélant deux états confinés transverses dans les Qdashes. La tension augmente de (c) à (e): (c) Fonction d'onde de l'état fundamental dans chaque QDashes pour une tension V = 750 mV. (d) La fonction d'onde du premier Qdash est étendu sur toute sa largeur, suggérant la superposition d'un état fondamental et d'un état excité en raison de l'élargissement thermique des niveaux d'énergie, tandis que le second QDash est toujours à la résonance (V = 798 mV) (e) Les deux QDashes sont dans un état résonant hybride état fondamental-état excité à des de tensions plus hautes que 863 mV.

systématiquement une densité d'état plus élevée comparée à celles des couches de plus fort indices, pour toutes les valeurs de tension au cours de la cartographie, suggérant une structure en marche d'escalier pour la densité d'états, comme attendu pour une dimensionnalité relative à un comportement 1-D ou 2-D. Dun autre côté, après un zoom des aires avec deux bâtonnets bien définis, montrés sur la figure STM 0.5a, des spectres STS individuels avec une haute résolution ont été pris pour chaque bâtonnet. Pour de tels spectres, comme illustrés sur la figure 0.5b(i), nous avons enregistré les images aux positions indiquées par les triangles colorés respectifs et des carrés dans les cartographie de la conductance différentielle (Figure 0.5b(ii) and (iii)). Les spectres indiquent des pics suivis par des marches lors de l'augmentation de la tension aux bornes de l'échantillon, ce qui est une signature typique de la densité d'état attendue pour des structures 1-D [34]; donc excluant une dimensionnalité 2-D ou plus élevée, mettant clairement en évidence un caractère 1-D des bâtonnets. Une caractéristique vraiment similaire de la densité d'états a déjà été observée par des mesures STS, dans de premières études récemment réalisées sur des nanotubes de carbone [35], tandis que la densité locale d'états de nos bâtonnets quantiques LDOS(V) présente aussi une différence claire de dépendance de dI/dV = f(V) par rapport aux mesures STS sur des puits quantiques 2-D [36]. Nous avons effectué de telles mesures au-dessus d'une variété de bâtonnets clivés, à différentes positions dans chaque bâtonnets et également dans le matériau de référence InGaAsP, afin de confirmer que toutes les structures présentent un comportement similaire. Une analyse statistique est réalisée sur quelques dizaines de QDashes, la plupart présentant 2 pics prononcés alors que d'autres présentent trois niveaux d'énergie confinés. Cette différence est due à la dimension latérale plus grande des Qdashes qui présentent un plus grand nombre de niveaux d'énergie. Les pics des spectres individuels semblent avoir des intensités relatives dépendantes de la position de mesure, ce qui est particulièrement évident pour le second pic de la figure 0.5b(i) qui a une intensité plus faible à proximité du centre du QDash. Cette variation correspond à la distribution spatiale de la fonction d'ondes, qui peut être imagée en enregistrant de tels spectres dI/dV sur une grille de points. Figure 0.5c-e montre une séquence de cartographie de conductance différentielle dans la même aire (Figure 0.5a), pour des tensions aux bornes de l'échantillon de 750 mV; 798 mV and 863 mV. Dans la Figure 0.5c, tous les Qdashes sont à la résonance. Dans la Figure 0.5d, la fonction d'onde du premier Qdash s'étend sur toute sa largeur. Nous supposons que cela est dû à l'hybridation résultant de la superposition du lobe localisé de l'état fondamental et de la distribution d'intensité étendue avec un nœud au centre, comme attendu pour le premier état excité. Le second bâtonnet est aussi à la résonance. Dans la figure 0.5e les QDashes correspondent à une hybridation GS et ES. La même séquence que sur la figure 0.3 apparaît, avec des QDashes localisé dans la couche de plus faible indice (plus proche de la partie dopée n de l'échantillon) arrivant plus tôt à la résonance. Nous avons observé seulement deux sous bandes confinées dans ces Qdashes, ce qui est consistant avec des résultats rapportés précédemment et les simulations. Afin d'avoir une meilleure compréhension et d'étayer notre analyse, tous nos résultats ont été comparés avec les simulations par éléments finis. Ces simulations ont été réalisées grâce au logiciel COMSOL MULTIPHYSICS, qui sont décrites en détails dans le manuscrit de thèse.

Lasers à bâtonnets quantiques InAs/InP émettant vers 2 µm pour la détection de gaz

La spectroscopie d'absorption infrarouge est un outil précieux pour la surveillance de l'environnement, que ce soit pour la détection de polluants dans l'atmosphère ou pour le contrôle de composants gazeux dans les processus industriels. Les diodes lasers à semiconducteurs à base de structures de basse dimensionnalité, telles que les boîtes et bâtonnets quantiques auto-organisés, sont bien adaptées à cette application car elles présentent un spectre de gain optique plus étendu que celui des composants conventionnels à base de puits quantiques. La longueur d'onde d'émission est ajustée en jouant sur l'épaisseur ou la composition des bâtonnets/boîtes quantiques La croissance épitaxiale est de plus réalisée directement sur substrat InP (001) ou un autre matériau en accord de maille, ce qui permet d'utiliser les procédés technologiques déjà développés pour l'industrie des télécommunications pour fabriquer les lasers émettant à plus longue longueur d'onde. Les bâtonnets quantiques demeurent cependant un système de matériau relativement nouveau et complexe pour la conception de lasers, et leur optimisation fait toujours l'objet d'études. Ils présentent un élargissement homogène et inhomogène inévitable durant leur croissance. Le premier effet est lié à l'interaction des bâtonnets quantiques avec leurs voisins et leur environnement qui se traduit par une largeur non nulle du spectre de luminescence. L'élargissement inhomogène est lié à la distribution en taille des nanostructures (principalement leur hauteur) et provoque un élargissement du gain optique de plusieurs dizaines de nanomètres. Cet effet est l'une des principales causes qui limite la performance des lasers bien qu'il soit avantageux dans des applications qui nécessitent un spectre de gain étendu, comme pour les lasers accordables pour la spectroscopie de gaz.

Structures à basse dimensionnalité –densité d'états

La réduction de la taille d'un semiconducteur à quelques mono-couches atomiques a un impact important sur les propriétés optiques et électroniques de la structure. Le confinement des porteurs de charge à quelques nanomètres, comparable à leur longueur d'onde de de Broglie, augmente la largeur de bande interdite effective du matériau et provoque des effets de quantification. Un paramètre très important souvent utilisé pour décrire la physique de ces nanostructures est la densité d'états (Density of States ou DOS). La densité d'états peut être définie comme le nombre de porteurs permis avec une certaine énergie, ou comme le nombre d'états permis par unité d'énergie et unité de volume. Une propriété remarquable des nanostructures est la réduction significative de leur densité d'états avec des pics à des valeurs spécifiques d'énergie. Une règle générale pour avoir une première idée de la dimensionnalité d'un matériau consiste à comparer ses dimensions physiques (hauteur, largeur et longueur) au rayon de l'exciton de Bohr dans le même matériau massif. Le régime du confinement quantique (fort ou faible) peut être estimé en comparant le volume de l'exciton et celui des nanostructures. La réduction en taille de la structure peut être réalisée de façon que les porteurs soient confinés dans une, deux, ou les trois dimensions de l'espace. Ceci résulte en un mouvement 'libre' respectivement dans deux dimensions (2D) dans les puits quantiques, une dimension (1D) dans les fils quantiques ou zéro dimension (0D) dans

Structure	Dimensionnalité	Densité d'états
Matériau Massif	3-D	√E
Puit Quantique	2-D	1
Fil Quantique	1-D	1/√E
Boîtes Quantique	"0-D"	δ(E)

Tableau 0.1 - Densité d'états pour électrons et trous en fonction de la dimensionnalité du système.

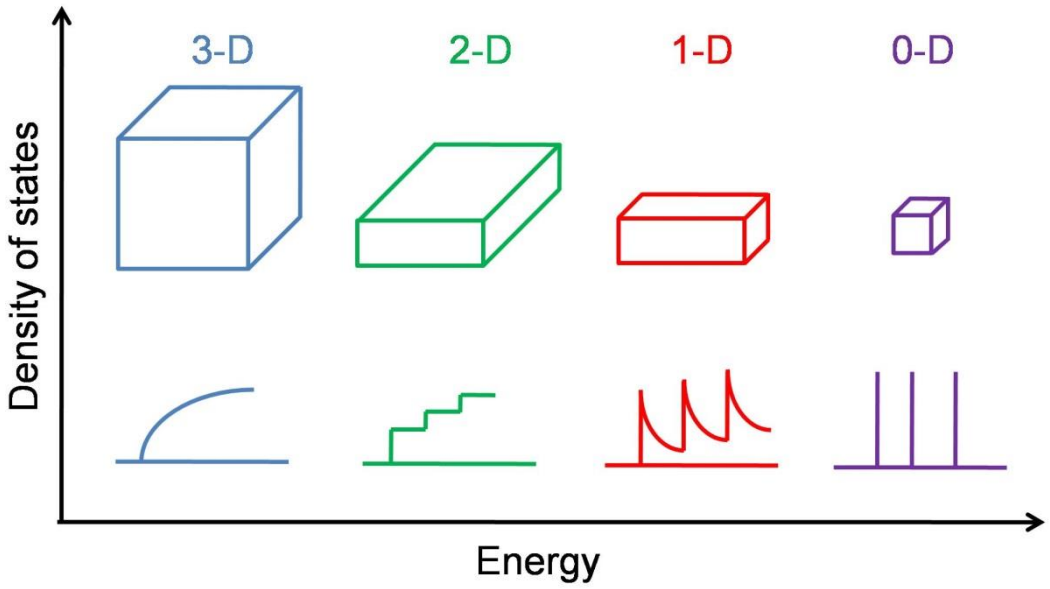

Figure 0.6 - Illustration de la densité d'états électroniques en fonction de l'énergie pour les semiconducteurs massifs, puits quantiques, fils et boîtes quantiques, respectivement.

les boîtes quantiques par rapport au cas 3D ou matériau massif où les porteurs de charge peuvent se déplacer dans les trois dimensions de l'espace. La dépendance en énergie de la densité d'états électroniques pour chaque dimension est donnée dans le tableau 0.1 et une représentation schématique est montrée sur la figure 0.6. On rappelle que la densité d'états de boîtes quantiques est théoriquement la fonction de Dirac (fonction delta) et un certain nombre de propriétés remarquables ont ainsi été prédites pour les lasers à base de ces nanostructures. Les plus importantes sont : augmentation du gain optique et du gain différentiel [38], réduction de la densité du courant de seuil et de sa dépendance (idéalement aucune) en température [1,2], réduction du facteur de couplage phase-amplitude [39,40], augmentation des bandes passantes de modulation [41]. Une autre façon de voir ces avantages potentiels des lasers à base de structures de basse dimensionnalité est que les électrons et trous injectés par pompage électrique, occuperaient exactement les niveaux énergétiques où ils contribuent le plus efficacement à l'effet laser. Cependant, comme déjà discuté dans l'introduction, en réalité la densité d'états est élargie de façon homogène dans le domaine énergétique. Cet élargissement est le résultat des propriétés intrinsèques des boîtes quantiques, lié à la durée de vie finie des porteurs dans chaque état confiné, et aussi aux interactions électron-phonon et électron-électron [42]. D'autre part, un ensemble de bâtonnets

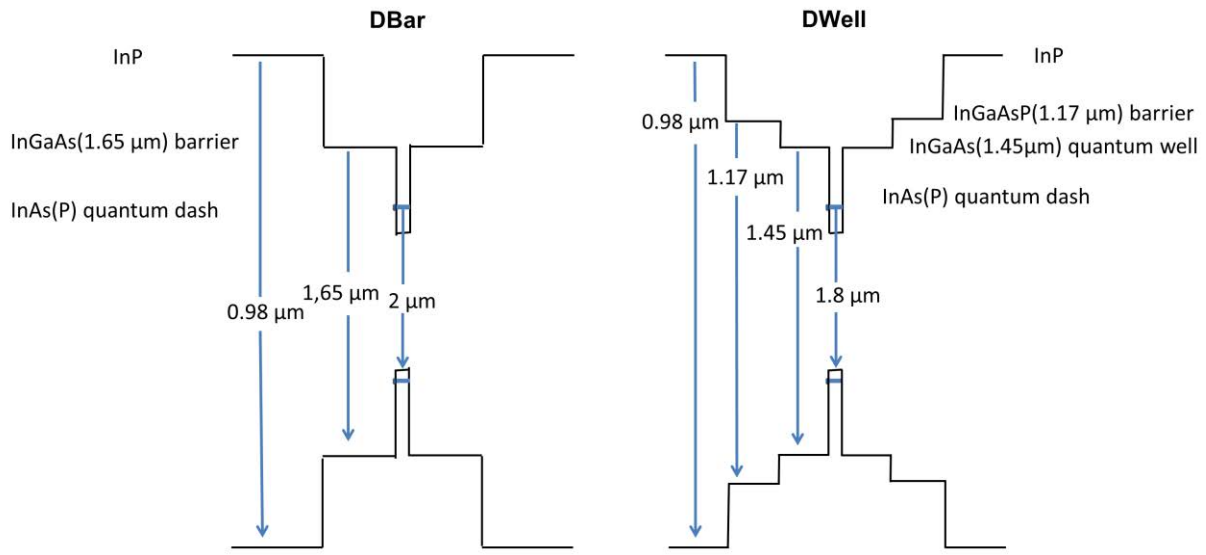

Figure 0.7 - Vue schématique de la structure de bande des structures DBar et DWell.

/boîtes quantiques obtenus par croissance épitaxiale présente une distribution finie de la taille des nanostructures, ce qui résulte en une distribution (généralement gaussienne) des niveaux énergétiques autour d'une valeur moyenne. Ces effets d'élargissement (homogène et inhomogène) se traduisent par une déviation des propriétés remarquables prédites par la théorie et font l'objet d'études jusqu'à présent. De plus, une autre conséquence qu'on peut mentionner, est que la densité d'états 1D des bâtonnets quantiques, avec peu de niveaux d'énergie confinés (deux dans notre cas), devient en pratique plus similaire à la densité 0-D des boîtes quantiques lorsque les deux fonctions sont élargies.

Structures lasers

Nous avons étudié deux types de structures à bâtonnets quantiques, l'une à bâtonnets dans la barrière (DBar) et l'autre à bâtonnets dans le puits (DWell), tels que représentés sur la figure 0.7. Dans les structures DBar les bâtonnets quantiques sont insérés dans des barrières InGaAs de bord d'absorption à 1,65 µm, alors que dans les DWell ils sont insérés dans des puits quantiques intermédiaires en quaternaire InGaAsP (λ_{PL} = 1,45 µm) d'épaisseur 6nm, eux-mêmes incorporés dans des barrières InGaAsP (λ_{PL} = 1,17 µm) d'épaisseur 40 nm. En plus des mesures initiales de photoluminescence (PL), des lasers ont été fabriqués et caractérisés pour chaque échantillon afin d'évaluer la qualité du matériau de base Ceci est une étape nécessaire car il est bien connu que le pic de photoluminescence ne garantit pas nécessairement la longueur d'onde d'émission du laser parce que ce dernier peut émettre sur un état excité ou ne pas fonctionner du tout. Deux types de laser ont été étudiés à cette étape pour une validation rapide du matériau : des lasers à contact large et des lasers à guide d'onde en arête (Figure 0.8). Sur la figure sont montrés un schéma simple des deux structures ainsi

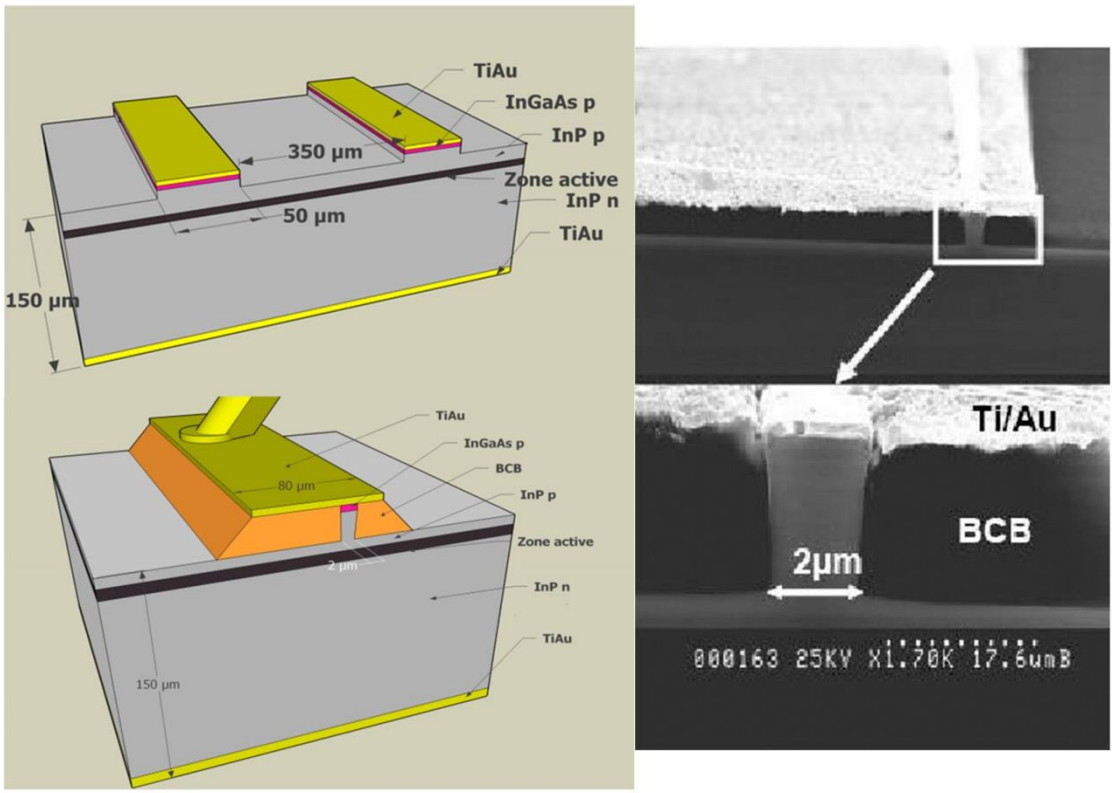

Figure 0.8 – Gauche : schéma d'un laser à contact large (haut) et à guide d'onde en arête (bas), Droite : vue au MEB de la section d'un laser à guide d'onde en arête fabriqué en salle blanche.

qu'une photo au microscope électronique à balayage (MEB) d'un laser à guide d'onde en arête.

Première campagne de croissance

Dans la première campagne de croissance la stratégie était de partir des structures déjà optimisées pour les applications à 1,55 µm et essayer d'étendre la longueur d'onde d'émission vers le rouge. La figure 0.9 montre les spectres de photoluminescence (PL) de tous les échantillons élaborés durant cette période. L'échantillon 62382 de PL à 1,6 µm sera utilisé comme référence pour les échantillons 62385 et 62391 de PL 1,8 et 2 µm respectivement. Pour les plus grandes longueurs d'onde à 2,05 et 2,1 µm, les conditions de croissance n'étaient pas optimisées, et les analyses structurales au Microscope Electronique à Transmission révélèrent des dislocations. Ces derniers échantillons ne furent donc pas traités en salle blanche. Des composants à contact large et à guide d'onde en arête ont été fabriqués et caractérisés à partir des couches ayant un pic de PL jusqu'à 2 µm afin d'évaluer la performance des lasers à bâtonnets quantiques. Les lasers à guide d'onde étroit ont été testés en injection continue alors que les lasers à contact large le furent en courant impulsionnel pour éviter les effets d'échauffement. Des longueurs de cavité entre 300 µm et 1,7 mm (sans traitement de face) furent étudiées pour l'extraction des propriétés de base de ces lasers. Les

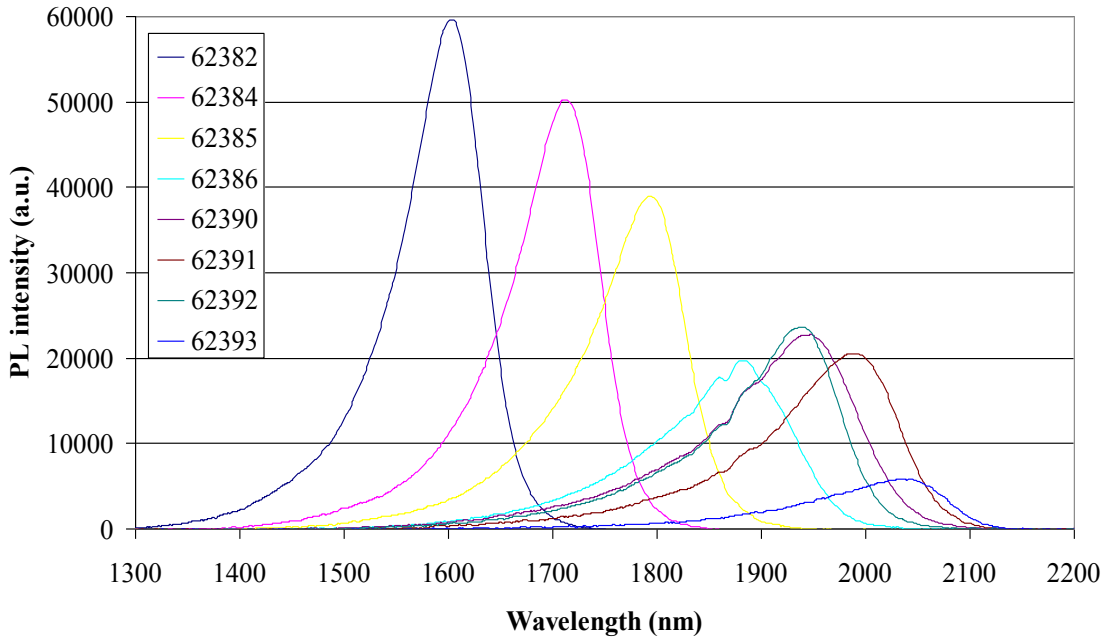

Figure 0.9 – Photoluminescence de tous les échantillons obtenus dans la première campagne de croissance, par variation de la hauteur des bâtonnets quantiques.

résultats pour l'échantillon de référence sont comparables à ceux des structures DWell optimisées pour une émission à 1,55 µm et préalablement testées au LPN. Quelques valeurs de paramètres clés ont été extraites des courbes densité de courant de seuil en fonction de l'inverse de la longueur de cavité (gain modal de 48 cm^{-1}) ou inverse de l'efficacité quantique différentielle (n_{ext}) en fonction de la longueur de cavité (pertes internes de 10cm^{-1}) . Des densités de courant de seuil de l'ordre de 1,5 kA/cm^2 ont été mesurées pour des longueurs de cavité variant entre 600 et 900 µm. Les caractéristiques électriques de ces lasers ont également été mesurées et les résistances série sont de l'ordre de 3 Ω. L'échantillon émettant à plus grande longueur d'onde (~1,8 µm) a également montré des performances satisfaisantes. Dans ce cas un produit Γg égal à 33 cm^{-1} a pu être mesuré pour les lasers à guide étroit avec des pertes internes de l'ordre de 12 cm^{-1}. Des courants de seuil relativement faibles , entre 50 et 70 mA, ont été relevés de façon routinière de même qu'une puissance élevée de l'ordre de 15 à 20 mW par face clivée a pu être obtenue. Ces résultats sont très satisfaisants étant donné que seule la taille des bâtonnets quantiques a été modifiée dans un empilement similaire à celui des lasers télécoms. D'autre part, pour les échantillons fabriqués à partir des plaquettes avec une PL ~ 2 µm, nous n'avons pas observé un effet laser. Notre interprétation en était que la barrière de potentiel pour les porteurs confinés dans le Qdash était trop profonde en raison de la grande différence d'énergie entre les Qdashes et le matériau barrière. Afin d'étudier cette hypothèse, différents types d'échantillons ont été préparés dans la deuxième campagne de croissance.

Deuxième campagne de croissance

Dans cette deuxième étape, le matériau de la barrière et donc les hauteurs des barrières pour les électrons et les trous ont été modifiées. Au lieu de la barrière élevée en InGaAsP (λ_{PL} = 1,17 µm) ou de la barrière intermédiaire en InGaAsP (λ_{PL} = 1,45 µm) pour les structures

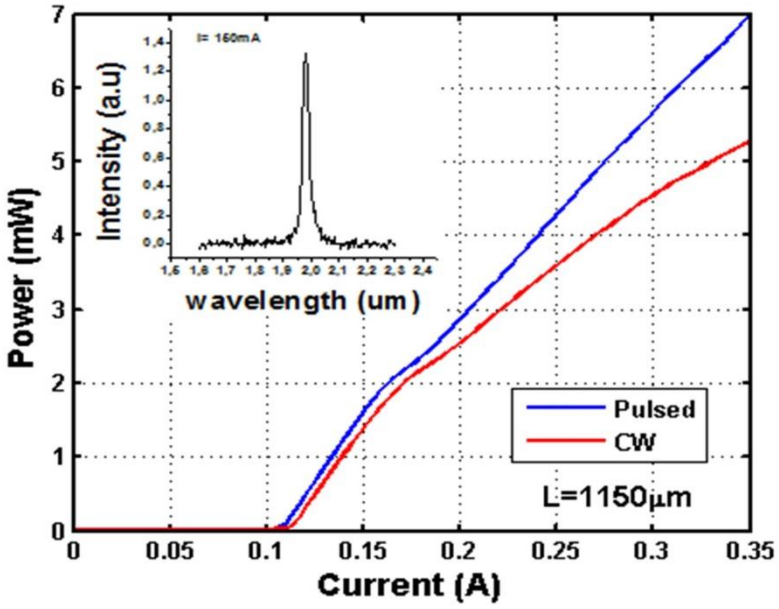

Figure 0.10 – Courbe L-I et spectre d'émission du laser Fabry-Pérot émettant à 1.99 µm.

DWell, une barrière basse en ternaire InGaAs a été utilisée. La composition de ce ternaire pour ~un accord en maille sur InP correspond à une largeur de bande interdite de λ~1,65 µm, et une composition $In_{0.53}Ga_{0.47}As$. L'idée était de réduire le nombre d'états excités de ces bâtonnets quantiques et également d'améliorer le transport des porteurs. Pour ce dernier point une couche supplémentaire de contact en quaternaire a de plus été introduite pour tous les nouveaux échantillons. Des lasers à contact large (100 µm) et à ruban étroit (2 µm), permettant un fonctionnement monomode transverse, ont été fabriqués et caractérisés. Une émission laser en continu à température ambiante a été démontrée jusqu'à une longueur d'onde de 2 µm. Les lasers émettant à 1,9 et 2 µm ont présenté un fort gain modal de l'ordre de 45 cm^{-1} et des pertes internes de 18 cm^{-1}. Des lasers à ruban de 2,5 µm de large ont montré des courants de seuil de 42 mA pour une cavité de 600 µm de long de type clivée/traitée AR. La figure 0.10 montre les caractéristiques P-I et le spectre optique d'un des meilleurs lasers de ce batch, avec des facettes clivées. La performance de ces lasers est satisfaisante en termes de gain et de courant de seuil bien qu'à des courants d'injection élevés en continu, nous avons été confrontés à des problèmes de saturation liée à un échauffement. Au vu des résultats obtenus sur l'ensemble de nos lasers**,** nous avons proposé de nouvelles structures épitaxiales, qui devraient résoudre ce problème tout en améliorant la performance globale des lasers émettant à 2 µm. De plus, nos résultats sont compatibles avec la possibilité d'étendre la longueur d'onde d'émission au-delà de 2 µm en utilisant le même système de matériau.

Lasers monomodes accordables pour la détection de gaz

Une fois que la longueur d'onde d'émission laser correspond au spectre d'absorption des espèces gazeuses à détecter, il est nécessaire d'utiliser des lasers mono-fréquences pour une meilleure résolution spectroscopique. Le premier laser dans des structures périodiques a été observé par Kogelnik et Shank en 1971 [43], et l'année d'après la théorie des modes couplés était introduite [44-46]. Une paire d'équations d'onde couplées sont résolues avec des conditions aux limites spécifiques. Le réseau de diffraction peut être décrit comme une variation périodique de l'indice de réfraction n(z) et/o du gain g(z) (ou pertes) dans le milieu laser. Tous les lasers accordables utilisés dans la spectroscopie des gaz peuvent être modélisés à l'aide de la théorie des modes couplés bien que différentes versions existent correspondant à des degrés de complexité et de performance différents. Dans ce travail nous nous sommes focalisés sur des solutions évitant une étape de re-croissance épitaxiale pour plus de simplicité de fabrication, paramètre important pour l'application visée. Les deux approches les plus communes qui ne nécessitent qu'une seule étape de croissance sont celles dite à accord par effet Vernier et par couplage latéral. Une seule (deux) électrode (s) est (sont) nécessaire(s) dans la partie guide d'onde et réseau de Bragg pour réaliser soit un 'LC-DFB' soit un 'LC-DBR'. Certains lasers DBR à couplage latéral incorporent en plus une section de phase pour une accordabilité en continu. Dans ces approches le réseau de Bragg peut être soit formé directement sur le guide d'onde après la gravure de ce dernier, soit inscrit sur les flancs du guide dans la même étape de gravure du guide. Une discussion détaillée de la littérature sur ces deux approches est donnée dans le manuscrit. En résumé, la technique de Vernier est relativement sensible aux effets de température avec des instabilités liées à de petits changements de température, ce qui nécessite une mise en module spécifique pour un fonctionnement fiable. Le coût de ces modules est alors en contradiction avec la spécification 'bas coût' pour les applications de détection de gaz. Par ailleurs les structures LC DFB/DBR ont montré, à notre connaissance, soit des coefficients de couplage relativement faibles ne pouvant garantir des taux de suppression des modes latéraux adéquats, soit des pertes optiques importantes dans le cas de réseaux de Bragg métalliques. Dans le cadre de ce travail de thèse, je me suis intéressé à la conception, à l'aide de la théorie des modes couplés, et fabrication de LC-DFB/DBR à base de réseaux de Bragg latéraux à semiconducteur à fort rapport cyclique**,** à même d'assurer un fort coefficient de couplage. Des valeurs > 40 cm^{-1} ont pu être atteintes.

Importance du coefficient de couplage du réseau de Bragg

De façon générale, les valeurs du coefficient de couplage normalisé κL rencontrées dans la littérature pour la conception de lasers DFB/DBR sont de l'ordre de ~ 1 – 1,25 , où κ est le coefficient de couplage et L la longueur de la section de Bragg. Cette valeur s'avère être empiriquement un bon compromis: pour des valeurs plus petites, le couplage entre les deux ondes contra-propagatives dans le guide d'ondes sera faible, donnant un taux de suppression des modes latéraux insuffisant. D'un autre côté, une valeur plus élevée serait responsable d'un effet bien connu et indésirable, le « spatial hole burning » (distribution non-uniforme des photons dans la cavité). En plus, pour obtenir une faible largeur de raie optique, un réseau

long, présentant un faible coefficient de couplage, doit être utilisé. Mais, lors de la conception de longs réseaux dans des lasers à deux sections, les pertes et donc le courant de seuil du laser augmenteraient ce qui est crucial pour des applications. Un bon compromis, en prenant en compte les considérations ci-dessus, serait de viser un coefficient de couplage de 35-40 cm^{-1} et une longueur de réseau de 300 μm. Réaliser de telles valeurs de κ n'est pas trivial pour des lasers à réseau latéral, dans lesquels le couplage est relativement faible, et a été obtenu jusqu'ici seulement par faisceau d'ions focalisés [47-49] pour la fabrication de lasers DBR à couplage latéral pour des applications en télécommunications. Dans ce travail, je montre qu'il est également possible de concevoir des réseaux à couplage latéral avec des valeurs suffisantes de κ après une conception judicieuse des paramètres du réseau, en utilisant la lithographie par faisceau d'électrons qui est une technique disponible dans de nombreux laboratoires scientifiques, et en évitant la reprise d'épitaxie sur des substrats comportant des réseaux gravés, ce qui est un défi technologique. Les détails de la conception sont discutés dans la prochaine section.

Conception et fabrication de lasers DFB/DBR à couplage lateral avec un coefficient κ optimisé

A partir de la théorie des modes couplés [44], le coefficient de couplage pour un réseau de section rectangulaire et de période constante peut être obtenu [50-51] :

$$\kappa = \frac{(n_1^2 - n_2^2)}{n_{eff}\lambda}\frac{\sin(\frac{m\pi w}{\Lambda})}{m}\Gamma_{grating} \qquad (1)$$

Où n_1 et n_2 sont les indices de refraction des matériaux au-dessus et en dessous du réseau, n_{eff} est l'indice effectif du mode guidé, Λ est la période du réseau de Bragg, m l'ordre de diffraction du réseau, w/Λ le rapport cyclique du réseau et $\Gamma_{grating}$ est la fraction du mode optique qui interagit avec le réseau. Comme on peut le voir d'après cette équation, en plus des paramètres de conception du réseau, afin d'obtenir une valeur pour cette expression, il faut aussi obtenir une estimation précise de l'indice effectif du mode n_{eff} et le facteur de confinement du mode guidé dans la région de Bragg. Comme les simulations 3D prennent beaucoup de mémoire, une alternative pour simuler la structure complète serait d'utiliser des simulations numériques à deux dimensions pour déterminer la distribution du champ électrique et l'indice effectif du mode, puis de choisir les paramètres de conception optimisée pour la valeur voulue de κ. Dans notre cas, l'analyse 2D a été réalisée à l'aide du Software Symphot Alcor, en utilisant l'approximation de l'indice effectif. Afin de simuler un laser DFB dans une telle configuration, le réseau doit être modélisé, à des fins de simulations 2D, comme une couche homogène avec un indice de réfraction moyen, calculé à partir de l'indice au-dessus et en dessous du réseau, afin d'obtenir une bonne approximation de la valeur de $\Gamma_{grating}$. Dans notre configuration LC-DFB, le matériau au-dessus du réseau est un diélectrique (BCB), alors que le matériau en-dessous du réseau est constitué de couches d'InP et d'InGaAsP. De telles valeurs pondérées peuvent être obtenues en utilisant les relations suivantes :

$$n_{grating}^2 = \frac{\Lambda 1}{\Lambda} n_{die}^2 + \frac{\Lambda 2}{\Lambda} n_{semicond}^2 \qquad (2)$$

Les couches d'InP et d'InGaAsP qui sont gravées et impliquées dans la fabrication du réseau peuvent être mise ensemble en utilisant l'équation 3. La valeur du paramètre $n_{semicond}$ dans l'équation 2 est obtenue selon la relation suivante:

$$n_{semicond}^2 = \frac{\sum_i t_i n_i^2}{t_{total}} \qquad (3)$$

où t_i et n_i correspondent à l'épaisseur et à l'indice de refraction de chaque matériau et t_{total} est l'épaisseur totale de la couche. Un examen attentif de l'équation 1 suggère que le paramètre clé pour augmenter le coefficient κ du laser à couplage lateral est le confinement optique du réseau, $\Gamma_{grating}$ (en plus bien sûr du contraste d'indice de réfraction). Il est alors évident à partir de nos simulations 2D que ce paramètre spécifique affecte fortement la valeur du $\Gamma_{grating}$, dont certains sont les paramètres du réseau et d'autres dépendent exclusivement de l'optimisation d'étapes de fabrication. Les paramètres qui devraient être utilisés pour l'optimisation de $\Gamma_{grating}$ sont listés ci-dessous :

1) Réduction de la distance latérale entre le guide et le réseau
2) Bon contrôle de la gravure du réseau (faible vitesse de gravure afin de s'arrêter juste au-dessus de la couche active pour maximiser le couplage avec un minimum de pertes)
3) Réduction de la largeur du guide
4) Optimisation de la valeur du rapport cyclique du réseau

Les paramètres 1 et 2 sont de purs paramètres d'optimisation de la conception qui requièrent des flancs de ridge complètement verticaux, sans re-déposition et un procédé de gravure à faible vitesse bien contrôlé pour des petits motifs. Nous avons réalisé une telle procédure d'optimisation afin de satisfaire à ces contraintes. Une ridge optimisé, obtenu par ICP est montré à droite de la figure 0.11. Sur la gauche, un ridge obtenu par gravure humide HCl utilisé dans notre procédé précédent est montré pour comparaison. Il apparaît évident que les ridges verticaux réduisent la distance latérale d'un réseau latéral à zéro, au contraire de ridges gravés chimiquement où la distance latérale est d'environ 150 nm. Des simulations 2D montrent qu'une telle distance latérale réduit de manière importante la valeur de $\Gamma_{grating}$, qui est directement proportionnelle à κ, par un facteur 3, par rapport au cas d'un ridge vertical à 90°. De plus, nous avons développé un procédé de fabrication de réseau de Bragg à faible vitesse, avec une bonne précision de contrôle de l'arrêt de gravure, répondant au critère n°2.

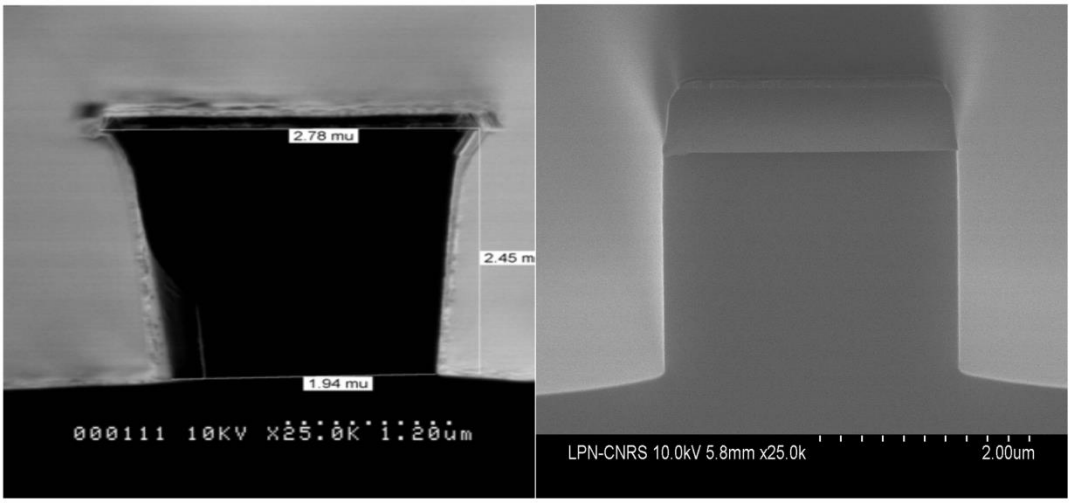

Figure 0.11 – Gauche: Guide d'onde en arête gravé en chimie humide par HCl au cours du procédé préliminaire. Droite : Guide d'onde en arête grave par voie sèche en ICP, compatible avec le procédé pour LC-DFB à coefficient de couplage élevé.

Le critère n°3, i.e. la réduction de la largeur du ridge est un paramètre très important pour réaliser une valeur de κ très élévée. Cependant, une réduction trop importante de cette valeur n'est pas souhaitable, car cela aurait des conséquences sur la puissance émise, sur les pertes intra-cavité et sur le contrôle de la valeur exacte de la valeur de κ (reproductibilité). Cette valeur de κ fluctue très vite pour des fluctuations de la largeur du guide. Pour cette raison, la largeur du guide a été fixée à 2 μm pour toutes les structures dans ce travail et l'ajustement de κ est obtenu en optimisant seulement le reste des paramètres mentionnés plus haut. La valeur du rapport cyclique, paramètre 4, est cruciale. L'examen de la littérature sur les lasers LC-DFB montre que les réseaux sont soit gravés soit réalisés par dépôt de métal, à partir d'un réseau de rapport cyclique 50% ou moins. Cependant, pour des applications pour lesquelles une valeur élevée de κ est requise, ce n'est pas un optimum. C'est parce qu'en augmentant le rapport cyclique au-delà de 50%, cela augmente la valeur de l'indice de

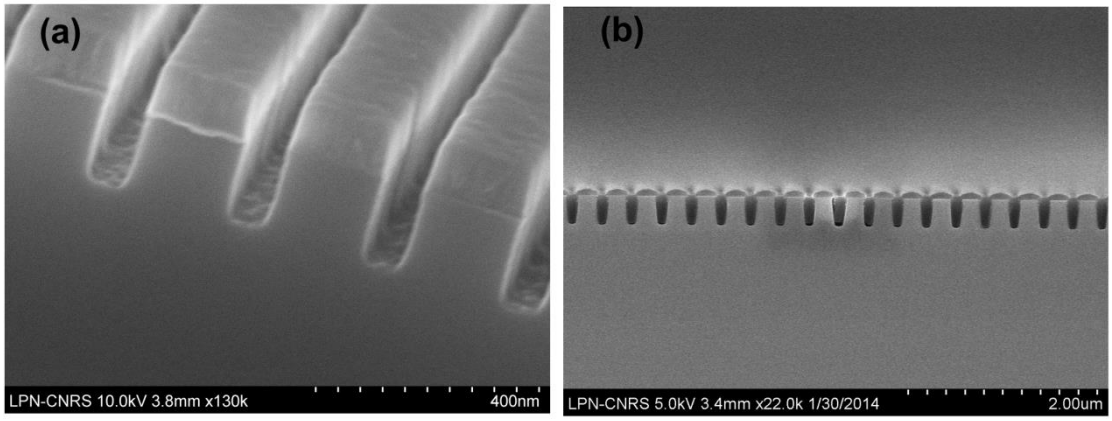

Figure 0.12 – Réseau de Bragg à rapport cyclique élevé, gravé avec un procédé de gravure sèche lent à base de CH_4-H_2 RIE. Gauche & droite: Avant bouchage des petites ouvertures par BCB.

réfraction pondéré (équation 2) dans la région du réseau et donc de $\Gamma_{grating}$, mais réduit la valeur du terme du sinus de l'équation 3.20, avec la condition aux limites d'absence de réseau où κ =0 pour un rapport cyclique de 100 %. A partir de ces considérations, il devient clair que le rapport cyclique optimum, qui dépend du couple d'indices de réfraction utilisée pour construire le réseau. Pour les structures discutées ici, nous avons trouvé à chaque fois qu'après chaque calcul du $\Gamma_{grating}$, le coefficient κ de l'équation (1) est maximisé pour un rapport cyclique de 79%. Nous avons fabriqué un réseau de Bragg avec un rapport cyclique élevé. Un exemple avant et après remplissage des ouvertures du réseau avec du BCB est illustré sur la figure 0.12 sur les photos droite et gauche respectivement. Tous les tests effectués et la procédure globale d'optimisation des étapes du procédé sont décrits en détails dans le chapitre 4. Les étapes du procédé décrites plus haut mèneraient à une amélioration du coefficient de couplage, avec nos simulations, suggérant qu'une valeur de 45 cm^{-1} est possible pour les paramètres déjà discutés ci-dessus, pour une largeur de guide de 2 μm. Cette hypothèse a été testée expérimentalement après fabrication de lasers LC-DFB émettant à 2 μm, en utilisant l'hétérostructure optimisée (wafer 63802). Un spectre d'émission centré à 1.986 μm, adapté pour la détection de NH_3, est représenté sur la figure 0.13. Les résultats expérimentaux confirment que ces valeurs élevées de κ peuvent être obtenues et que des lasers LC-DFB avec des SMSR élevés, plus grand que 40 dB (limités par le rapport signal-à-bruit de notre banc expérimental), ont été démontrés. Cette valeur est suffisante pour la fabrication de lasers LC-DBR utilisant cette technologie. Finalement, il est important de noter que pour n'importe quelle application, une amélioration du κ peut être obtenue avec ce design, simplement en réduisant la largeur du ridge. Cette conception est complètement générale

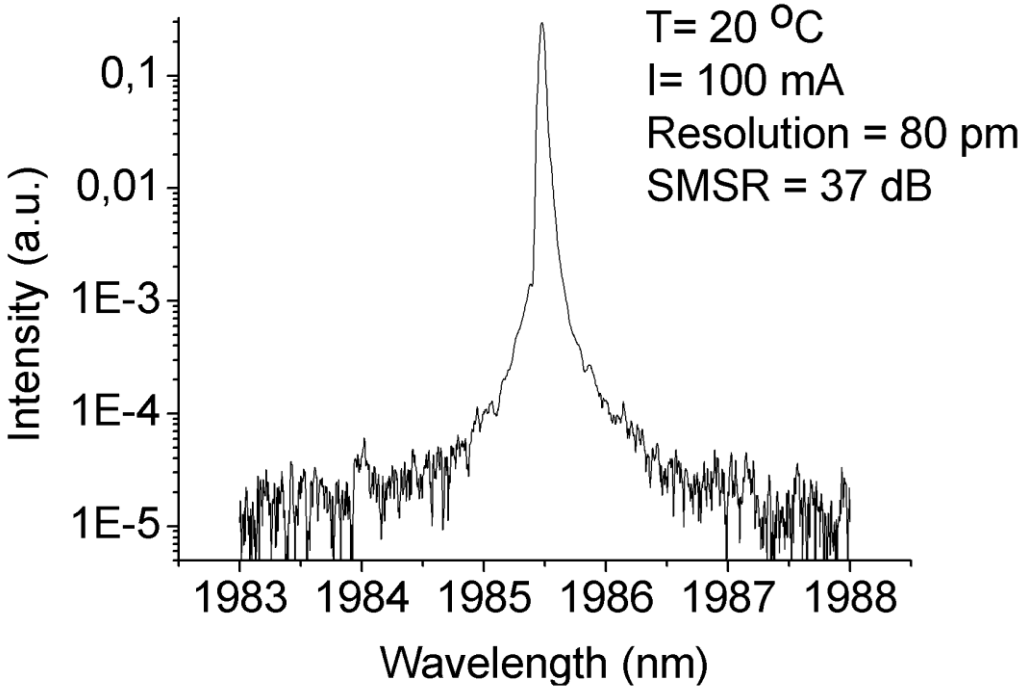

Figure 0.13 – Spectre d'émission du laser DFB, centré à 1,986 μm, adapté pour la détection de NH_3.

et applicable à n'importe quel système de matériau, tant que des recettes de gravure pour des tranchées étroites sont disponibles, afin d'obtenir une bonne qualité de gravure de réseau de Bragg.

Conclusions

Au cours de ce travail, nous avons évalué les propriétés fondamentales de bâtonnets quantiques, dans une diode laser en utilisant la microscopie à effet tunnel et la spectroscopie. Les principaux résultats concernent la question de la nature de la dimensionnalité des QDash, sonder la structure électronique des nanostructures individuelles par rapport à la localisation précise de la jonction p-i-n et imager la fonction d'onde électronique des batônnets quantiques par des mesures de conductivité différentielle. D'autre part, nous avons évalué ces batônnets quantiques comme matériau actif pour des applications de détection de gaz. Nous avons optimisé le matériau à base de QDashes démontrant une émission en régime continu jusqu'à 2 μm avec des hautes performances, alors que nos résultats expérimentaux et simulations sont très prometteurs pour augmenter encore la longueur d'onde. De plus, un nouveau procédé a été développé pour la fabrication de réseau à couplage latéral complexe en utilisant le concept de haut rapport cyclique de réseaux, ce qui améliore significativement le coefficient de couplage (>40 cm^{-1}).

Ce procédé n'introduit pas d'étape de reprise d'épitaxie sur des susbstrats corrugués, assurant une simplicité et un bas coût au procédé, tandis que le coefficient de couplage est obtenu sans utilisation conventionnelle de réseau absorbant métallique, qui introduit des pertes significatives. Nous avons développé cette approche sur nos wafers optimisés et démontré un SMSR élevé (>37dB) à 1.986 μm, adapté pour la détection de NH_3. De telles hautes valeurs de κ, de faibles pertes, des lasers LC-DFB obtenus en utilisant des réseaux gravés sont des résultats préliminaires compatibles avec la fabrication de lasers deux sections LC-DBR utilisant la même technologie dans le futur. Un tel laser combinerait un procédé de fabrication grandement simplifié, avec un feedback suffisant, une accordabilité de > 10 nm, et des pertes induites par le réseau négligeables, trouvant ainsi des applications potentielles pour la détection et les applications en télécommunications.[1]

[1] A part of the Résumé, has been adopted with permission from (K. Papatryfonos, G. Rodary, C. David, F. Lelarge, A. Ramdane, and J.C. Girard, "One-Dimensional Nature of InAs/InP Quantum Dashes Revealed by Scanning Tunneling Spectroscopy," Nano Lett. **2015** 15 (7), 4488-4497; DOI: 10.1021/acs.nanolett.5b00963.). Copyright (2015) American Chemical Society.

Références

1) Y. Arakawa and H. Sakaki, Appl. Phys. Lett., vol. 40, pp. 939-941, (1982).

2) M. Asada, Y. Miyamoto, and Y. Suematsu, IEEE J. Quantum Electron., 22, 1915-1921, (1986).

3) G. T. Liu, A. Stintz, H. Li, K.J. Malloy and L.F. Lester, Electron. Lett. 35 1163–1165, (1999).

4) K. Mukai, Y. Nakata, K. Otsubo, M. Sugawara, N. Yokoyama and H. Ishikawa, IEEE J. Quantum. Electron. 36, 472–478, (2000).

5) J.P Reithmaier, A. Somers, S. Deubert, R. Schwertberger, W. Kaiser, A. Forchel, M. Galligaro, P. Resneau, O. Parillaud, S. Bansropun, M. Krakowski, R. Alizon, D. Hadass, A. Bilenca, H. Dery, V. Mikhelashvili, G. Eisenstein, M. Gioannini, I. Montrosset, T.W. Berg, M. van der Poel, J. Mork, B.J. Tromborg, J. Phys. D 2005, 38, 2088-2102., J. Phys. D, 38, 2088–2102, (2005).

6) K. Papatryfonos, S. Joshi, K. Merghem, S. Bouchoule, S. Guilet, L. Le Gratiet, A. Martinez, A. Ramdane, Indium Phosphide and Related Materials (IPRM), 26th International Conference on, 10.1109/ICIPRM.2014.6880538, 1-2 (2014).

7) W. Zeller, M. Legge, A. Somers, W. Kaisser, J. Koeth and A. Forchel, Electron. Lett. 44, 5 (2008).

8) F. Lelarge, B. Dagens, J. Renaudier, R. Brenot, A. Accard, F. Dijk, D. Make, O. L. Gouezigou, J.-G. Provost, F. Poingt, J. Landreau, O. Drisse, E. Derouin, B. Rousseau, F. Pommereau, and G.-H. Duan, IEEE J. Sel. Top. Quantum Electron. 13(1), 111–124 (2007).

9) R. Rosales, S. G. Murdoch, R. T. Watts, K. Merghem, A. Martinez, F. Lelarge, A. Accard, L. P. Barry, and A.Ramdane, Opt. Express 20(8), 8649–8657 (2012).

10) H. Dery, E. Benisty, A. Epstein, R. Alizon, V. Mikhelashvili, G. Eisenstein, R. Schwertberger, D. Gold, J. P. Reithmaier, and A. Forchel, J. Appl. Phys. 95(11), 6103–6110 (2004).

11) M. Gioannini, IEEE J. Quantum Electron. 40(4), 364–373 (2004).

12) S.C. Heck, S. Osborne, S.B. Healy, E.P. O'Reilly, F. Lelarge, F. Poingt, O. le Gouezigou, and A. Accard, IEEE J. Quantum Electron. 45, 12, (2009).

13) H. Saito, K. Nishi, and S. Sugou, Appl. Phys. Lett. 78, 267 (2001).

14) C. Ni. Allen, P. J. Poole, P. Marshall, J. Fraser, S. Raymond, and S. Fafard, Appl. Phys. Lett. 80, 3629 (2002).

15) K. Klaime, C. Calò, R. Piron, C. Paranthoen, D. Thiam, T. Batte, O. Dehaese, J. Le Pouliquen, S. Loualiche, A. Le Corre, K. Merghem, A. Martinez, and A. Ramdane, Optics Express, 21, 23, 29000-29005 (2013).

16) A. Lenz, F. Genz, H. Eisele, L. Ivanova, R. Timm, D. Franke, H. Künzel, U. W. Pohl, and M. Dähne, Appl. Phys. Lett. 95, 203105, (2009).

17) F. Genz, A. Lenz, H. Eisele, L. Ivanova, R. Timm, U. W. Pohl, M. Dähne, D. Franke, and H. Künzel, Journal of Vacuum Science & Technology B 28, C5E1 (2010).

18) A. Musiał, P. Kaczmarkiewicz, G. Sęk, P. Podemski, P. Machnikowski, J. Misiewicz, S. Hein, S. Höfling, A. Forchel, Phys. Rev. B 85, 035314 (2012).

19) P. Kaczmarkiewicz and P. Machnikowski, Semicond. Sci. Technol. 27, 105012 (2012).

20) M. Gioannini, IEEE J. Quantum Electron. 42, 3 (2006).

21) J. P. Reithmaier, G. Eisenstein, and A. Forchel, Proc. IEEE, 95, 1779 (2007).

22) T. Mensing, L. Worschech, R. Schwertberger, J. P. Reithmaier, and A. Forchel, Appl. Phys. Lett. 82, 2799, (2003).

23) B. Salem, N. Chauvin, T. Benyattou, G. Guillot, C. Bru-Chevallier, G. Bremond, C.Monat, P. Rojo-Romeo, and M. Gendry, Nanotechnology 16, 444, (2005).

24) N. Chauvin, B. Salem, G. Bremond, G. Guillot, C. Bru-Chevallier, and M. Gendry, J.Appl. Phys. 100, 073702, (2006).

25) M. Z. M. Khan, T. K. Ng, U. Schwingenschlogl, P. Bhattacharya and B.S. Ooi, Optics Express, 19, 14, (2011).

26) M. Z. M. Khan , T. K. Ng , C.-S. Lee , P. Bhattacharya and B. S. Ooi, IEEE Photon. J. 5, 4, 1501308 -1501308, (2013).

27) L. Dusanowski, A. Musiał, A. Maryński, P. Mrowiński, J. Andrzejewski, P. Machnikowski, J. Misiewicz, A. Somers, S. Höfling, J.P. Reithmaier, G. Sęk, Phys. Rev. B 90, 125424, (2014).

28) K. Suzuki, K. Kanisawaa, S. Perraud, M. Ueki, K. Takashina, Y. Hirayama, J. Cryst. Growth, 301–302, 97–100, (2007).

29) A. Bera, S. Dey, A.J. Pal, Nano Lett. 14, 2000−2005, (2014).

30) B. Fain, I. Robert-Philip, A. Beveratos, C. David, Z. Z. Wang, I. Sagnes, and J. C. Girard, Phys. Rev. Lett. 108, 126808, (2012).

31) nextnano: General Purpose 3-D Simulations, S. Birner, T. Zibold, T. Andlauer, T. Kubis, M. Sabathil, A. Trellakis, P. Vogl, IEEE Trans. Electron Devices 54, 2137, (2007).

32) B. Fain, Ph.D. Thesis, Ecole Polytechnique, September (2012), pp. 46–51

33) R M Feenstra, Y Dong, M P Semtsiv and W T Masselink, Nanotechnology 18, 044015, (2007).

34) A.C. Ford, S.B. Kumar, R. Kapadia, J. Guo, and A. Javey, Nano Lett. 12, 1340−1343, (2012).

35) H. Lin, J. Lagoute, V. Repain, C. Chacon, Y. Girard, J.-S. Lauret, F. Ducastelle, A. Loiseau and S. Rousset, Nature Mater. 9, 235 (2010).

36) S. Perraud, K. Kanisawa, Z.Z. Wang and Y. Hirayama, J. Phys.: Conf. Ser. 61 926, (2007)

37) G. Sęk, M. Motyka, K. Ryczko, J. Andrzejewski, R. Kudrawiec, J. Misiewicz, F. Lelarge, B. Rousseau, G. Patriarche, Proc. SPIE 6481, 64810D, 1-7, (2007).

38) D. Deppe, H. Huang, and O. Shchekin, IEEE J. Quantum Electron. 38(12), 1587–1593, (2002).

39) D. Bimberg, N. Kirstaedter, N. N. Ledentsov, Z. I. Alferov, P. S. Kop'ev, and V. M. Ustinov, IEEE J. Sel. Top. Quantum Electron., 3, 2, 196 –205, (1997).

40) M. Willatzen, T. Tanaka, Y. Arakawa, and J. Singh, IEEE J. Quantum Electron. 30, 3, 640 –653, (1994).

41) S. M. Kim, Y. Wang, M. Keever, and J. S. Harris, IEEE Photon. Technol. Lett. 16, 2, 377 –379, (2004).

42) P. Borri, W. Langbein, J. Mørk, J. Hvam, F. Heinrichsdorff, M.-H. Mao, and D. Bimberg, Phys. Rev. B 60, 11, 7784–7787, (1999).

43) H. Kogelnik and C.V. Shank, App. Phys. Lett., 18, 152-154, (1971).

44) H. Kogelnik and C.V Shank, Journ. of Appl. Phys. 43, 2327-2335, (1972).

45) A. Yariv, IEEE J. Quantum Electron. 9, 919-933, (1973).

46) A. Othonos and K. Kalli, "Fiber Bragg gratings: fundamentals and applications in telecommunications and sensing", Artech House, (1999).

47) S. Rennon, L. Bach, J.P. Reithmaier and A. Forchel, IEEE J. Sel. Top. Quantum Electron. 7(2), 306–311, (2001).

48) L. Bach, S. Rennon, J. P. Reithmaier, A. Forchel, J. L. Gentner, and L. Goldstein IEEE Photon. Technol. Lett. 14, 7, 1037-1039, (2002).

49) L. Bach, W. Kaiser, J. P. Reithmaier, A. Forchel, M. Gioannini, V. Feies, and I. Montrosset, IEEE Photon. Technol. Lett. 16, 1, 18-20, (2004).

50) G.P. Agrawal and N.K. Dutta (Van Nostrand Reinhold, New York), (1968).

51) W.-Y. Choi, J.C. Chen, C.G. Fonstad, Jpn. J. Appl. Phys. 25, 4654-4659, (1996).

Acknowledgements

First, I would like to thank A. Ramdane and A. Martinez for their enormous support, guidance and trust that they have provided me. Thanks to their continuous help, I have carried out this PhD thesis with confidence and enthusiasm.

I express my gratitude to Jean-Yves Marzin and Dominique Mailly, directors of CNRS Laboratory for photonics and nanostructures (LPN) during my PhD studies, for allowing me to conduct my research work in the lab under very nice conditions.

I also thank the members of the doctoral committee: A. Vicet, A. Le Corre, A. Krier, and A. Benlarbi-Delai for having willingly examined and judged this PhD dissertation.

Working with K. Merghem at the LPN has been a great pleasure. He provided my whole initial training and helped me with very valuable and fruitful discussions under the whole period of my thesis. I thank him for his constant support.

I would also like to thank the members of the LPN clean room technical service as well as the entire PHODEV group, who contributed directly or indirectly in the fabrication and processing of the lasers used within this work, and in particular, S. Bouchoule, S. Guilet, L. le Gratiet and A. Cattoni. I collaborated with them intensively during the development of novel clean room processes, aiming to optimize the fabrication steps for LC-DFB lasers as much as possible. Within this framework, we performed with them many interesting and stimulating discussions, throughout my stay at LPN, which enabled me to acquire a lot of new knowledge.

I am also very grateful to D. Kazazis, who, even though not a member of the clean room stuff or my group, never hesitated to offer me valuable advices about clean room processing, whenever I had some question or uncertenty.

I am very grateful to the Scanning Tunneling Microscopy group, J.C Girard, G. Rodary and C. David, for the collaboration we had for the investigation of the fundamental properties of individual quantum dashes. It has been an amazing experience which I really enjoyed, I have learned a lot from it, and I am particularly satisfied with the final results we obtained.

My project has been a part of the European Marie Curie Initial Training Network PROPHET. I would like to acknowledge the network for the funding that enabled me to perform my studies, and all the individual members of the network for the very fruitful discussions and exchanges we had during the workshops and conferences organized by PROPHET. I would like to particularly acknowledge the members of the network with whom we initiated very

close collaborations, as members of the Work Package III that focused on environmental applications. First of all I would like to thank the work package leader, A. Krier for his guidance and valuable advices. In addition, the researchers from the III-V lab, F. Lelarge and S. Joshi for providing the epitaxial structures used in this project, Q. Lu from the University of Lancaster for his collaboration on low-temperature photoluminescence and laser measurements on our samples during my secondments visit in their lab, the researchers from the Tyndall National Institute, D. Salatukha, T. Ochalski and G. Huyet, for their collaboration on high-resolution measurements on our Fabry-Perot and DFB lasers and K. Kloss and F. O'Dehorty from Procal for their valuable advices related to industrial gas sensing applications.

I thank the whole IT and administrative staff of the LPN for their continuous and kind assistance which allowed me to conduct my research work in an efficient way.

Throughout my stay at the LPN, I have benefitted from the acquaintance of many people. I enjoyed very much both the scientific and general discussions I had with them, as well as their friendship and closeness, inside and outside of the lab; they made may stay in France a very pleasant experience. Special thanks, first of all to my office mates who shared a very big number of important moments with me: R. Rosales, C.Calo, V. Panapakkam and D. Kazazis and of course to: D. Kazazis, O. Mollet, A. Cattoni, J. Carimalo, S. Belahsene, K. Merghem, D. Kimura, S. Portalupi, N. Somaschi, A. Itawi, C. Gomez, N. Dubrovina, J. Lee, K. Pantzas, V. Kumaresan, M. Morassi, J. Castro, J. Chaste, F. Parmentier, S. Jesouin, E. Pallecchi G. Rodary from LPN and M. Anagnosti and S. Joshi from III-V lab.

Last but not least, I would like to express my special thanks to my good friends from Cyprus, Christos Apostolides and Christoforos Kronis, who even though not involved in the project or my research laboratory, they have helped me very much, through their expertise in computer science, to optimize the Matlab codes that I developed for the purpose of modelling the Bragg grating structures behavior, for their implementation in DFB and DBR lasers.

Finally, I deeply thank all of my beloved family for their endless and unconditional support.

Introduction

Semiconductor quantum dots (QDs) have attracted a lot of attention in the last decades owing to their expected remarkable properties arising from their carrier confinement in all three spatial dimensions [1,2]. As a result they exhibit a discrete energy spectrum which may be tailored during their epitaxial growth by simply adjusting their composition, shape or size. Particular interest has been given to laser applications with low threshold current densities and high temperature insensitivity, which have been readily demonstrated in the InAs/GaAs material system covering the O-band telecommunications window at 1.3 μm [3,4]. For the C-band window at 1.55 μm, as well as for other applications such as high resolution absorption spectroscopy for gas sensing, requiring emission wavelengths at around 2 μm, the InP based material system needs to be utilized [5,6]. While the lattice mismatch between InAs and GaAs is ~7%, leading to the formation of quantum dots for an InAs layer above the critical thickness, this value is by a factor of 2 less in the InAs/InP case. The differences in the growth conditions result in the growth of elongated InAs islands on [001] oriented InP substrate, often referred to as quantum dashes (Qdashes) [7]. These nanostructures have a (1-10) cross section similar to that of a shallow quantum dot, 3-4 nm X 10-20 nm, while their length in the [1-10] direction is of the order of 200-300 nanometers. Such quantum dash structures have shown to have advanced laser characteristics suitable for practical applications [8], as well as superior mode locking characteristics [9] and their impact on laser dynamics has been investigated theoretically in some detail [10-12]. Growing of InAs QD's on InP substrate is difficult [10] although at specific growth conditions it can be possible and some have been demonstrated [13-15]. However, in this work we restricted our focus on Qdashes due to the fact that up to present they systematically exhibit superior device performances to QD's in this wavelength range.

In the present work Qdash nanostructures have been investigated experimentally, firstly in regard to their fundamental properties aiming to get a better insight into their electronic structure and secondly by the assessment of laser device performances, wherein Qdash ensembles have been incorporated as the active material; aiming to exploit their advantages at specific applications, with particular interest to the Gas Sensing application.

In the first part, of our work, low-temperature cross-sectional scanning tunneling microscopy and spectroscopy (X-STM/STS) has been performed on InAs(P)/InGaAsP/InP(001) quantum dashes, which were embedded in a diode-laser structure. The laser active region is un-doped and consists of nine quantum dash layers separated by the quaternary alloy barriers. The investigation included both large-scale measurements, across the whole active region as well as high-energy-resolution measurements on individual Qdashes obtained after focusing in a smaller area. On large-scale tunneling spectroscopic measurements, the effect of the p-i-n junction build-in potential on the band structure has been evidenced and quantified: By comparing the tunneling current onset channels in successive quantum dash or barrier layers, a consistent energy shift has been measured each time, either for the ground state energy of the quantum dashes or for the conduction band edge of the barriers. The extracted values are quantitatively in very good agreement with the theoretical band structure calculations, demonstrating the high sensitivity of this spectroscopic measurement to probe the electronic structure of individual nanostructures, relative to spatially resolved local potential variations. Furthermore, it is shown that by taking advantage of the doping-induced band bending feature in dimensionality studies, a hypothetical 0-D behavior can be ruled out. In order to acquire further proof and fully address the open question concerning the quantum dash dimensionality nature, we focused on individual quantum dashes obtaining high-energy-resolution measurements. The study of the local density of states clearly indicates a 1-D quantum-wire-like nature for these nanostructures whose electronic squared wavefunctions were subsequently imaged by differential conductivity mapping. This measurement exhibited a twofold fundamental interest, since in addition to the comprehensive Qdash experimental investigation, it has been shown that the X-STM/STS wavefunction imaging obtained from high stability conductance maps measurements at low temperature (T=5K), could be extended to practical device structures with low-doped area, offering further insights into the behavior of semiconductor nanostructures.

In the second part, we developed Qdash based laser diodes emitting in the long wavelength range, suitable for high resolution absorption spectroscopy for Gas sensing. This work has been part of a close collaboration between the PHOTDEV group at LPN and Alcatel-Thales III-V lab. At LPN we performed the laser processing, basic characterization and material design for the following growth campaigns, while III-V lab were in charge of performing the material growth. The whole project was part of the Initial Marie Curie

Training Network (ITN) PROPHET and within this network further laser characterization was performed, whenever this was necessary, in collaboration with our academic partners: The Tyndall National Institute at Cork, Ireland and the University of Lancaster at the U.K. As a starting point, both PHOTEV and III-V lab had strong expertise at the fabrication of Qdash based lasers emitting at 1.55 μm, which have been previously very well studied and successfully used for applications in telecommunications. During this project the main target has been to push the emission wavelength out towards longer wavelengths while maintaining satisfactory performances. The main motivation for this would be to use such lasers for optical gas detection, benefiting by the fact that many important polluting gases have strong absorption lines at 2 μm or at longer wavelengths, which combined with the fact that water has weak absorption in this wavelength range, enables high resolution absorption spectroscopy for gas sensing. The nominal composition for the Qdashes was binary InAs, while in this part of the project the barrier composition was changing depending on the targeted emission wavelength, following our optimization procedure which will be explained in detail in Chapter 2. All of our experiments and device processing have been performed on S-doped InP(001) substrate. The emission wavelength change has been achieved by increasing the Qdash sizes, with the Qdash height being the dominant parameter that determines its value. A step-by-step circular process was followed, in which the emission wavelength (Qdash size) was shifted by a certain amount, and subsequently the whole structure was optimized in respect to the new emission wavelength, before attempting a further shift. After several runs of material growth and laser processing and characterization we have achieved satisfying performances for emission wavelength up to 2 μm, while our results combined with additional simulations show to be very promising for achieving even longer emission wavelengths, with the same material system, in the future. A description of the main steps of the whole material optimization procedure will be provided within this manuscript.

After achieving the appropriate emission wavelength in respect to the gas resonances, in order to target high-resolution gas detection single-frequency lasers are highly desirable. Therefore, another aim of this project has been the processing of distributed feedback (DFB) or distributed Bragg reflector (DBR) lasers out of our optimized epi-wafers. According to our industrial partners within the PROPHET network, in order to be competitive to alternative technologies while designing laser diodes for future industrial applications in the field of gas sensing, one needs to have in mind two important parameters: namely the laser fabrication

cost and the threshold current should be minimized as compared to what is available at the moment.

In an attempt to address the above targets we developed a novel clean-room process suggesting the laterally-coupled DFB (LC-DFB) lasers with high-duty-cycle etched semiconductor gratings. The laterally-coupled design addresses the target of lowering the cost, by significantly simplifying the fabrication process neglecting the very demanding regrowth steps; the etched grating addresses the need for lower threshold current and higher output power due to the substitution of the conventional highly-absorbing metal Bragg gratings; while the high-duty-cycle ensures maintaining a sufficient coupling coefficient between the grating and the guided mode, which was not achieved in any of the previously reported LC-DFB lasers with etched gratings. Using this process we succeeded in demonstrating single-mode DFB lasers with a high side mode suppression ratio (SMSR) of the order of 40 dB and threshold current and output power which have similar values to the Fabry–Pérot (FP) lasers obtained from the same wafer. In addition, we show that the coupling coefficient of these fabricated lasers is of the order of 40 cm^{-1} which is sufficient for the fabrication of laterally-coupled DBR (LC-DBR) lasers with sufficiently small grating sections (~300 - 400 μm) using the same technology but in two- or three-section configurations. Furthermore, this technology is completely general and may be used in any material system as long as sufficient etching recipes for fabricating high-quality gratings are developed. All the details concerning the simulation based design, the optimization of the processing steps and final results will be provided within this manuscript.

In accordance with the research strategy outlined above, this thesis is structured as follows:

In the first Chapter, after a brief introduction and literature revue on the concept of the Qdash electronic structure, the motivation behind the performed scanning tunneling spectroscopic measurements is outlined and the main results are depicted and analyzed.

Chapter 2 focusses on the material optimization process, analyzing the different steps that were followed. Furthermore, it summarizes the potential advantages of Qdashes as the active material for laser fabrication and subsequently presents our main results in this aspect and compares them to the current state of the art. The Chapter concludes with future perspectives in material design and indicates the possibility of achieving even longer

wavelengths in the future with this material system, in respect to our final design for 2 μm emission.

In Chapter 3 after a brief introduction on the coupled-mode theory, we analyze our simulations methodology. Based on the results, we underline the perspective in using high-duty-cycle etched semiconductor gratings for the fabrication of LC-DFB/LC-DBR lasers in respect to the desired specifications of the gas sensing industry, as they were outlined by our industrial partner within the PROPHET ITN network.

Chapter 4 details the optimization of the processing steps for the realization of such devices and illustrates our results on Qdash based LC-DFB lasers emitting at 2 μm. The last section the Chapter underlines the opportunities in achieving LC-DBR lasers by benefiting from this design in the future, in respect to the high coupling coefficients evidenced in the DFB results.

Finally, conclusions and general future perspectives of this work are drawn.

Chapter 1

Cross-sectional scanning tunneling microscopy and spectroscopy on single Quantum Dashes

Qdashes are relatively new nanostructures that exhibit particular physical dimensions, lying between those of QD's and nanowires (NWs), as well as peculiar shapes. While an important number of successful experimental demonstrations using Qdash ensembles have already been reported, the literature has been rather contradictive concerning the physical properties of Qdashes such as their electronic structure and dimensionality nature. A better knowledge would be beneficial both from a fundamental as well as a practical point of view. In the work described in this Chapter we aimed to obtain a better insight in to the basic properties of single Qdashes that where incorporated within a laser structure, using cross-sectional scanning tunneling microscopy and spectroscopy. The main results included addressing the Qdash dimensionality nature, probing the electronic structure of individual nanostructures in respect to their precise location in the p-i-n junction and imaging of the Qdash electronic squared wavefunctions by high-stability differential conductivity mapping.

The Chapter is organized as follows: In section 1.1 a brief introduction concerning the Qdash expected dimensionality nature and electronic structure is provided in respect to the available literature and to the different points of view. The motivation behind performing this measurement is outlined. Sec 1.2 consists of an introduction of the operation principles of our STM experimental setup, while in sec 1.3 an introduction to our STS spectroscopic measurements and the underlying theory is provided. In sec 1.4, the sample preparation and the experimental procedure are briefly described. In sec. 1.5, we present large-scale, but low-resolution, measurements across the whole active region and report our results on probing the quantum dash electronic structure in respect to spatially resolved local potential variations. The experimental results are then compared to theoretical band structure calculations, obtained after solving self-consistently the Schrodinger-Poisson equations. In sec 1.6, we present results after focusing on a smaller area, obtaining high-energy-resolution spectroscopic measurements. The open question on the Qdash dimensionality nature has been addressed by spatially-resolved differential conductance measurements, which is proportional

to the local density of states (LDOS(E)). In sec. 1.7, by acquiring both spatially and energetically resolved differential conductance maps, imaging of the electronic squared wavefunctions on a cross-sectional area of a single Qdash has been performed. Finally, finite-element simulations of the Qdash wavefunctions are presented in sec 1.8 and compared to the experimental results. The Chapter is concluded with the discussion of sec 1.9.[2]

1.1. Introduction

Qdashes have a cross section similar to that of a shallow quantum dot, while their length in the [1-10] direction is of the order of 200-300 nanometers. Such nanostructures have been used as the active material in semiconductor lasers and optical amplifiers sowing to have advanced characteristics suitable for practical applications [8] and their impact on laser dynamics has been investigated theoretically [10-12]. In addition, the atomic structure of InAs Qdashes in a similar material system, as well as the observed decomposition of the InGaAsP quaternary matrix material have been recently analyzed using cross-sectional scanning tunneling microscopy (X-STM) [16-18]. However, while a number of open questions were raised and discussed in the related literature, Qdashes being relatively new nanostructures, they are not yet fully described in terms of their physical properties, such as the electronic density of states. A comprehensive experimental study on their dimensionality nature has been lacking up to the present, the distinction between Qdashes and QDs has not been clear and both terms can be found in literature used for nanostructures with similar lateral geometry. Common ways traditionally used in order to predict whether a nanostructure will exhibit a QD-like behavior, such as comparing its physical dimensions to the exciton Bohr radius, cannot be directly applied to the Qdash case due to the very high asymmetry of these structures; Qdash is a particular material, compared to conventional nanowires or QD's due to its high length-to-width and width-to-height ratios (of the order of 10), as well as strong shape fluctuations including local widenings and zigzag bends. For example, as it can be seen in the TEM plan view of Figure 1.1, strong fluctuations in the cross section characteristic length of single dashes are observed. As also discussed by Dery et al. [10], such fluctuations are likely to introduce further localization of carriers and might lead to a zero dimensional (0-D) electronic density of states behavior for some or all of the dashes. In later

[2] A part of this Chapter, has been adopted with permission from (K. Papatryfonos, G. Rodary, C. David, F. Lelarge, A. Ramdane, and J.C. Girard, "One-Dimensional Nature of InAs/InP Quantum Dashes Revealed by Scanning Tunneling Spectroscopy," Nano Lett. **2015** 15 (7), 4488-4497; DOI: 10.1021/acs.nanolett.5b00963.). Copyright (2015) American Chemical Society.

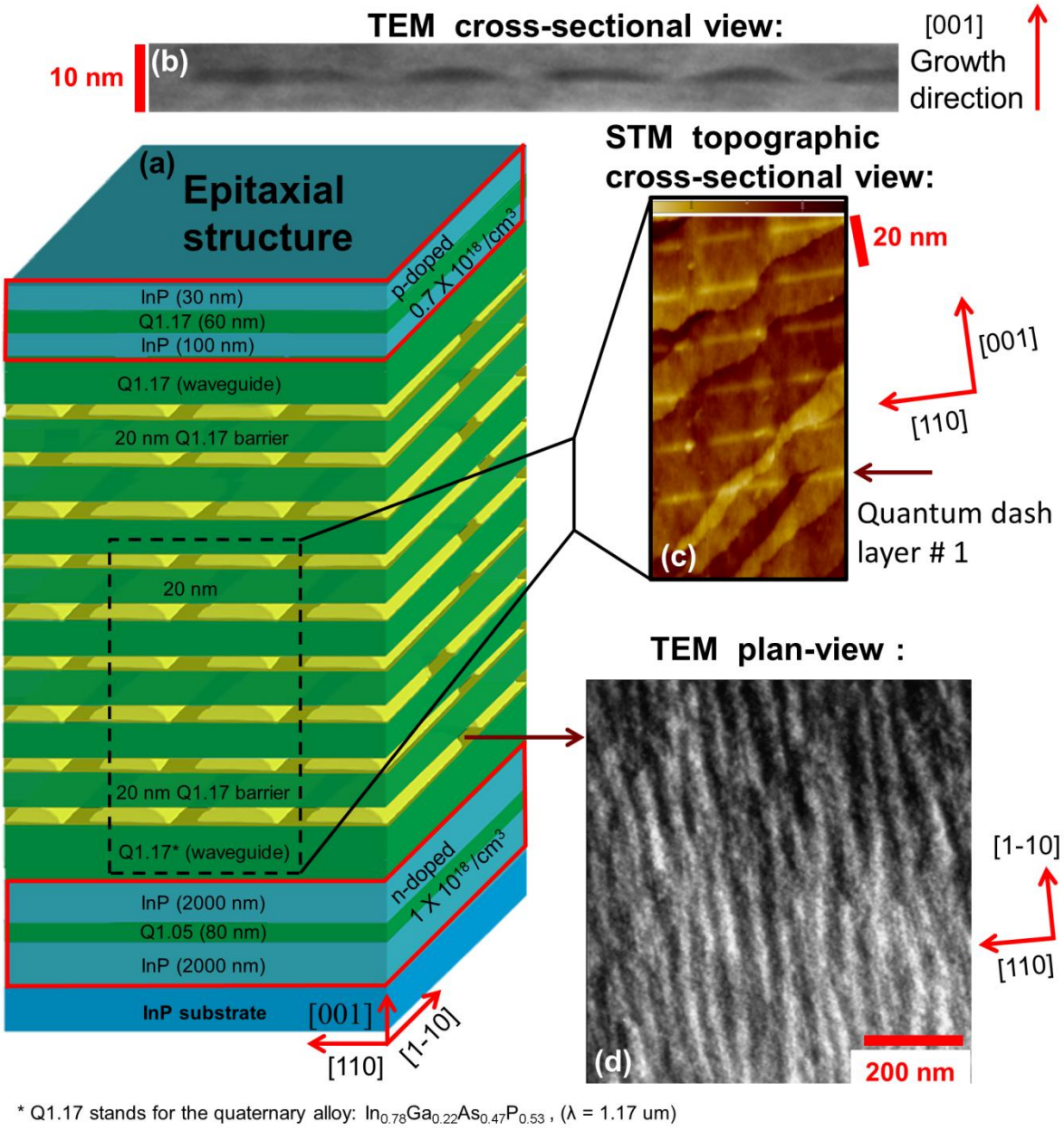

Figure. 1.1 - (a) Schematic of the epitaxial structure, (b) TEM cross-sectional view, (c) STM cross-sectional topographic image and (d) TEM plan-view of the studied sample. The structure was grown on an S-doped InP(001) substrate. The un-doped active laser area consists of nine quantum dash layers separated by 20 nm thick quaternary alloy InGaAsP(λ=1.17 μm) barriers, sandwiched between two thicker quaternary waveguide layers. The lower buffer layers are n-doped while the upper layers are p-doped. The investigated sample does not include the regrown upper cladding and contact layers that are used in laser device fabrication, but would play a negligible role in our STM/STS experiments.

works, it has been predicted that zigzag bends, similarly to local widenings [19] as well as compositional inhomogeneities and the related non-uniform strain distribution, [20] might also act as carrier localization centers. Some studies started by assuming wire-like density of states in their gain analysis of Qdash ensembles and showed good agreement

between measured and simulated device performance [10,11,21,22]. Other experiments were interpreted to support a behavior of Qdashes being more similar to QD's [8,23-25] or characterized them as quasi-zero-dimensional objects [26-28]. On the other hand, dashes with larger lateral dimensions, may exhibit a 2-D character, having sufficient spatial quantum confinement only in their height along the [001] growth direction. Most importantly, taking into account the inhomogeneous size and shape distributions occurring during the self-assembled growth, some individual dashes may exhibit a different behavior to others. This would degrade the device performances compared to an ideal situation. Therefore a better knowledge of the local electronic structure of individual Qdashes is of interest, both from a fundamental and a practical point of view. Recent advances in cross-sectional scanning tunneling microscopy and spectroscopy (X-STM/STS) and *in situ* cleavage techniques, enabled accessing the LDOS(E) of buried nanostructures, by measuring at a specific location the differential conductance, dI/dV(V) spectra [29,30]. Furthermore, by acquiring both spatially and energetically resolved differential conductance dI/dV(V,x,y) maps, i.e. accessing the spatial distribution of LDOS as a function of energy over a cross-sectional area, real-space analysis of their squared wavefunctions is possible [31]. In consequence, the X-STM/STS technique delivers at present, one of the most direct and fundamental ways for exploring the dimensionality nature of individual nanostructures. It should be noted, that even though X-STM/STS is applied at a cross-sectional area, the result is sensitive to the whole (remaining after cleavage) 3-D geometry of the object. In fact, the density of states measured through the tunneling electrons at the surface, depends on both the cross-sectional physical dimensions (height and width) and the sub-surface length, which determine the available electronic states insight the nanostructure. In the following we present X-STM/STS measurements performed under ultra-high-vacuum (UHV) conditions at low temperature (T = 5K) on cleaved (1-10) InAs(P) quantum dashes. The Qdashes under investigation are incorporated in the intrinsic zone of a p-i-n junction, as the active material of a diode-laser structure, which was optimized prior to the experiments under review. The optimization concerned the Qdash growth conditions, as well as the material choice (optimum band offsets) and doping profile of the structure, taking into account photoluminescence (PL) and device results, after several runs of material growth and laser processing. An unprocessed sample of the final structure has been used in the present study; we can assume, therefore, a high Qdash material quality.

1.2. STM experimental setup – Principles of operation

In the following two sections, we briefly present the main principles of operation of our STM equipment and an introduction concerning the STM and STS basic principles. For a more detailed review, we refer the reader to the reference [35] and the references listed therein (especially Refs. 88 and 89, 93 and 95).

Scanning Tunneling Microscopy was invented in the early 1980's by G. Binnig and H. Röhrer in the IBM Laboratories, in Zurich. Its main purpose has been to study, in real space, the topographic and electronic properties of surface conductive materials (metals, semiconductors, and superconductors). The principle of operation of the STM is based on the quantum tunneling process, where an electron is having a non-zero probability to cross a potential barrier which is higher than the kinetic energy of the electron. More precisely, in an STM experiment, electrons move from one metal tip to a studied sample, or vice versa, through the tunnel barrier of intermediate air or vacuum, that separates the tip from the sample. Since the energy barrier is very high, in order for tunneling to occur, the sample and the tip should be sufficiently close to one another, spaced by a distance of typically 1 nm. The probability of tunneling depends exponentially on the distance between the tip and the sample, which then allows STM to measure topographic variations of the order of less than 1 pm. In addition, the tunneling current is established mainly by the "last" atom located at the apex of the tip, which allows for a very high lateral resolution. The topographic STM measurements may be supplemented by STS measurements. The local measurement of the conductance and differential conductance of the sample allows probing the electronic structure of individual nanostructures. The underlying theory is described in sec 1.3. It should be noted that in tunneling microscopy experiments, the constraints on the preparation of the surface are drastic. The atomic scale studies require surfaces atomically flat and are performed under high vacuum conditions, in order to eliminate the role of residual contamination and oxidation. In the case of semiconductor surfaces, which are very reactive, special preparation conditions are required, and the sample needs to be thinned and subsequently cleaved *in situ* in an ultra-high vacuum chamber as discussed later in the text. During our measurements we have used a commercial Low Temperature Omicron STM, which is shown in Figure 1.2. The STM operates under ultra-high vacuum (10^{-11} mbar), which is achieved using ion pumps (200 L/h), and it includes the preparation chamber and the STM room. The STM room houses the STM head, which thermally and mechanically isolated from the outside environment. It is surrounded by two concentric screens which may move in a

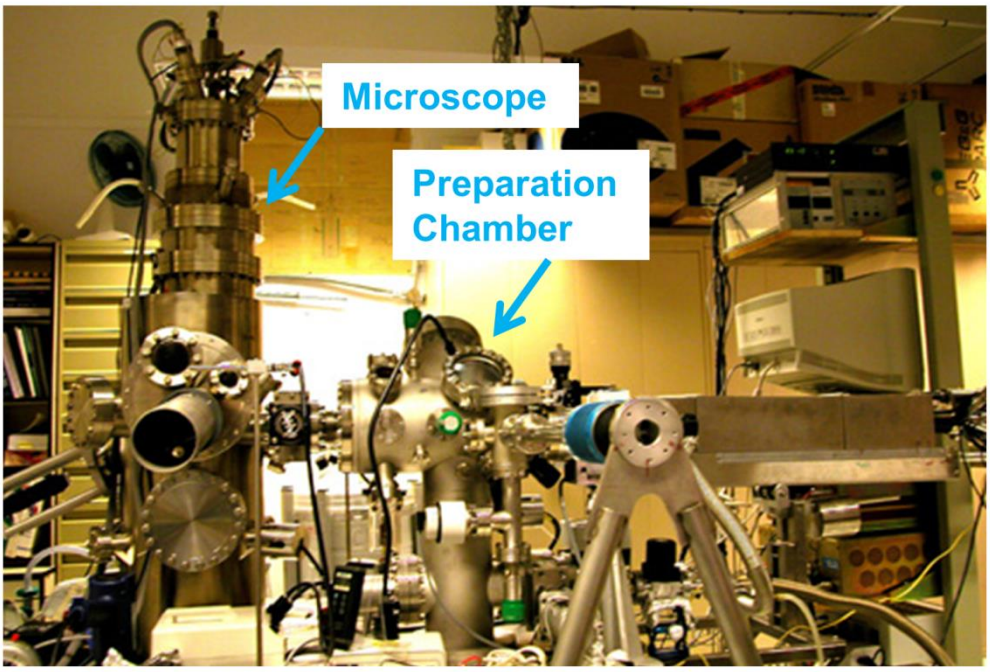

Figure 1.2 – Photograph of our scanning tunneling microscope. The measurements are performed within the Microscope, on the left part, which is connected to the Preparation Chamber that lies in the right part. A transfer arm allows moving the samples between the different parts.

way, such that either to give access to the STM head, or to isolate it as much as possible from the outside. An intermediate position can isolate STM head while maintaining an optical access for a camera. The homogeneous cooling of the STM head is provided by two concentric cryostats. The outer cryostat contains liquid nitrogen, while the inner cryostat, of a capacity of approximately 4 L, may contain liquid nitrogen or liquid helium, depending on the desired operation temperature. The temperature of the STM head is measured by a silicon diode, placed just below the sample receiving tray. The STM head is brought into contact with the inner cryostat in order to achieve rapid cooling, and is subsequently decoupled from it in the measurement position, in order to minimize heat losses. The thermal contact is then ensured by the springs. We have precisely measured the system's autonomy time (time when the whole amount of helium is consumed) in order to maximize the available time for spectroscopic measurements at a constant temperature. In the measurement position, the helium consumption is less than 170 mL/h. The STM head may remain at a temperature below 5K for 24 hours, with the temperature drift being less than 50 mK/h. In addition, we found that the STM head can be maintained at low temperature for another two hours, if optical access is completely eliminated. The mechanical isolation of the STM head is a

necessary to maintain the tip at a distance less than 1 nm within the desired accuracy (~ few pm). A decrease in the stability leads to a higher noise during the measurements or even mechanical damage of the tip and the sample if they arrive in contact. The mechanical isolation of the microscope is provided by three complementary means: i) the microscope is installed on a slab, uncoupled from the concrete floor, ii) the STM head is suspended by a spring system, and iii) it is equipped with a damping device using eddy currents. The tip is located under the sample, which is inserted into a receptacle, integrated with a piezoelectric tube, which allows controlling the movement with accuracy of the order of pedometers, over a spatial extent of 1.8 μm x 1.8 μm at 4K. The coarse positioning of the tip relative to the sample in all three spatial directions is provided by inertial piezoelectric motors that have a course of 5 mm in a horizontal plane and 1 cm along the vertical axis. The tunneling current is driven by a shielded cable from the STM head to a preamplifier that converts the tunneling current to voltage with a gain of 10^8 V/A.

The STM preparation chamber is equipped with an oven and a resistance located under the sample holder. This allows heating the sample (degassing, annealing) to temperatures up to above 1000 °C, while being under high vacuum. A scalpel blade, whose movement is controlled by an outer knob, is used to press the sample and cause cleavage.

1.3. STS Spectroscopic measurements – an Introduction

Using the Fermi golden rule, it may be shown that the transition probability from an electronic state of the sample, $\mathcal{X}_\nu$ to an electronic state of the STM tip, ψ_μ is given by the matrix element, $M_{\mu\nu}$ of the tunneling matrix as follows [35]:

$$M_{\mu\nu} = -\frac{\hbar^2}{2m}\int_S (\mathcal{X}_\nu^* \nabla\psi_\mu - \psi_\mu \nabla\mathcal{X}_\nu^*) dS \qquad \textbf{(1.1)}$$

Where m in the electron mass, and $\hbar$ is the reduced Planck constant. The integration should be performed over the surface that lies between the tip and the sample. The transmission probability may be then deduced from the tunneling matrix for a given potential profile, say $U(z)$:

$$T(U) \propto exp\left(-2\int_{barrier} \frac{\sqrt{2mU(z)}}{\hbar}\, dz\right) \qquad \textbf{(1.2)}$$

In the particular case of a tunneling barrier, where the potential may be well approximated by a rectangular profile, the transmission probability is a function of only the distance z between the tip and the sample, the electron energy E in respect to the Fermi energy and the applied sample voltage, V:

$$T(E, eV, z) \propto exp\left(-\frac{2z}{\hbar}\sqrt{2m(\frac{\phi_s+\phi_t}{2}) + \frac{eV}{2} - E}\right) \qquad \textbf{(1.3)}$$

Where $\phi_s$and ϕ_t are the work functions of the sample and the tip respectively and e is the electron charge. Now, the STM tip may be modelled quantum mechanically by a wave function of type s. As a consequence of this, Tersoff and Haman have shown that the tunneling current is proportional to the local density of states of the sample, ρ_s if the value of the applied sample voltage is small as compared to the work function ($|eV| \ll \phi_t$). The local density of states, ρ_s which represents the probability density of all the electronic states in the sample at a specific position, $\overrightarrow{r_T}$ may thus be written as:

$$I(V \cong 0) \propto \rho_s(\overrightarrow{r_T}, z, E_F) \qquad \textbf{(1.4)}$$

However, this low-voltage approximation is not always valid during STM experiments with semiconductors, such as the ones we performed. In these experiments the applied sample voltage, V varies during the spectroscopic measurements and typically takes values up to 1 V. In order to more realistically approximate the experimental conditions, a second model, applicable in semiconductors, has been proposed in 1985 and later further developed [35]. In this, in the low-temperature limit approximation (T=0K), the tunneling current is determined by the contributions of the electrons having an energy lying between the Fermi level, E_F and the Fermi level of the tip, $E_F - eV$:

$$I(V) \propto \int_{E_F}^{E_F-eV} \rho_s(\overrightarrow{r_T}, z, E)\rho_t(E + eV)T(E, eV, z)dE \qquad \textbf{(1.5)}$$

Where ρ_t is the local density of states of the tip. If we assume $\rho_t(E_F)$ and $\rho_s(\overrightarrow{r_T}, z, E)$ corresponding respectively to the density of states of the tip and the sample at the

Fermi level, thus assuming a $\rho_t(E_F)$ independent of E, the calculation of the tunnelling current takes the following form:

$$\frac{dI}{dV}(V) \propto \rho_s(\overrightarrow{r_T}, z, E_F - eV)\rho_t(E_F)T(E_F - eV, eV, z) + \int_{E_F}^{E_F - eV} \rho_s(E)\rho_t(E_F)\frac{dT(E, eV, z)}{dV}\, dE$$

(1.6)

Where the first term is proportional to the density of states of the sample. Furthermore, we can neglect the second term, assuming that $T(E, eV, z)$ varies slowly as a function of the applied sample voltage, V and therefore its derivative is approximately equal to zero. We have then, in the first approximation:

$$\frac{dI(V)}{dV} \propto \rho_s(\overrightarrow{r_T}, z, E_F - eV) \qquad \textbf{(1.7)}$$

The derivative of the tunneling current, i.e. the differential conductivity is proportional to the density of states of the studied sample, which may thus be directly accessed by our STS measurements. Based on equation 1.7 we have deduced the density of states of individual Qdashes as will be discussed in later sections of this Chapter. Details on our measurements specifications and resulting energy resolution are provided within Appendix A.

1.4. Sample preparation

The quantum dash sample under investigation was grown by gas source molecular beam epitaxy (GSMBE) on n-doped InP(001) substrate. The core of the laser dedicated heterostructure, composed of nine InAs Qdash layers separated by 20 nm thick quaternary alloy barriers $In_{0.78}Ga_{0.22}As_{0.47}P_{0.53}$ (labelled Q1.17 in reference to its emission wavelength at λ = 1.17 μm) was sandwiched between two thicker Q1.17 waveguide layers. The lower cladding layers consisted of highly n-doped (10^{18} cm^{-3}) InP and InGaAsP (labelled Q1.05; λ = 1.05 μm). Finally, p-type (0.7 x 10^{18} cm^{-3}) InP/InGaAsP/InP layers were grown on top. The investigated sample does not include the regrown upper cladding and contact layers that are necessary in laser device fabrication, but would play a negligible role in our STM/STS experiments. The room-temperature PL peak is at 1.55 μm. Parts a-d of Figure 1.1 present

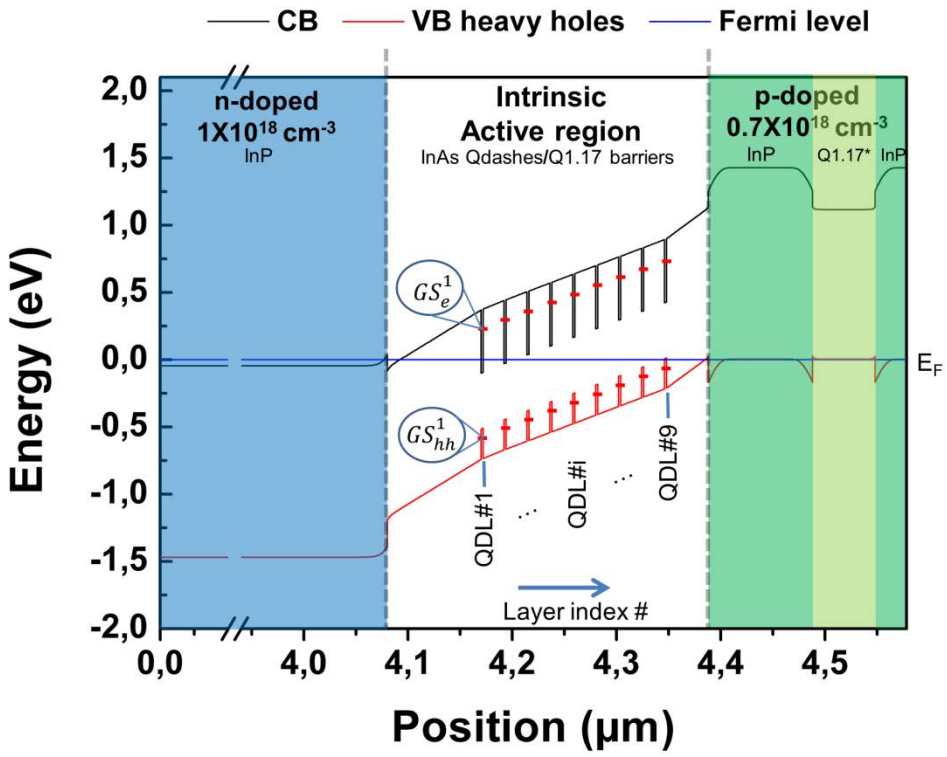

Figure 1.3 - Conduction band and heavy-hole valence band profile of the investigated sample. The Qdash layers have been labeled as QDL# i, with counting (i=1 to 9) starting from the n-doped InP buffer layers of the laser structure. Only the ground state electron and heavy hole energy levels are depicted for each Qdash. The blue line denotes the Fermi level energy.

respectively a schematic of the epitaxial structure, cross-sectional TEM, cross-sectional (1-10) topographic STM and plan view TEM images of the investigated sample. The Qdashes in our topographic STM image have very similar dimensions and stacking manner to the ones reported by Genz and co-workers in [18]. On the contrary, cleavage steps are evident in our sample, which we attribute to the presence of larger amount of strain. The barriers used in [18] are twice thicker (40 nm), which enables further strain relaxation prior to the following Qdash layers growth. Figure 1.3 shows a diagram of the calculated band structure of our sample obtained by solving self-consistently the Schrodinger-Poisson equations at T = 5K, using the nextnano software [32]. The Qdash layers have been labeled n_i (i=1 to 9), starting from the n-doped InP buffer layers of the laser structure (left to right). The Qdash nominal composition is pure InAs and we will use this notation in the text, even though in reality As/P exchange occurs during their growth, which is taken into account in our simulations as discussed below. The sample was cleaved *in situ* in a preparation chamber under UHV condition ($P < 10^{-10}$ mbar). The cleavage was performed perpendicular to the long [1-10] axis to intentionally expose the Qdashes cross section in respect to their smaller characteristic length. The sample was transferred afterwards in the precooled (T = 5K) STM head. In our

STS analysis, the differential conductivity dI/dV_{sample} was directly acquired using a lock-in technique (V^{rms}=8 mV, f=923 Hz).

1.5. Probing the quantum dash electronic structure in respect to local potential variations

Figure 1.4 on the left panel, shows a large-scale error current STM image (100 nm x 100 nm area; V_{sample}=1.0 V and I_{tunnel}=100 pA) including five quantum dash layers (#3 - #7, counting starts from left to right in the growth direction) separated by 20 nm thick barriers. On the right panel a series of individual dI/dV(V) spectra measured on Qdashes in these layers and on the intermediate barriers are presented. Each colored curve was acquired at the specific location indicated by its respective color triangle- or square-mark in the error current STM image, illustrating the energy shift of the conduction band (CB) edge at different positions in the structure caused by the built-in potential in the depletion region of the p-i-n junction. The corresponding behavior of the valence band (VB) edge is strongly affected by the tip induced band bending (TIBB) effect, which is known to produce quantitative energy level arm distortion, dependent of the tip geometry, doping level and sample voltage [35,36]. This effect bends the bands just below the STM tip and this is also the reason why the bandgap appears to be larger in our STS spectra compared to the PL peak. The TIBB effect is not symmetric between the VB and CB and it has also different magnitude between Qdash layers that are slightly (non-intentionally) doped. The latter is due to the fact that for the VB - at negative applied sample voltage values - the TIBB bends the band downwards in both cases (p- and n-doped), while the band bending is larger when moving from n- to p- type semiconductor [37,38]. This explains why in Figure 1.4, within our scanning range, the valence band is only seen for Qdash layer #4 and not for Qdash layers #5-7, which are positioned closer to the p-type part of the sample. Due to TIBB the valence band edge for the Qdash layers #5-7 is shifted to higher negative voltage values than -1.5 V, at which our scan started. This is the reverse feature to what would be expected in the absence of the TIBB effect (Figure 1.3), according to which the valence band would appear in less negative voltage values as the Qdash layer #index increases. Full quantitative treatment of the TIBB in the VB structure is beyond the scope of the present study and will be subject of future work. Our focus has been mainly in analyzing the electronic states, for which the energy separation is larger and thus measurable within our energy resolution. In the dI/dV(V) spectra measured on Qdashes, we systematically observe small peaks corresponding to their quantum resonances,

in contrast to the ones measured on the barrier material. However, those peaks are not well resolved energetically during these large-scale, but low-resolution, measurements. This has been addressed by high-resolution measurements, obtained in a smaller area, which are illustrated in Figure 1.6 and discussed later in the text. Figures 1.5a–d show differential

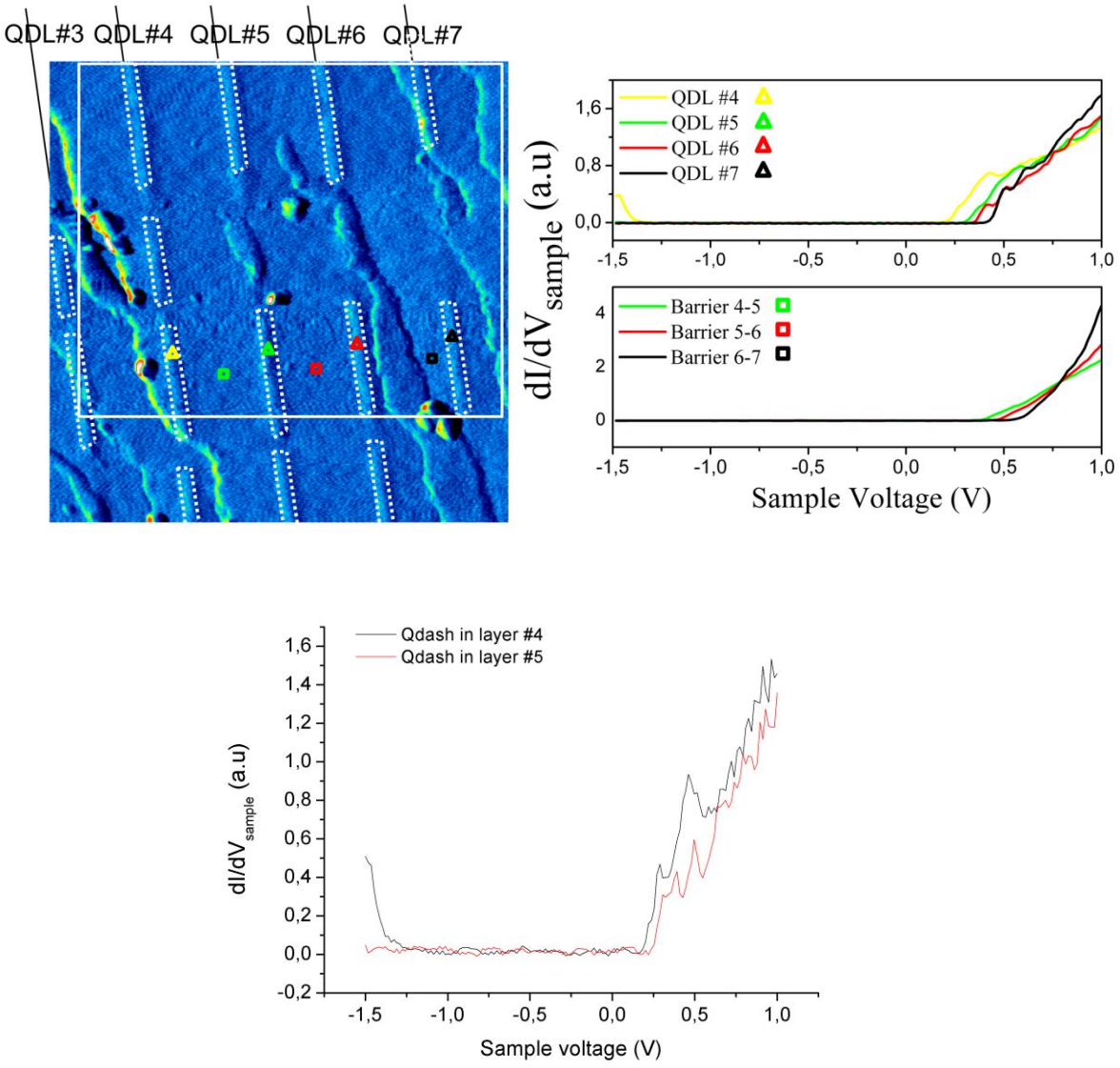

Figure 1.4 - Left: Large scale error current STM image of a 100 nm x 100 nm area showing 5 InAs Quantum Dash layers, referred as QDL#3 to QDL#7, separated by 20 nm of InGaAsP quaternary barrier (Q 1.17 barrier). (T = 5K; I_t = 100 pA, V_t = +1V). White dots contours are drawn to identify Qdashes and black oblique lines mark the successive layers. The white rectangle shows the area where the differential conductance maps (see Fig. 1.5) where acquired. Right: Individual dI/dV spectra acquired on successive Qdash layers and barriers. The exact positions are denoted by the respective colored triangles and squares in the STM image. Bottom: Another example of comparing individual dI/dV spectra taken at the center of two similar-sized Qdashes, one placed in layer # 4 and one placed in layer # 5. An interesting feature is that for layer # 4 the valence band edge may be seen at -1.25 V in contrast to layers #5 - #7, due to the TIBB effect [35,36].

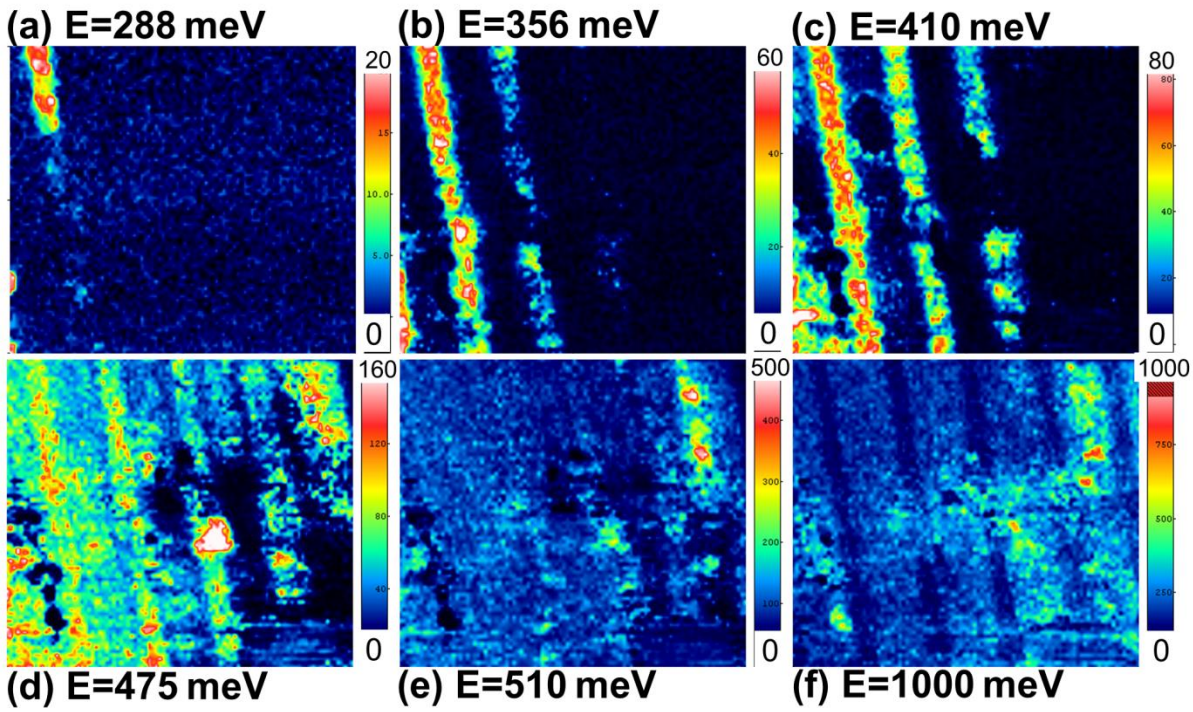

Figure 1.5 - Differential conductance dI(V,x,y)/dV images acquired on Qdash layers #4 to #7 (selected area of 95 nm x 80 nm outlined by the white rectangle in the STM image of Fig. 1.4). (a) – (d) STS maps are shown at the respective band edge energies of their step-like LDOS, V= 288 meV; 356 meV; 410 meV ; 475 meV, for successive layers. For each STS image the dI/dV-color (from blue: low LDOS to red: high LDOS) is adapted to the variation of the LDOS as a function of the sample voltage V. Maps (e) and (f) are acquired at some voltage related to specific conditions for which either no contrast is observed at V= 510 mV or dark contrast is observed on Qdashes at V= 1000 mV.

conductance maps at sample voltage V= 288 meV; 356 meV; 410 meV; 475 meV respectively, for the selected area (95 nm x 80 nm) outlined by the white rectangle in the STM image of Figure 1.4. The selected sample voltage values correspond to the energies where subsequent Qdashes show their band edge. We observed in this sequence of local density of states (LDOS(x,y,V)) maps, bright contrast light successively on Qdash layers from left to right while increasing the sample voltage. Each specific voltage step raises the energy level of the tunneling electrons in front of the n_i to n_{i+1} successive layers, opening a new conduction channel for injected electrons from the tip into the Qdashes states that become energetically accessible. The position-dependent shift of the ground state (GS) energy for the different Qdash layers as a function of their precise location in the p-i-n junction of the laser structure, is clearly evidenced in these maps and is a direct manifestation of the slope potential landscape (see Figure 1.3). The measured for similar-sized Qdashes GS energy shift between adjacent layers, $\Delta E = E_{000}^{(i+1)} - E_{000}^{(i)}$ (or conduction band edge shift between adjacent barriers, ΔE_c) compares well with the theoretical band bending slope (potential gradient)

predicted after solving self-consistently the Poisson and Schrodinger equations for our structure. The calculated value of the potential energy shift as a function of the distance from the n-doped layers is 3 meV/nm, or a ΔE = 60 meV for adjacent Qdash layers. The experimental values taken from the images of Figure 1.5a-d vary between 50 and 70 meV and therefore fairly good agreement with the theoretical value may be inferred, keeping in mind that our energy resolution during this measurement has been ~17 meV (for further details concerning the measurements resolution, see Appendix A). Figures 1.5e,f include maps acquired at some voltage related to specific conditions for which either no contrast is observed at V= 510 mV (complex compensation of tip-surface distance, band bending and electronic density of states) or dark contrast is observed on Qdashes at V= 1000 mV (due to higher tunneling in the continuum of the barrier layers).

1.6 Dimensionality nature of quantum dashes

Another feature that deserves attention in Fig. 1.5a,b concerns the dimensionality nature of Qdashes, as the 0-D assumption may already be ruled out. This is because for hypothetical discrete energy level spectra, for 0-D nature, in reference to our previous (X-STM/STS) study in InAs(P) QDs, the density of states of the Qdash layer #4 should have vanished in between Figures 1.5a and b in which Qdash #5 is in resonance, while increasing the sample voltage. (The same argument may be applied by comparing the Figures 1.5b-c and so on). On the contrary, our measurements show that the dashes of the layer #4 always exhibit a higher density of states compared to the ones in the higher-index layers, for all the voltage values during the dI/dV maps (not shown here). This suggests a step-like structure for their density of states, as expected for a dimensionality of 1-D or 2-D electronic behavior. On the other hand, after zooming in an area with two well-defined Qdashes, shown in the STM image of Figure 1.6a, individual high-energy-resolution STS spectra were taken on each Qdash. Four such spectra, are illustrated in Figure 1.6b(i), acquired at the positions indicated by the respective colored triangles and squares in the differential conductance map image shown in Figure 1.6b(ii) and (iii). The spectra reveal sharp peaks followed by steps while increasing the sample voltage, which is a typical feature of the density of states expected for 1-D structures [37]; thus excluding a dimensionality of 2-D or higher, clearly favoring a 1-D Qdash character. A very similar density of states feature has been already observed by STS measurements, in pioneering studies recently performed on 1-D carbon nanotubes [38], while our Qdash LDOS(V) also appears to have a clearly different dependence of dI/dV = f(V) to

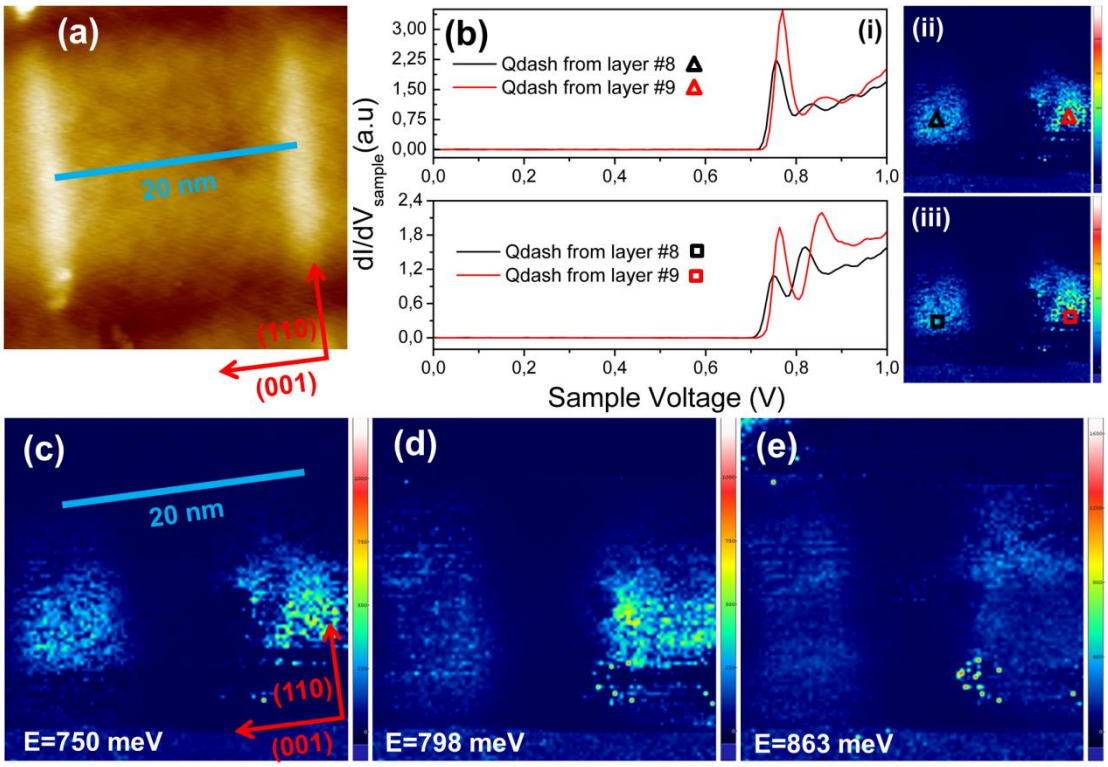

Figure 1.6 - (a) Constant current topographic X-STM images (Vsample=1.0 V and Itunnel=100 pA) focusing on two quantum dashes. (b) Individual dI/dV spectra taken on Qdashes from the layers #8 and #9 at the positions indicated by the respective colored triangles and squares in the differential conductance map image shown in 5b(ii) and (iii). (c-e) Differential conductance maps at different sample voltages, revealing two confined transversal states within the dashes. The sample voltage is increasing from (c) to (e): (c) Ground state wavefunction in both dashes for sample voltage V=750 mV. (d) The wavefunction of the first Qdash is extended over its full width, suggesting a ground and excited state superposition due to energy levels broadening, while the second dash is still at a GS resonance (V=798 mV) (e) Both Qdashes are in a hybrid ground-excited state resonance at a higher voltage of 863 mV.

the one reported in STS measurements on a 2-D quantum well [39]. We performed such measurements on a variety of cleaved Qdashes, at different positions in each dash as well as in the surrounding InGaAsP material for reference, in order to confirm that all the structures exhibit a similar behavior. In a time-consuming limited statistic, a few dozen of individual quantum dashes have been investigated, most of which exhibit two sharp peaks while some show to have three confined transversal eigenstates (subbands). This difference is due to the larger lateral sizes of the Qdashes that exhibit a higher number of confined states.

1.7 Wavefunction imaging

The peaks of the individual spectra appear to have relative weights dependent on the measurement positions, which is especially evident for the second peak of Figure 1.6b(i) that

has a much weaker intensity closer to the center of the Qdash. This variation corresponds to the spatial distribution of the wavefunctions (see Figure 1.6c-e and Figure 1.7), which may thus be imaged by recording such dI/dV spectra on a sufficiently dense grid of points, over the whole area of interest. Figure 1.6c-e shows a sequence of differential conductance maps taken in the same area (Fig. 1.6a), at sample voltages 750 mV; 798 mV and 863 mV respectively. In Figure 1.6c both Qdashes are at the GS resonance. In Figure 1.6d the wavefunction of the first Qdash extends over its whole width, which we assume is due to a hybrid state resulting from the superposition of the GS elliptic localized lobe and the extended intensity distribution with one node in the center, expected for the first ES. The second Qdash is still in a GS resonance. The ground and excited state superposition is a result of the energy levels broadening. Its value has been ~13 meV during our measurements, given by adding the thermal broadening at 5K with the broadening induced by the lock-in modulation, and is larger than the longitudinal eigenstate energy separation (see Figure 1.7). In addition, our energy resolution during this measurement has been 7 meV (for further details concerning the measurements resolution, see Appendix). In Figure 1.6e both Qdashes are in a hybrid GS and ES. The same sequence as in Figure 1.4 appears, with dashes placed in lower index layers (closer to the n-doped part of the sample) arriving earlier at resonance. It should be explicitly noted that during this work, we use the terms GS and ES to express the eigenstates resulting from the transversal confinement along the Qdash width ([110] direction), which are separated by few tens of meV. Due to the larger sub-surface size of the Qdashes, the longitudinal [1-10] direction gives rise to eigenstates separated by only a few meV (see Figure 1.7c-j), which cannot be resolved by our STS measurement. As a result, all these eigenstates correspond to the same lobe in the cross-sectional view (Figure 1.6c-e; Figure 1.7c,d). These closely separated eigenstates form subbands at RT, and in combination with the well-separated eigenstates along the Qdash height and width directions, give rise to the one-dimensional Qdash nature. We have observed two subbands within these Qdashes which is consistent with previously reported experimental results [40] as well as our simulations, discussed below. In QD/Qdash-based lasers the potential barrier is optimized in order to achieve the best compromise between low threshold current and high output power. In addition, the transversal excited state(s) (ES) should either lie within the continuum or split far away from the GS, such that they would not be detrimental to the laser dynamics and other important parameters such as the linewidth enhancement factor [12,41]. This optimization procedure leads to relatively small conduction band offsets in the $In_{1-x}Ga_xAs_yP_{1-y}$ material system [12] which results to the observed small number of confined subbands, that are well-

separated. At last, it is worth noting that our dI/dV maps in Fig. 1.6c-e do not show any lateral electronic coupling between adjacent Qdashes; it can be rather seen that the wavefunction is well confined within the Qdash both for the GS and ES. This discrepancy between our findings and the theoretical prediction of [21], in which quantum mechanical coupling between adjacent Qdashes through the wetting layer (WL) was predicted for the ES, may be explained by the fact that in our Qdash sample the WL is very thin (not even visible in our cross-sectional TEM image shown in Fig. 1.1b, therefore expected to have a thickness of < 0.5 nm). On the contrary, for the InAs Qdashes in InGaAlAs matrix of [21] the WL has an apparent thickness of ~1.5 nm and therefore plays a very important role in the Qdash behavior.

1.8 Finite-element simulations of the Qdash wavefunctions

In order to achieve a better insight and quantitatively support our analysis, finite element simulations of the electronic wave functions, using the software COMSOL MULTIPHYSICS, were carried out. In Figure 1.7a,b the two different Qdash geometries used in the simulation are shown. The parabolic shape shown in Figure 1.7a has been used in previous Qdash numerical calculations [11,21] and is close to the shape extracted from our TEM cross-sectional view, while shape of Figure 1.7b is closer to the one shown in our STM images of Figures 1.4 and 1.6. Both structures gave very similar calculated electron eigenenergies (difference is limited to a few per cent) which gives us confidence that the realistic quantum dash shape, which is in reality in-between those two, is well approximated with this approach. In both cases we used the Qdash dimensions of 3 x 22 nm for the cross section, extracted from the analysis of our STM image and 100 nm depth, assuming an initial Qdash length of 200 nm, cleaved in the center. In labeling the calculated quantum states, we follow the convention in which the ground state is denoted (000), and the excited states along the different axes are identified as (nmp), where the letters n, m, and p correspond to the number of the wavefunction nodes in the [1-10], [110], and [001] directions, respectively. This notation originates from the theoretical case of a 0-D quantum box and is widely used for QDs of different shapes using simple projection considerations. In our Qdash case, even though it is not physically a 0-D system, we initially consider finite length quantization effects in all three dimensions and it will be shown that the eigenenergies separation in their long [1-10] axis is very small, well below the thermal energy at room temperature (RT). Simulated wavefunction slices, at the interface plane between the cleaved Qdash and vacuum,

which represents the measurement plane where the STS spectra were taken, are shown in Figure 1.7c,d, corresponding respectively to the (n 0 0) and (n 1 0) eigenstates, (n=0,1,..). Figure 1.7e-j includes examples of top views of the 3-D spatial wavefunctions for (n 0 0) and (n 1 0) eigenstates, at specific n values, in which the corresponding eigenenergies are denoted. All the 3-D spatial wavefunctions of the (n 0 0) type (Figure 1.7e-g) correspond to the same wavefunction slice profile at the STM measurement plane, but with relative intensities (due to their different 3-D spatial distributions). This is shown in Figure 1.7c, in which an arbitrary color scale has been used. Similarly, all the 3-D wavefunctions of the (n 1 0) type, correspond to the same slice of Figure 1.7d, if an arbitrary color scale is used. The 3-D spatial wavefunctions and wavefunction slices are shown only for the geometry of Figure 1.7a due to similarity. The Qdash is surrounded by InGaAsP except at the cleavage surface (red plane in Figure 1.7 (c-j), which is exposed to vacuum. which represents the measurement plane where the STS spectra were taken, are shown in Figure 1.7i,j, corresponding respectively to the (n 0 0) and (n 1 0) eigenstates. The 3-D spatial wavefunctions and wavefunction slices are shown only for the Figure 1.7a geometry due to similarity. The Qdash is surrounded by InGaAsP except at the cleavage surface (red plane in Fig. 1.7 c-j), which is exposed to vacuum.

Simulation methodology, approximations and results: In our model, the confined states of a single dash have been obtained by calculating the eigenvalues of the single-particle Schrodinger equation in the effective mass approximation, considering finite barriers and different effective masses for the dash and barrier materials. The coupling with the light-hole and split-off bands has been neglected since these two bands are split far away from the VB edge and play a negligible role in the presence of compressive strain [43]. Also, many-body effects [44] have been assumed to be negligible, as this was previously shown to be a very good approximation in such STS experiments [31]. It is known that during MBE growth, As/P exchange reactions are unavoidable for the first few monolayers at material interfaces [45,46], which determines the total amount of InAs incorporated in the nanostructures. For the simulation to be more realistic, it is important to take this into account, as the material bandgaps are strongly affected by composition fluctuations. Since this is difficult information to obtain quantitatively, we used a different approach in order to get a good approximation by running our simulation in two steps, as follows: In the first step we assumed a binary composition for the Qdashes taking into account the InAs/InGaAsP band offsets at room temperature. After calculating the GS energies for electrons and holes the composition and therefore the bulk bandgap of the Qdash was adjusted accordingly such that we could obtain

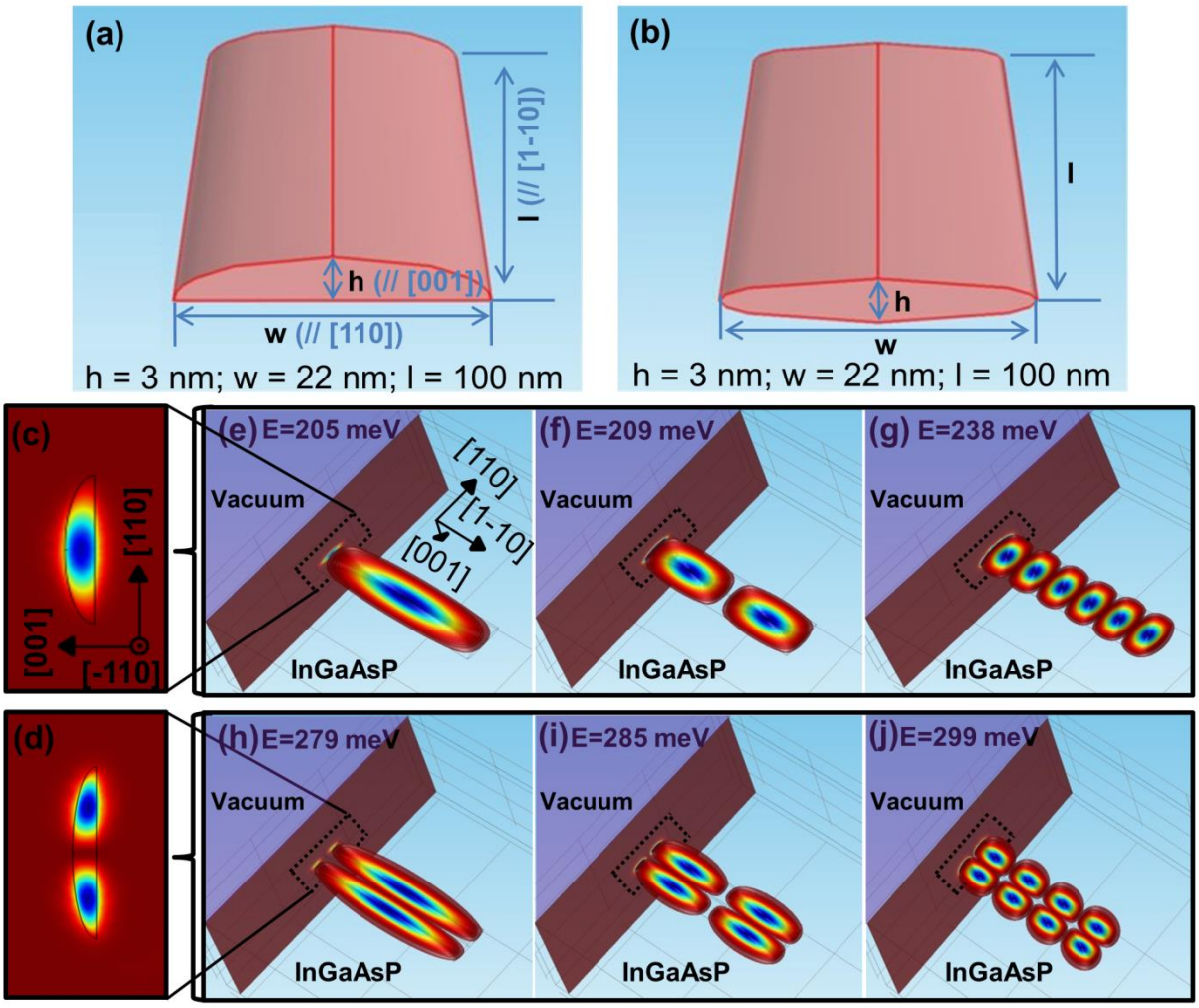

Figure 1.7 - (a,b) The two different Qdash geometries used for the simulations. (c,d) Wavefunction slices taken at the cleavage plane corresponding to the (n 0 0) and (n 1 0) eigenstates respectively. (e-g) Top view of 3-D spatial wavefunctions for the (n 0 0) eigenstates: (e) n = 0, (f) n = 1, (g) n = 5. The corresponding eigenenergies are denoted. (h-j) Top view of 3-D spatial wavefunctions for the (n 1 0) eigenstates: (h) n = 0, (i) n = 1, (j) n = 3. 3-D spatial wavefunctions and wavefunction slices are shown only for the geometry (a) due to similarity. For (c,d) an arbitrary color table scale was used, while for (e-j) the relative intensity ratios at the cleavage plane may be seen. The simulation reproduces the cross-sectional STM measurement with the tip in the vacuum site probing the density of states in the (1-10) cleavage plane of the Qdash surrounded by InGaAsP.

1.55 μm (0.8 eV) PL emission at room temperature, which is our validated experimental value. During this step the heavy hole energies have been calculated as well, to take into account for the PL emission, given by definition as the summation of the electron (E_{GSe}) and heavy hole (E_{GShh}) GS quantum energies with the InAs bulk band gap [PL = $E_{bandgap} + E_{GSe} + E_{GShh}$]. At this point, the deformation potential induced by the strain has been taken into account empirically, by modifying the InAs band edges and by introducing an increased effective mass for the electrons and different hole effective masses in the parallel

(growth) and transversal planes [11, 47]. In the second step, using the new Qdash composition we estimated the bulk bandgap at 5 K, and performed new simulation runs in which the quantum states and wavefunctions have been calculated. After fixing this parameter, a similar two-step procedure has been used in order to obtain more accurate values for the electron effective masses, which were taken as weighted average between the respective value in the dash and the barrier (taking into account the confinement factor of the wavefunction in the Qdash – obtained in the first step). Subsequently, the electronic structure of the Qdashes has been calculated with the main results being presented Fig 1.7. We find 2 confined transversal states in the dash using the material parameters at 5K, which is consistent with our experimental results.

Subband energy spacing: Another important quantity, especially for laser structures, is the energy level separation between the GS (0 0 0) and ES (0 1 0) in the transverse direction (subband energy spacing). For the dash geometries used, we find this value to be approximatively 75 meV. If we compare this value to experimental results obtained by modulation spectroscopy [40] in which the GS-ES difference ($\Delta E_e + \Delta E_{hh}$), was measured to be 150 meV, we notice an important difference; our calculated ΔE_{hh} has been ~10 meV. To further investigate this discrepancy, we performed additional simulations varying the Qdash width and height. We find that the transversal energy level separation is indeed strongly dependent on the Qdash width, while the GS emission strongly depends on the height, as expected. We obtained a much closer value to the experimental results ($\Delta E_e + \Delta E_{hh}$) ~130 meV for 12-13 nm Qdash widths. Therefore we can conclude that the Qdash dimensions during our STM studies and subsequent simulations have been slightly different compared to the sample used in the measurements in [40], probably due to strain relaxation after cleavage and perhaps some differences in the initial growth conditions. Our experimental value of the subband energy spacing may be obtained by comparing the onset of the GS and ES in dI/dV maps such as the ones shown in Figure 1.6. We note at this point that Figure 1.6c is not showing the onset of Qdash #8 ground state; it is just a specific voltage value at which both Qdashes from layers #8 and #9 are in GS resonance. On the other hand, Figure 1.6d is indeed the onset of the first excited state. The true onset of Qdash #8 GS is at 727 meV (not shown), and therefore the experimental transversal energy separation extracted from this dI/dV map is ~71 meV, in very good agreement with the finite element simulations (74 meV).

Qdash ground and excited state energy levels: Comparison between our experimental and calculated values of the GS and ES energies of the respective wavefunctions is not straightforward and needs to be done with caution. This is because in our finite element simulations the quantum energy levels were extracted considering an InAs(P) Qdash embedded in InGaAsP(λ= 1.17μm) matrix, neglecting the rest of the structure. Thus, neither the effect of the build-in potential in the p-i-n junction nor the lever arm effect on the energy value, caused by TIBB, were taken into account. These effects are not uniform between the different Qdash layers and therefore treatment of the experimental data is needed, before directly comparing the values. We approximated this problem in the following manner: first, we performed an additional band structure simulation assuming a fully undoped structure, in order to acquire a first approximation of the absolute effect of the build-in potential on each Qdash layer (by comparing this to the result of the doped structure - Figure 1.3). Subsequently, after implementing the appropriate correction for the TIBB effect (at the onset sample voltage for each Qdash), we estimated the corrected experimental energy levels for the GS and ES. Finally, remembering that an energy difference of 60 meV per Qdash layer, due to the built-in potential, was extracted by the band structure calculations for the real structure, we confirmed that the results were self-consistent. For example, after following this methodology the experimental results for the GS and ES for the Qdash of layer #8 shown in Figure 1.6, were corrected to 215 meV and 295 meV respectively. These values compare well with the results shown in Figure 6e,h (GS at 205 meV and ES at 279 meV). In general, comparing our experimental results to the simulated values, after implementing the appropriate corrections for the TIBB effect (not detailed here), we find a difference of the order of ~10 % or less which is a fairly good agreement, given the approximations introduced in the model and the imperfect knowledge of certain parameters which affect the simulation results. In order to quantify the impact of the STM cleavage position on the GS energy we performed several simulation runs with reduced Qdash depths, which suggest a negligible effect for cleaved Qdashes with remaining sub-surface lengths > 40 nm, while for shorter ones it begins to become important.

Longitudinal eigenstates separation: At last, we investigated the longitudinal eigenstates energy separation for which we do not have any experimental measure, because all these states appear as the same lobe in the STM measurement plane (see Fig. 1.6c-e, Fig. 1.7c,d). Even though they are expected to have different intensities (see Fig. 1.7e-j), they may not be distinguished; this is due to the fact that their energy separation is very small, which

causes them to be mixed as a result of the energy levels broadening. Therefore, this separation has been assessed purely by the simulation. The simulated values varied between 4-12 meV for electrons and no more than 5 meV for holes, which is well below the thermal energy at RT (~25 meV) and is therefore further supporting our interpretation for a 1-D Qdash nature. The longitudinal eigenstates separation is even smaller if we consider longer (non-cleaved) Qdashes.

Discussion on the generality of our results in respect to uncleaved Qdashes: At this point, it is important to explicitly note that even though during this work, we have studied cleaved Qdashes, our conclusions concerning their dimensionality nature are general and also valid for uncleaved Qdashes. This certainty arises by the fact that the Qdashes were cleaved perpendicular to their long axis. It has been seen through our high-resolution STS spectra and subsequent dI/dV maps, shown in Figure 1.6, that the quantum confinement effect is clearly evident in the visible Qdash dimensions: only one confined eigenstate has been observed in the Qdash height direction (// to [001]), while along the width of the Qdash (// to [110]), we have two confined states which we measured to have an energy separation of ~71 meV, well above kT at RT. This is consistent with the fact that the 1-D density of states nature is arising from the longer sub-surface axis of the Qdashes (// to [1-10]). Even though we do not have any way to measure the remaining sub-surface-length of the cleaved Qdashes, it is expected that for most of them it is much larger than their lateral dimensions (besides few exceptions where the cleavage may occur very near the edge of the Qdash). In accordance to this, after investigating a few dozen of individual Qdashes during our study, the big majority showed a 1-D-like behavior, with very few exceptions. Since the uncleaved Qdashes would have an even larger length and smaller cross-section (some strain relaxation occurred after cleavage) than the investigated cleaved ones, we may infer that Qdashes are, in general, 1-D in nature.

1.9 Discussion

In this Chapter we presented low-temperature (T=5K) cross-sectional scanning tunneling microscopy and spectroscopy (X-STM/STS) on single semiconductor quantum dashes (Qdashes), embedded in a diode-laser structure. The main results include addressing the Qdash dimensionality nature, probing the electronic structure of individual nanostructures in respect to their precise location in the p-i-n junction and imaging of the Qdash electronic squared wavefunctions by high-stability differential conductivity mapping. We consider this work to exhibit a twofold fundamental interest.

(i) In respect to the nature of the investigated nanostructures. Scanning tunneling spectroscopic measurements are performed on Qdashes for the first time. Even though a relatively high number of publications related to Qdash based material has been released during the last decade, owing mostly to its very promising laser performances, a comprehensive experimental report on the fundamental physical properties of Qdashes, such as their electronic density of states, had been lacking up to present. The distinction between Qdashes and quantum dots (QDs) had not been clear and both terms could be found in literature used for nanostructures with similar lateral geometry. As a result, in a rather contradictive manner, a number of reports characterized Qdashes as quantum-dot-like, others referred to them as quantum-wire-like structures, while the term quasi-zero-dimensional has also appeared in recent related reviews. Theoretical studies have also not been conclusive due to the very particular shapes and high length-to-width and width-to-height size ratios that Qdashes exhibit. We analyzed within Section 1.1 the reasons why we believe that a better understanding would be of interest, both from a fundamental as well as a practical point of view. Due to recent advances in scanning tunneling spectroscopy and *in situ* cleavage techniques, it is becoming a very powerful tool in providing clear answers to such questions, by enabling direct access to the local density of states ((LDOS(E)) of buried nanostructures, while probing their cross-sectional structural characteristics with atomic resolution. In the manuscript we believe to provide conclusive evidence on the 1-D dimensionality nature of Qdashes through our high-energy-resolution X-STS measurements. Furthermore, their electronic squared wavefunctions were subsequently imaged and the results were compared to our finite-element simulations, after implementing the appropriate corrections for the tip induced band bending (TIBB) effect.

(ii) In respect to the measurement technique. (X- STS) measurements are, for the first time, extended to a real device (laser) structure. We have analyzed the electronic structure of individual Qdashes that were placed in the multi-layer undoped active laser area, in respect to their precise location in the p-i-n junction. The potential gradient has been measured and found in good quantitative agreement with our theoretical band structure calculations obtained by solving self-consistently the Schrodinger-Poisson equations, demonstrating the high sensitivity of this spectroscopic measurement to (spatially resolved) local potential variations. In addition, we demonstrate that the potential gradient has been beneficial in our Qdash dimensionality studies, offering access to additional information. This would suggest that, in general, such device configurations can be beneficial in offering further

insights into the behavior of semiconductor nanostructures, in comparison to traditional studies in which nanostructures directly deposited on a substrate were investigated.

Chapter 2

Long wavelength Quantum Dash based lasers for Gas Sensing

Monitoring the environment, whether it be the level of pollutants in the atmosphere, or gaseous components in industrial manufacturing processes, has been well served by photonics, utilizing infrared absorption characteristics for gas sensing. Semiconductor laser diodes, based on low-dimensional structures, such as self-assembled quantum dots or quantum dashes, are very promising candidates for this application, owing to their ability to cover a wider wavelength range than the conventional quantum well (QWell) designs. The desired emission wavelength can be achieved by either adjusting the height or the composition of the Qdash/Qdot, during their epitaxial growth, which allows for very precise wavelength selection and the coverage of a very wide wavelength range for a given material system, since the requirement in strained QWell growth for active layers below the critical thickness is no longer a necessity.

In addition they can be grown directly on InP(001) substrate or lattice-matched material, which allows the already mature processes and mass-production procedures that were developed for the telecommunication lasers, to be utilized for the fabrication of long-wavelength lasers.

However, Qdashes, even though very promising, are a complex system for laser design; and being relatively new nanostructures, their optimization is still underway. For example, during their epitaxial growth Qdash ensembles exhibit an inevitable homogenous and inhomogeneous broadening. The former effect is due to the interactions of a Qdot/Qdash with the neighboring dots and environment, causing the luminescence spectrum to have a non-zero linewidth, and the latter is due to the size dispersion of the self-assembled dots (mainly the height). Consequently the gain spectrum is broadened to several tens of nanometers, and inhomogeneous broadening is at present one of the major problems limiting the laser performances.

On the other hand, the broadening can also be seen as an advantage for applications which require a broad gain spectrum, such as tunable lasers for gas spectroscopy.

Another necessary consideration when designing Qdot/Qdash material is that, taking into account the dots thickness and lateral dimensions, the optical confinement factor has been estimated to be as small as 0.15% per layer in a typical single-transverse-mode laser structure, in Ref. [8]. The value is sufficiently lower as compared to that obtained in Quantum Wells structures (~1% per QWell). This effect is advantageous for mode-locking characteristics [48], but is also limiting the maximum available gain per dot/dash layer. Thus, both of these effects, the broadening of the gain spectrum and the relatively low optical confinement factor in the Qdashes, lead to the necessity of layer stacking in order to maintain a sufficient modal gain [49,50]. However, layer stacking results in changes in the dimensions of nanostructures, and the dots size distribution leads in turn to the broadening of the PL spectra, followed by a reduced modal gain for a given wavelength bandwidth. Therefore, the optimum number of layers depends on the specific targeted application and on the emission wavelength. Furthermore, besides these general considerations, other parameters that are very important for the laser performances, also strongly exhibit strong wavelength dependence and special caution needs to be taken when designing material for longer wavelength emission. Such parameters are the Qdash growth quality, the material choice (optimum band offsets), the doping profile and the waveguide thickness.

In this Chapter we describe our work on material design and optimization in respect to all the above aspects, targeting Qdash based lasers for gas sensing applications and present results at the wavelengths that were investigated, namely 1.6, .1.8 and 2 μm. A description of the investigated quantum dash active layers is presented together with systematic PL and laser results that allowed for their optimization.

The rest of the Chapter is organized as follows: In Sec 2.1 a brief introduction on the electronic density of states and expected potential advantages of low-dimensional structures will be provided. In sec 2.2 we focus on the Qdash growth and properties, while in sec 2.3 the Qdash based laser structures that were investigated are discussed. Sections 2.4 and 2.5 provide information on the different growth campaigns and precisely on the investigated quantum dash active layers together with PL, low-temperature PL, broad area laser and ridge-waveguide laser results. In section 2.6 our results are compared to the current state of the art, while in sec. 2.7 we present new wafer designs for future work, based on our results, literature review and additional simulations.

2.1 Low dimensional structures

The reduction of the size of a semiconductor down to a small number of atomic layers has a significant impact on the optical and electronic properties of the structure. The confinement of carriers, electron or holes down to nanometers, comparable to their de Broglie wavelengths, increases the effective bandgap of the material and leads to quantization effects. A very important parameter often used in describing the physics of such nanostructures is the density of states (DOS). The density of states may be defined as the amount of carriers allowed at a given energy position, or the available number of states per unit energy, per unit volume. An outstanding property of nanostructures is that in general they have a significantly reduced DOS, but which has peaks at specific energy values. A rule of thumb in order to get a first idea on the dimensionality nature of a material is to compare its physical dimensions, height width and length, to the exciton Bohr radius in its bulk material. The regime of the quantum confinement (strong or weak) may be estimated by comparing the exciton and the nanostructure volumes. The reduction of the structure size can be made such that the carriers are quantum confined in one, two, or all three space dimensions, leading respectively to “free” motion in to two dimensions 2D (quantum well), one dimension 1D (quantum wire) and “zero” dimensions 0D (quantum dot) structures, as opposed to the 3D or bulk structure in which carriers can move freely in all three dimensions. The energy dependencies of the electronic density of states for each dimensionality are shown in table 2.1, while a schematic is shown in Figure 2.1. We should note that the QD density of states is theoretically a delta-function and a number of benefits for Qdot based lasers have been predicted as a result of this. Some of the more important ones are: Increase in both optical and differential gain [51], decrease in threshold current density, reduced (ideally zero) temperature sensitivity [1,2], reduced linewidth enhancement factors [52,53] and high modulation bandwidths [54]. Another way to visualize this potential advantages is that in a semiconductor laser with an active region consisting of low-dimensional structures the electrons and holes injected by electrical pumping, would be restricted to the exact energy levels where they can contribute most efficiently to the lasing process. However, as mentioned earlier in the introduction, in reality the DOS function is homogeneously broadened in the energy domain. This broadening is a result of the intrinsic properties of the quantum dot due to the finite carrier lifetime in each confined energy state, as well as carrier-phonon and carrier-carrier interactions [55]. On the other hand, an epitaxially grown Qdot/Qdash ensemble has a finite distribution of the sizes of the nanostructures which leads to a (usually Gaussian) distribution of the Energy

Structure	Dimensionality of the free electron motion	Energy dependence of the density of states
Bulk Material	3-D	$\sqrt{E}$
Quantum Well	2-D	1
Quantum Wire	1-D	$1/\sqrt{E}$
Qantum Dot	"0-D"	$\delta(E)$

Table 2.1 - Energy dependence of the state density of electrons and holes as a function of the dimensionality of the system.

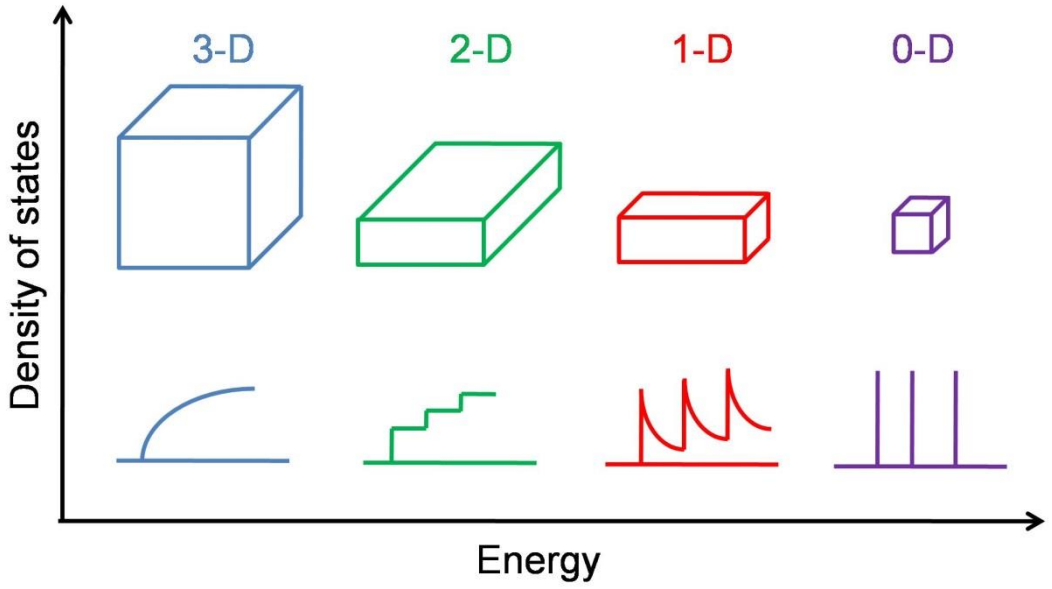

Figure 2.1 - Illustration of the electronic states density as a function of Energy in bulk semiconductors, Quantum Wells, Quantum Wires and Quantum Dots respectively.

levels around a central value. As a result to these broadening effects, the question on how close can the experimental results approach the theoretically predicted extraordinary advantages of a low-dimensional system, is subject to continuous investigation up to present. In addition, another consequence of this effect that it's worth mentioning, is that 1-D Qdash DOS, with only few (in our case two) confined energy levels, becomes in practice more similar to the QD 0-D DOS when both functions are broadened. As also mentioned briefly above, another important difference to conventional material, is that both QD's and Qdashes have a significantly reduced volume of the laser active layer, which results in a lower optical confinement factor in the active material (Γ). Γ is defined as the fraction of the optical field overlapping with the active material, and may be calculated using the Equation 2.1:

$$\Gamma = \frac{\int_{-d/2}^{d/2} \int_{-w/2}^{w/2} |\, E(x,y)\,|^2 \, dx\, dy}{\int_{-\infty}^{\infty} \int_{-\infty}^{\infty} |\, E(x,y)\,|^2 \, dx\, dy} \qquad \textbf{(2.1)}$$

where d and w are the active layer height and width respectively. This directly affects the available modal gain (Γg_0). By remembering the well-known laser threshold condition stating that the modal optical gain must balance the total losses at the threshold current, i.e.:

$$\Gamma g(I_{th}) = a_i + \frac{1}{2L} \log\left(\frac{1}{R_1 R_2}\right) \qquad \textbf{(2.2)}$$

with $\Gamma g(I_{th})$ the modal gain at threshold, a_i the internal losses of the laser structure, L the cavity length and $R_{1,2}$ the facet reflectivities, it can be seen that if the laser cavity is made too short, a very low confinement factor may limit the modal gain and thus suppress the lasing effect. Therefore several QD/Qdash layers need to be vertically stacked, separated by thin barriers in order to achieve high performance lasers. The modal gain is in general a very important parameter in evaluating material quality for lasers and for this reason we have calculated this value for all the structures under investigation in this work: After processing and cleaving laser bars of different cavity lengths, the modal gain is deduced using linear fits of the logarithm of the threshold current density to the inverse cavity length. Detailed values and discussion will be provided in following sections.

2.2 Qdash Structures

After the conception of quantum dots was reported by Arakawa and Sakaki [1], different techniques were employed in order to achieve the desired system in practice. Some of the initial efforts included selective area growth after patterning by optical lithography [56], e-beam lithography followed by wet etching [57-59] followed by etching, strain induced definition [60] and selective growth on pre-patterned substrates [61]. However, the self-organized, so-called Stranski-Krastanov (SK) growth mode, even though not offering direct controllability on the QD/Qdashes sizes or positioning, has been most popular and successful approach to achieve high quality material, up to the present [62-65]. The growth is achieved by molecular beam epitaxy and exploits the small mismatch between the lattice constants of the deposited material and the substrate (InAs and InP for our Qdashes). First, the deposited material starts as a two-dimensional layer called the "wetting-layer" (WL), but when it exceeds a critical thickness, there is a transition into a three-dimensional growth mode, in order to relax the strain accumulated by the lattice mismatch. This leads to the formation of

QD's when InAs is deposited on GaAs (or its lattice-matched material) where the lattice mismatch is ~7 %, or to the formation of Qdashes when InAs is deposited on InP (or its lattice-matched material) where the lattice mismatch is ~3.5 %. The dots are subsequently capped with the barrier material and then the same procedure repeats in order to grow the next Qdot/Qdash layer. The exact size and material composition of a QD/Qdash and the band offset with the barrier are the three main parameters that determine its energy structure and emission wavelengths. The main advantages of self-organized growth are that it is a single growth step process and that it results to low defect density and high QD/Qdash density. It is very difficult to grow isotropic dots on InP(001) substrate. Some have been demonstrated recently, using the Metal-Organic Chemical Vapor Deposition (MOCVD) growth technique [13,14,66,67]. It is easier to grow such dots on InP(311)B substrate and results in the formation of high-density quantum dots [68], although this substrate is less compatible with the standard processing methods. This work is restricted in studying InAs Qdashes on InP(001) substrate. The devices that will be presented have been grown by Gas Source Molecular Beam Epitaxy (GSMBE) at III-V lab. Figure 2.2 shows examples of typical plan-view and cross-sectional TEM images of such optimized Qdashes for a dash-in-a-well structure (see sec 2.3). The shown reference sample exhibits PL emission at 1.55 μm. The surface density of these Qdashes is of the order of 2×10^{10} cm^{-2} (filling factor ~50%) [8].

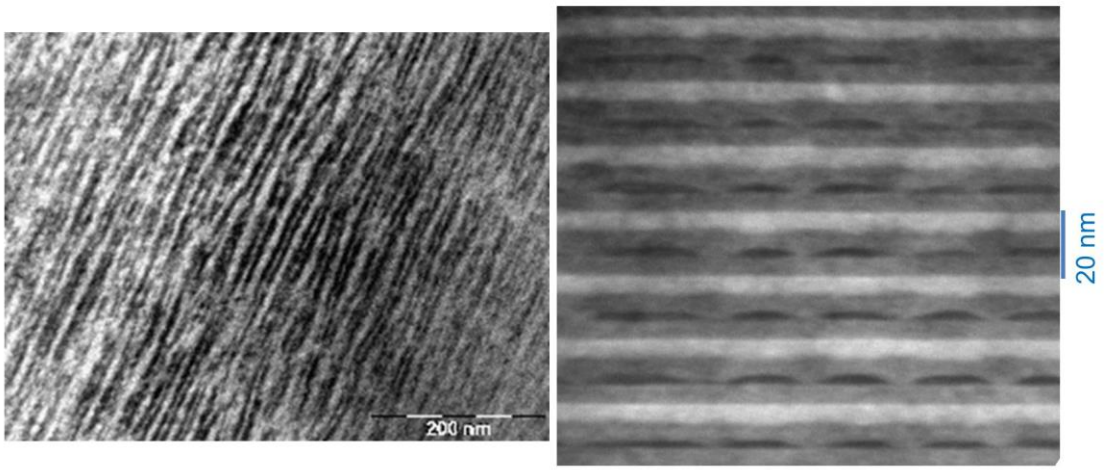

Figure 2.2 - TEM images of optimized Qdashes in a dash-in-a-well structure. Left: TEM plan-view- The Qdashes grow in a dense and parallel manner. Right: Cross-sectional TEM- The Qdashes are aligned along the growth axis; this is due to the strain field which propagates across the barriers and modifies the chemical potential of the growth surface, leading to preferential seeding of Qdashes on top of buried Qdashes. The Qdash height, which is controlled by the nominal thickness of the InAs layer to achieve PL emission at 1.55 μm, is about 2.5 nm. The typical width of the dashes in this sample is about 15–20 nm.

2.3 Laser Structures

We have investigated two types of Qdash based laser structures, namely the dash-in-a-barrier (DBar) structure, where the dashes are directly inserted in the barriers and the dash-in-a-well (DWell) structure where the dashes are embedded in intermediate quantum wells. Figure 2.3 shows simple schematics of the band structure of these two designs.

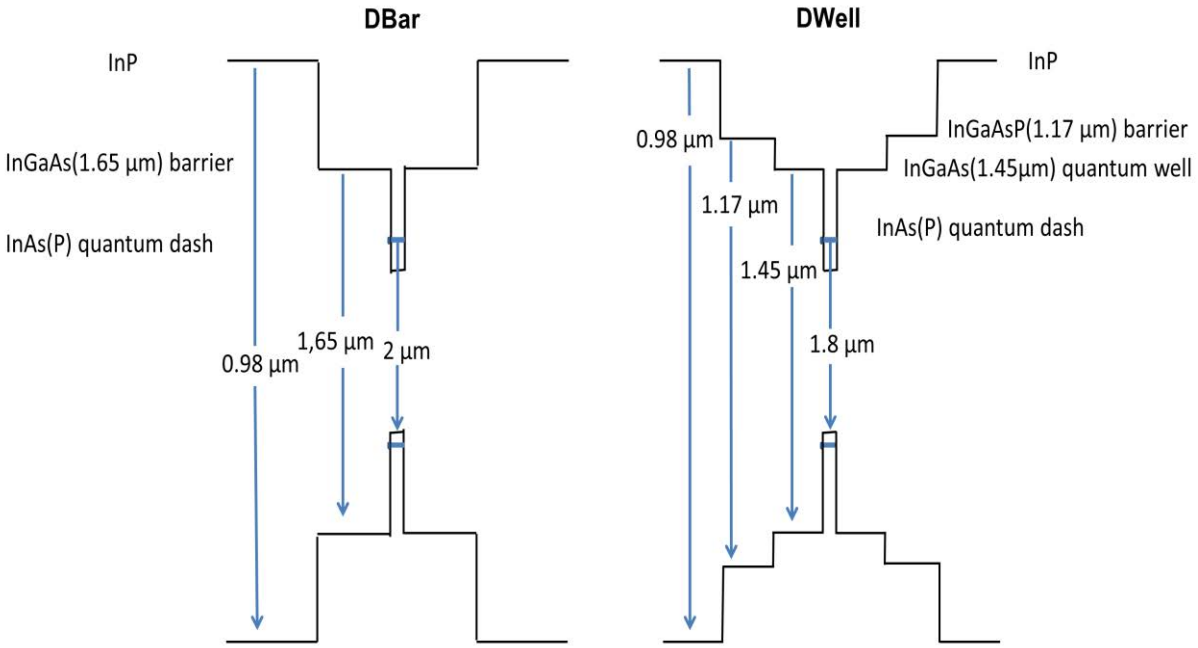

Figure 2.3 - Simplified schematics of the band structure of the DBar and Dwell structures.

In the DBar design the Qdashes were placed in ternary InGaAs barriers with absorption edge at 1.65 µm, while in the DWell they were embedded in 6 nm thick intermediate quaternary InGaAsP quantum wells with λ=1.45 µm which were then sandwiched between 40 nm thick InGaAsP λ=1.17 µm barriers. In order to evaluate our material performance besides the initial PL characterization, laser structures were fabricated and characterized for each sample. This is a necessary step in evaluating material for laser applications, because it is well known that the PL peak does not necessarily guarantee the laser wavelength because the laser may operate in an excited state or even not lase at all. Rather simple laser designs are sufficient for this step as the quick evaluation of the material has been the main target at this stage. Schematics of the two laser structures used are shown in Fig. 2.4, while an SEM image of a fabricated ridge-waveguide laser is shown in Fig. 2.5. Further details concerning the design and fabrication of all the types of lasers used in this

work are categorized in Chapter 4. The broad area lasers are particularly useful for material assessment, because their performances almost solely depend on the material quality, while ridge-waveguide lasers can provide valuable information concerning single-transverse-mode operation.

2.4 First growth campaign

In the first growth campaign the strategy was to start from the already optimized structures emitting at 1.55 μm and push the emission wavelength out, while maintaining the rest of the structure unchanged. Figure 2.6 shows the PL of all the samples that were grown during this growth campaign. In these, the Qdash height, and therefore the emission wavelength, has been adjusted by varying the InAs nominal thickness, while all other growth parameters were kept the same. In general, the exact emission wavelength of Qdash ensembles is dependent on the substrate temperature and the group-III/V flow ratio and growth rate [5]. It should also be noted that, for the same growth parameters, control of the

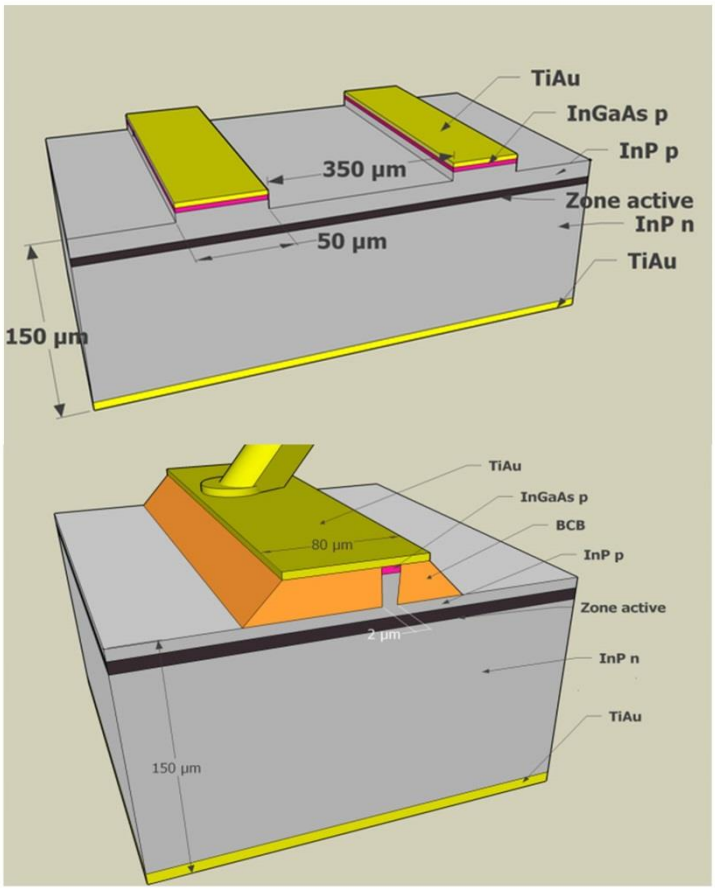

Figure 2.4 – Schematics of a broad area laser (top) and ridge-waveguide laser (bottom).

emission wavelength is high. Table 2.2 shows the epitaxial structure of three of these samples that we will use in our discussion. As it can be seen Sample 1, having a PL peak at 1.6 μm will be used as reference, for the Samples 2 and 3 with PL peaks at 1,8 and 2 μm respectively. The only difference in the epitaxial structure between these samples is the size of the Qdashes. The exact size has not been measured precisely, using TEM analysis, for each sample. This would have provided very interesting additional experimental information for analyzing the fundamental Qdash behavior as a function to their precise physical dimensions and shapes. Instead of this, during the current work, PL measurements have been used, as directly measuring the emission wavelength is a much less time-consuming and low cost way; which from a practical point of view, in regard to material optimization for laser fabrication, provides equivalent information. Such a detailed TEM analysis would however be very interesting from the basic research point of view; it has never been performed up to the present, and will be perhaps subject to future work. For samples aiming at PL peak at 2.1 μm the growth conditions had not be optimized yet during this campaign, and therefore the TEM analysis revealed the appearance of material dislocations as it may be seen

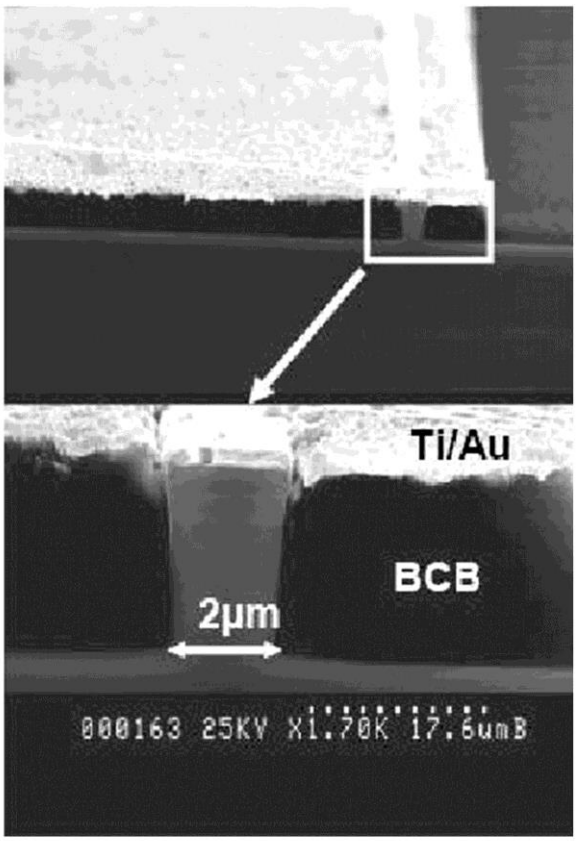

Figure 2.5 – Cross-section SEM image of a finalized ridge-waveguide laser process.

in Fig. 2.7. As a consequence no lasers were processed for such samples as the dislocations would apparently lead to degraded performances, most probably completely suppressing the lasing effect at RT. In order to obtain a first evaluation of the Qdash laser performances, broad area lasers and single-transverse-mode ridge-waveguide lasers have been fabricated and tested, for the samples with PL-peak up to 2 μm. Ridge lasers were tested in continuous wave operation, while broad area lasers were operated in pulsed mode due to internal heating effects. Cavity lengths with as-cleaved facets varied from 300 μm to 1.7 mm, for the extraction of the basic properties of these lasers. The results of the reference sample where comparable to the optimized DWell samples emitting at 1.55 μm, previously tested at LPN [9], as expected. To indicate some of the key performance values of these lasers, a high modal gain, Γg_0 of 48 cm^{-1} was deduced from a linear fit of the logarithm of the threshold current density to the inverse cavity length, while the internal losses were estimated to 10cm^{-1}, after plotting the inverse external differential quantum efficiency (n_{ext}), as a function of the cavity length (see Equation 2.4). Typical threshold current densities were measured to ~0.9-0.7 kA/cm^2 for cavity length of 600–900 μm. The internal losses α_i and the threshold current density for a nominal infinite cavity length $J_{th(inf)}$ were extracted from the following relations:

$$ln(J_{th}) = \frac{(2L)^{-1}}{\Gamma g_0} \ln\left(\frac{1}{R_1 R_2}\right) + \frac{\alpha_i}{\Gamma g_0} + \ln(J_0) \quad \textbf{(2.3)}$$

$$\frac{1}{n_{ext}} = \frac{1}{n_i}\left(1 + \frac{2\alpha_i}{\ln\left(\frac{1}{R_1 R_2}\right)} L\right) \quad \textbf{(2.4)}$$

Where $n_{ext} = \frac{q}{\hbar\omega}\frac{\Delta P}{\Delta I}$ is the external differential quantum efficiency, $\frac{\Delta P}{\Delta I}$ is the slope of the light-current characteristics (slope efficiency), $\hbar\omega$ is the photon energy, J_0 is the transparency threshold current density, q is the electron charge, and n_i the internal quantum efficiency. Output power per facet as high as 50 mW has been measured for 900 μm long devices. The electrical characteristics of these lasers were tested as well, showing a series resistance of ~3 Ω. Satisfying performances were also obtained for the sample emitting at ~1.8 μm. In this case a Γg_0 of 33 cm^{-1} has been achieved for the ridge waveguide lasers while the internal losses remain of the order of 12 cm^{-1}. Relatively low threshold currents of 50-73 mA have been routinely measured during this process and a high output power per facet of 15-20 mW have been realized for the different cavity lengths of 600-900 μm in the 1.8 μm devices. We considered these performances very satisfying, given the fact that only the Qdash

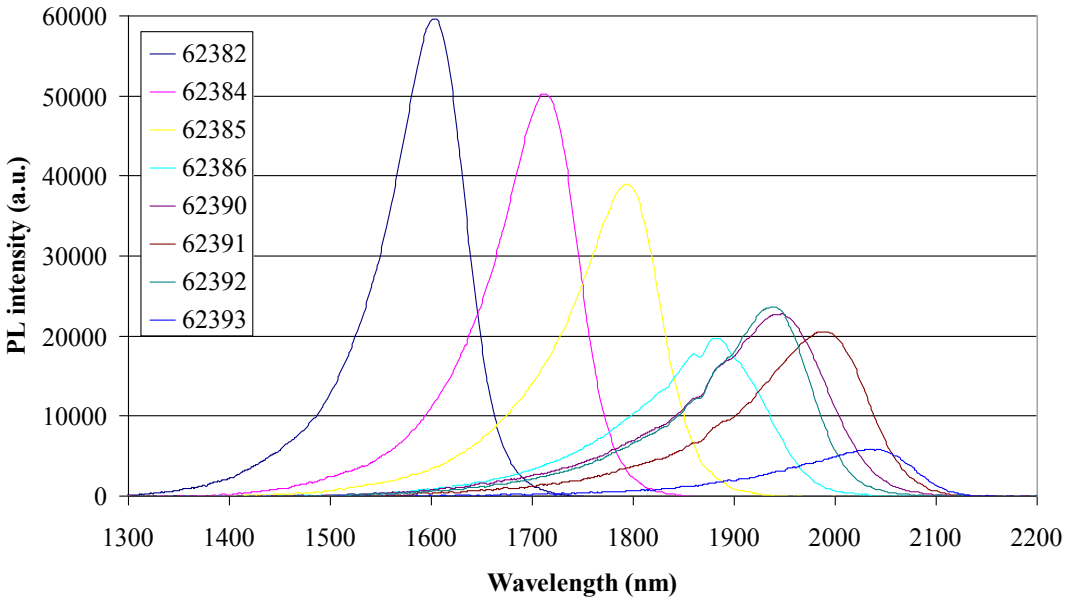

Figure 2.6 – Room temperature photoluminescence for all the samples of the first growth campaign. The Qdash height, and therefore the emission wavelength, has been adjusted by varying the InAs nominal thickness. All other growth parameters were kept the same.

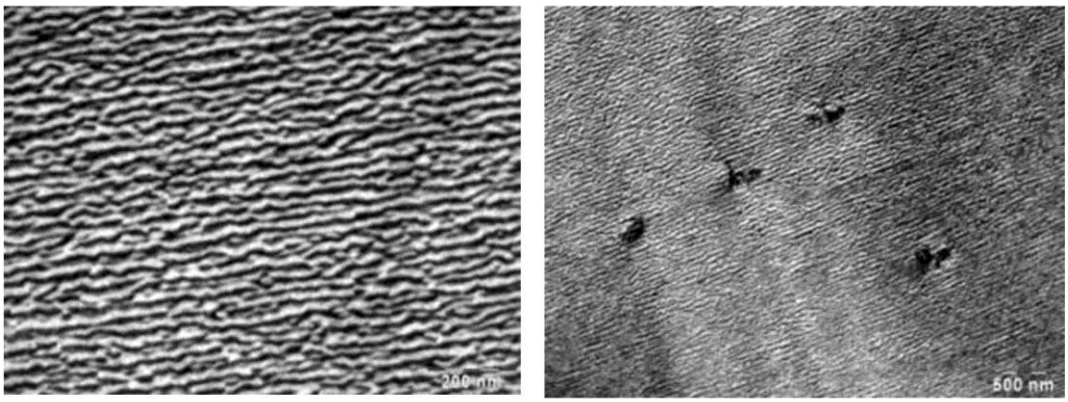

Figure 2.7 – Plan view TEM images of large Qdashes intended for 2.1 µm emission showing the formation of long dashes (left) and the apparition of dislocations (right).

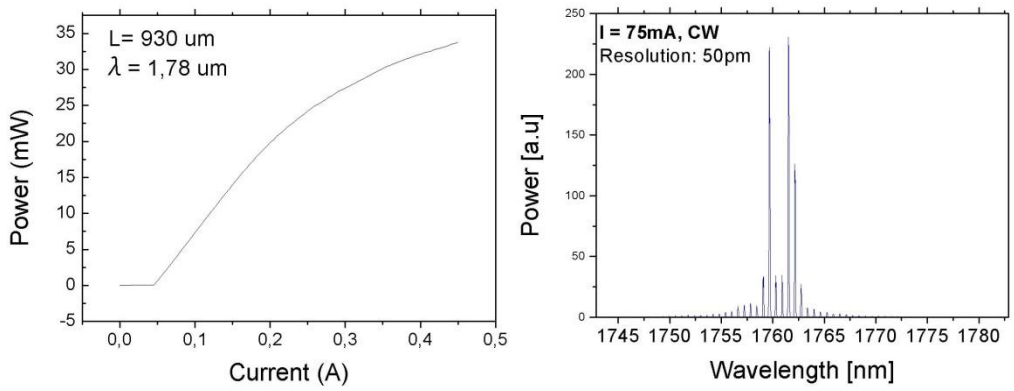

Figure 2.8 – L-I curve and spectrum of a laser emitting at 1,76 µm. (spectrum was measured at Tyndall National Institute).

Function	Material	Thickness (nm)	Comment
Contact	InGaAs	300	p^{++}-doped (Be)
Upper Cladding		1550	p^{+}-doped (Be)
Etch Stop	$In_{0.78}Ga_{0.22}As_{0.47}P_{0.53}$	35	p^{+}-doped (Be)
Top	InP	100	p^{+}-doped (Be)
SCH	$In_{0.78}Ga_{0.22}As_{0.47}P_{0.53}$	40	
Barrier	$In_{0.78}Ga_{0.22}As_{0.47}P_{0.53}$	40	X6
QWell	InGaAsP	3	X6
Qdash	InAs	1	X6 (PL at 1.6; 1.8; and 2.0 μm)
QWell	InGaAsP	3	X6
Barrier	$In_{0.78}Ga_{0.22}As_{0.47}P_{0.53}$	40	
SCH	$In_{0.78}Ga_{0.22}As_{0.47}P_{0.53}$	40	
Buffer	InP	1000	n^{+}-doped (Si)
Substrate	InP		n^{+}-doped (S)

Table 2.2 - Epitaxial structure of the Samples 1-3 of the first growth campaign, designed for emission at 1.6 μm (reference sample); 1.8 μm and 2.0 μm respectively. The different PL emission wavelengths have been achieved by changing the sizes of the Qdashes in the active region of the different samples, by adjusting the growth conditions.

sizes were modified and the whole structure remained the same in respect to the telecom lasers. Fig 2.8 shows a typical L-I curve and spectrum for a laser emitting at 1.78 μm. On the other hand, the lasers fabricated from the wafers with PL at ~ 2 μm, did not lase at all. Both the presence of a higher number of material dislocations and the increased nonradiative Auger recombination rate at longer wavelengths, are expected to affect the laser performances at 2 μm. However, our analysis showed that they should not have been severe enough to totally suppress the lasing effect. Our interpretation for this, was that the potential barrier for the confined electrons in the Qdash was too deep due to the high conduction band offset between the Qdashes and the barrier material, causing a large number of excited electronic states being present within the Qdashes. This situation reduces the number of carriers in the ground state, available for stimulated emission, and has also negative effects on carrier transport. In order to investigate this assumption different kind of samples were grown in the second growth campaign, which will be discussed in the next section.

2.5 Second growth campaign

In the second growth campaign, the barrier material and therefore the band offsets were changed. Instead of the high InGaAsP(λ=1.17 μm) barrier or the respective DWell structure with an intermediate InGaAsP QWell(λ=1.45 μm), this time a ternary InGaAs low barrier was used. The InGaAs composition for almost lattice matched material to InP essentially corresponds to a material bandgap of ~λ=1.65 μm, or a composition of $In_{0.53}Ga_{0.47}As$. The two main samples that we will discuss in this growth campaign were labelled with wafer numbers 63797 and 63802 and their epitaxial structures are shown in table 2.3. The targeted lasing emission wavelengths at 1.92 and 2.0 μm. At this point it should be noted that the exact emission wavelength also depends on the laser cavity length, which has been systematically observed in previous studies. For example as reported in [69], wavelengths shifted gradually from 1.52 to 1.55 μm when the cavity length is increased from 0.8 to 2.5 mm. In addition during our experiments the emission wavelength is always slightly red-shifted as compared to the PL-peak. This is due to the fact that our PL measurements are taken prior to the final MOCVD regrowth step, which is performed for growing the upper cladding and contact layers. This MOCVD step is performed at different temperature than the GSMBE growth which is used for growing the active layers of the structure. The difference between these two samples (63797 and 63802) is the Qdash sizes, and therefore the Qdash/barrier band offsets as well. The differences of the new samples in comparison to the first growth campaign, (besides the changes in the Qdash sizes and the change of the barrier material which was the main purpose of the design) have been the omission of the thicker separate confinement heterostructure (SCH) layer that was used in the first growth campaign (to reduce the optical waveguide thickness) and the addition of a thin quaternary contact layer to reduce the series resistance and facilitate carrier transport in the new structure. In addition, it should be noted that in the second growth campaign only DBar structures have been investigated. From our previous results, it is known that a mode confinement of around 0.15 % per Qdash layer produces good quality lasers. On this basis, the new active layer has been designed, keeping in mind that the confinement per quantum dash layer should exceed this given value. The ternary material has a significantly higher refractive index compared to the previously used InGaAsP barrier materials. The advantage arising by this fact is that the mode will be more attracted into the barrier material, thus increasing the optical confinement, while a disadvantage is that the higher refractive index is also expected to “easier” induce a bimodal behavior for larger ridge widths. The optical refractive indices were calculated for mid-

Function	Material	Thickness (nm)	Comment
Contact	InGaAs	200	p^{++}-doped (Be)
Quaternary Contact	$In_{0.78}Ga_{0.22}As_{0.47}P_{0.53}$	20	p^{++}-doped (Be)
Upper Cladding	InP	1550	p^{+}-doped (Be)
Etch Stop	$In_{0.78}Ga_{0.22}As_{0.47}P_{0.53}$	35	p^{+}-doped (Be)
Top	InP	100	p^{+}-doped (Be)
Barrier	$In_{0.53}Ga_{0.47}As$	40	X6
Qdash	InAs	1	X6 (PL at 1.92 and 1.97 µm)
Barrier	$In_{0.53}Ga_{0.47}As$	40	
Buffer	InP	1000	n^{+}-doped (Si)
Substrate	InP		n^{+}-doped (S)

Table 2.3 - Epitaxial structure of the samples 63797 and 63802 designed for emission at 1.95 and 2 µm respectively.

infrared wavelengths (2 µm) based on the theoretical model by Broberg et al [70]. Simulations were performed using the software Symphot-Alcor to evaluate the optimum value of the thickness of the active layer. It has been observed in these simulations that an

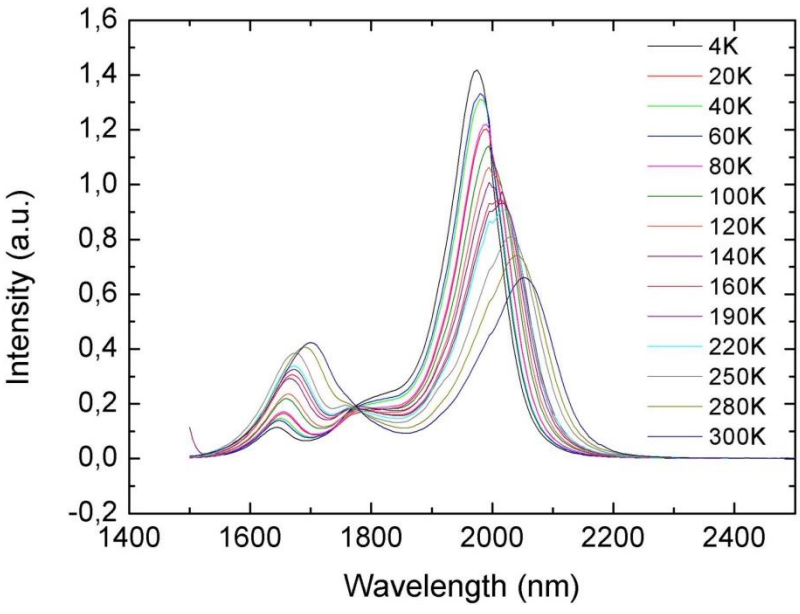

Figure 2.9 – temperature-dependent PL spectra for the sample 63802 ranging from 4 K up to RT (spectra obtained in collaboration with the University of Lancaster during K. Papatryfonos secondments within the PROPHET network).

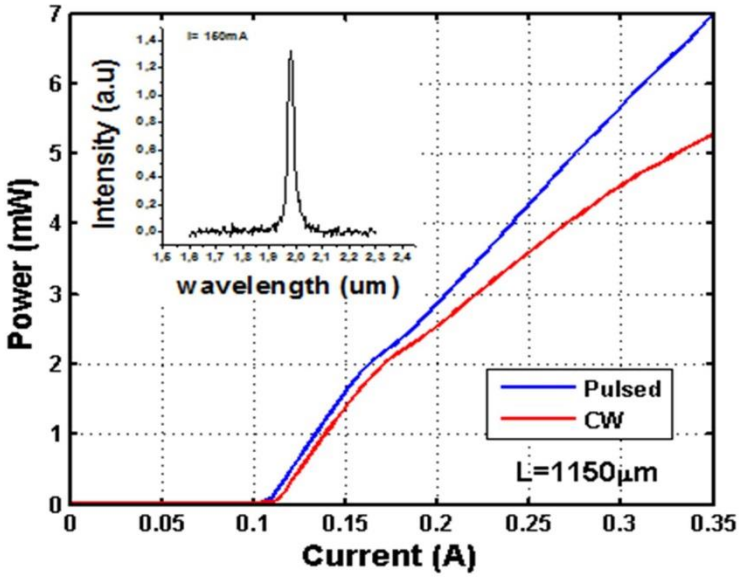

Figure 2.10 – L-I curve of a ridge-waveguide laser emitting at 1.99 µm. The spectrum shown in the inset is taken from a broad area laser from the same epi-wafer.

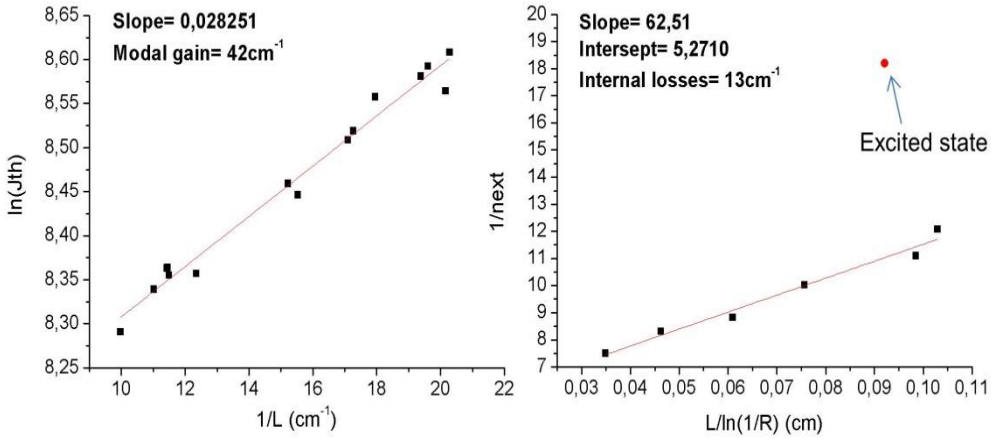

Figure 2.11 – Modal gain and internal losses extracted from broad area lasers emitting at 1.99 µm with cavity lengths varying from 400 µm to 1.7 mm.

active layer width of 280 nm to 300 nm results in the best possible optical confinement per Qdash. Figure 2.9 shows temperature-dependent PL spectra for the sample 63802, with a PL peak at 2.05 µm, ranging from 4 K up to RT. The temperature-dependence trend is very similar to the one of previously measured telecom lasers at 1.55 µm, while the ground-excited state distance is also in good agreement (visible as the small peak of Fig. 2.9, which lies between the Qdash and the barrier emission, ~1.8 µm at RT). These spectra were obtained in collaboration with the University of Lancaster our academic partner within the PROPHET network. In the following the main results obtained from these two samples will be presented and subsequently will be compared to the current state of the art in the next section. 100 µm broad area lasers as well as 2 µm ridge-waveguide lasers for single transverse mode operation

have been processed and characterized. The 2 μm wide ridges were defined by photolithography and then were transferred into the semiconductor by a combined ion beam etching and wet etching step. Continuous wave (CW) lasing at room temperature (RT) at 2μm for the sample 63802 and 1.91 μm for the sample 63797 has been achieved. The 1.9 and 2 μm lasers had a high modal gain of the order of 45 cm^{-1} and internal losses of 18cm^{-1}. The 2.5 μm ridge-waveguide lasers had a threshold current as low as 42 mA for an HR coated/as-cleaved laser of a 600 μm long cavity, while laser bars with L=1.15 mm exhibited an output power per facet of ~5.5 mW at CW operation. Figure 2.10 shows an L-I curve and spectrum of a ridge

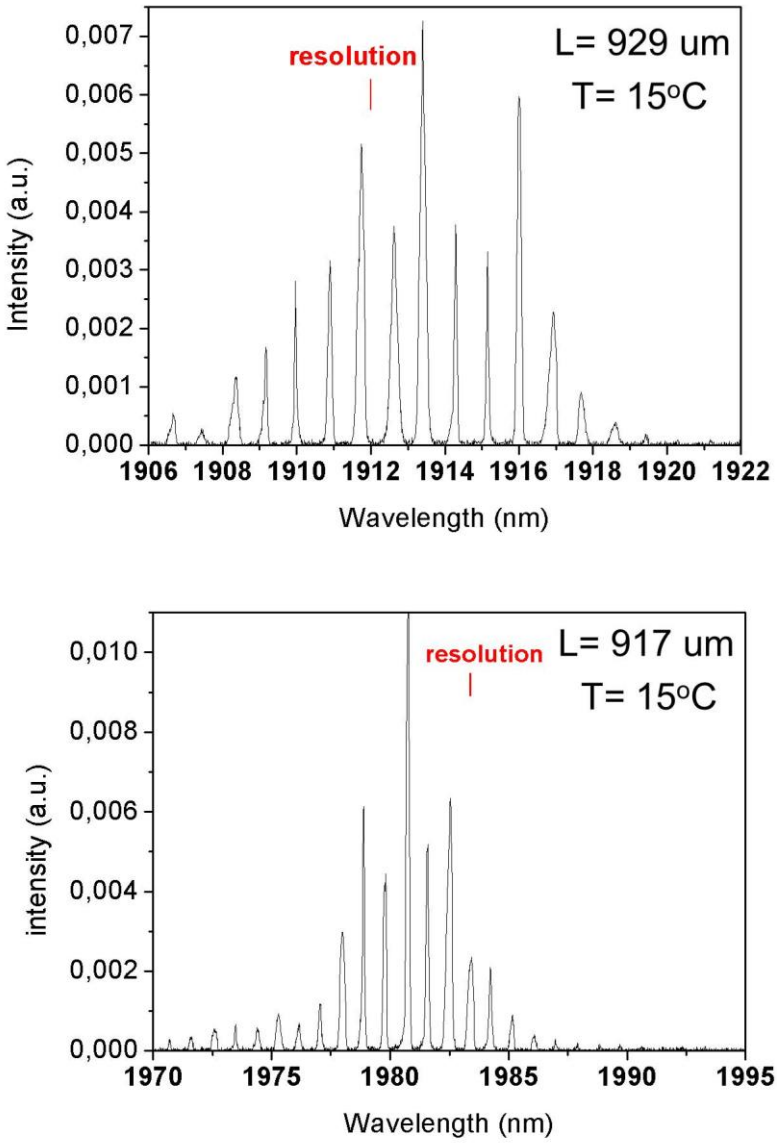

Figure 2.12 – High resolution spectra of ridge-waveguide lasers with cavity length ~900 μm obtained after processing the wafers 63797 (top) and 63802 (bottom). (In collaboration with Tyndall National Institute).

laser with a cavity length of 1150 μm. Figure 2.11 depicts the extraction of the modal gain and internal losses from broad area lasers emitting at 1.99 μm with cavity lengths varying from 400 μm to 1.7 mm obtained from the wafer 63802, using the method and equations described in the previous section. Examples of high-resolution spectra obtained for both samples, emitting at 1.91 and 1.98 μm (from the wafers 63797 and 63802 respectively), taken from lasers with cavity length of ~900 μm are shown in Figure 2.12. Figure 2.13 on the top panel, depicts a high resolution spectrum of a longer cavity of 1562 μm from wafer 63802, emitting exactly at 2 μm. In should be noted that the emission wavelength also slightly redshifts when the injection current is higher, which is due to carrier induced internal device heating. The spectra from the sample 63802, for moderate injection currents, go up to 2.07 μm (dependent on the cavity length) which compares with the longest wavelength reported up to present using InAs Qdashes on InP substrate [7] (see Section 2.6). A low-resolution spectrum of the 2.07 μm emission in a 2 mm long laser cavity is also shown in Figure 2.13, on the bottom panel. These measurements were realized in collaboration with Tyndall National Institute at Cork. A final issue that will be discussed in this section concerns the properties of our lasers after device heating due to higher injection levels. As we mentioned in the introduction, Qdashes are expected to have superior temperature insensitivity as compared to conventional QWells. However, in laser designs this parameter also strongly depends on the barrier material. Therefore, when evaluating a new design, the barrier should also be tested in respect to this parameter. A first indication can already be observed in Figure 2.13 on the bottom panel, where in the inset an emission from the barrier is apparent. This suggests a carrier escape process from the Qdashes into the barrier during laser action and is consistent with a leakage path due to insufficient barrier height. As it has also been mentioned in [71] during a QWell study, low barriers are optimum for low-threshold emission, but when the injection levels are higher, carrier thermal roll-over may appear, which very much limits the possible maximum output power. Our assumption is further supported after comparing our ridge-waveguide laser L-I curves at Pulsed and CW current operation. In such curves, we observe power saturation, even followed by a power drop at high injection currents at CW operation. This feature is likely to be caused by either the carrier thermal roll-over, or by the appearance of a bi-modal behavior, if the the ridge-waveguide width is not optimally designed, which would also lead to a similar behavior at high CW currents. As mentioned above, single transverse mode behavior might be a major issue in our 2 μm lasers due to the very high refractive index of the ternary material. Therefore, before concluding if the degradation of the CW L-I curves is due to carrier escape, it should also be tested in respect to

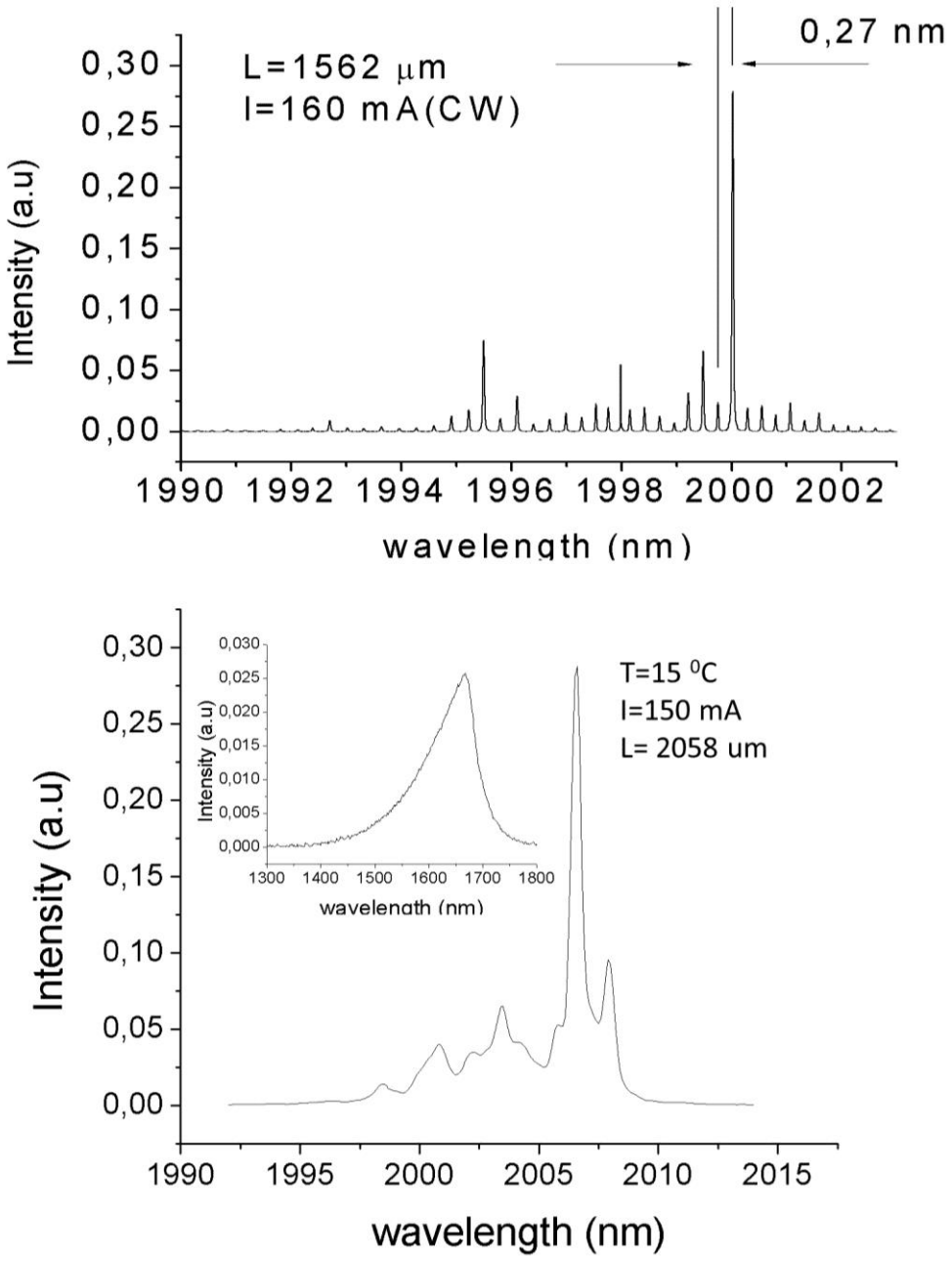

Figure 2.13 – Top: High resolution spectrum of a ridge-waveguide laser with cavity length ~1500 μm, emitting exactly at 2 μm. Bottom: Low resolution spectrum of a ridge laser from the wafer 63802 emitting at 2.07 μm which is equal to the longest lasing wavelength reported to date using InAs Qdashes. (In collaboration with Tyndall National Institute). The inset shows the relative emission from the barrier material.

the transverse-mode behavior of our lasers. In order to address this issue, we performed far field measurements at LPN. In order to validate our interpretation that the insufficient barrier height has been the reason for our observed power saturation, a new process with variable ridge-widths ranging from 1.8 μm to 2.8 μm has been realized and the transverse mode behavior of these lasers has been assessed. We observed that such ridge lasers remain single-transverse-mode for a much wider injection current interval, than the one

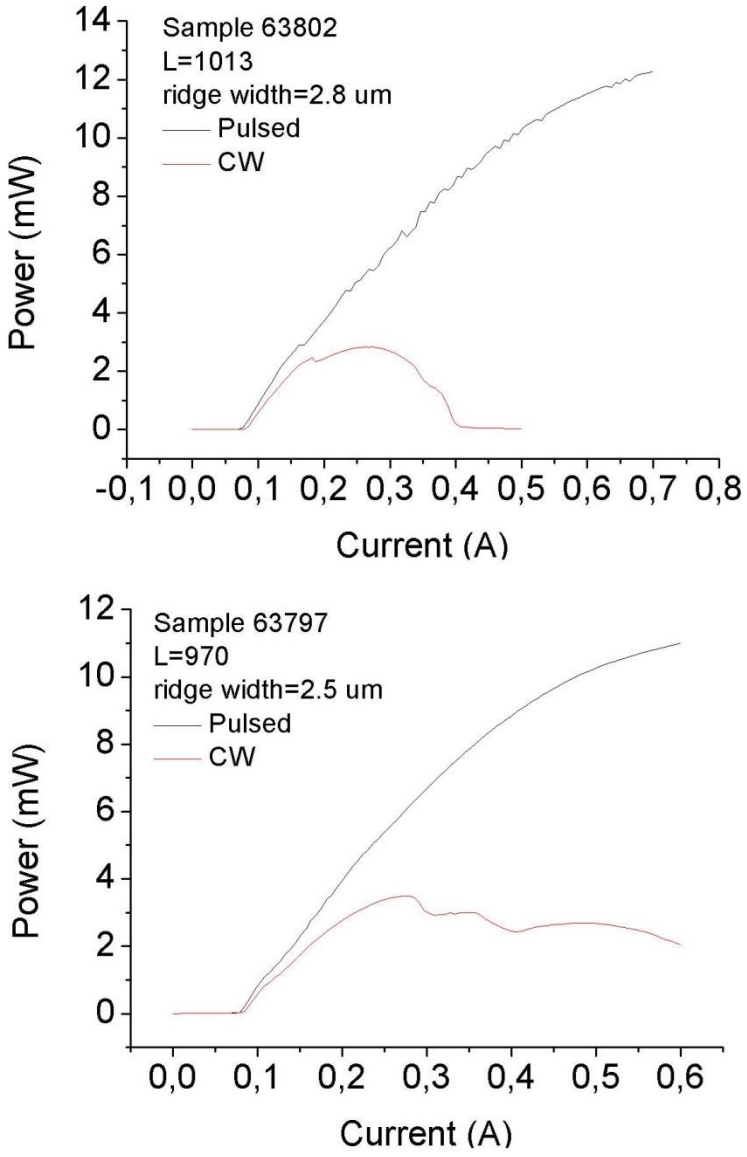

Figure 2.14 – Example comparison graphs between Pulsed and CW operation for the samples 63802 (top) and 63797 (bottom).

at which they exhibit the systematically observed output power saturation, similar to the one shown in Figure 2.14, appears. Furthermore the narrow-ridge lasers (below 2.5 μm) show to remain single-mode up-to high injection current, while their CW L-I curves already saturate at moderate currents (Figure 2.15 top panel). Therefore, we could conclude on the reason causing the saturation and based on this interpretation, new wafers similar to 63802 and 63797 but with a different barrier material, have been designed for future growth campaigns in order for this assumption to be further evaluated. These designs are aiming to continue exploiting the very promising results observed in our lasers, in terms of long emission wavelength, low threshold current densities and decent output power, while at the same time will be able to operate at higher CW currents. Our results are further supported by

the extraction of the Characteristic Temperature (T_0) for these lasers. These measurements were performed for the two 2 μm wafers, 63797 and 63802 as well as for a typical telecom reference sample, emitting at 1.55 μm. The I_{th} was tested at pulsed current in different temperatures. The T_0 for the long wavelength samples has been evaluated to ~40 K in the temperature range of 15-40 degrees ^oC, and further decreases at higher temperatures. On the other hand, for the 1.55 μm laser the T_0 is 85 K in the whole 15-75 ^oC range. This poor high temperature performance suggests that we have small electron confinement in addition to the

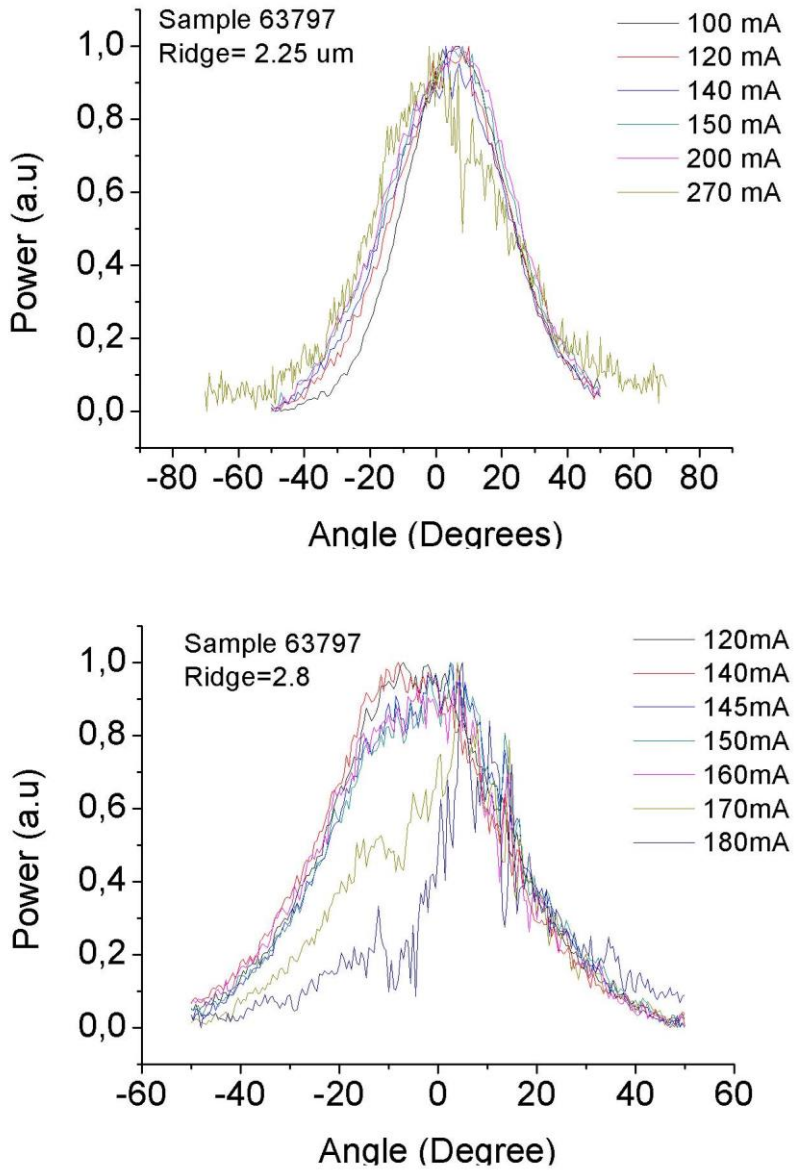

Figure 2.15 – Example far field patterns for two lasers with different ridge widths, 2.25 μm (top) and 2.8 μm (bottom). The laser with the narrow ridge remains single-mode up to high injection current, while the 2.8 μm wide ridge-waveguide exhibits bimodal behavior above 160 mA.

increased non-radiative Auger recombination rate, that is known to be wavelength dependent, having a much higher coefficient at longer wavelengths [72-75].

2.6 State of the art

In this section the current state of the art in the literature will be presented and compared to our results. Four main approaches may be found in literature concerning long-wavelength applications in the 2.0-3.5 μm wavelength range. All approaches have their own advantages and disadvantages. Therefore, we will attempt an evaluation and comparison of these approaches in terms of laser performances and longer-wavelength emission as well as their future perspectives in respect to our obtained results in Qdash based lasers. The state of the art reported in literature to date is summarized in Table 2.4. A direct comparison between our results to the Qdash based lasers with InGaAlAs barriers in a DWell structure previously reported [7], reveals an equal emission wavelength of ~2.01 μm in both cases, in combination

Emission Wavelength	Material/Structure	References/comments
2.05 μm at RT	GaSb based (two) QWell structure	LC-DFB with et Front facet AR coated (Reflectivity 2%) [76]
2.01 μm at RT	InP based Dwell structure	DFB lasers fabricated by Nanoplus [7]
2.3 μm at RT	InAs/$In_{0.53}Ga_{0.47}As$ QWells (on InP)	DFB lasers fabricated by NTT [77-78]
2.55μm at RT	GaInAs/GaAsSb/InP type II QWells	Lasing record wavelength on InP [79]
3 μm at RT	GaInAs/GaAsSb/InP type II QWells	PL emission record on InP
3.06 (at RT)	GaInAsSb/AlGaInAsSb Type I QWells	Sb-based DFB Lasers for Gas Sensing applications [80]
3.3 (at RT)	GaInAsSb/AlGaInAsSb Type I QWells	Sb-based DFB Lasers for Gas Sensing applications [81]

Table 2.4 – State of the art in terms of laser performances and long-wavelength emission in the 2.0-3.5 μm wavelength range, including the four main competing technologies: QDs/Qdashes on InP(001) substrate, Type I QWells on InP, Type II QWells on InP and Sb-based material.

with comparable device performances. On the other hand our results using the final DBar design (wafer 63802), suggest the possibility for further shifting the emission wavelength out towards longer wavelengths in the future, using the low ternary InGaAs barrier which is compatible with such designs as discussed in the previous section. Such designs will be presented in section 2.7. An alternative approach using Type-I QWell aims to use the technological advantages of using the InP(001) substrate while maintaining very competitive device performances in terms of low-threshold current and high output power. Such lasers emitting up to 2.3 μm have been reported by NTT. However this wavelength is the absolute limit for such lasers because they are limited by the QWell critical thickness which may not be further increased due to the apparition of dislocations. The alternative approach which exploits Type II QWells on InP(001) can in principle go much further in terms of emission wavelength, but the laser performances are very compromised. Finally the Sb-based lasers, operating at their natural wavelengths exhibit at the moment superior performances in this wavelength range at which they have already been fully optimized. However in terms of industrial applications, fabrication techniques and mass production possibilities the InP substrate is clearly favorable, if achieving comparable performances to their Sb-based counterparts proofs to be possible. This is the reason why even though Sb-based lasers fulfill all the requirements for high-resolution absorption spectroscopy, a lot of attention is recently given to InP-based material for the fabrication of gas sensors by different research groups worldwide. The Type II QWells as well as our Qdash approach are relatively

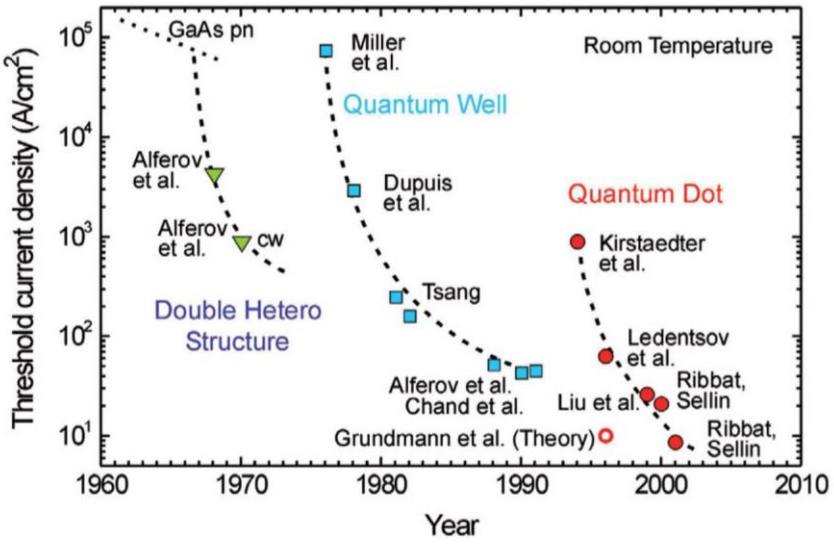

Figure 2.16 – Development of the threshold current-density of heterostructure lasers. A marked decrease of threshold was accomplished by introducing structures with reduced dimensionality: quantum wells and quantum dots. (After Bimberg et al. [83]).

new strategies in this field and are currently under investigation, while the other two mentioned approaches are already matured. They are still under development and therefore the question remains open, on how far they can go in comparison to the current state of the art. Their recently obtained results show a positive perspective. In addition, the graph presented in Figure 2.16, recently reported by Bimberg et al., shows the state of the art in terms of threshold current density reduction, which suggests a positive trend for low-dimensional structures for future laser applications, thus favoring QDs and Qdashes.

2.7 Material design for future work

In this section we present our suggestions for future continuation of this work, based on the evaluation of our results and additional simulations. The designed structures are summarized in tables 2.5-2.8. We have concluded by both our experimental results that the ternary InGaAs barrier resulted is successful for relatively low-threshold lasing, but it is not the optimum for 2 μm emission due to the fact that thermally induced carrier roll-over dominates above certain current-injection values due to device heating. Since in Gas Sensing the device cost is a very important parameter, integrated cooling systems in not an option, therefore we believe that a higher barrier would be preferable. Since our experimental results also show that the InGaAsP(1.17 μm) barrier is not optimum either, because in this case the barrier is too high, allowing a big number confined excited states within the Qdash which is detrimental for the laser performances, we propose that InGaAsP(1.36 μm) seems to be a good compromising solution. On the other hand, the InGaAs barrier that has been already used in our last 2 μm designs showing good material quality, is a very good candidate for longer wavelength emission with our simulations showing no limitation for up to even 3 μm as long as the Qdash quality does not degrade as a result of the increment of their size. If InAs Qdashes cannot be grown sufficiently large to support this, InAsSb Qdashes should be utilized, maintaining all the potential advantages in using the InP(001) substrate and low-dimensional structures. Such a design is schematically shown in Table 2.5. All the designs have been tested to be single-transverse-mode compatible by our effective-index simulations as well as to maintain an optical confinement factor of about 0.15 % in the Qdashes. Table 2.6 presents the new design for 2 μm emission based on the intermediate InGaAsP barrier that is lattice matched to InP [84]. Furthermore, based on the results presented in Sections 2.4-2.5, we suggest that a material with fewer Qdash layers is worth to be tested in future work. Such a sample is schematically shown in Table 2.7. The motivation for this would be to further

reduce the threshold current density of the lasers, by reducing the active layer volume, as well as the inhomogeneous broadening, which is known to increase by stacking a higher number of layers. If this assumption is correct, the benefit of the initial threshold current density reduction will be even further increased because the Auger recombination rate that goes like n^3 will also be reduced. Since we are operating in the long-wavelength range, the possibility

Function	Material	Thickness (nm)	Comment
Contact	InGaAs	200	p^{++}-doped (Be)
Quaternary Contact	$In_{0.78}Ga_{0.22}As_{0.47}P_{0.53}$	20	p^{++}-doped (Be)
Upper Cladding	InP	1550	p^{+}-doped (Be)
Etch Stop	$In_{0.78}Ga_{0.22}As_{0.47}P_{0.53}$	35	p^{+}-doped (Be)
Top	InP	100	p^{+}-doped (Be)
Barrier	$In_{0.53}Ga_{0.47}As$	40	X6
Qdash	InAs	1	X6 (PL at 2.3-3.0 μm)
Barrier	$In_{0.53}Ga_{0.47}As$	40	
Buffer	InP	1000	n^{+}-doped (Si)
Substrate	InP		n^{+}-doped (S)

Table 2.5 – The material design is compatible with longer wavelength emission.

Function	Material	Thickness (nm)	Comment
Contact	InGaAs	200	p^{++}-doped (Be)
Quaternary Contact	$In_{0.78}Ga_{0.22}As_{0.47}P_{0.53}$	20	p^{++}-doped (Be)
Upper Cladding	InP	1550	p^{+}-doped (Be)
Etch Stop	$In_{0.78}Ga_{0.22}As_{0.47}P_{0.53}$	35	p^{+}-doped (Be)
Top	InP	100	p^{+}-doped (Be)
Barrier	$In_{0.71}Ga_{0.29}As_{0.68}P_{0.32}$	40	X6
Qdash	InAs	1	X6 (PL 1.97 μm)
Barrier	$In_{0.71}Ga_{0.29}As_{0.68}P_{0.32}$	40	
Buffer	InP	1000	n^{+}-doped (Si)
Substrate	InP		n^{+}-doped (S)

Table 2.6 – Material design for 2 μm emission based on the intermediate barrier $In_{0.71}Ga_{0.29}As_{0.68}P_{0.32}$.

of reducing the active layer volume, due to our high modal gain, will be much more beneficial as compared for example to conventional lasers operating 1.55 μm, due to the difference in the Auger recombination coefficient. Another way to reduce the Auger problem is to increase the optical confinement factor which is served in this case by a high index barrier. However, the low energy barrier is a mentioned above, not favorable for the new 2 μm designs due to the previous assumptions, but it may serve for this purpose in longer-wavelengthemission. Finally, Table 2.8 presents another possible design to push the emission wavelength to 2.7 μm using a DWell design with a strained quantum well and, InGaAs (1.65 μm) barriers. The QWell used has a bandgap energy of 2 μm. Such QWells have been systematically reported in literature using compressively strained $In_{0.75}Ga_{0.25}As$ QW on InGaAs and other barriers. The thickness of the QW is well below the critical thickness and is ~10 nm (it varies a little between the different references reported, for example [85-87]). Dwell designs are known to push the emission wavelength further, compared to a DBar design with same Qdash sizes. Also in some cases, they were reported to have superior laser characteristics. From the literature, it is known that in a Dwell structure, the QWell is better to be as deep as possible (close to the Qdash transition energy). In our case a 2 μm QWell was chosen as the deepest realizable design, because the growth of multiple QWells with higher strain would be difficult. However, DWell structures were reported so far in literature, but only using quantum wells with material lattice matched to InP. A Dwell structure based on

Function	Material	Thickness (nm)	Comment
Contact	InGaAs	200	p^{++}-doped (Be)
Quaternary Contact	$In_{0.78}Ga_{0.22}As_{0.47}P_{0.53}$	20	p^{++}-doped (Be)
Upper Cladding	InP	1550	p^{+}-doped (Be)
Etch Stop	$In_{0.78}Ga_{0.22}As_{0.47}P_{0.53}$	35	p^{+}-doped (Be)
Top	InP	100	p^{+}-doped (Be)
Barrier	$In_{0.71}Ga_{0.29}As_{0.68}P_{0.32}$	40	X4
Qdash	InAs	1	X4 (PL 1.97 μm)
Barrier	$In_{0.71}Ga_{0.29}As_{0.68}P_{0.32}$	40	
Buffer	InP	1000	n^{+}-doped (Si)
Substrate	InP		n^{+}-doped (S)

Table 2.7 – Material design for 2 μm emission based on the intermediate barrier $In_{0.71}Ga_{0.29}As_{0.68}P_{0.32}$.

Function	Material	Thickness (nm)	Comment
Contact	InGaAs	200	p^{++}-doped (Be)
Quaternary Contact	$In_{0.78}Ga_{0.22}As_{0.47}P_{0.53}$	20	p^{++}-doped (Be)
Upper Cladding		1550	p^{+}-doped (Be)
Etch Stop	$In_{0.78}Ga_{0.22}As_{0.47}P_{0.53}$	35	p^{+}-doped (Be)
Top	InP	100	p^{+}-doped (Be)
SCH	$In_{0.53}Ga_{0.47}As$	80	
Barrier	$In_{0.53}Ga_{0.47}As$	40	X4
QWell	InGaAsP	5	X4
Qdash	InAs	1	X4 (PL at 2.0 μm)
QWell	$In_{0.75}Ga_{0.25}As$	5	X4
Barrier	$In_{0.53}Ga_{0.47}As$	40	
SCH	$In_{0.53}Ga_{0.47}As$	80	
Buffer	InP	1000	n^{+}-doped (Si)
Substrate	InP		n^{+}-doped (S)

Table 2.8 – A DWell structure based on strained QWells.

strained QWell has never been reported. Therefore, it would be very interesting to investigate this possibility, but it remains uncertain whether the realization of such structure might be feasible.

Chapter 3

Tunable single-mode lasers for Gas Sensing

After achieving the appropriate emission wavelength in respect to the gas resonances, in order to target high-resolution gas detection single-frequency lasers are highly desirable. This necessity is schematically illustrated in Figures 3.1 and 3.2, in which the signal change expected in an HCl gas detection experiment, using a Fabry Perot laser has been simulated by our industrial partner PROCAL for the purpose of this project. In Figure 3.1 a typical spectrum of a FP laser is plotted together with the HCl absorption lines. The parameters used in the simulation assumed laser output power of P=1 mW, current sensitivity of the InGaAs photodetector of R_i= 0.8W/A and transparence gain of the preamplifier G= 10^4 V/A. Taking these parameters the expected signal, if all the power is focused on the detector without any additional losses would be Signal= $P * R_i * G$ = 8V. The expected signal change due to absorption of 200 ppm HCl in 1 bar atmosphere and 1 m path length is depicted in Figure 3.2. It may be seen that the change of the laser power impinging on detector is so small, that any effect is not observable, unless the absorption would be increased by ~ two orders of magnitude. The change in laser power due to absorption is shown in the graph of the bottom panel of Figure 3.2, corresponding to an integrated power of 0.215μW. This would suggest that in order to measure the effect of introducing HCl gas into the path length of such a FP laser, we would try to see a very small (0.215 μW * 0.8A/W *10^4 V/A= 1.7mV) signal change on top of 8V background. This would lead to non-observable effects or in the best case to detection with a very low sensitivity. Therefore, another aim of this project has been the processing of distributed feedback (DFB) or distributed Bragg reflector (DBR) lasers out of our optimized epi-wafers. Such lasers may be fabricated by using an additional Bragg grating to the conventional ridge-waveguide fabrication process, with different schemes being possible. Namely, the Bragg grating may be buried, patterned and etched after growth interruption, sidewall, this fabricated during the ridge fabrication step, or lateral, fabricated in a final step after the definition of the waveguide. Details on the fabrication steps are given in Chapter 4. Therefore a better understanding of the grating influence to the modal behavior is

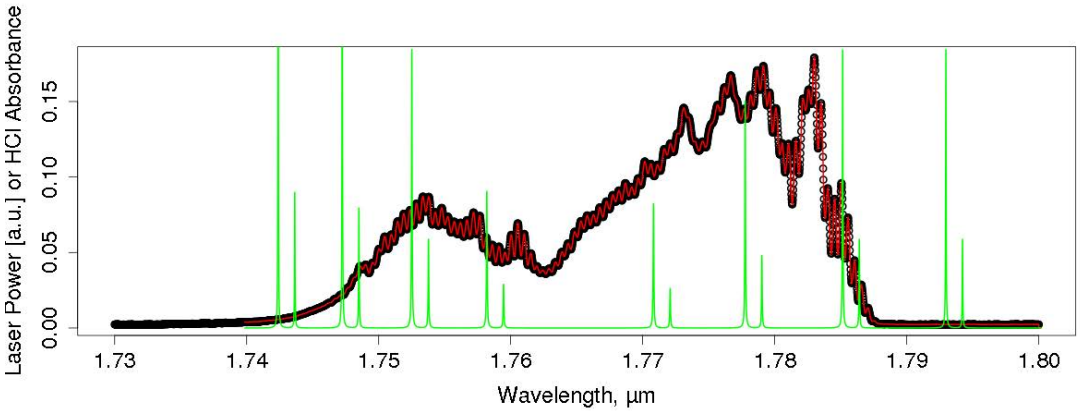

Figure 3.1 – FP Laser power (red is interpolation to match grid of absorbance and laser power) as a function of wavelength versus HCl absorbance calculated using HITRAN 2012 database. (Courtesy of K. Klos, ITN PROPHET).

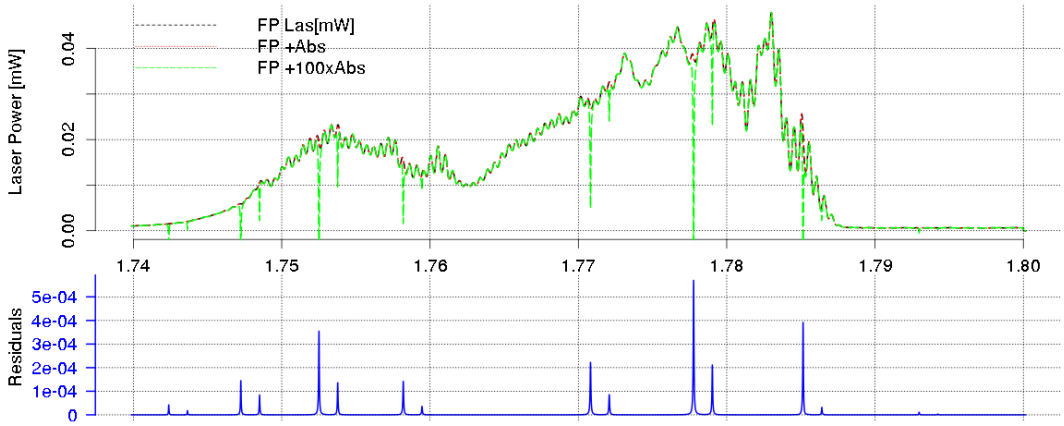

Figure 3.2 – Top: Characteristic of FP laser power (black) and effects of HCl gas absorbance (red), and 100x larger absorbance (green). Bottom: Change in laser power due to absorption. (Courtesy of K. Klos, ITN PROPHET).

important for properly designing such DFB lasers. The particular needs for commercial gas sensing applications require for particular attention in reducing the laser production costs (simplification of the laser processing as compared to conventional telecom lasers), reduction of the threshold current required to operate the laser and sufficient wavelength tunability to scan over at least one laser absorption line. In this Chapter we will analyze our simulation methodology and outline our design selection in respect to the above parameters. We will furthermore compare it to other interesting alternative designs proposed in literature, which we will also briefly introduce. The Chapter is organized as follows. In Sec 3.1 an introduction to the Coupled-mode theory [88-90] and the most important equations for modelling DFB and DBR lasers based on the Bragg grating photonic bandgaps, are provided.

In Sec 3.2, the principles of evanescent waves and lateral feedback are introduced in respect to the proposed design of laterally-coupled DFB lasers for gas sensing applications. For completeness, references and brief description of the most important alternative approaches that would be, in our opinion, the most suitable for gas sensing applications are provided in Sec 3.3. Sec 3.4 underlines the importance of the coupling coefficient value, κ, in such laterally coupled designs and subsequently our design optimizing this parameter, using high-duty-cycle Bragg gratings, is described. Based on the results, we underline the perspective in using the high-duty-cycle etched semiconductor gratings for the fabrication of LC-DFB/LC-DBR lasers in respect to the desired specifications of the gas sensing industry, as they were outlined by our industrial partner, PROCAL, within the PROPHET ITN network.

3.1 Theory of Bragg gratings

The rapid development in the fields of single mode semiconductor lasers and fiber Bragg gratings inscription, in combination with the recent developments in integrated optics fabrication methods which have resulted in the capability of producing a large variety of periodic and aperiodic structures, created the requirement to carefully model their behavior. The effort has been to achieve the best possible description of the propagation of electromagnetic fields in optical waveguides and of the physical mechanisms behind their interaction with Bragg gratings. This can be obtained with several computational methods; the most important of them can give reliable results in logical computational times. In this Chapter, we will focus on giving a brief description of the mostly utilized method to date, the coupled-mode theory. In addition, based on this theory, we will provide a detailed description of the piecewise uniform approach combined with the Transfer Matrix method, for simulating non-uniform, almost-periodic, grating structures.

The first laser action in periodic structures was observed by Kogelnik and Shank in 1971 [91], and in the following years the well-known coupled-mode theory [88-90] was introduced. A pair of coupled wave equations are solved under specific boundary conditions, where the diffraction grating can be described as a longitudinal periodic variation of the refractive index $n(z)$ and/or the gain $g(z)$ (or loss) in the laser medium. Since then numerous active devices have been reported based on Bragg gratings and they are generally categorized in two types, the DFB and the DBR lasers. In the former, the grating is placed along the whole length of the laser cavity. The mode selectivity is then provided by the Bragg grating, as a result of the fact that the threshold gain is different for the different guided modes,

increasing with their spectral distance from the Bragg resonance. This is because, in general, the threshold increases as the coupling is lowered, as the resonances deviate from the Bragg condition [88]. In the later, the grating is placed in some part of the laser cavity, acting as a selective mirror on one or both ends of the laser, replacing the as-cleaved facets of a FP laser. In this case the mode selectivity is provided by a higher reflection of the resonant (Bragg) mode, which is thus further amplified due to a higher number of cavity round-trips and is favored during gain competition. In both cases a detailed understanding of the physics of the grating involved in the structure is of great interest. The basic principle of operation of Bragg gratings is Fresnel reflection. When an electromagnetic wave propagates between two media with different refractive index, a part of the radiation is reflected at the interface and the remaining part is diffracted and transmitted through the other medium. Similarly, when an electromagnetic wave propagating in a waveguide reaches each segment of a Bragg grating, a part of its radiation is being scattered. If the segments of the grating have an appropriate period, such that the Bragg condition is satisfied, then the reflected signals from each part of the grating interfere constructively and produce a strong reflected (resonant) signal. The wavelength of the reflected signal is determined solely by the parameters of the grating. Other wavelengths that do not satisfy the Bragg condition are transmitted through the grating almost unaffected, with very low losses, as their reflected signals interfere destructively. At its most basic form, a Bragg grating is constructed by a periodic modulation of the refractive index (index-guided), perpendicular to the wave propagation in a waveguide. The Bragg condition is nothing else but the requirement that through a Bragg grating energy and momentum should be conserved. Energy conservation requires that the frequencies of the incident and reflected radiation are the same ($\hbar\omega_f = \hbar\omega_i$). Momentum conservation requires that the incident wavevector $\boldsymbol{k_i}$ plus the grating wave vector $\boldsymbol{K}$ should equal the wavevector of the scattered radiation $\boldsymbol{k_f}$. This is simply stated as:

$$\boldsymbol{k_i + K = k_f} \qquad \textbf{(3.1)}$$

Where the grating wavevector $\boldsymbol{K}$, has a direction normal to the grating planes with a magnitude equal $2\pi/\Lambda$ (with Λ the period of the grating). The diffracted wavevector, $\boldsymbol{k_f}$ is equal in magnitude, but opposite in direction to the incident wavevector, $\boldsymbol{k_i}$. Hence, the momentum conservation reads:

$$2\left(2\pi\frac{n_{eff}}{\lambda_B}\right)=\frac{2\pi}{\Lambda} \qquad \textbf{(3.2)}$$

which simplifies to the first-order Bragg condition:

$$\lambda_B = 2n_{eff}\Lambda \qquad \textbf{(3.3)}$$

Where λ_B is the central wavelength and n_{eff} is the modal effective index. Equation 3.3 already provides the Bragg wavelength for a grating with constant period. However, this Equation does not offer any information on the bandwidth of the photonic bandgap of the grating, or the coupling coefficient magnitude. Such information is often highly desirable. In addition, some specific applications require that the Bragg grating pitch be non-uniform. One advantage of this would be for example the reduction of undesirable sidelobes that are so prevalent in uniform grating spectra. One extremely effective way for reducing these features is the so-called apodization of the refractive index, or an alternative way would be by chirping the grating period. In the first case the coupling coefficient of the Bragg grating varies throughout its length, while in the second case the varying parameter is the grating period. A big number of important applications, including achieving a higher SMSR, would immediately be favored by the reduction of such side lobes. To obtain this information a more sophisticated theory needs to be implemented. The coupled-mode theory during over the last four decades has proven to be a very powerful tool in predicting the grating response either in fiber Bragg grating based sensors or in active devices such as DFB and DBR lasers. Due to its very high quantitative accuracy, very intuitive formalism and ability to model almost any type of grating structures, this theory has been intensively used and tested in numerous scientific reports up to present. It is for this reason that while alternative approaches exist, during this work we have mainly focused on this approach. Within this text, we do not provide a derivation of coupled-mode theory, as this has been detailed in numerous articles and text books (see for example [92]). According to the ideal mode approximation to the coupled-mode theory the propagation of an electromagnetic wave through a Bragg grating can be approximated by the propagation in an ideal waveguide (of constant refractive index) and then a correction considering a perturbation in the field, as a result of the presence of the grating, is introduced. The non-perturbative and perturbative solutions are subsequently connected through coupled differential equations. Our notation follows most closely that of Othonos and Kalli and T. Erdogan [90,93]. While the propagating modes in an ideal waveguide are orthogonal, and hence do not exchange energy, the presence of the dielectric perturbation

caused by the presence of a Bragg grating results in mode coupling such that the amplitudes A_j and B_j of the j_{th} mode evolve along the z-axis according to the following equations [90].

$$\frac{dA_m}{dz} = i\sum_q A_q\left(C_{qm}^T + C_{qm}^L\right)\exp\left[i\left(\beta_q - \beta_m\right)z\right] + i\sum_q B_q\left(C_{qm}^T - C_{qm}^L\right)\exp\left[-i\left(\beta_q + \beta_m\right)z\right] \quad \textbf{(3.4)}$$

$$\frac{dB_m}{dz} = -i\sum_q A_q\left(C_{qm}^T - C_{qm}^L\right)\exp\left[i\left(\beta_q + \beta_m\right)z\right] - i\sum_q B_q\left(C_{qm}^T + C_{qm}^L\right)\exp\left[-i\left(\beta_q - \beta_m\right)z\right] \quad \textbf{(3.5)}$$

Where β_q and β_m are the propagation constants and C_{qm}^T is the transverse coupling coefficient for modes q and m given in general by:

$$C_{qm}^T = \iint_\infty \Delta\varepsilon(x,y,z)e_q^T(x,y)\, e_m^T(x,y)dxdy \quad \textbf{(3.6)}$$

With $\Delta\varepsilon(x,y,z)$ the dielectric constant perturbation and $e_q^T(x,y)$ and $e_m^T(x,y)$ account for the transverse mode electric fields for modes q and m. For uniform Bragg gratings with a constant period Λ, the couple mode equations simplify and may be solved in closed form solutions. The refractive index change in a Bragg grating with constant period may be described by the following function:

$$n(z) = n_o + \Delta n \cdot \cos\left(\frac{2\pi z}{\Lambda}\right) \quad \textbf{(3.7)}$$

Where n_0 is the refractive index of the unperturbed waveguide and Δn is the magnitude of the refractive index contrast. Then, the reflectivity of such grating may be calculated by the following equation. The derivation is detailed in Ref. [94]:

$$R(l,\lambda) = \frac{\kappa^2 \cdot \sinh^2\left(s \cdot l\right)}{\Delta\beta^2 \cdot \sinh^2\left(s \cdot l\right) + s^2 \cdot \cosh^2\left(s \cdot l\right)} \quad \text{for } \kappa^2 > \Delta\beta^2$$

(3.8)

$$R(l,\lambda) = \frac{\kappa^2 \cdot \sin^2\left(Q \cdot l\right)}{\Delta\beta^2 - s^2 \cdot \cos^2\left(Q \cdot l\right)} \quad \text{for } \kappa^2 < \Delta\beta^2$$

Here, $R(l,\lambda)$ is the reflectivity of the grating which is a function of the gratings length, l and the wavelength, λ. κ is the coupling coefficient, $\Delta\beta = \beta - \pi/\lambda$ is the detuning wavevector, $\beta = 2\pi n_0/\lambda$ is the eigen propagation constant and $s^2 = \kappa^2 - \Delta\beta^2$ or $Q^2 = \Delta\beta^2 - \kappa^2$. At the central Bragg wavelength the detuning of the wavevector equals to zero, $\Delta\beta = 0$ and the relation 3.8 for the reflectivity becomes:

$$R(I,\lambda) = \tanh^2(\kappa d) \quad \textbf{(3.9)}$$

From the above analysis, we can extract several useful conclusions. First, it is obvious that the reflectivity of a Bragg grating is increased with the refractive index contrast. At this point though, we should note that a very large index modulation would lead to saturation of the reflectivity of the grating and in this case, broadening of the reflected spectrum. In addition, as the grating length is being increased the reflectivity increases as well, as expected intuitively. However, in DBR lasers long grating sections are undesirable due to the fact that they introduce additional losses, therefore high index contrast gratings are highly preferable, especially in the case of laterally-coupled lasers in which the grating strength is an important

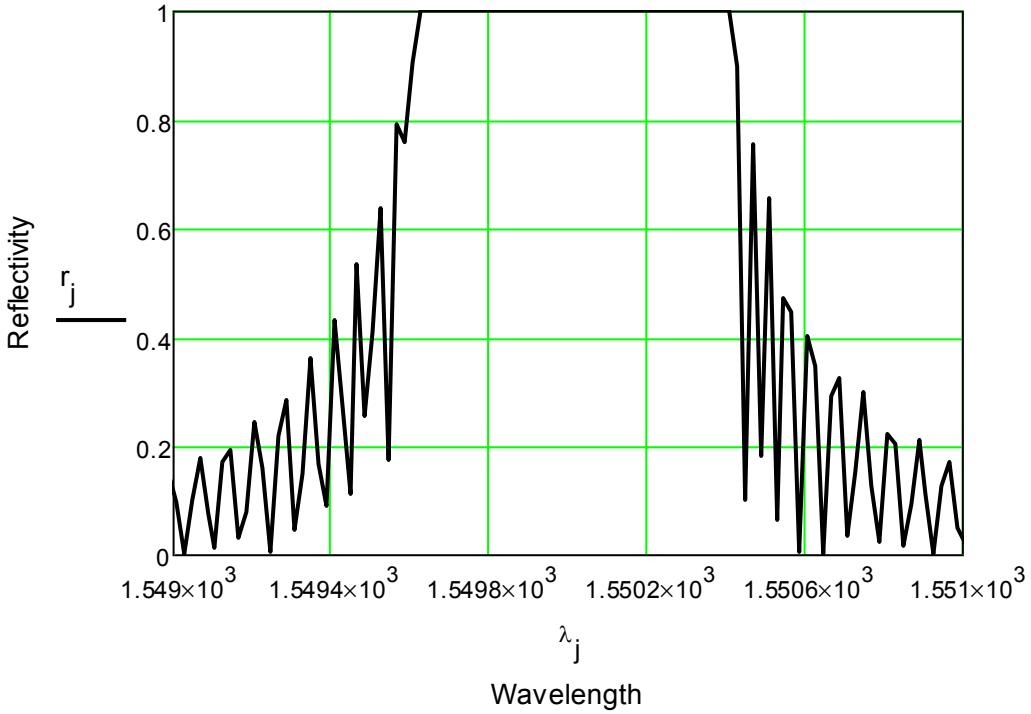

Figure 3.3 – Example of typical reflection spectrum of a uniform Bragg grating, simulated using the software MathCAD. The reflection spectrum is saturated for a strong grating with κL=8.

issue and needs to be substantially increased. A typical spectrum of a uniform grating has been simulated using the software MathCAD and is depicted in Figure 3.3. The side lobes which are observed on both sides of the central wavelength in such constant period gratings are a result of the interferences of the multiple reflections which take place on the grating planes. Finally it should be pointed out that the sine spectrum arises mathematically from the Fourier transform of a harmonic signal having finite extend; an infinitely long grating would transform to an ideal delta function response in the wavelength domain. In the case of non-uniform gratings, closed form solutions to the coupled-mode equations do not exist and these equations need to be solved numerically, after the appropriate approximations are introduced in order to maintain an acceptable computational time. In this work non-uniform gratings will be approximated using the "two-mode coupling method" [90,95]. There are two effective ways to obtain the reflection and transmission spectra using this method. First, one may numerically integrate the coupled-mode equations. Second, one may apply a piecewise-uniform approach [95]. In the former approach, the grating is divided into sub-gratings with length higher than the grating period, but with the limitation that each subsection may not be too long. Thus, each section can be considered to have an approximately constant period, but the periods of the different segments can vary, when modelling non-uniform gratings. The advantage of this approach is that, since we are approximating each sub-grating to have a uniform period, the coupled-mode equations have closed formed solutions in each of these subsections. As a result, 2x2 matrices may be written, starting from the coupled-mode equations, representing these uniform sub-gratings, and the so-called Transfer Matrix method may be used in order to calculate all the desired parameters. These matrices include all the information for each "uniform" grating section in closed form, and may thus be used as simple input-output ports in the calculations for propagating light waves, in a way which will be presented below. Then, the information for the whole grating is obtained by multiplying all these 2x2 matrices together, in order to "reconstruct" the whole grating. This has proven to be a very powerful and computationally effective approach giving accurate results for non-uniform gratings of any length. As mentioned above, we can assume for simplicity the Bragg grating to be a perturbation to the effective refractive index n_{eff}. For non-uniform gratings the relation of Equation 3.7 generalizes to [90]:

$$\delta n_{eff} = \overline{\delta n}_{eff}(z)\left[1 + F\cos\left(\frac{2\pi}{\Lambda}z + \phi(z)\right)\right] \qquad \textbf{(3.10)}$$

Where F is the fringe visibility of the index change, Λ is the nominal period, $\phi(z)$ is a

function describing the grating chirp and $\overline{\delta n}_{eff}$ is the index change spatially averaged over a grating period. Then, getting back to Equations 3.4 and 3.5 and remembering that for a Bragg grating the dominant interaction lies near the central Bragg wavelength (for which reflection from a mode of amplitude $A(z)$ into an identical counter-propagating mode $B(z)$ occurs), these equations may be re-written in a simplified form, given by Equations 3.11 and 3.12 [90].

$$\frac{dA}{dz} = i\zeta^{+}A(z) + i\kappa B(z) \quad \textbf{(3.11)}$$

$$\frac{dB}{dz} = i\zeta^{+}B(z) + i\kappa^{*}A(z) \quad \textbf{(3.12)}$$

In this simplification we have actually removed the rapid oscillating terms that do not contribute to the change of the amplitudes A_k and B_k, and introduced ζ^{+}, as the general "dc" self-coupling coefficient defined as:

$$\zeta^{+} = \delta_d + \zeta - \frac{1}{2}\frac{d\phi}{dz} \quad \textbf{(3.13)}$$

with δ_d being the detuning parameter, which is independent of z and is defined as follows:

$$\delta_d = 2\pi n_{eff}\left(\frac{1}{\lambda} - \frac{1}{\lambda_B}\right) \quad \textbf{(3.14)}$$

Figure 3.4 shows a schematic representation of the piecewise uniform approach. As it can be seen, a grating can be made up of M sub-gratings given by matrices describing approximately uniform gratings, with A_k, B_k being the amplitudes of the counter propagating electric fields, when transmitting through the k_{th} section. Thus, after setting the boundary conditions as: $A_0=A(-L/2)=1$, $B_0=B(L/2)=0$, we may calculate the forward and backward propagating amplitudes up to the last section $A_M=A(L/2)$ and $B_M=B(L/2)$. Here we have assumed the centre of the grating to be positioned at $L=0$ and incident wave only from left to right with an amplitude of $A_0(-L/2)=1$, when reaching the first grating segment. The transmission through the k_{th} uniform sub-grating is given by the matrix T_k as follows:

$$\begin{pmatrix} A_k \\ B_k \end{pmatrix} = T_k \begin{pmatrix} A_{k-1} \\ B_{k-1} \end{pmatrix} \qquad \textbf{(3.15)}$$

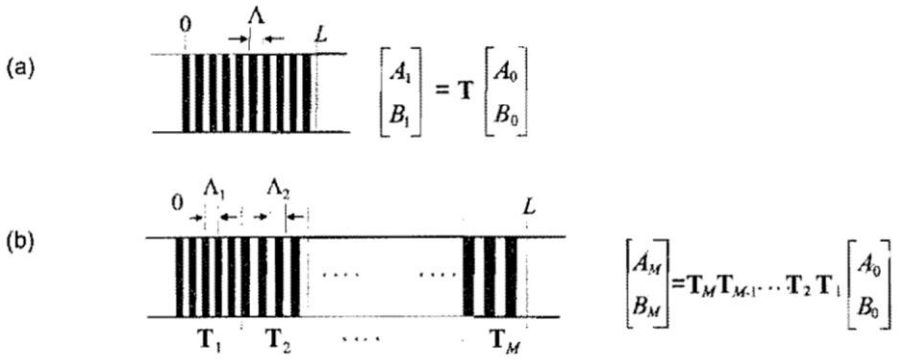

Figure 3.4 – Illustration of the piecewise-uniform approach: (a) a single uniform Bragg grating and (b) a series of gratings with different periods back to back (after Ref. 90).

Where the matrix T_k is defined as follows [90]:

$$T_k = \begin{pmatrix} \cosh(\Omega dz) - i\frac{\zeta^+}{\Omega}\sinh(\Omega dz) & -i\frac{\kappa}{\Omega}\sinh(\Omega dz) \\ i\frac{\kappa}{\Omega}\sinh(\Omega dz) & \cosh(\Omega dz) + i\frac{\zeta^+}{\Omega}\sinh(\Omega dz) \end{pmatrix} \qquad \textbf{(3.16)}$$

Where dz is the length of the k_{th} uniform section, ζ^+ and κ are the local coupling coefficients for the k_{th} section and

$$\Omega = \sqrt{\kappa^2 - \zeta^{+2}} \qquad \textbf{(3.17)}$$

The total grating structure may finally be expressed as:

$$\begin{pmatrix} A_M^+ \\ B_M^+ \end{pmatrix} = T_M \cdot T_{M-1} \cdot \ldots \cdot T_\kappa \cdot \ldots \cdot T_1 \begin{pmatrix} A_0^+ \\ B_0^+ \end{pmatrix} \qquad \textbf{(3.18)}$$

The piecewise-uniform approach is ideal for analyzing chirped gratings which is the example illustrated in Figure 3.4. In the case of linearly chirped gratings the total structure may be made up of M subgratings, each with period Λ_k, which increases linearly as shown in Figure 3.4. However, in such simulations it is also important to keep in mind the constraints under which the performed assumptions are still valid. It should be noted that the number of the M sub-sections to which the grating will be divided may not be arbitrarily large. This is

because the approximations we made to obtain Equations (3.11) and (3.12) are no longer valid if a uniform sub-grating length is only as big as a few grating periods. For this reason, one needs to be very careful when making the choice of M, which on the other hand determines the accuracy of the calculations. In general, the piecewise–uniform approach can be applied for apodized and chirped Bragg gratings by simply assigning constant values to ζ, κ and 0.5 $d\varphi/dz$, which are evaluated at the center of each section. In the case of a phase-shifted Bragg grating, which has been studied in detail during the present work due to its great importance for the fabrication of DFB lasers, this approach is again very effective. This is due to the fact that phase shifts of any magnitude and at any position in the Bragg grating may be introduced into the model by simply inserting during the multiplication procedure of Equation 3.18, additional matrices, $\overline{\boldsymbol{T_k}}$ corresponding to the given phase shift, placed in-between the Transfer matrices, T_k and T_{k+1}. Such a phase-shift matrix has the following form:

$$\overline{T_k} = \begin{bmatrix} exp\left(-\frac{i\varphi_k}{2}\right) & 0 \\ 0 & exp\left(\frac{i\varphi_k}{2}\right) \end{bmatrix} \quad \textbf{(3.19)}$$

In the case of discrete phase shifts, φ_k is the shift in the phase of the grating, where for sampled gratings placed some finite distance apart, say Δz_0, $\frac{\varphi_\kappa}{2} = \frac{2\pi n_{eff}}{\lambda}\Delta z_0$. Where Δz_0 is the separation between the grating sections. As mentioned above, phase-shifted gratings are particularly important in DFB laser fabrication. In these devices, the mode selectivity is provided by the Bragg grating, as a result of the fact that the threshold gain is different for the different guided modes, increasing with the spectral distance from the Bragg resonance. This is because, in general, the threshold gain increases as the coupling is lowered, as the resonances deviate from the Bragg condition [88]. However, due to symmetry there are two modes, one on each side of the photonic bandgap exhibiting equal threshold gains, thus preventing true single-mode behavior when uniform Bragg gratings are utilized in conventional DFB lasers. This degeneracy can be lifted by the introduction of a phase-shift in the Bragg grating structure and it is for this reason that phase-shifted gratings are particularly interesting for single-frequency lasers. The most commonly used is the λ/4 phase shifted DFB laser, in which a single defect in the grating period, equal to $\Lambda/2$, is placed at the center of the grating. The phase shift lifts this degeneracy problem as it leads to single-mode operation of the mode corresponding to the defect state that is created within the photonic bandgap, having

now the lowest threshold gain as compared to all other modes. The phase shift however, also leads to an extremely inhomogeneous photon density distribution, which then causes a non-uniform longitudinal power density, often referred to as spatial hole burning [96]. This phenomenon can lead to a decreased yield [96,97], an increased linewidth [98] and nonlinearities in the light-current characteristics [98]. To reduce this effect alternative phase-shift schemes have also been proposed in which the phase shift is distributed to smaller parts throughout the whole cavity. For example it was suggested that the 2 x λ/8 or 4 x λ/16 phase shifts can be used instead of a single λ/4-phase shift, with the later indeed giving satisfactory results concerning the spatial hole burning effect, due to a flattened photon density. Further details concerning this very interesting investigation may be found in Reference [99]. Finally, it should be noted that a drawback of the λ/4-shifted gratings is their complex fabrication with respect to precision (especially in the fact that the facets need to be anti-reflection-coated and if the coating is not ~100% sufficient the side mode suppression ratio (SMSR) is much degraded). However, recent developments in the InP based material processing techniques enable these high requirements to be fulfilled. Finally, as mentioned above, a very important parameter in laser design is the grating coupling coefficient, κ. This parameter is especially important in laterally-coupled DFB/DBR lasers, which we will study in detail in the later sections, since in this type of lasers the amount of coupling strength between the guided mode and the Bragg grating may often be insufficient. Especially for the fabrication of laterally-coupled DBR lasers, in which the grating lengths would be shorter, this parameter needs to be optimized in order to achieve a sufficient SMSR for gas detection. Even though the coupled-mode theory suggests that sine-shaped Bragg gratings would offer slightly higher coupling coefficients, rectangular-shaped gratings are preferable in laser fabrication due to their ease of fabrication. This is partly because the difference of the relative κ values is not too large. For rectangular shaped gratings its expression simplifies to the following expression [100,101]:

$$\kappa = \frac{(n_1^2 - n_2^2)}{n_{eff}\lambda} \frac{\sin(\frac{m\pi w}{\Lambda})}{m} \Gamma_{grating} \qquad \textbf{(3.20)}$$

Where n_1 and n_2 are the refractive indices of the material above and below the grating, n_{eff} is the effective index of the guided mode, Λ is the grating period, m is the relevant grating diffraction order, w/Λ is the grating duty cycle and $\Gamma_{grating}$ is the fraction of the optical mode that interacts with the grating.

3.2 Evanescent waves/ Lateral feedback

As mentioned in sec 3.1, conventional DFB lasers used in telecommunications applications, require the fabrication of phase-shifted Bragg gratings and extremely high quality anti-reflection coatings of the facets in order to achieve high SMSR single-mode operation. Most importantly they require a growth interruption and so an overgrowth step, after patterning and etching the Bragg grating. This results in increased processing complexity, making them less attractive for applications such as gas sensing, in which lowering the fabrication costs is one of the major concerns. For this reason we focus our attention on approaches requiring a single growth step. In such approaches a Bragg grating may be fabricated during or after the definition of the waveguide. Even though in this case the grating is not placed directly above the active region interacting with the main part of the optical mode, sufficient distributed feedback may still be provided through the interaction between the evanescent fields of the mode with the Bragg grating. Different schemes have already been proposed in literature, all based on the above concept, although different versions exist depending on the performance requirements and complexity. These included vertical gratings [102], surface gratings [103-105], etched lateral gratings [106-109] or metal lateral gratings leading to gain- (loss) coupled LC-DFB lasers, with demonstrations in

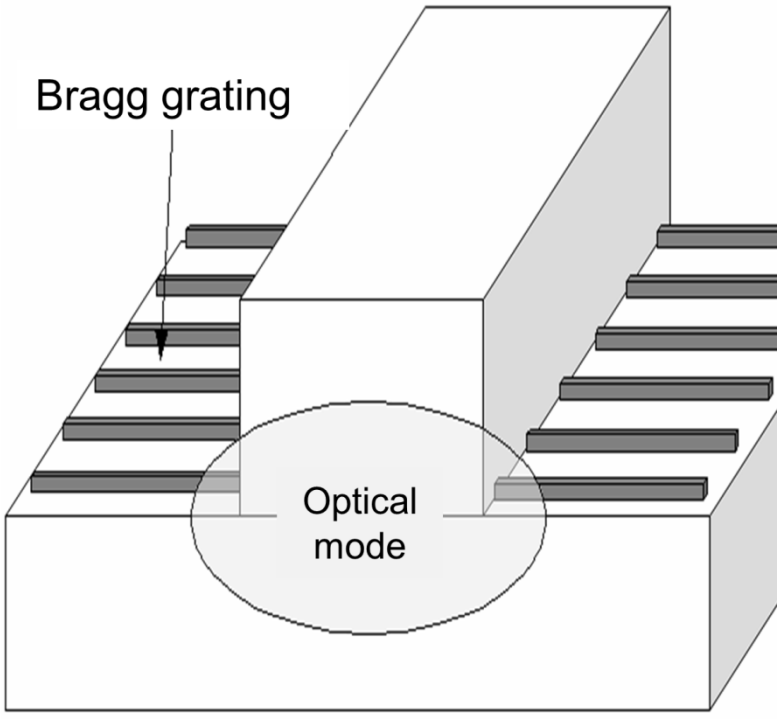

Figure 3.5 – Simple schematic of a laterally-coupled DFB laser.

different material systems [110-116]. Laterally coupled DFB lasers were first described in [106], where gratings were etched deeply into the cladding layer on both sides of the contact stripe, but it was later found that it is preferable to fabricate the ridge waveguide first and to etch then the grating on either side of the already-formed ridge-waveguide [107-109]. A simple schematic for such a LC-DFB laser is shown in Figure 3.5. Such simpler technologies are particularly suited for low cost applications, or for material systems in which regrowth is very challenging. A detailed review comparing the different surface grating techniques and comparing the DFB laser performances obtained by the different processing versions is provided in Ref [117]. In principle both the conventional and laterally-coupled DFB approaches are compatible with our material system since being Al-free it is compatible with regrowth processes, as techniques well established in the telecommunications industry may be used. However, in this work we will focus solely on the laterally-coupled DFB and DBR laser which is superior for absorption spectroscopy applications. The interaction of the evanescent part of the optical mode with the grating provides the mode selectivity, whose magnitude may be quantified by the coupling coefficient in the couple-mode theory, given by Equation 3.20. The grating providing the lateral feedback can be either a metal grating (usually Cr) which is fabricated using a liftoff process after pattering with electron beam lithography, or an etched grating, using PMMA as a mask to etch a thin SiN_x layer, which will be then used as mask for etching the semiconductor material. The etched grating is superior due to the fact that it has much decreased losses compared to its metal counterpart [76] which in turn provides the necessary flexibility for our increased coupling design, which will be described in Sec 3.4.

3.3 Tunable lasers - Alternative designs

Having decided on the feedback mechanism and therefore the general design of our DFB laser, it remains to investigate the method by which sufficient laser tunability may be achieved, in order to scan over the gas absorption lines of interest. Since we decided to focus on suggesting monolithic approaches (again for manufacturing cost reasons), the two main technologies commonly used are the so called Vernier tuning and the LC-DBR laser with isolated electrodes in the waveguide and grating sections (some include a phase section as well). In the Vernier tuning scheme, two slightly detuned multiwavelength reflectors are integrated in a two-section DFB laser and single longitudinal mode operation occurs when there is an overlap of one of the modes. With this scheme a small index change may shift the

lasing wavelength by a large amount, leading to very wide tuning possibilities [118]. A tunability range up to 80 nm for multispecies detection and scanning over multiple absorption lines of the same gas has been reported by this approach [119]. This approach has the advantage that almost arbitrary grating shapes may be used and the lasing spectrum may be tuned with great flexibility finding the best possible compromises between long-range tunability for scanning over the different absorption lines of the same gas and short-range tunability for sufficiently scanning over each absorption line of interest before the next mode jump occurs. In addition due to the freedom in each grating design these devices exhibit fundamental interest in the fields of photonic bandgaps and light manipulation, which has not been fully explored yet. In fact, it has been demonstrated that such scheme may be implemented with integrated sampled [120], superstructured [121], binary superimposed gratings [122] and recently with gratings with aperiodic sequences [123]. The principle of the Vernier tuning DFB laser is shown schematically in Figure 2.6. In the LC-DBR scheme a Bragg grating is defined across one part of the ridge waveguide (approximately 20 % of the total cavity length), replacing one of the FP as-cleaved mirror with a selective mirror. Then the grating and non-grating parts of the laser cavity are electrically isolated through the

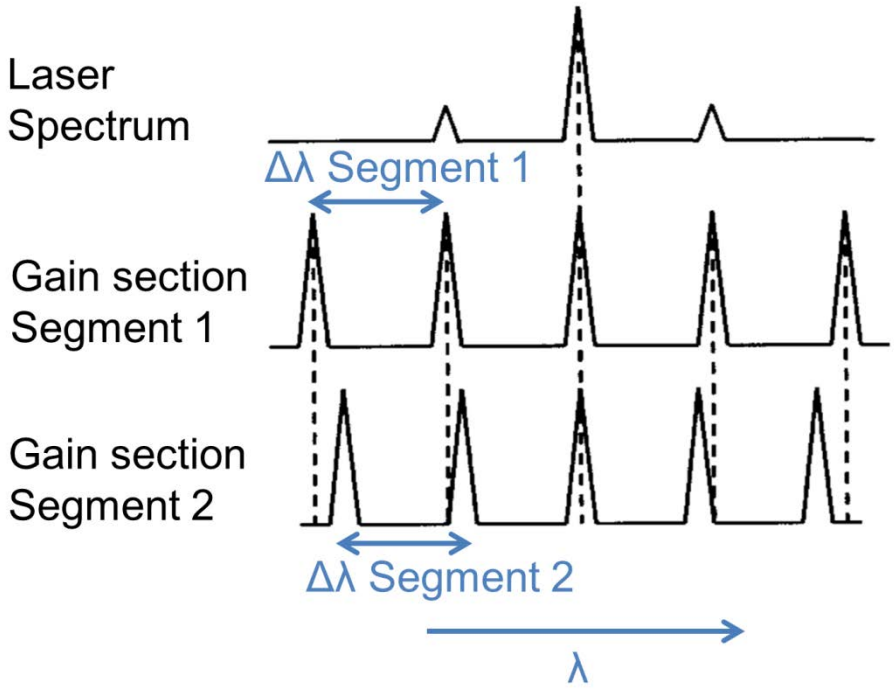

Figure 3.6 – Schematic illustration of the operation principle of Vernier tuning in a two-section DFB laser. The gratings should be fabricated such that for specific values of injected current, one of the modes of the two gratings overlaps and at the same time there is a negligible overlap between the rest of the modes (adjusted from Ref [118]).

etching of the electrodes and the highly p-doped contact layer, and tunability of the lasing spectrum is provided by injecting different currents in the active and passive (Bragg grating sections). The change of the injection current of the Bragg section, leads to a change in the refractive index, which alters the central Bragg wavelength of the grating following Equation 3.3 and thus, the lasing mode. Using such scheme a continuous tunability of the order of ~10 nm may be achieved. However, besides their already discussed advantages, both of these methods have significant drawbacks up to present and improvements would be necessary if such lasers are to be useful in industrial applications. The former approach, namely the two-section DFB lasers taking advantage of the Vernier effect, exhibits a very high temperature sensitivity. Small temperature changes lead to big changes of the lasing mode if the gratings are not very precisely defined and up to present they may not be operated reliably unless sophisticated packaging and temperature control schemes are utilized. However such temperature control schemes would substantially increase the device cost and are not adopted for gas sensing applications. On the other hand LC-DBR lasers suffer from insufficient coupling. In fact, up to present, to the best of our knowledge, the only successful demonstration has been achieved by using focused ion beam lithography, in which sufficient κ has been achieved due to implantation induced quantum well intermixing aligned with the index grating, which enabled the realization of a two section LC-DBR laser [124-126]. Other efforts to achieve LC-DFB lasers using etched gratings based on lower-cost/readily available in scientific laboratories techniques led to coupling coefficients lower than 10 cm^{-1} [106-109]. In this work we will focus on the design and fabrication possibilities of LC-DFB and LC-DBR lasers with sufficient coupling coefficients using electron beam lithography and we will analyze the optimization procedure which would enable achieving sufficient κ values. In the later sections we will demonstrate both simulation and LC-DFB laser results confirming that κ values of at least ~40 cm^{-1} have been achieved, while even higher values are also possible using our high-duty-cycle Bragg grating design and optimization of the processing steps. These results open the way for the fabrication of tunable LC-DBR lasers with sufficient SMSR, using only e-beam lithography.

3.4 Importance of the Bragg grating coupling coefficient for the design of LC-DFB and LC-DBR lasers with an optimized value

A rule of thumb often given in literature for the design of DFB/DBR lasers, is that the normalized coupling coefficient value κL should be of the order of ~ 1-1.25, where κ is the

coupling coefficient and L is the length of the grating section. This value is empirically found to be a good compromise, since for smaller values the coupling between the two counter propagating waves in the waveguide will be too weak leading to an insufficient SMSR. On the other hand, a higher value would lead to spatial hole burning (non-uniform photon distribution insight the cavity), which is undesirable as discussed in further detail within Sec 3.1. In addition, for achieving a narrower linewidth, a very long, weak grating, should be utilized. But, when designing longer gratings the losses and thus the threshold current of the laser would increase. A good compromise for our purpose, taking into account all the above, would be to target a coupling coefficient of 35-40 cm^{-1} and design grating regions of 300 μm length. Achieving such values of κ is not straightforward for laterally coupled lasers, in which the coupling is relatively weak, and has been so far achieved only with the use of Focused Ion Beam lithography and only for the fabrication of laterally coupled DBR lasers for telecommunication applications. Within this work we show that it is also possible to design laterally coupled gratings with sufficient values of κ, after carefully designing the grating parameters and optimizing the processing steps, using only e-beam lithography and avoiding any epitaxial regrowth over corrugated substrates. The expression for the calculation of κ for rectangular shaped gratings has been derived from the coupled-mode theory in Sec 3.1 and is given by Equation 3.20. As it can be seen from this equation, besides the grating design parameters, in order to obtain a quantitative value for this expression, one should also obtain accurate estimations about the modal effective index n_{eff} and the confinement factor of the guided mode in the Bragg grating region, $\Gamma_{grating}$. Since 3-D simulations for DFB lasers are computationally very demanding, an alternative way to simulate the whole structure would be to use a two-dimensional numerical simulation to determine the electric field distribution and the modal effective index and subsequently to choose optimized design parameters for the desired value of κ. In our case the 2-D analysis was performed with the software Symphot Alcor, using the effective index approximation. A typical electric field distribution obtained in such 2-D simulation, after using the typical parameters of our ridge-waveguide and DFB laser processing, is depicted in Figure 3.7. In order to simulate a DFB laser in such configuration the grating may be modelled, for the 2-D simulation purposes, as a homogeneous layer with a weighted averaged refractive index between the materials above and below the grating, in order to acquire a good approximation for the $\Gamma_{grating}$ value. In our LC-DFB configuration the material above the grating is a dielectric (BCB) while the materials below the grating are

semiconductor InP and InGaAsP layers. Such weighted averaged values may be obtained using the following relations:

$$n_{grating}^2 = \frac{\Lambda 1}{\Lambda} n_{die}^2 + \frac{\Lambda 2}{\Lambda} n_{semicond}^2 \quad \textbf{(3.21)}$$

The InP and InGaAsP semiconductor layers that are etched and thus involved in the grating fabrication may be lamped together using Equation 3.22. Thus, the value of the parameter $n_{semicond}$ in Equation 3.21 is obtained as follows:

$$n_{semicond}^2 = \frac{\sum_i t_i n_i^2}{t_{total}} \quad \textbf{(3.22)}$$

Where t_i and n_i correspond to the thickness and the refractive index of each material and t_{total} is the total thickness of the layer. A careful look in Equation 3.20, would suggest that the key parameter in order to increase the value of κ in a laterally-coupled laser is the optical confinement factor in the grating, $\Gamma_{grating}$ (in addition of course to the refractive index contrast). In becomes obvious from our 2-D simulations that specific design parameters strongly affect the value of $\Gamma_{grating}$, some of which are grating design parameters and some are exclusively dependent on the optimization of some of the processing steps. The parameters that should be used in the optimization of $\Gamma_{grating}$ are listed below.

1) Reduction of the lateral distance between the ridge and the grating
2) Well controlled grating etching (slow etch rate in order to stop just above the active region for maximizing the coupling with minimum losses)
3) Reduction of the Ridge Width
4) Optimizing the value of the duty cycle (w/Λ) of the grating

Parameters 1 and 2 are purely design optimization parameters requiring a completely vertical etching of the ridge, without any re-deposition and a well-controlled slow etch-rate process for narrow patterns. We have performed such an optimization procedure in order to

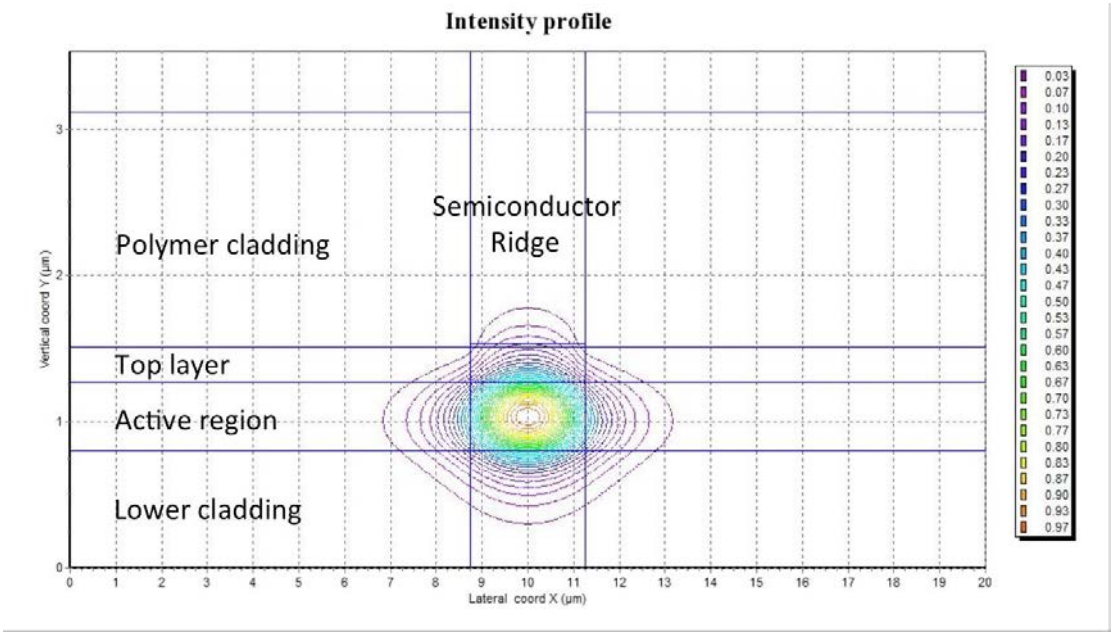

Figure 3.7 – 2-D mode distribution in a ridge laser configuration using the software Symphot Alcor.

fulfill these requirements. An optimized ridge waveguide, obtained by inductively coupled plasma (ICP) is shown on the right panel of Figure 3.9. On the left panel of Figure 3.9, a ridge obtained by HCl wet etching, used in our previous processes, is shown for comparison. It becomes obvious that the vertical ridge reduces the lateral distance of a potentially patterned lateral grating to null, as opposed to the wet etched ridge of our preliminary approach which led to lateral distances of ~150 nm. Our 2-D simulations show that such lateral distances substantially reduce the value of $\Gamma_{grating}$, which is directly proportional to κ, by a factor of 3, as compared to the zero-distance case of the 90^o vertical ridge. In addition, we have developed a slow etch-rate process for the Bragg grating etching; with very high etch termination accuracy, thus fulfilling the requirement number 2. Related figures and discussion concerning this will be provided in Chapter 4, during the detailed illustration of the laser processing steps. The parameter number 3, i.e. the reduction the ridge width is a very important parameter if one wants to achieve a very high value of κ. However, on the other hand, reducing this value too much is unwanted, as this would have an impact on the output power, on the intra-cavity losses and on the control of the exact value of κ (reproducibility). The latter is because the κ value fluctuates very fast for small fluctuations in narrow ridges. For this reason, the ridge width has been fixed to 2 µm for all the structures in this work and the adjustment of κ is achieved by optimizing only the rest of the parameters

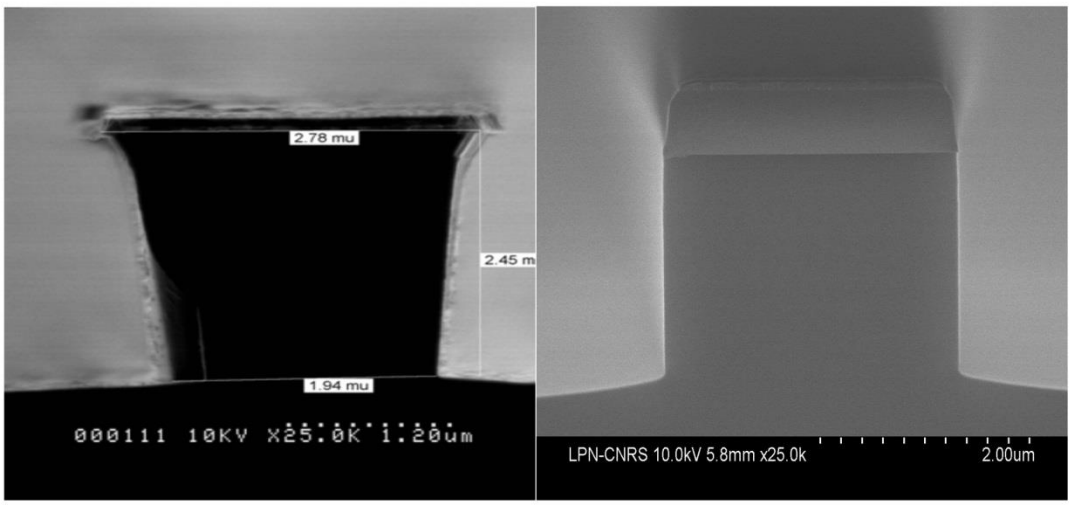

Figure 3.8 – Left: Ridge waveguide etched using HCl wet etching during our preliminary process. Right: Optimized ridge waveguide etched using ICP dry etching, compatible with our high-coupling-coefficient LC-DFB process.

mentioned above. The value of the duty cycle, parameter number 4, is very crucial. To the best of our knowledge all LC-DFB lasers reported so far in literature, either with etched or metal gratings, used a grating duty cycle of 50 % or less. However, for applications in which a higher κ is required this is not the optimum value. This is because, increasing the duty cycle above 50 %, increases the value of the weighted refractive index in the grating region and thus the $\Gamma_{grating}$, but reduces the value of the sine term in Equation 3.20, having the no-grating limit and therefore κ=0 for a 100 % duty cycle. From the above considerations it becomes clear that there is an optimum duty cycle value, which depends on the pair of refractive indices used to construct the grating. For the structures reported here, we found that, after calculation each time $\Gamma_{grating}$ from our 2-D simulations, κ in Equation 3.20 is maximized for a duty cycle of 79 %. This would lead to a further increment of the coupling coefficient value, with our simulations suggesting that a value of 45 cm^{-1} is possible for the above discussed parameters, for a ridge width fixed at 2 μm. This assumption has been tested experimentally after fabricating LC-DFB lasers emitting at 2 μm, using our optimized material structure for this purpose, described in Chapter 2. Figure 3.9 shows the simulated coupling coefficient values as a function of the processing parameters, for our wafer 63802 structure, for typical design values. Our experimental results confirm that such high values may be achieved and LC-DFB lasers with high SMSR, of at least 40 dB (limited by our experimental setup), have been demonstrated. This value is sufficient for the fabrication of a LC-DBR laser using this technology in the future. These LC-DFB results will be detailed in

Chapter 4. Finally it is worth noting that for any application were it might be required, further increment of κ can be readily achieved with this design, by simply further reducing the ridge width. Also, this design is completely general for use in any material system, as long as sufficient etching recipes for narrow trenches, in order to achieve .a good quality etching for the Bragg grating may be available.

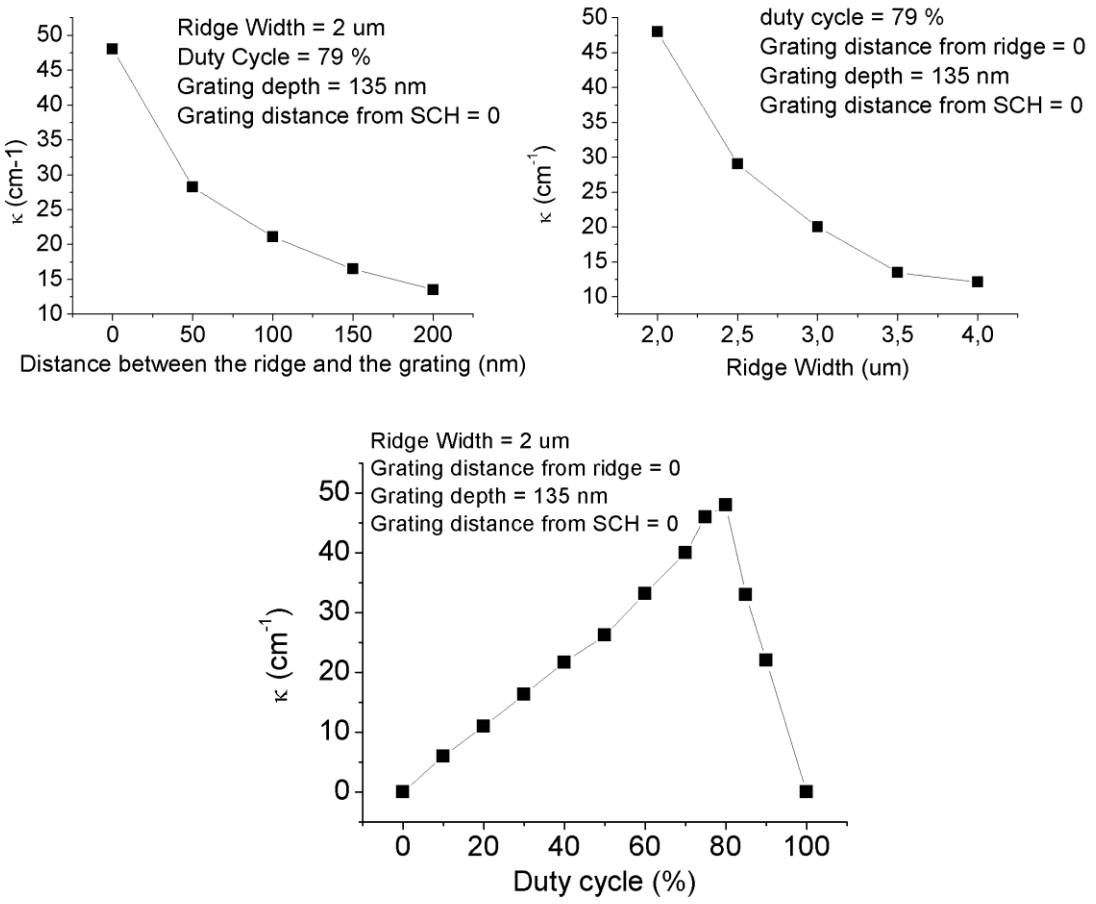

Figure 3.9 – Calculated coupling coefficient as a function of the processing parameters, for typical design values: (a) Distance between the ridge and the grating; (b) Ridge width; (c) Duty cycle.

Chapter 4

Laser Processing

In this Chapter, the fabrication process for the different types of lasers used during this work will be presented. The Chapter is organized as follows. In Sec 4.1 we will present the fabrication process for our broad area lasers, which were used to characterize the quality of our Qdash based epitaxial structures, as discussed in Chapter 2. In Sec 4.2 we will describe our ridge-waveguide laser fabrication process. The preliminary ridge-waveguide process gave satisfactory results for FP lasers, but was not compatible with LC-DFB lasers fabrication by simply adding a Bragg grating on the side of the ridge. The reasons for this will be pointed out in Sec 4.3 and in Sec 4.4 the development of a novel process, which was optimized for the fabrication of LC-DFB lasers with high coupling coefficients will be described. Finally, our main LC-DFB laser results are presented in Sec 4.5 and future perspectives arising from this design are discussed.

4.1 Broad area lasers for quantum dashes on InP(001) substrate

For all our structures, prior to any FP or DFB lasers process, a piece of the wafer has been characterized by the fabrication and assessment of broad-area lasers. This allows controlling the quality of the grown wafer obtaining reference parameters such as the modal

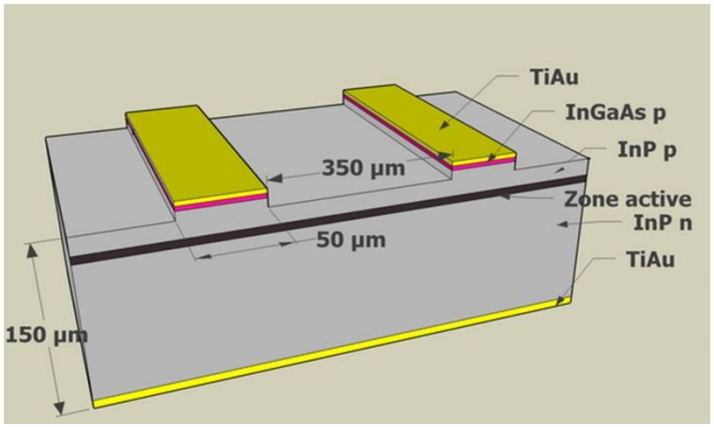

Figure 4.1 – Schematic of a laser bar including two broad area lasers (courtesy of K. Merghem - LPN).

gain, the internal losses, and the internal efficiency, as well as the threshold current density for an infinite cavity length, the typical output power, the series resistance and the characteristic temperature. Broad-area lasers have been fabricated with a width of either 50 or 100 μm. This technology is simple as only the p+ InGaAs contact layer is etched and Ti/Au contacts are added on the top and bottom of the sample. We performed this technology for all the samples described in Chapter 2, thus with the emission wavelength ranging between 1.6 and 2.0 μm. It is worth noting that for the wafers for which both 50 μm and 100 μm wide broad area lasers were processed, and therefore the results were compared, we observed that the overall performances followed a very similar trend. The only observable difference has been that for some of the 50 μm wide lasers kinks were present in the l-I curves, which was never the case for the 100 μm wide lasers. This behavior was observed only for a sample with emission wavelength at 2 μm and for this reason all the subsequent samples targeting at 2 μm emission, were processed using 100 μm wide stripes. A schematic of the final device is shown in Figure 4.1, while the exact fabrication steps that were followed are listed below.

1) *Native oxide removal*

Deoxidation of the surface has been performed in a 1 min bath of 40% HF, which is followed by a 3-min rinse in deionized (DI) water.

2) *Definition of the openings for the p-type contacts deposition*

50 μm- or 100 μm- wide stripe openings were produced by optical lithography, using the image reversal photoresist AZ 5214E. A ~1.5 μm thick film was spin-coated on the sample (velocity (v) = 4000 rpm; acceleration (a) = 2000 rpm; time (t) = 30 s) and the pre-bake was performed for 1 min 30 s at 125 °C. Subsequently, sample exposure using Suss MicroTec MJB4 mask aligner and post-bake for 1 min 30 s at 125 °C, flood exposure without mask, followed. Finally, the sample was developed for 1 min in AZ 726 MIF developer.

3) *Electrodes lift-off deposition*

Electron beam evaporation of a Ti/Au (200/2000 Å) bilayer has been performed in a Plassys MEB 550 SL reactor. Lift-off in acetone was subsequently used to define the BA laser p-contact and cleaning in isopropanol followed.

4) *Etching of the p+ InGaAs contact layer*

The highly doped p+ InGaAs contact layer was chemically etched in a bath of $H_3PO_4/H_2O_2/H_2O$ (ratio 1:1:8), using the Ti/Au defined electrode as mask. The etching rate has been calibrated to ~ 3000 Å/min. In should be noted that we continued the etching into a small part on the InP top cladding layer, in order to make sure that the whole p+ InGaAs layer was removed, since even a very thin remaining layer would have created an important leakage path.

5) Substrate thinning and back-side metallization

The substrate is thinned down to about 120 μm using an alumina based slurry and subsequently polished using a solution of 5% bromine in methanol (Br_2/H_3COH). The purpose of this to facilitate laser bars cleaving, as well improved thermal dissipation of the lasers. Then, the sample was stuck top-side-down to a Si-substrate and the n-contact evaporation consisting of a Ti/Au (200/2000 Å) bilayer.

6) Finalization of the process

Finally, the sample was removed from the Si-substrate by dissolving the sticky was using trichloroethylene, and the sample was cleaned in acetone and isopropanol baths prior to laser cleaving and characterization.

The characterization of the broad area lasers has been detailed in Chapter 2, as a part of our Qdash based material optimization process and therefore it will not be repeated here.

4.2 Shallow ridge waveguide lasers

After the verification that the structures exhibit satisfying static performances, we proceeded with the fabrication of shallow ridge waveguide lasers. These lasers are useful for further material characterization, which may not be performed using broad area lasers due to the fact that they operate only in the pulsed injection current (PU) regime. Such a characterization concerns for example the carrier thermal roll-over which was evidenced in our 2 μm samples after such ridge waveguide lasers assessment in continuous wave (CW) operation. In addition, since these lasers have a very similar geometry, and therefore refractive index profile to the LC-DFB lasers that we aimed at, they are useful for experimentally extracting the gain peak and modal effective refractive index, which will aid to more accurately design such LC-DFB lasers prior to their fabrication. Another important

issue that can be assessed in such ridge waveguide lasers is the transverse mode behavior, which also strongly depends on the material structure, and is very important for these lasers in maintaining high performances and nice L-I characteristics. Furthermore, a bi-modal behavior, if present, would be very harmful in our efforts to later fabricate LC-DFB lasers using a similar geometry, since the two transverse modes would see slightly different effective indices and therefore two different wavelengths would be in resonance with the Bragg grating, thus preventing single-mode behavior. Since the transverse mode behavior is also affected by the current injection, through the current induced changes of the refractive index, it should be noted that our ridge lasers design should guarantee single transverse mode operation not only at threshold, but for up to high CW injection current. Due to the high importance of this matter and the fact that this has been the first time that our research group aimed to fabricate shallow ridge lasers emitting at 2 μm, we attempted to obtain a first approximation of the suitable parameters, prior to the fabrication process, through simulations. More specifically, we have determined the ridge width and etching depth in the upper cladding layer, necessary to allow for single transverse mode operation, through effective refractive index simulations that were performed using the software Symphot ALCOR. The results showed that typically, a ridge width of ~ 1.8-2 μm and residual cladding thickness values of about 50-200 nm above the active region would be sufficient. This was later confirmed by our experimental results that were discussed, for this type of lasers also, in Chapter 2. A typical guided mode profile has been shown in Figure 3.8 and a schematic illustration of a shallow ridge waveguide laser is shown in Figure 4.2. It is also worth noting that since contact photolithography with resolution of about 0.5 μm is generally used for ridge patterning, sufficient tolerances are considered in the design of the waveguide geometry.

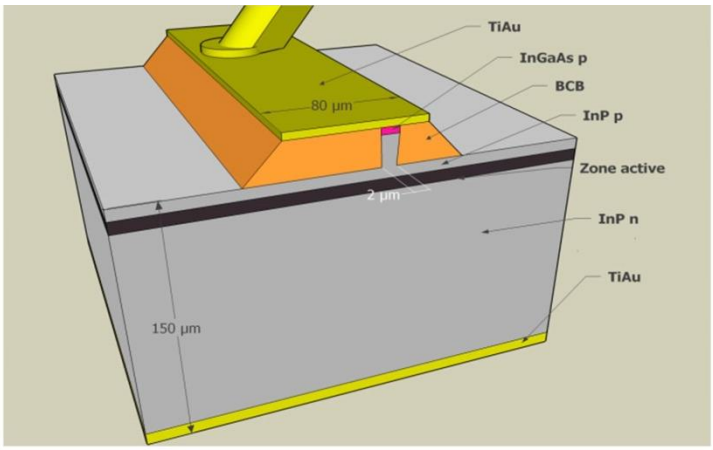

Figure 4.2 – Schematic of a shallow ridge waveguide laser (courtesy of K. Merghem - LPN).

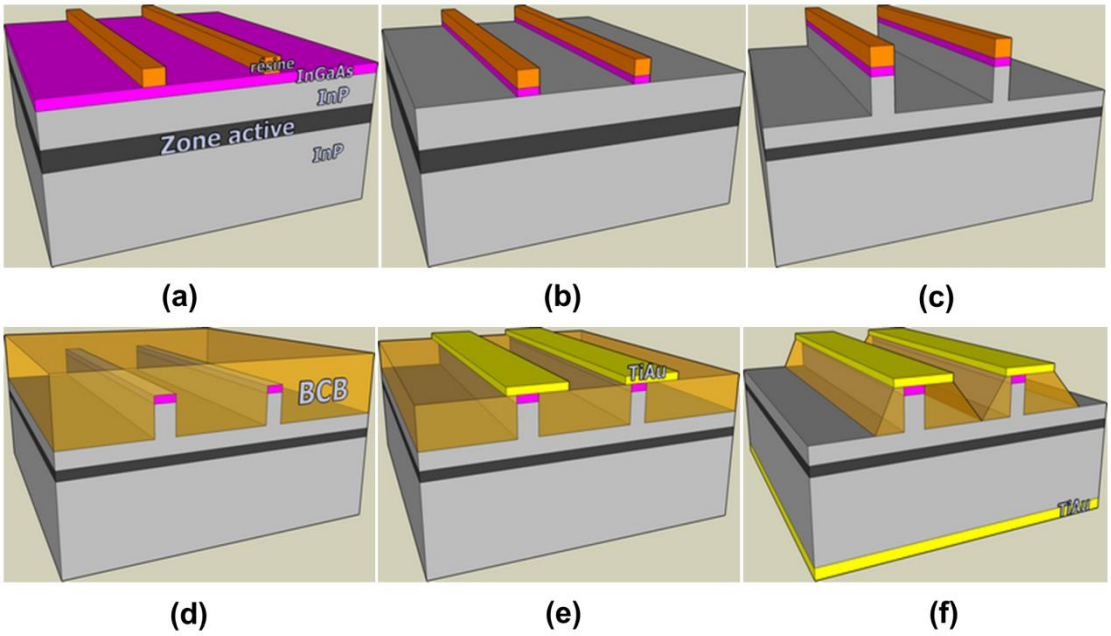

Figure 4.3 – Schematic illustration summarizing the most important shallow ridge fabrication steps: (a)- etching mask patterning; (b)- Removal of the InGaAs contact layer by ion beam etching; (c)- InP ridge waveguide etching using an HCl bath; (d) BCB deposition; (e) Etching the BCB to release top of ridges and deposition of the top Ti/Au electrodes; (f) Wafer lapping and deposition of the back side Ti/Au electrodes metallization (courtesy of K. Merghem - LPN).

However for the design of LC-DFB lasers a more strict design is required to account for the necessary tradeoffs and in this case we have used e-beam lithography to pattern the ridge as will be detailed in the following section. The main parts of the fabrication are summarized schematically in Figure 4.3 and the whole process is subsequently detailed below. Some of the steps which are identical to the corresponding ones that were already described during the broad area laser process, will be just mentioned with the details not being repeated.

1) Native oxide removal

2) Definition of mask for ridge waveguide etching

First, a Ti/Au (200/2000 Å) bilayer, was uniformly evaporated on the sample, as described in the section for the broad area lasers, followed by a 700 nm thick SiN_x which has been deposited at a rate of ~ 20 nm/min in an Unaxis D200 plasma-enhanced chemical vapor deposition (PECVD) equipment, using SiH_4 and NH_3 precursors. Then, optical lithography (photoresist AZ 5214E) was used to define 2 μm openings and a 100 nm thick Al layer was

deposited by lift-off and used as etching mask for the SiN_x layer below. Subsequently the SiN_x is used to transfer the mask into the Ti/Au and semiconductor layers.

3) Ridge waveguide etching

During this process the ridge waveguide etching has been performed in two steps. First, ion beam etching (IBE) was used for the Au/Ti/p+ InGaAs contact layers, penetrating a little bit (~100 nm) down to the InP layer to ensure that the whole InGaAs layer is removed over the whole wafer area. The latter is necessary since the IBE is not completely uniform over a quarter wafer area which was used in our ridge waveguide process. The etching has been controlled using a mass spectrometer which is incorporated in our Roth&Rau IBE equipment. An etching angle of 20° between the sample, glued on a cooled holder, and the Ar+ ion beam, resulted an average etching rate of ~ 40 nm/min for the contact layer stack and of 15-20 nm/min for the dialectic mask. Subsequently crystallographic etching in 37% HCl solution for 1 min has been used to remove the remaining InP top cladding layer, defining ridges oriented in the [110] direction. SEM images of a ridge defined used this process, after step (3), is shown in Figure 4.4, on the left panel.

4) Etching mask removal

The residual SiN_x mask has been etched by CCP-RIE, using SF6 plasma, at a pressure of 30 mTorr.

5) Laser structure planarization

For this purpose benzocyclobutene (BCB) resin (Dow cyclotene 3022-46) has been spin-coated on the sample (v=2000 rpm; a=2000 rpm; t=30 s). Because adhesion of BCB is hampered by the possible presence of water droplets on the sample surface, the sample was annealed at 120 °C for 5 min and an adhesion promoter (Dow AP3000) has been used (v=2000 rpm; a=2000 rpm; t=30 s) before the resin. Soft cure of BCB on a hot plate at 120 °C for 1 min followed, before a 2-hour hard bake at 250 °C under nitrogen atmosphere in a quartz tube furnace.

6) BCB etching to release top of ridges

During this step the BCB was etched until the top of the ridges have been revealed, to

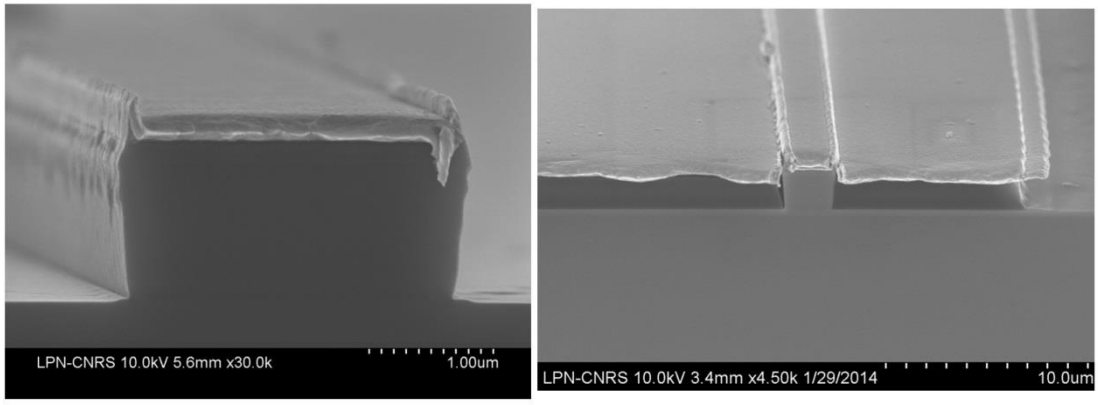

Figure 4.4 – Left: SEM image of a ridge waveguide defined by a combined IBE and wet etching step as described in (3). Right: SEM image of a ridge waveguide laser after the finalization of the process described in Section 4.2.

allow for the subsequent definition of the metal contacts. This step was performed by CCP-RIE, using a 5:1 O_2/SF_6 gas mixture at 100 mTorr, together with interferometric monitoring of the process. It is important, in this step, to reveal the ridges but without over-etching the BCB on their side, ideally maintaining a height difference between the top of the ridge and the BCB, of ~300-500 nm for most of the ridges in the wafer. In order to well control this parameter, the etching has been carried out in multiple etching steps, alternated by profilometry measurements and microscopy inspections. The procedure concluded when the desired height difference was achieved and after confirming that no BCB residues were observed on the top of the waveguides, at least over an area of 80-90 % of the sample. In a different case, an additional etching step of small duration was added, since such residues are detrimental for current injection. It is however unavoidable that some part of the surface, ~10-20 % of the sample will be unexploitable after this step, due to non-sufficient opening of the top of some of the ridges. This is because BCB planarization results in a larger resin thickness on the sample edges than on the center, and BCB over-etching trying to reveal all of them is not advisable since this would create a too high ridge/BCB height difference for the central ridges, which may cause inefficient current injection in the laser diodes, or mechanical instabilities of the ridges.

7) Deposition of p-type contacts

For this step, first 100 μm wide stripe openings were produced in negative resist AZ 2070 by photolithography (v= 4000 rpm; a= 2000 rpm; t= 30 s). The pre-bake time has been 1 min 15 s at 97 °C on a hot-plate and the resulting resist's thickness approximately ~ 5 μm.

Prior to sample exposure, the mask exhibiting 100 μm wide stripes has been aligned on previously patterned ridge waveguides, so as to produce large openings of ~ 90 μm on one of the sides of the ridges. Post-exposure bake for 1 min 15 s at 97 °C was then performed, followed by 1 min development in AZ 726 MIF to allow for negative sidewall profiles. Just before the contact deposition, further etching of about 100 nm of BCB is carried out, in order to remove the portion of resin possibly affected by water absorption, which may hinder electrode adhesion. A Ti/Au (200/3000 Å) bilayer was subsequently evaporated on the sample, at a deposition angle of 10° in order to allow for conformal deposition on the ridge side facing the 90 μm wide opening, followed by a liftoff in an acetone bath and subsequent sample cleaning with isopropanol.

8) Substrate thinning and deposition of n-type contacts

Exactly the same process as described for broad area lasers has been followed in this, with an additional step of removing the remaining BCB that lies between the ridges, after the whole process is completed. This was performed by CCP-RIE, using a 5:1 O_2/SF_6 gas mixture at 100 mTorr, and the purpose is to facilitate the subsequent laser cleaving. An SEM image of a ridge waveguide laser after the finalization of the process and cleavage is shown in Figure 4.4 on the right panel. Similar to our broad area lasers, the results obtained during our shallow ridge waveguide processes for all the samples discussed in this work, have already been presented in Chapter 2, during our material quality discussion, and will not be repeated here.

4.3 Laterally coupled DFB laser/ Compatibility of the process/ tests-discussion

As discussed during the Section 3.4 of Chapter 3, even though, in principle, our LC-DFB laser design requires only the addition of the Bragg grating to the conventional ridge waveguide lasers design, some of the processing steps are critical for the value of the coupling coefficient. The arising requirements create the necessity that some of the steps of Section 4.2, would need to be changed to more effective ones, in respect to coupling optimization. During this section, we will detail the steps that we decided to optimize/substitute with others and the reasons behind these decisions and we will present results on the new processing steps that we developed for this purpose. First, the necessity to reduce the lateral distance between the Bragg grating and the ridge was outlined during the presentation of our LC-DFB simulations. In order to reduce this distance, the etching of the ridge should be completely vertical; otherwise, the angle of the ridge would prevent the patterning of the grating in the

first ~150 nm close to the ridge, as it can be seen in the SEM image on the left panel of Figure 4.4. This may not be achieved with wet etching using HCl, since such etching follows the crystallographic axis and therefore the etching angle is unavoidable. Due to this, we decided to optimize a new process in order to perform the etching of the ridge using ICP, in which the ratio of the etching gases may be adjusted such that the etching is completely vertical. However, our tests showed that in this case, the steps prior to the etching of the ridge would have to be modified as well, due to the fact that after using a combination of IBE process to etch the Au, Ti and InGaAs layers and subsequently an ICP process for etching the InP, it is impossible to maintain a good surface quality, under any conditions. In our previous process the surface has been rough after IBE etching, but subsequently smoothed, after performing the wet etching, In addition, we have observed that gold redeposition on the mask was inevitable

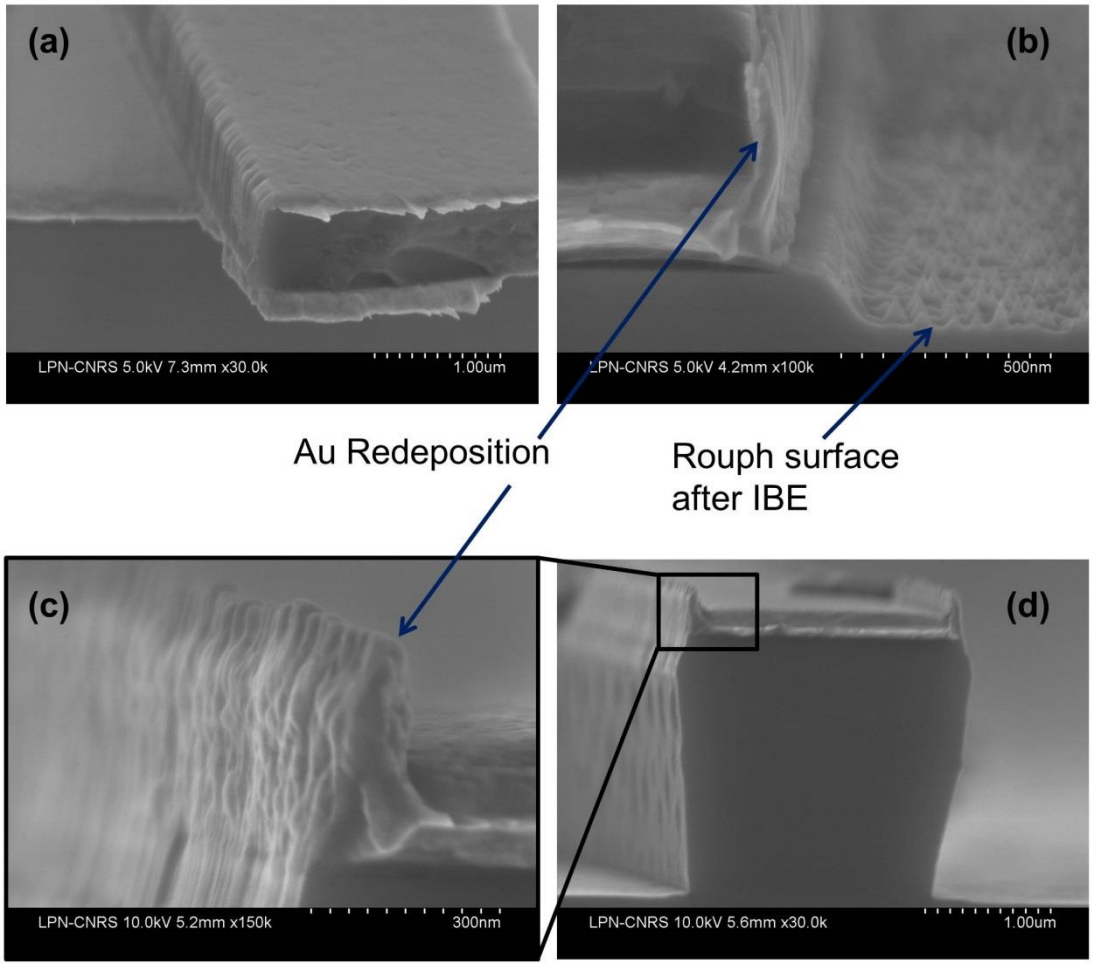

Figure 4.5 – (a) SEM image after opening the SiN_x mask, by CCP-RIE, using SF6 plasma (Step 2). In the subsequent step the Au / Ti / InGaAs layers have been etched using IBE. The gold redeposition on the SiN_x mask and surface roughness after this etching step are evident in this SEM image. The gold redeposition remains even after the residual mask removal as in may be seen in the SEM images of (c),(d).

during IBE, which is not removed during the residual SiN_x mask removal. This would be harmful in an LC-DFB process as it would result in increasing the lateral distance between the ridge and the grating even further. Example SEM images after and before the IBE etching of the Au, Ti and InGaAs layers of the previous process revealing the problem of Au redeposition on the mask are shown in Figure 4.5. In order to further investigate the redeposition problem we performed additional tests to ensure whether the problem was indeed deposition of Au on SiN and to see weather this effect might be reduced by introducing minor changes to the process. In the first test, we used a photoresist mask to directly etch the SiN, instead of the thin Al layer defined by liftoff, which was used in our ridge waveguide process. In the second test we added a thin Cr layer of 10 nm on top of our Au layer to see whether this

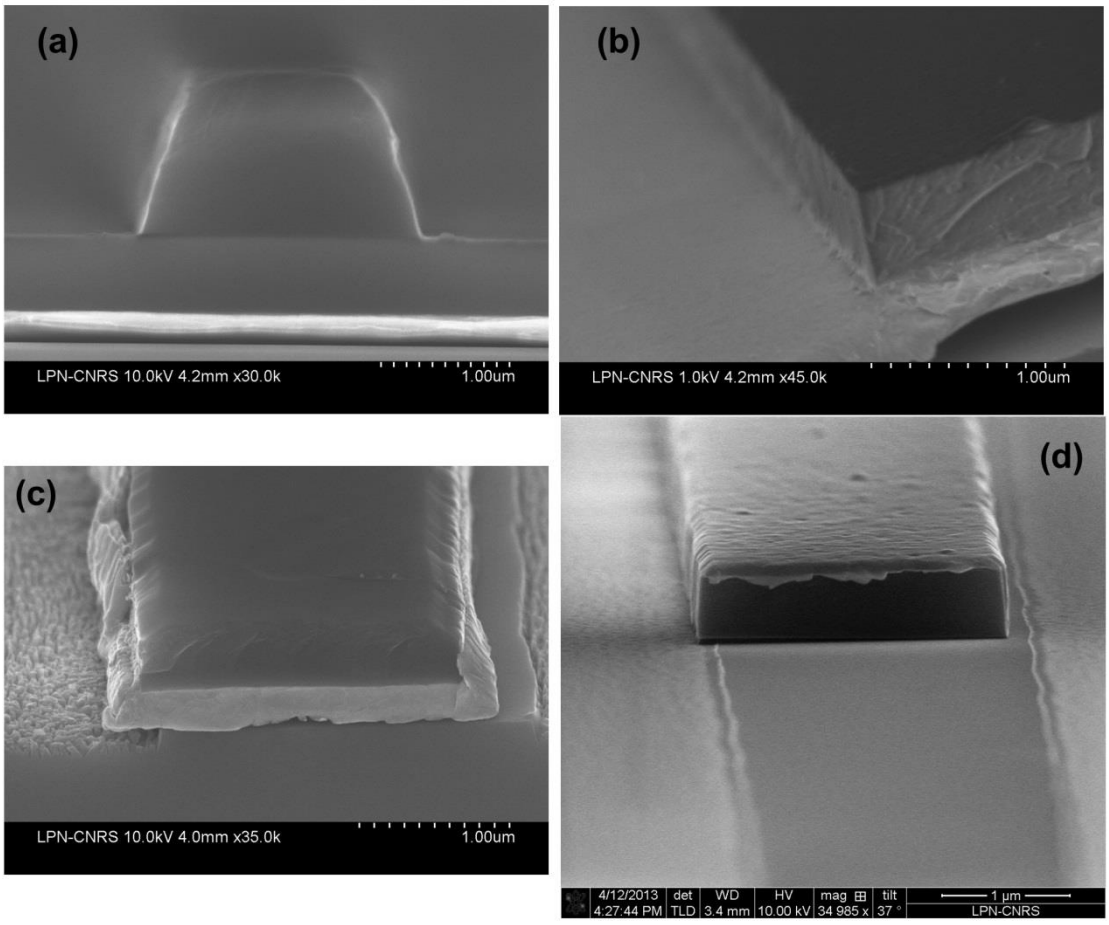

Figure 4.6 – (a) SEM image of the photoresist mask after development. (b) the photoresist mask has been used to etch the SiN_x layer and subsequently the residual mask has been removed. (c) The SiN_x mask has been used to etch the Au/Ti/InGaAs layers. The Au redeposition of the mask is evident, as well as the fact that the ridge definition is not straight. The latter is clearly evidence because the top layers of the ridge moved during cleavage prior to the SEM observation. (d) SiN_x mask definition of the conventional ridge waveguide process is also not straight when the Al mask is defined using photolithography.

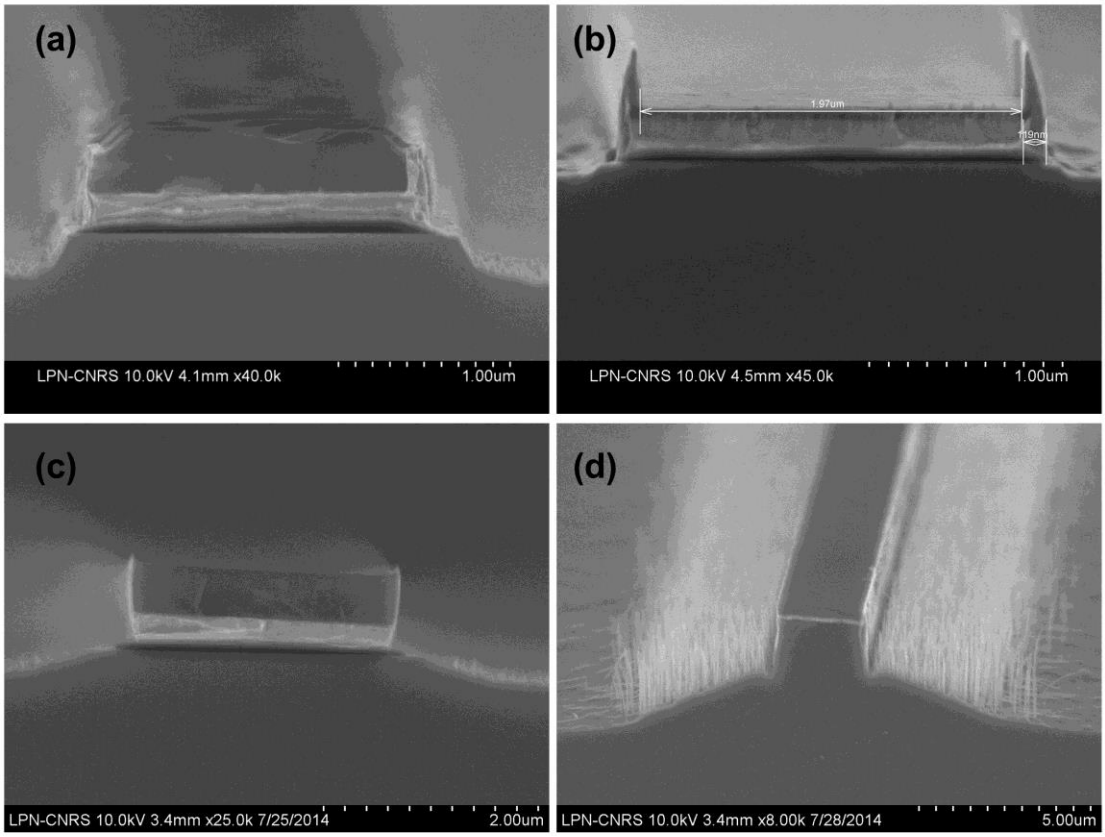

Figure 4.7 – (a) SEM image after IBE with an etching angle of 20°. (b) The redeposited Au remains on the sidewall of the ridge even after the residual mask has been removed. (c) SEM image after IBE with an etching angle of 45°. (d) If ICP is performed after etching the metal layers with IBE, the surface roughness is always transferred to the InP top cladding layer. This SEM image is an example of a Cl_2/H_2 ICP process performed after IBE etching of Au/Ti with an etching angle of 45°.

would reduce the effect. In both cases the results were negative in the sense that Au redeposition occurred at the mask and subsequently remained on the ridge in a similar manner as in the previous ridge process. Example SEM images of such tests including the use of the photoresist mask, are depicted in Figure 4.6. An additional information extracted in Figure 4.6c, is that the sidewall of the ridge when defined using the photoresist mask process, is not straight, which is clearly visible in this SEM image because the top layers of the ridge have slightly moved after cleavage. A similar conclusion is extracted in Figure 4.6d, in which the SiN_x mask (opened using an Al mask obtained by the conventional photolithography process as described in step 2 of our shallow ridge waveguide process), was displaced during the cleavage prior to the SEM observation; revealing the non-straight ridge sidewall definition, which introduces additional losses. Finally, it is worth mentioning that we also tried to replace the SiN_x mask with hydrogen silsesquioxane (HSQ), a negative e-beam sensitive resist that transforms into SiO_2 after exposure, but the redeposition problem was evident in that case

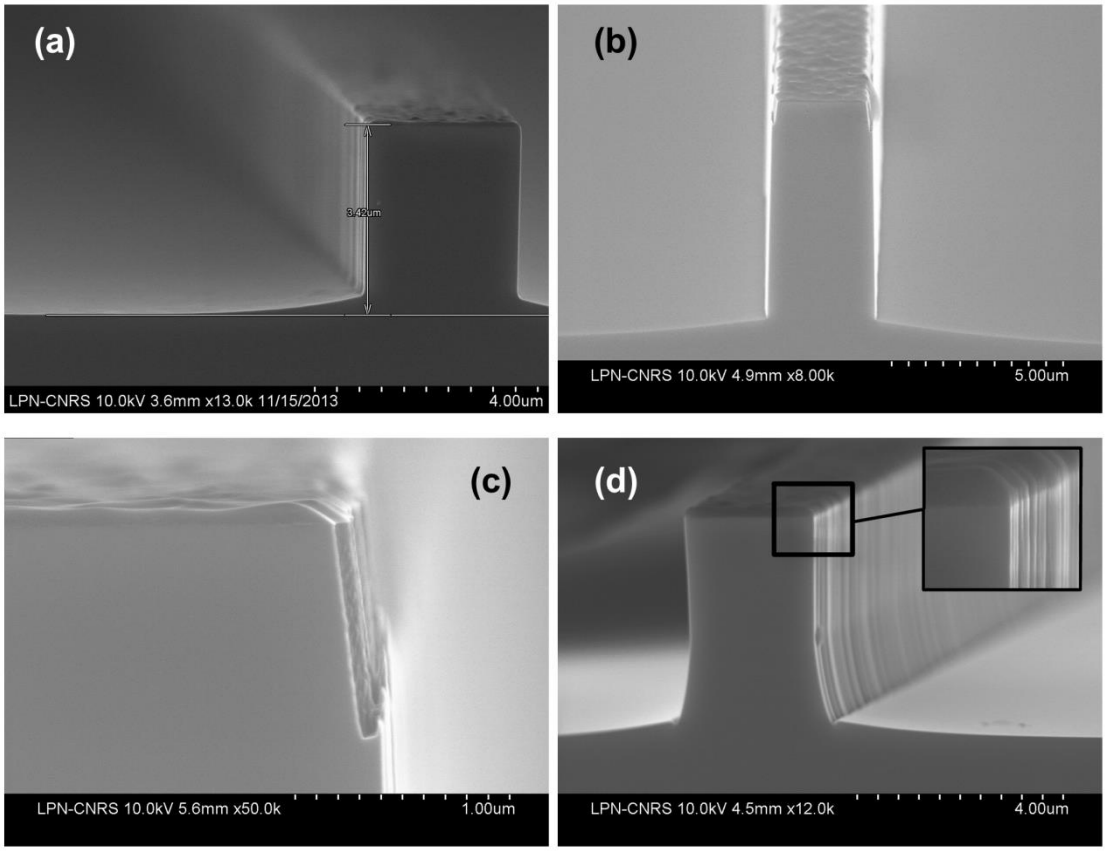

Figure 4.8 – (a) SEM image of a highly anisotropic etching with a fast etch-rate obtained by our optimized $Cl_2/H_2/O_2$ process. (b) This process has also been tested for future deep ridge applications, resulting in high verticality for an etching depth above 7 μm. (c) Some of the initial tests exhibited an undercut in the beginning of the process, which has been solved in later tests (d) by reducing the initial time in which etching in the absence of O_2 is performed during the first few seconds of the process.

also. Figure 4.7 shows the surface quality after an ICP process using $Cl_2/H_2/O_2$ based plasma, on the same sample. It can be seen that the ICP process transfers the surface roughness that resulted from the IBE step, creating a bad result at the end of the process. We tried different conditions, including different etching angles (0^o; 20^o; 45^o) during our IBE etching or combined etching steps (IBE for Au, CC-RIE for Ti, ICP for InGaAs and subsequently for InP) in order to reduce the surface roughness prior to ICP, but the final result was in all these cases non-satisfactory. It should be noted that our ICP process has been previously optimized in test samples, which simple included the usual SiN_x mask on InP substrate. The result of this is shown in Figure 4.8. It may be seen in these tests results that if we start with a smooth surface, our ICP process results in nice polished surface on both sides of the ridge, which would be ideal for patterning a Bragg grating for the LC-DFB purpose. Such a ridge obtained by our Cl_2/H_2 process, using small quantity (0.5 sccm) of O_2 for additional passivation, resulting in a fast etch-rate of ~1 μm/min, is shown in Figure 4.8. We

have achieved a similar quality result, but with slower etch-rate using an HBr/O_2 gas mixture diluted in He gas (HBr- 10 sccm; O_2- 0.5 sccm; He- 35 sccm; P= 0.5 mT), which may be used in applications where it is critical to stop the etching at a specific position of the structure (above a specific layer). In our case this is indeed an important issue, as the etching should be stopped above a the specifically designed layer for the Bragg grating definition, but this has been addressed using the $Cl_2/H_2/O_2$ process, combined with interferometric monitoring and a selective wet etching step for the last few hundreds of nanometers, which will be discussed in detail later on. The verticality in this process is a result of the sidewall passivation during the etching, which in our case is achieved partly by the O_2 introduced in our process and partly by Si, taking advantage of Si-based radicals introduced in the reaction chamber due to the use of a 4-inch silicon substrate placed underneath the sample to etch. Another feature that deserves attention in Figure 4.8, is the fact that in our preliminary tests un undercut on the top part of the ridge such as the one shown in Figure 4.8c, was observed. The reason for this is that always the ICP etching begins without the passivation gas (in our case O_2), for the first tens of seconds, which enables the vertical etching to be initiated. However during these few tens of seconds the horizontal etching component is also stronger as compared to the optimized conditions which occur for the rest of the process, which at the end results to the observed undercut. This undercut is again undesired for our LC-DFB process, again for issues related to the Bragg grating positioning as close as possible to the ridge. We have addressed this issue by optimizing this non-passivation time that is needed to initiate the etching. This time should be long enough to initiate the vertical etching component but also short enough to avoid the

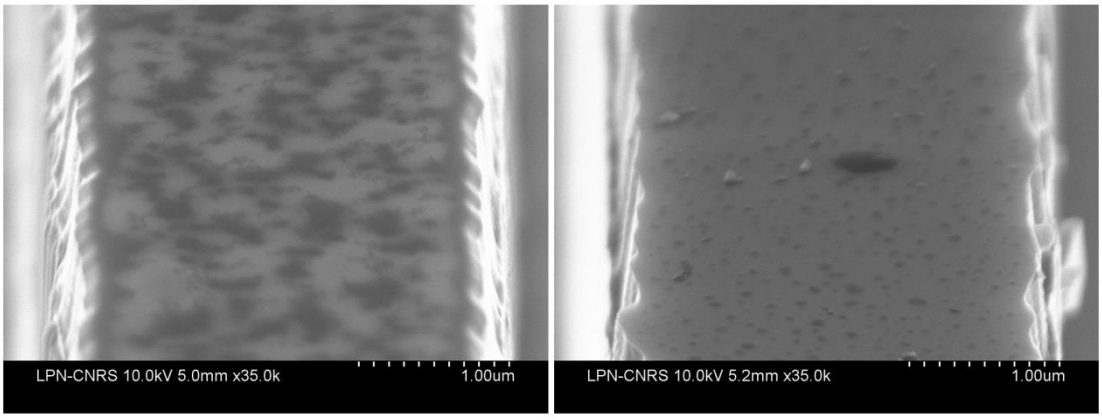

Figure 4.9 – Attempts to remove the residual SiN_x mask from the top of the ridge, in a test process where the mask has been directly patterned on top of the p+ InGaAs layer and the Ti/Au metal layers, which were used in our ridge waveguide process, have been omitted. Left: After 15 minutes in CCP-RIE SF_6 plasma. Right: After 10 minutes in an HF (concentration 40%) bath.

effect of Figure 4.8c. An initial etching time of 5 s is satisfactory and gives results with negligible undercut, such as the one shown in Figure 4.8d. From all the tests performed up to this point, it became clear that one should get rid of the roughness resulted by IBE on Au, in order to get a nice final result. We have investigated few different options, towards this target, in order to achieve the best possible compromise between satisfactory etching results and process simplicity. A first attempt to achieve a smooth surface, has been to try omitting the metallization part and define the ridge using similar steps as before, but for patterning the SiN_x mask directly over the p+ InGaAs layer. Such process could be functional in terms of current injection, even after the absence of the top metal contact, remembering the fact that our top p+ InGaAs layer is very highly doped and may thus act like a metal itself. However, while this effort resulted in good ridge-waveguide etching profile, as expected, it is not suitable for applications in this scheme, due to the fact that it is practically impossible to well-

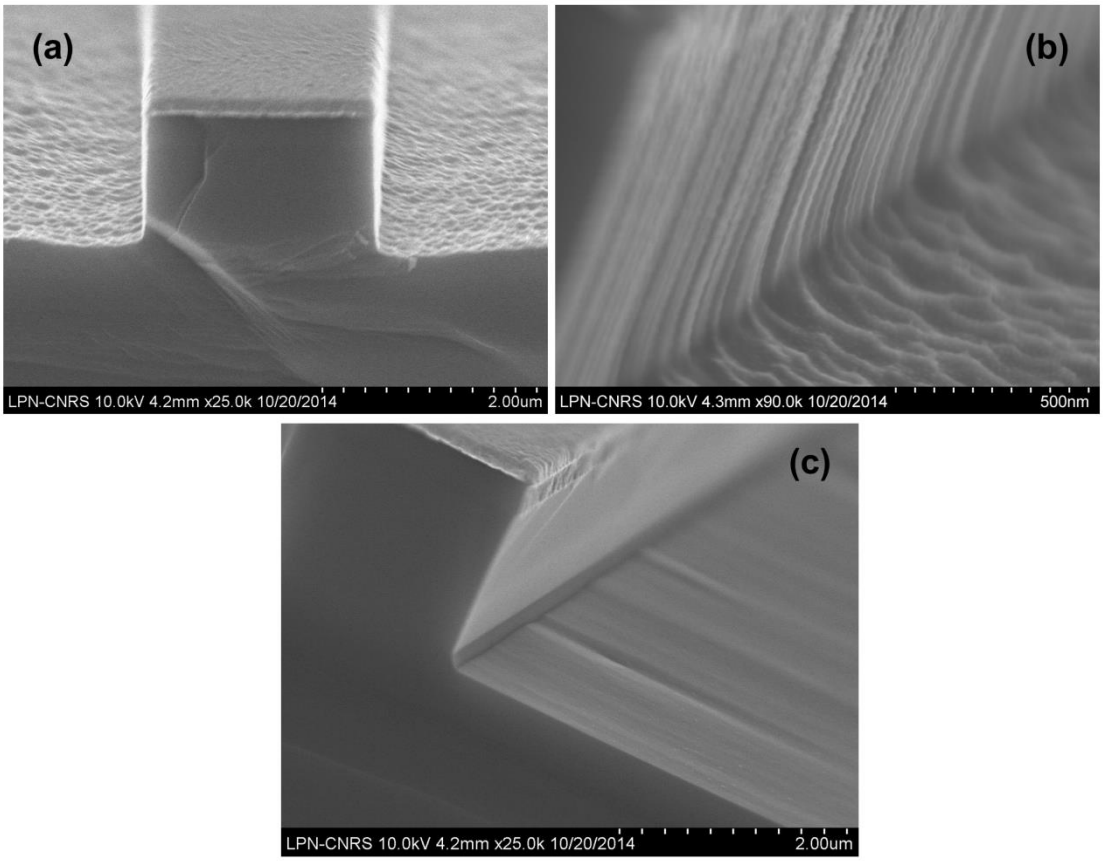

Figure 4.10 – (a) SEM image of the ridge profile after etching using a slow etch-rate RIE $Ch_4/H_2/O_2$ process using a Au mask. (b) Shows the surface and sidewall roughness. (c) Both the surface and sidewall roughness are improved after using an additional wet etching step with a diluted HCl solution to H_3PO_4, with ratio 1:4. Our InGaAsP(λ=1.17 μm) layer that is dedicated for the Bragg grating definition is a stop-etch for this solution. Even though the surface quality is improved after the utilization of the solution, the surface quality that we previously observed using ICP dry etching is superior.

remove the residual part of the SiNx mask remaining on the p+ InGaAs layer, after the etching is completed. Examples of such attempts, using SF6 based dry etching in CCP-RIE for t= 15 minutes, and baths in wet solutions (HF, concentration 40 %) for t= 10 minutes, are shown in Figure 4.9, on the left and right panels respectively. Therefore, the above approach has been rejected. A second attempt has been to directly deposit a patterned instead of a uniform Ti/Au layer, and subsequently use this as a mask for etching the semiconductor layers using dry etching. Preliminary results for this process, gave very poor results in ICP etching which was expected due to the fact that Au is a soft mask and therefore an increased sidewall roughness has been evidenced. Instead gold would be much less attached by an RIE $Ch_4/H_2/O_2$ based etching at low etch rate and therefore we decided to try the latter. Results on such etching are depicted in Figure 4.10. Due to the slow etch-rate this process needed to be performed for ~20 minutes to cover the appropriate shallow ridge depth of 1.5 μm. A Au layer with 300 nm starting thickness has been found to be enough, due to the very low Au etch rate in the CH_4/H_2 processes. A residual Au mask of ~40 nm has been measured

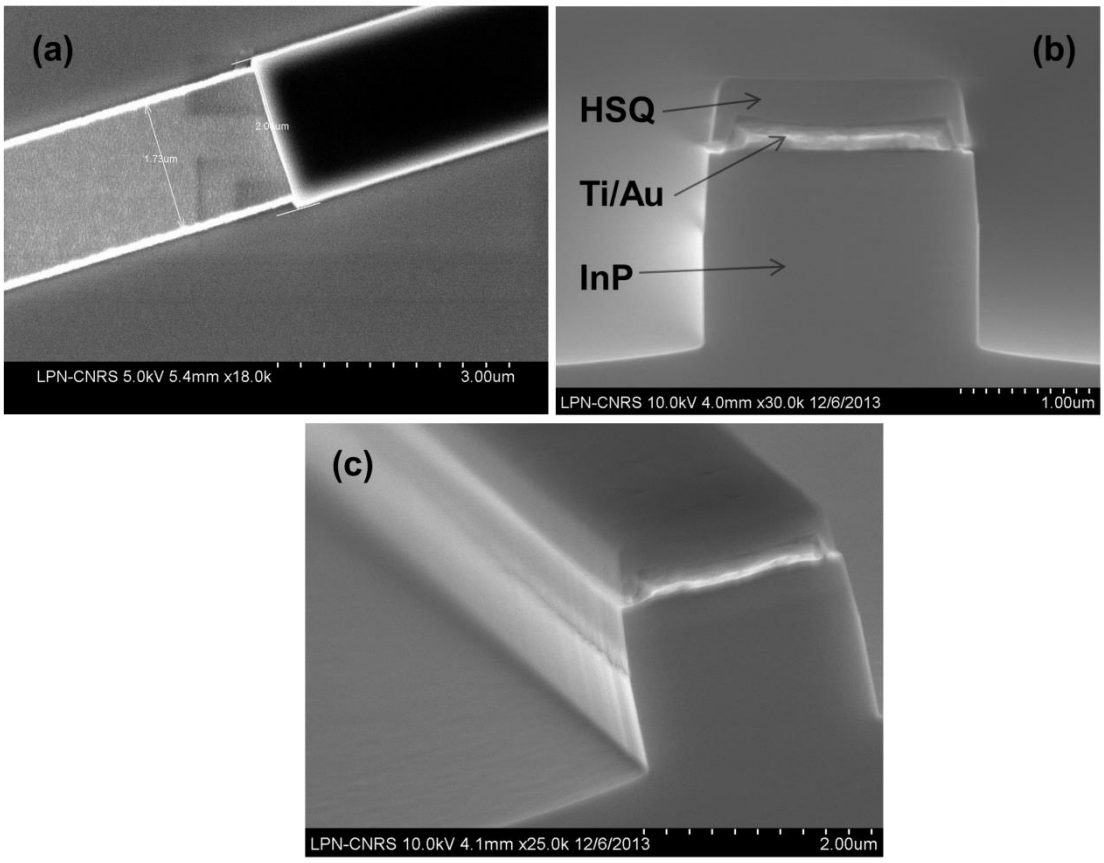

Figure 4.11 – SEM images of the alignment process using e-beam lithography, including the metal Ti/Au layer and the HSQ mask. (a) Top view after the alignment step and development of the HSQ. (b) Cross-sectional image of the finalized ridge. (c) Side-view revealing the resulting sidewall and surface quality.

when the etching was finalized. It can be seen from the results of Figure 4.10, that some surface roughness is produced during this dry etching process. By introducing a subsequent wet etching step, using a weak solution of HCl diluted in orthophosphoric acid, H_3PO_4 (ratio 1:4), the surface as well as the sidewall roughness may be reduced, while the InGaAsP layers that will be used for our Bragg grating definition is a stop-etch for this solution. However, the surface quality is still worse as compared to the polished surface that we can achieve using the optimized $Cl_2/H_2/O_2$ process previously discussed. For this reason we performed an alternative test, in which the Ti/Au patterned layer was again deposited above the p+ InGaAs layer, and subsequently a patterned HSQ mask has been aligned above the metal layers. Using this process we aim to both omit the harmful for the surface IBE step, while at the same time maintaining the beneficial metallization above the ridge, which enables our residual organic mask to be removed at the end of the etching process and use the ICP recipe; enabling for a polished surface on both sides of the ridge, for optimum patterning of the Bragg grating as well as reduced losses as a result of a reduced surface roughness. In addition, the utilization of e-beam lithography for the definition of the ridge would substantially reduce the sidewall roughness effect, that was evidenced in Figure 4.6, which is also high beneficial for our LC-DFB design. For the purpose of the alignment the HSQ mask is design to be slightly (50 nm) wider that the metallization in order to make sure that the Ti/Au layer will be fully covered within the e-beam positioning tolerances. An SEM image showing a top view after the alignment step and development of the HSQ is shown in Figure 4.11a. A cross-sectional image of the finalized ridge is shown in Figure 4.11b, while a side-view revealing the resulting sidewall and surface quality is depicted in Figure 4.11c. Considering all the information obtained by our preliminary tests, three important reasons suggest the utilization of e-beam lithography for the definition of the ridge. In summary, these reasons are the following:

1) We obtain the best sidewall quality, minimizing the roughness.
2) The ridge width may be defined with a much higher accuracy, using a resolution of 20 nm (remembering that optical lithography has a resolution of ~0.5 μm), which will enable us to seek the best possible compromise between the laser output power and the DFB coupling coefficient.
3) We will be able to achieve a vertical ridge using ICP dry etching, while omitting the IBE step, thus obtaining a very smooth surface on both sides of the ridge.
4) An additional advantage which has not been discussed up to now is that using this

process we will also be able to define alignment marks together with the ridge definition by e-beam lithography, which will subsequently allow for a simpler and very accurate alignment of the Bragg grating.

In addition we may conclude that a combined ICP and wet-etching step would provide an optimized surface, which is smooth and flat near the vicinity of the ridge, making it is ideal for the subsequent Bragg grating patterning. As mentioned above, another issue of great importance in our LC-DFB design is that the etching of the ridge should stop above the

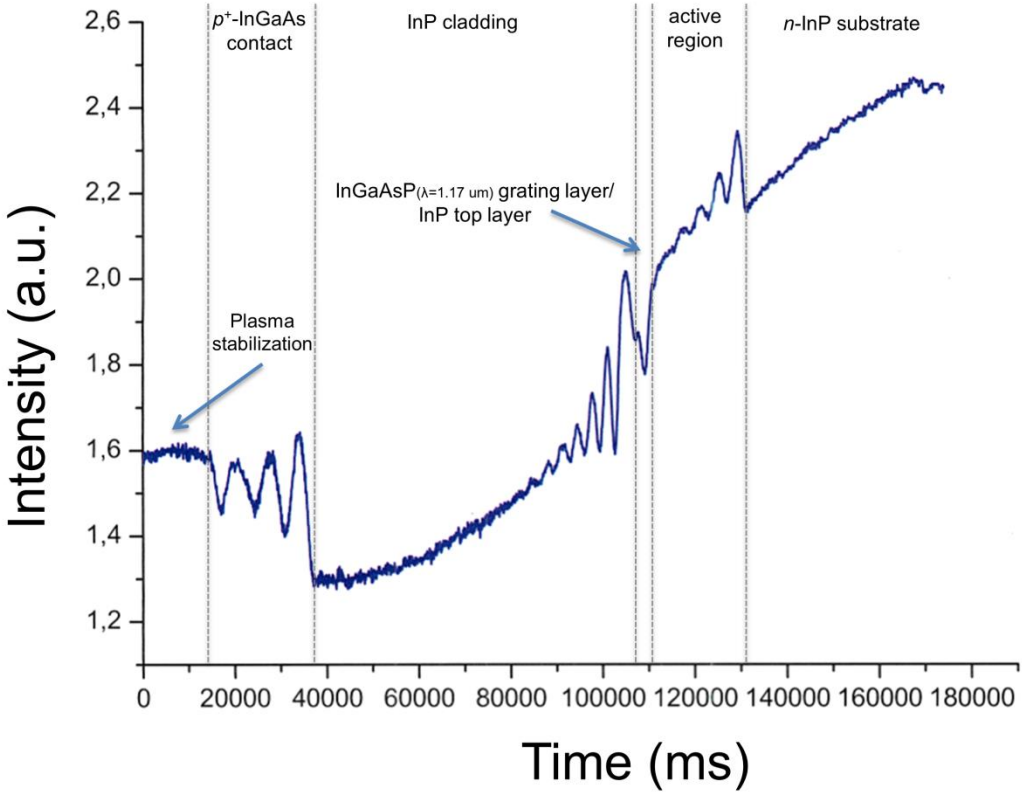

Figure 4.12 – Example of an ICP interferogram for one of our Qdash structures. The etching of the Ridge should be interrupted before the InGaAsP grating layer which has been designed for the fabrication of the Bragg grating. Phase shifts in the interferogram indicate material transitions.

InGaAsP(λ=1.17 μm) layer, which was specifically designed for the fabrication of the lateral Bragg grating during the growth of our structures. First one needs to ensure that this layer will not be etched during the ICP process. This has been achieved by *in situ* interferometric monitoring of the etching as follows: A very small piece of the wafer was cleaved and etched all the way until the substrate, while recording an interferogram such as

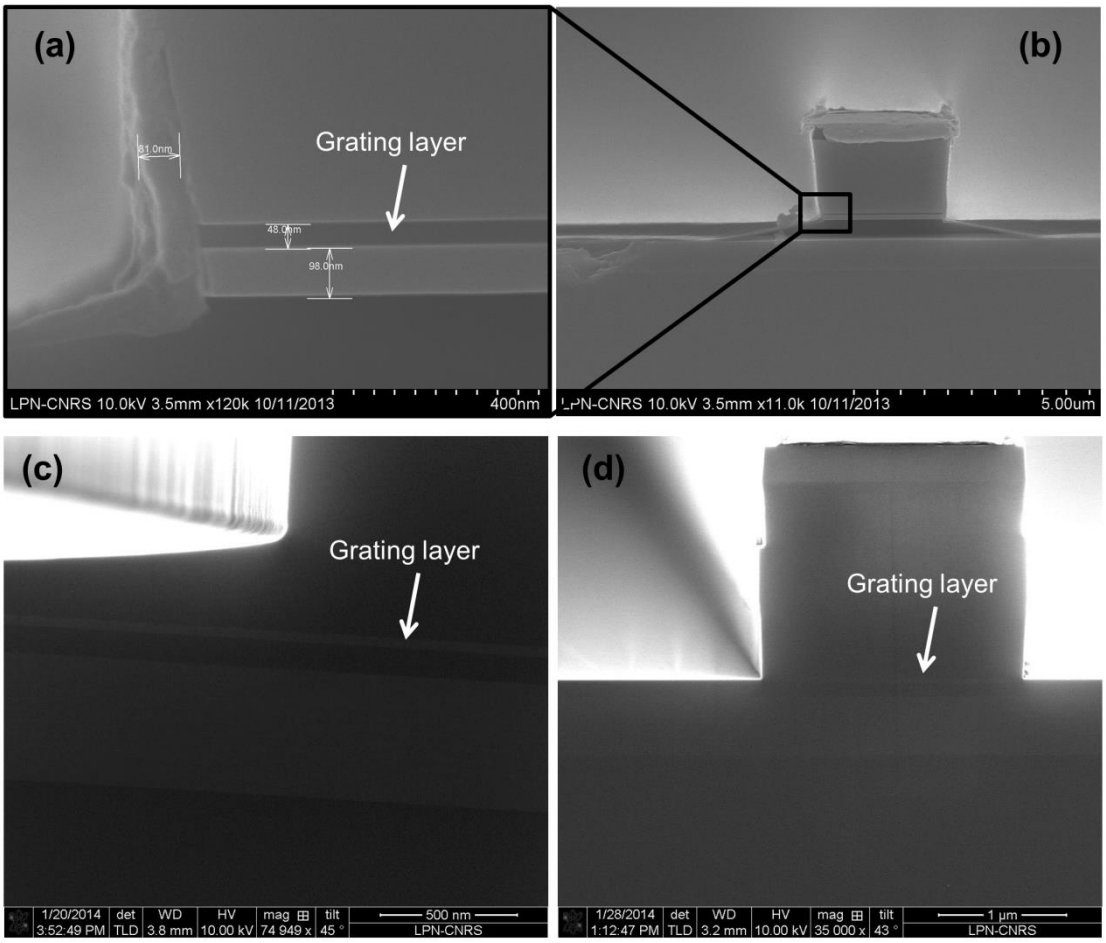

Figure 4.13 – (a,b) A ridge etched by ICP and subsequently by an HCl (37%) solution has been observed after exposing its cross section to a KFeCn solution for ~20 seconds. (a) is a zoom-in of (b). (c,d) The wet etching using HCl (37%) has been replaced with a diluted solution HCl/H3PO4 (ratio 1:4), in another piece of the same sample. The observation using our high-resolution SEM reveals that the grating layer acted as a stop-etch for this solution and remained in the structure, as required. (c) is a zoom-in of (d).

the one shown in Figure 4.12. The reflectivity of such interferograms depends on the top materials thickness and thus, oscillations are observed while etching and phase shifts indicate material transitions. After the etching of the small test sample has been completed, we used the resulting interferogram to identify all the epitaxial layers of interest in our sample, which are indicated in Figure 4.12. Subsequently the real sample has been etched while recording *in situ* a new interferogram, on top of the previous one, and we manually stopped the ICP etching few seconds before reaching the InGaAsP(λ=1.17 μm) layer. After that, we have performed a subsequent etching step for completing the etching, which aims to remove the remaining 50-150 nm of InP in the ridge vicinity, and further smooth the ridge sidewall and surface in case there are any imperfections. It should be noted that this etching will follow the crystallographic axis, and therefore an angle will be introduced, but since its

vertical depth will be only for 150 nm at most, the overall resulting angle will be very small as compared to the case in which the whole ridge was etched using an HCl solution, during our ridge waveguide process. We have used two different observation methods in order to verify that our grating layer would not be removed, which are schematically shown in Figure 4.13. First we exposed a cross section of our etched ridge to a KFeCn solution (for ~20 seconds), which has different etch rates for InP and InGaAsP(λ=1.17). This results for the grating layer to appear darker in our SEM images, as it can be seen in Figure 4.13a,b. Second, after optimizing the parameters of our high-resolution SEM it became possible to directly observe the InGaAsP(λ=1.17), which has slightly brightest contrast as compared to the surrounding binary InP material. During our tests we found that using "pure" HCl (concentration 37 %), even for a very short time, resulted in breaking the grating layer and the etching stopped on top of our InGaAs SCH layer, which us undesirable. On the contrary we found out that for an HCl solution diluted in orthophosphoric acid (H_3PO_4) with a ratio 1:4, our grating layer behaved as a stop-etch, producing the desired result. Figure 4.13 presents example SEM images for our two observation techniques. In Figures 4.13 a and b, a ridge etched by ICP and subsequent HCl (37%) solution has been observed after exposing its cross section to a KFeCn solution for ~20 seconds. It may be seen that the grating layer was etched away in this test. In Figures 4.13 c and d, the wet etching using HCl (37%) has been replaced with a diluted solution HCl/H_3PO_4 (ratio 1:4). The observation using our high-resolution SEM reveals that the grating layer acted as a stop-etch for this solution and remained in the structure, as required. Finally, the last technological test that requires special attention is the definition of the Bragg grating. A first parameter that should be taken into account is the etching rate. This should be as low as possible, while maintaining good etching quality (minimum roughness). This is because the etching depth should be very well controlled, because not enough depth would cause insufficient coupling coefficients, while an etching depth more than necessary would cause the grating to penetrate into the etching layer or even the active region, which is known to introduce significant additional losses. For this purpose we tested an ICP process based on HBr/H_2 diluted in an He gas, an ICP process based on Cl_2/H_2 with very low pressure and an RIE process based on a CH_4/H_2 plasma. While the investigated ICP processes gave very satisfactory results concerning the etching quality and relatively low etch rates, the RIE process was by a factor of 4 slower, enabling for a very accurate termination of the etching at the desired position, having an etch-rate of ~120 nm/min. However, some roughness was evidenced on the top parts of the grating as it may be seen in Figure 4.14a. We managed to treat this roughness using subsequent oxygen cleaning

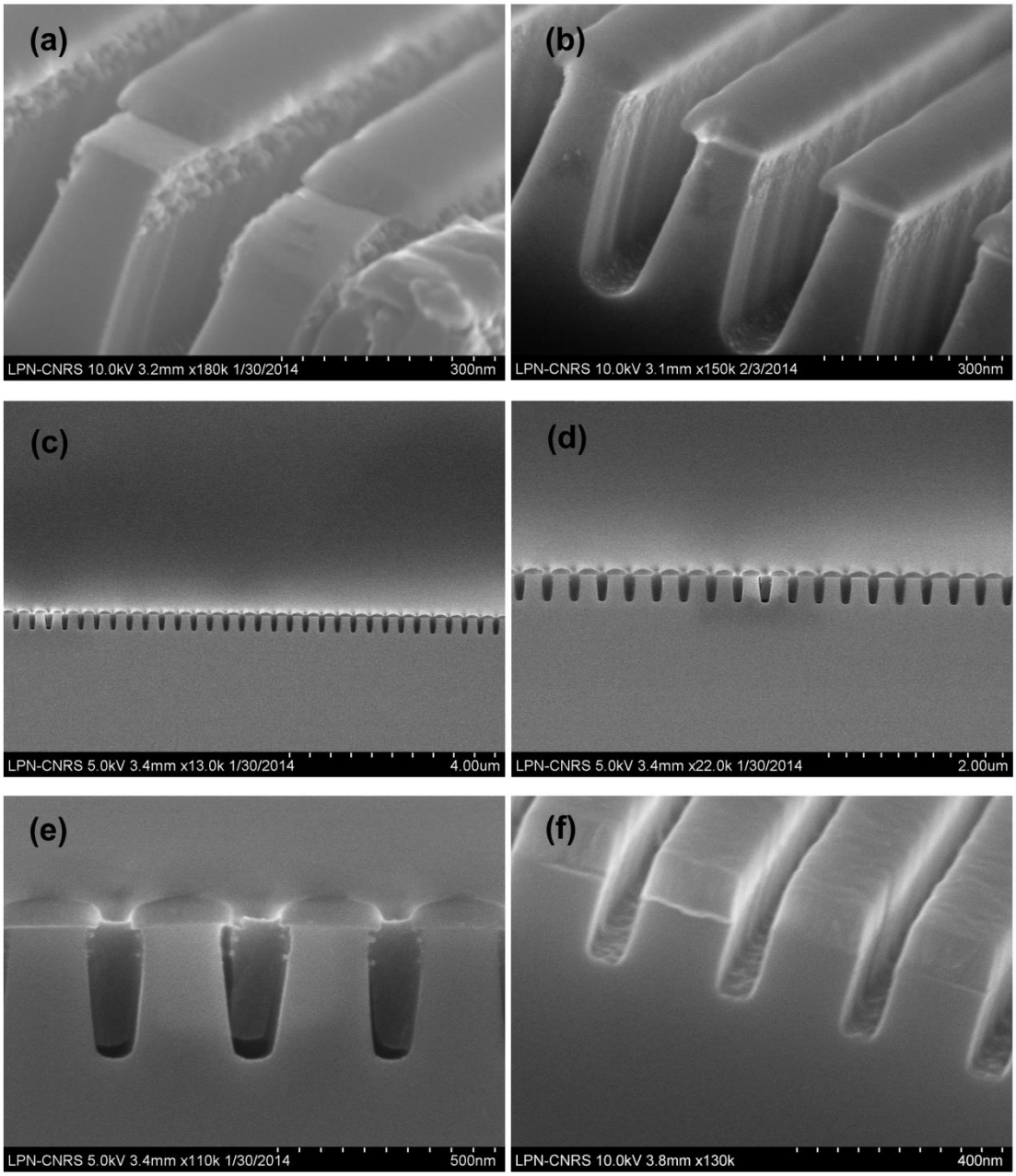

Figure 4.14 – (a,b) Bragg grating etched using an RIE CH_4/H_2 process with low etch-rate: (a) before oxygen cleaning and bath in an HNO3 solution ; (b) after oxygen cleaning and bath in an HNO3 solution. (c-e) Tests reveal that the spin-coated BCB penetrates into the 60-nm-wide narrow trenches of the Bragg grating. (f) Our finally optimized high-duty-cycle Bragg grating.

within the RIE reactor followed by a bath in an HNO_3 solution diluted with water (ratio 1:4). The result is depicted in Figure 4.14b. A final concern was whether the BCB would penetrate in the grating's narrow trenches, remembering that the openings are only 60 nm wide. Our tests were positive showing that all the Bragg grating openings are filled with BCB as it may be seen in Figures 4.14c-e. An image of our finally obtained high-duty-cycle

Bragg grating obtained by the RIE CH_4/H_2 process, prior to removing the residual SiN_x mask, is depicted in Figure 4.14f.

4.4 LC-DFB optimized process

After completing the whole series of tests and trade-off considerations, as described in the previous sections, the new processing steps have been selected and finalized in respect to achieving the desired κ -values. These processing steps, forming our new optimized LC-DFB fabrication process, will be listed together within this Section and in the following Section 4.5, the first experimental LC-DFB results, obtained by this process, will be presented. Some of the steps which are identical to the corresponding ones that were already described during either the broad area laser or the shallow ridge waveguide process, will be just mentioned with the details not being repeated.

1) *Native oxide removal*

2) *Definition of mask for ridge waveguide etching*

First, 1.9 μm wide openings with a 400 μm distance between them where patterned with e-beam lithography, using PMMA e-beam resist and then a Ti/Au/Cr (200/2000/100 Å) bilayer was evaporated and lifted off. The thin Cr layer on top has been used to facilitate better adhesion of the HSQ in the latter step, as it is well-known that the HSQ adhesion to Au is not good. Subsequently, a second e-beam lithography step, aligned with the first one, was used to define 2 μm wide HSQ trenches, of ~300 nm thickness, covering the previously patterned 1.9 μm wide Ti/Au trenches. The HSQ has used as the mask to transfer the pattern into the semiconductor. (The main property of HSQ is that it turns into ~SiO_2 after e-beam exposure with proper doses and is thus a very good mask for etching semiconductors, which can be directly defined after a single step of exposing and development. Furthermore, HSQ has a very high resolution)

3) *Ridge waveguide etching*

During this process the ridge waveguide etching has been performed in two steps. First, the top p+ InGaAs and the biggest part of the InP top cladding layer have been etched using our optimized $Cl_2/H_2/O_2$ ICP process, giving 90^o vertical profiles (etching time ~1 min. 15 sec.). In this, we stopped the etching manually ~100 nm before the whole InP top cladding

layer was etched, with the use of *in situ* interferometric monitoring such as the one described in Figure 4.12. The remaining InP has been etched using a solution of 37% HCl and H_3PO_4, with a ratio 1:4, for an etching time of 30 seconds and subsequent cleaning with deionized water for 3 min. It has been previously confirmed that our InGaAsP(1.17 μm) layer acts as a stop-etch for such a solution and is this preserved for the subsequent definition of the Bragg grating.

4) *Etching mask removal*

The residual HSQ (SiO_2) mask has been etched by CCP-RIE, using SF_6 plasma, at a pressure of 30 mTorr.

5) *Definition of mask for Bragg grating etching*

First, a 60 nm thick SiN_x layer has been deposited using PECVD and then a third e-beam lithography step, aligned with the first two, has been used to define the pattern of the Bragg grating mask beside the ridge, using PMMA resist. Subsequently, the pattern is transferred from the PMMA to the SiN_x layer underneath, using an RIE SF_6/CHF_3 process (SF_6 is generally used for isotropic etching of SiN and CHF_3 is used for passivation in order to achieve a 90^o vertical etching). The residual PMMA mask is removed using an oxygen based process, before removing the sample from the reactor.

6) *Bragg grating etching*

The Bragg grating has been etched using our RIE process based on a $CH_4/H_2/O_2$ plasma with a very slow etch rate (~120 nm/min), where the sidewall passivation is achieved partly due to the presence of the Si residuals coming from the Si substrate over which our sample is placed during the etching, and partly due to the presence of O_2 in our recipe, resulting in ~90^o vertical sidewalls of the grating. Due to the great importance of well controlling the grating depth and due to the fact that small changes in the reactor conditions may result in different etch rates, a test sample is always etched just before the Bragg grating etching in the laser sample; the etching rate is re-calibrated at that moment by SEM.

7) *Laser structure planarization*
8) *BCB etching to release top of ridges*
9) *Deposition of p-type contacts*

10) Substrate thinning and deposition of n-type contacts

The final cleaved devices are mounted junction side up onto copper C-block. No AR/HR coatings are implemented, in accordance to our efforts for maintaining the process as simple as possible in order to be compatible for the gas sensing applications needs.

4.5 Results and discussion

Following the process described in Sec 4.4, on our wafer 63802 lasing at ~2μm described in Chapter 2, we fabricated LC-DFB lasers targeting at ~1.96-1.98 μm, at which our industrial partner, PROCAL was particularly interested because it is suitable for the detection of the NH_3 gas. It should be noted that due to the fact that the refractive indices of our material at λ= 2 μm are not measured experimentally, but they have been calculated using experimental data at λ= 1.55 μm in combination with theoretical models, imperfect knowledge should be considered. For this reason, in combination with the fact that electron beam lithography has a finite accuracy for defining the desired Bragg period, we fabricated DFB lasers using three different nominal periods, in order to increase the chances of achieving the desired emission wavelength for gas detection. Indeed, the middle designed Bragg period reached 1.98 μm, which is optimum for NH_3 detection. Figure 4.15a-c shows the L-I curve and spectra for two such LC-DFB lasers, with nominal Bragg periods of 305 and 306 nm. The cavity length of these lasers is 910 μm and the output power is 4-4.5 mW per facet, which is above the output power of FP lasers fabricated from the same wafer, thus confirming the low losses of the etched semiconductor gratings as compared to their metal counterparts. The SMSR measured for these lasers has been limited by the signal to noise ratio of our spectrum analyzer, but it is confirmed from this measurement that its value lies above 29 dB. In a subsequent measurement for another LC-DFB laser fabricated in the same process (L=630 μm), shown in Figure 4.16, we managed to improve the signal to noise ratio by using a detector with a higher sensitivity and this measurement showed that our SMSR is even above 37 dB, which confirms the theoretical prediction for our process including the high-duty-cycle Bragg gratings as presented in Chapter 3. Both the output power and SMSR of our lasers, as well as the emission wavelength accuracy are within the requirements for high sensitivity detection of NH_3. The total tunability of our laser is 1.6 nm as it may be seen in Figure 4.15d,e. The tunability is limited by the thermal rollover, which limits our laser operation at higher CW current or higher temperatures. Unfortunately our LC-DFB lasers, similar to the FP layers studied in Chapter 2, do not operate at CW current at higher

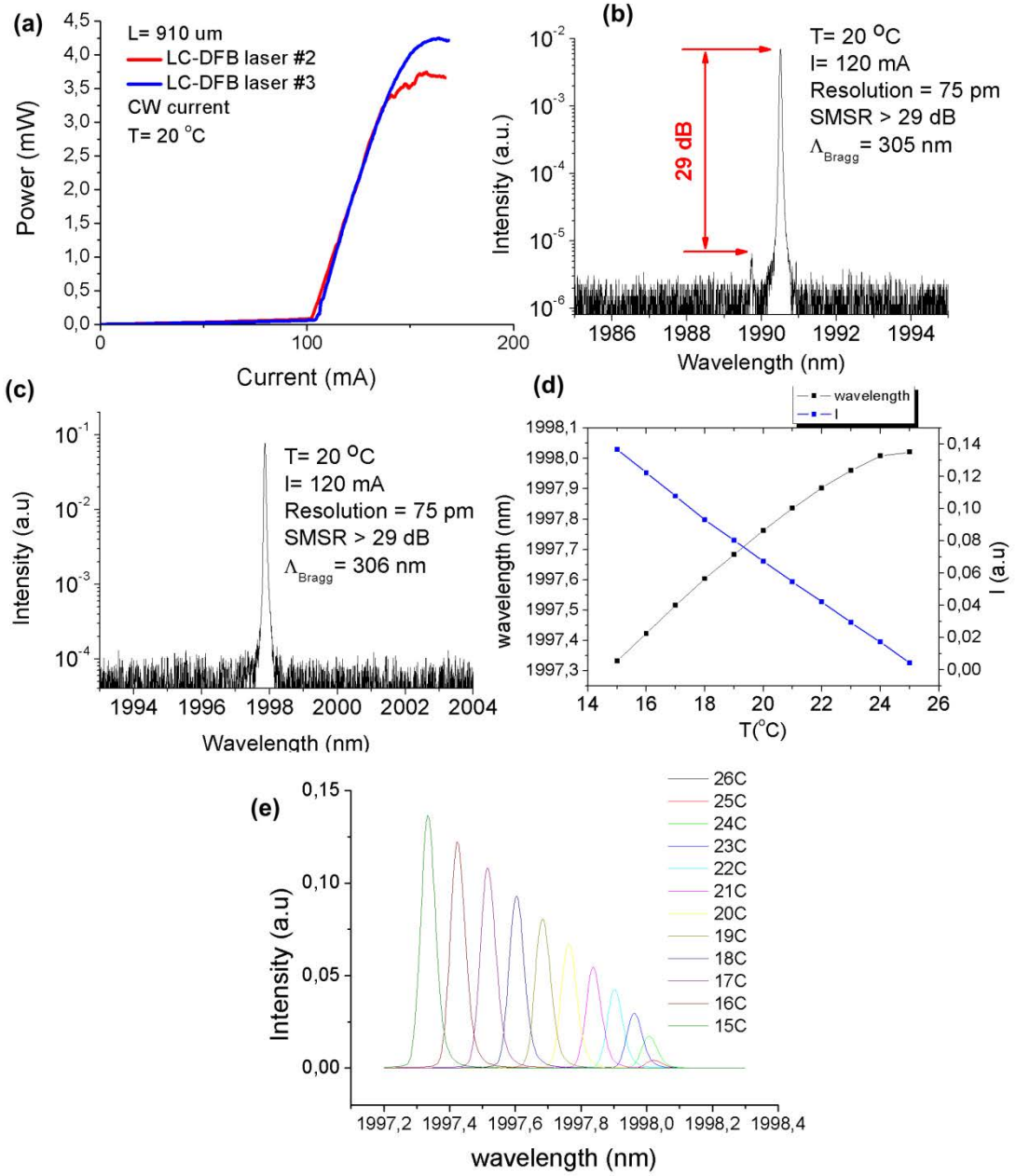

Figure 4.15 – LC-DFB laser results obtained for the process described in Section 4.4 on the wafer 63802 emitting at 2 µm (a) L-I curves for two LC-DFB lasers with different nominal Bragg period and a cavity length of 910 µm. (b,c) The corresponding spectra of these lasers. (d,e) Tunability of the emission wavelength and laser intensity drop as a function of temperature (spectra measured at Tyndall National Institute).

temperature. The maximum operation temperature for FP lasers is 40 °C while for the very best LC-DFB has been up to 30 °C. This is due to our material properties, namely the small conduction band offset caused by using the low InGaAs(1.65 µm) barrier. Therefore, this problem is expected to be solved for our optimized material design proposed in section

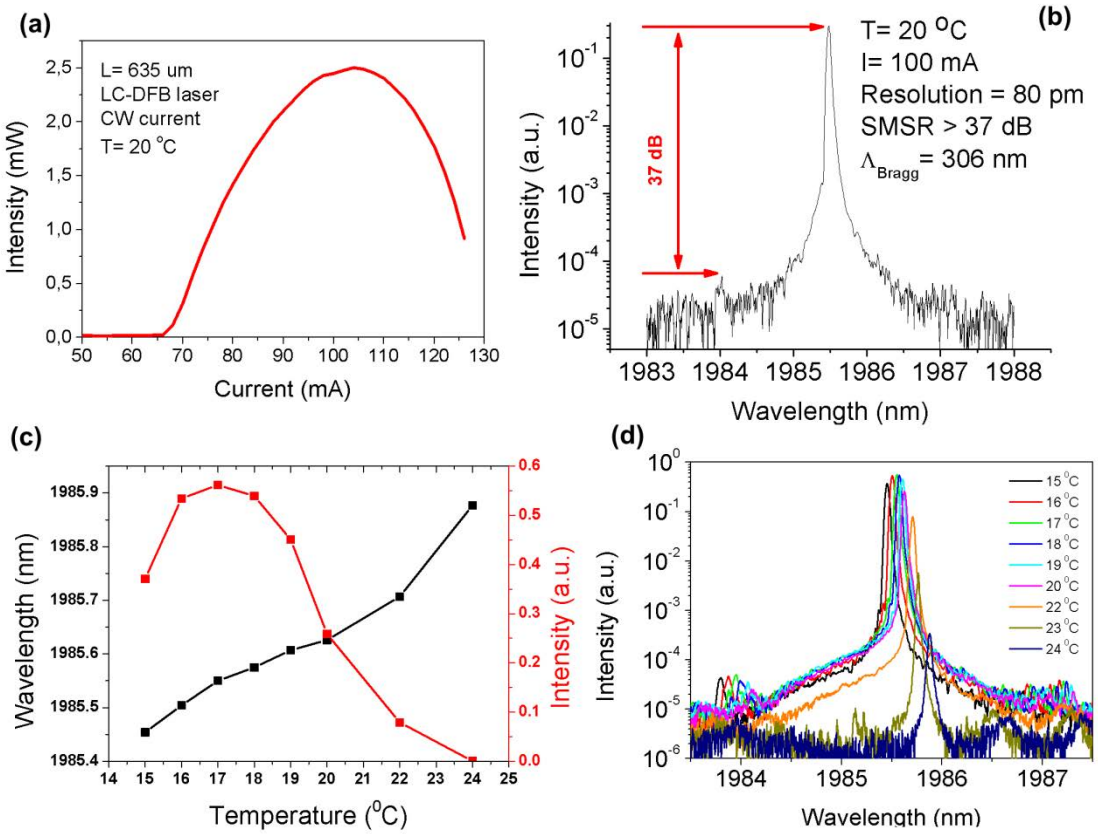

Figure 4.16 – LC-DFB laser results obtained for the process described in Section 4.4 on the wafer 63802 emitting at 2 µm (a,b) L-I curve and spectrum for a LC-DFB laser with a cavity length of 630 µm. (c,d) Measured wavelength tunability as a function of temperature. The output power substantially decreases for temperatures above 25 °C (spectra measured at Tyndall National Institute).

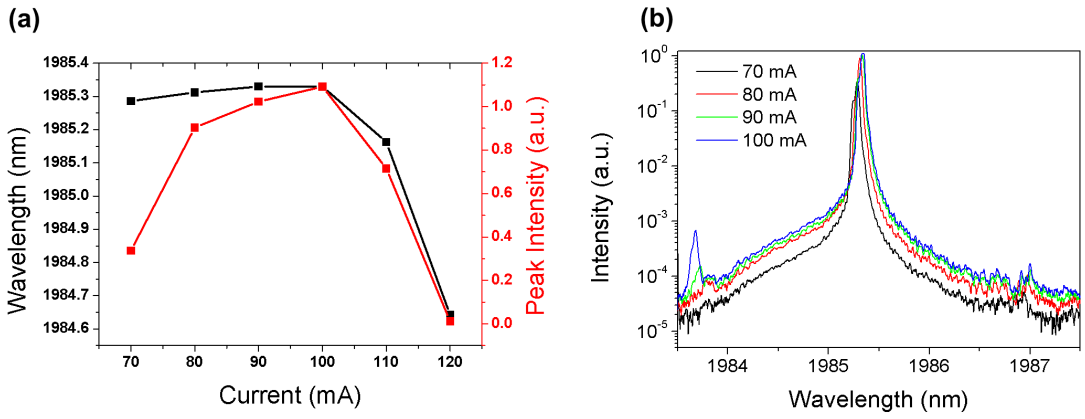

Figure 4.17 – Wavelength tunability and output power drop for higher CW injection currents observed for our LC-DFB laser caused by thermal-rollover caused by thermal effects as a result of the low conduction band offset in our material structure (spectra measured at Tyndall National Institute).

2.7. On the other hand, it is worth mentioning that since the SMSR also depends on the output power of the laser and the fact that our LC-DFB lasers maintain a high SMSR even above 20 ^{o}C at higher CW currents, where the power decreases below 0.5 mW, is a promising property of our novel LC-DFB process, using high-duty-cycle etched semiconductor gratings. Figure 4.17 shows the emission wavelength for our long cavity LC-DFB laser which confirms a quick power drop with increasing the CW injection current. Also, when the power substantially decreases the SMSR starts to degrade as well, where for this particular laser single mode behavior suitable for high resolution gas sensing (SMSR > 25 dB) is prevented for an injection current above 120 mA. As mentioned in section 4.4, our process is compatible with the fabrication of a tunable (>10 nm) LC-DBR laser which may be fabricated by simply adding a non-grating region in our e-beam mask and an electrical isolation step, prior to the wafer thinning, back-side metallization and laser cleaving in our process. We already tried fabricating such a laser in our last LC-DFB quarter wafer process, by modifying the mask as shown in Figure 4.18. In this process, we used an e-beam mask in which both grating and non-grating regions were integrated, while a fourth e-beam step was introduced to enable

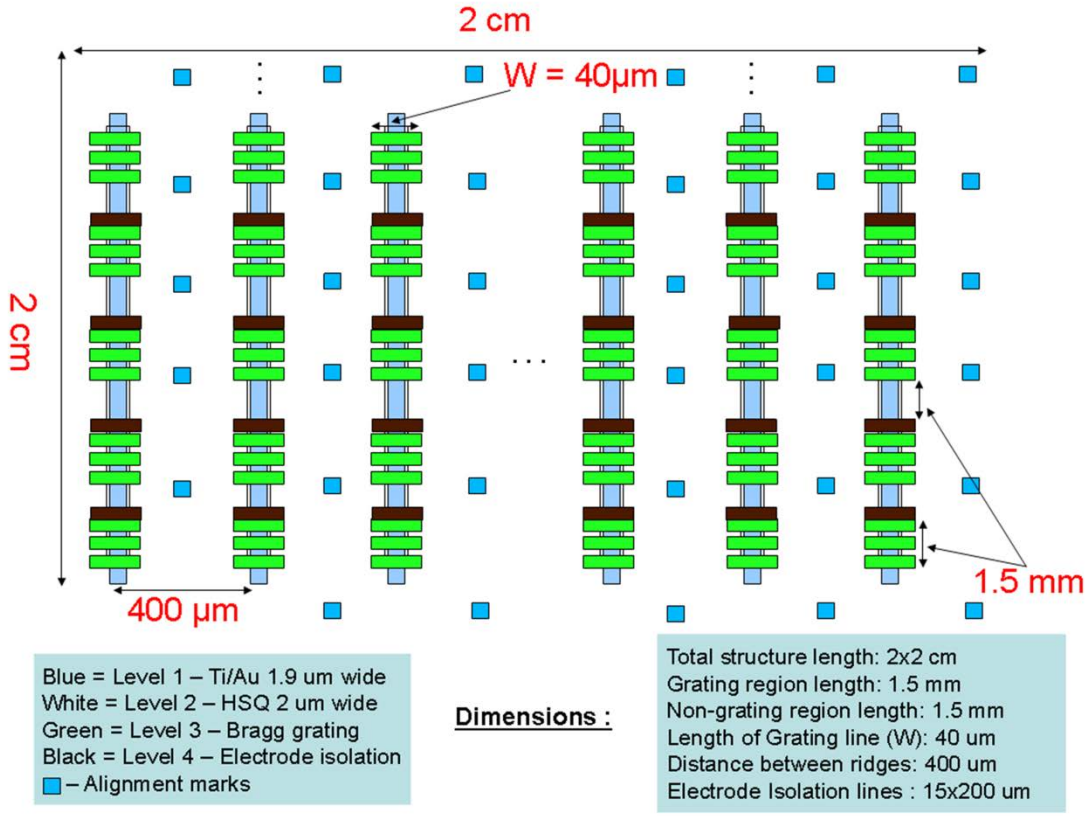

Figure 4.18 – Schematic of our e-beam mask, including grating and non-grating regions of 1.5 mm length each, attempting the fabrication of FP, LC-DFB and LC-DBR lasers in the same process.

electrode isolation in some parts of the wafer, such that we would be able to cleave at the end of the process all types of lasers of interest; including FP, LC-DFB and LC-DBR lasers. While the LC-DFB laser operated showing CW lasing at RT, as shown in Figures 4.15-4.17, no LC-DBR laser was operational. This may be due to the fact that the LC-DBR lasers would need to operate in a higher CW injection current, but also due to the fact that relatively few LC-DBR devices have been fabricated using this mask; we thus propose that this process would need to be further tested in future relate work, in a separated process in which a higher number of devices will be available for testing. Finally, in addition to the material properties, concerning the future perspective for the fabrication of an LC-DBR laser emitting at 2 μm, in respect to our preliminary tests, we propose possible improvements for the fabrication process. In fact, after observing the HSQ mask definition and subsequent sidewall profile after ICP etching, some roughness is still evident in our sidewall profile, even though due to the ridge definition using e-beam lithography an improvement is observed as compared to our previous shallow ridge waveguide process using optical lithography. This may be seen in Figure 4.19. By further optimizing the e-beam lithography parameters a smoother sidewall profile should be possible to obtain, thus permitting further reduction of the waveguide losses. This fact will facilitate the effort of fabricating an LC-DBR laser emitting at 2 μm, using the proposed process.

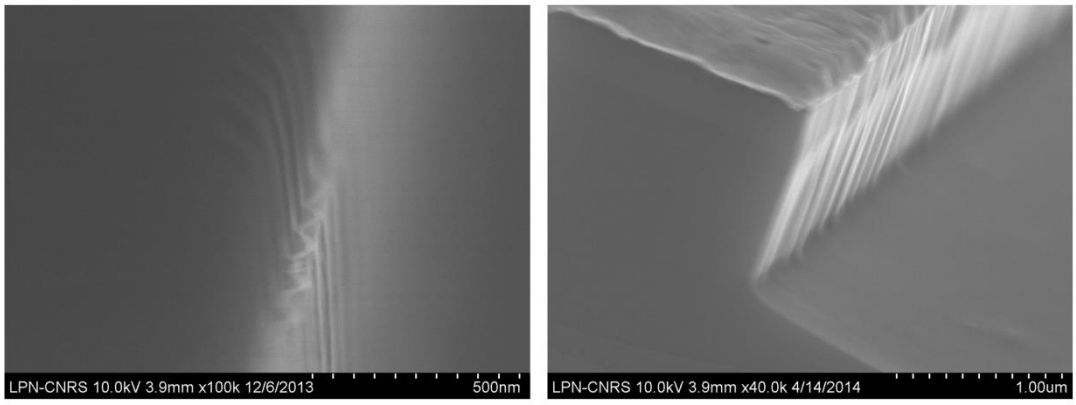

Figure 4.19 – HSQ mask definition (left) and subsequent waveguide sidewall profile after ICP etching (right).

Conclusions

During this work, we investigated the fundamental properties of single Qdashes, embedded in a diode-laser structure using cross-sectional scanning tunneling microscopy and spectroscopy. The main results included addressing the open question of the Qdash dimensionality nature, probing the electronic structure of individual nanostructures in respect to their precise location in the p-i-n junction and imaging of the Qdash electronic squared wavefunctions by high-stability differential conductivity mapping. We consider this work to exhibit a twofold fundamental interest. Firstly, in respect to the nature of the investigated nanostructures; scanning tunneling spectroscopic measurements are performed on Qdashes for the first time. Even though a relatively high number of publications related to Qdash based material has been released during the last decade, owing mostly to its very promising laser performances, a comprehensive experimental report on the fundamental physical properties of Qdashes, such as their electronic density of states, had been lacking up to present. The distinction between Qdashes and quantum dots (QDs) had not been clear and both terms could be found in literature used for nanostructures with similar lateral geometry. As a result, in a rather contradictive manner, a number of reports characterized Qdashes as quantum-dot-like, others referred to them as quantum-wire-like structures, while the term quasi-zero-dimensional has also appeared in recent related reviews. Theoretical studies have also not been conclusive due to the very particular shapes and high length-to-width and width-to-height size ratios that Qdashes exhibit. We analyzed within Section 1.1 the reasons why we believe that a better understanding would be of interest, both from a fundamental as well as a practical point of view. Due to recent advances in scanning tunneling spectroscopy and in situ cleavage techniques, it is becoming a very powerful tool in providing clear answers to such questions, by enabling direct access to the local density of states ((LDOS(E)) of buried nanostructures, while probing their cross-sectional structural characteristics with atomic resolution. In the manuscript we believe to provide conclusive evidence on the 1-D dimensionality nature of Qdashes through our high-energy-resolution X-STS measurements. Furthermore, their electronic squared wavefunctions were subsequently imaged and the results were compared to our finite-element simulations, after implementing the appropriate corrections for the tip induced band bending (TIBB) effect. Secondly, in respect to the measurement technique; (X- STS) measurements are, for the first time, extended to a real device (laser) structure. We have analyzed the electronic structure of individual Qdashes that

were placed in the multi-layer undoped active laser area, in respect to their precise location in the p-i-n junction. The potential gradient has been measured and found in good quantitative agreement with our theoretical band structure calculations obtained by solving self-consistently the Schrodinger-Poisson equations, demonstrating the high sensitivity of this spectroscopic measurement to (spatially resolved) local potential variations. In addition, we demonstrate that the potential gradient has been beneficial in our Qdash dimensionality studies, offering access to additional information. This would suggest that, in general, such device configurations can be beneficial in offering further insights into the behavior of semiconductor nanostructures, in comparison to traditional studies in which nanostructures directly deposited on a substrate were investigated.

In addition, we have investigated Qdashes as the active material of semiconductor lasers in respect to the gas sensing application. We optimized Qdash based material demonstrating CW lasing up to 2 μm emission wavelength with high performances, while our experimental and simulation results show to be promising for further pushing the emission wavelength out towards longer wavelengths in the future. Furthermore, a novel process has been developed, for the fabrication of laterally-coupled DFB lasers using the concept of high-duty-cycle semiconductor gratings, which significantly improved the coupling coefficient (>40 cm^{-1}). This process does not introduce any regrowth step over corrugated substrates, maintaining a very simple and thus low-cost process, while the high coupling coefficient value is achieved without using the conventional highly absorbing metal gratings, which introduce significant additional losses. We implemented this approach on our optimized epi-wafer and demonstrated high SMSR (>37dB) LC-DFB lasers emitting at 1.986 μm, with output power per facet up to 4.5 mW and I_{th} down to 65 mA for a 630 μm cavity length, suitable for detection of the NH_3 gas, which is important for industrial applications. Such high-κ, low loss, LC-DFB lasers achieved using etched gratings are a preliminary result which is compatible with the fabrication of a two-section LC-DBR laser using the same technology in the future. Such a laser, would combine a significantly simplified process, with sufficient feedback, continuous waveguide tunability and negligible grating-induced losses, finding potential applications both in sensing and telecommunications applications.

Appendix A: X-STM/STS measurements parameters and resulting resolution

During our large-scale measurements, summarized in Figures 1.4 and 1.5 the measurement procedure has been the following: We initially took topographic images of 100 x 100 nm (512 x 512 pixels), with a step size $\Delta x = \Delta y =$ 0.2 nm. At every 5 pixels in the x-direction we stopped scanning, opened the feedback loop, and recorded a spectroscopy from -1.5 V to 1.0 V with 145 points. This gives a numerical energy resolution of ΔE = 17.24 meV. This measurement is repeated every 5 lines in the y-direction, which gives a spatial resolution for the spectroscopy dI/dV map of 0.98 x 0.98 nm.

The data set for the spectroscopy contains 103 x 103 spectra, each spectrum requires a measurement of 5.19 s duration, therefore the acquisition time has been 55061 s. The total acquisition time for the whole measurement has been 56923 s.

During our small-scale measurements, summarized in Figure 1.6 of the main manuscript, the grid had been improved in order to acquire high-resolution measurements. In this case, the energy and spatial resolution for the spectroscopy dI/dV maps have been ΔE = 7.14 meV and $\Delta x = \Delta y$ = 0.29 nm respectively. The total acquisition time for the whole measurement has been 54500 s.

The temperature during all the measurements has been set to 5K and the lock-in parameters to fmod = 918 Hz; Vmod = 5 meV rms.

All the parameters of our large- and small-scale measurements are summarized in Tables A1.1 and A1.2 respectively, while the grid during our large-scale measurements that are shown in the film is illustrated in Figure A1.1.

Topographic Image Parameters				
	Scan size (nm)	Number of pixels	Step size (nm)	Time (s)
X	100	512	0.20	1862
Y	100	512	0.20	
	scan speed (nm/s)	55		

Parameters for the Spectroscopy				
Voltage start (V)	Voltage end (V)	Number of points	Energy resolution meV	Time (s)
-1.5	1	145	17.24	5.19

Parameters for the dI/dV maps				
	Step size (pixels)	Number of curves	Step size (nm)	Time (s)
X	5	103	0.98	55061
Y	5	103	0.98	

Table A.1.1. Parameters used during our large-scale topographic images, individual spectroscopic measurements and *dI/dV* maps.

Topographic Image Parameters				
	Scan size (nm)	Number of pixels	Step size (nm)	Time (s)
X	30	512	0.06	1024
Y	30	512	0.06	
	scan speed (nm/s)	55		

Parameters for the Spectroscopy				
Voltage start (V)	Voltage end (V)	Number of points	Energy resolution meV	Time (s)
0	1	140	7.14	5.04

Parameters for the dI/dV maps				
	Step size (pixels)	Number of curves	Step size (nm)	Time (s)
X	5	103	0.29	53475
Y	5	103	0.29	

Table A.1.2. Parameters used during our small-scale topographic images, individual spectroscopic measurements and *dI/dV* maps.

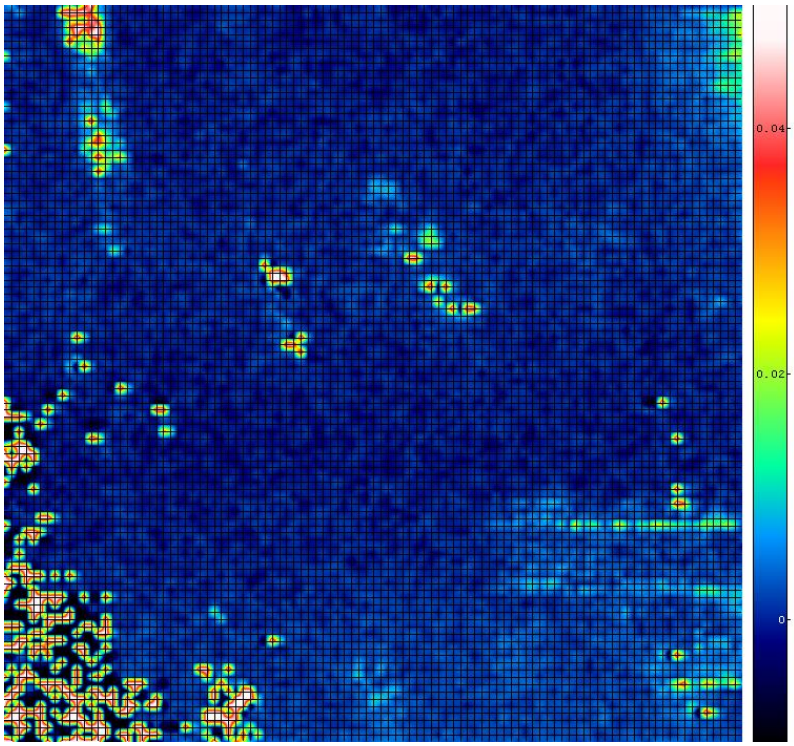

Figure A.1.1. The grid of points over which the spectroscopic measurements during our large-scale dI/dV maps have been performed. Such measurements are illustrated in Figure 1.5 of the main manuscript. The area shown here has dimensions of 100 x 100 nm; the parameters of the measurement are summarized in Table A.1.1.

Appendix B: Additional individual dI/dV spectra

The conduction band edge shift as a function of the precise location in the p-i-n junction has been shown in Figure 1.4 of the main manuscript, by comparing individual STS spectra taken on similar-sized Qdashes from layers #4 - #7. In that series of spectra, the valence band edge was only visible for Qdash layer #4 (at -1.4 V) and not visible for Qdash layers #5 - #7, within our scanning range - for applied sample voltage up to -1.5 V. This counterintuitive feature is a result of the tip induced band bending effect. We have provided within the main manuscript a detailed qualitative explanation concerning this effect, indicating the reason why we observe the valence band only for Qdash layer #4 in Figure 1.4. We also point out that the expected feature appearing for the valence band edge shift would be different than that of the conduction band as a result of this measurement artifact. Finally, we analyze why the TIBB effect is not symmetric between the different Qdash layers which are slightly, non-intentionally, doped. The later effect is much more pronounced in the valence band - for negative applied sample voltage values. This is illustrated schematically in Figure A.2.1, in which individual spectra taken on Qdashes from layers #3, #4 and #5 have been plotted together. Both the conduction and valence band are visible for layers #3 and #4, with the Qdash of layer #3 having the VB edge at a less negative voltage value compared to #4 and #5.

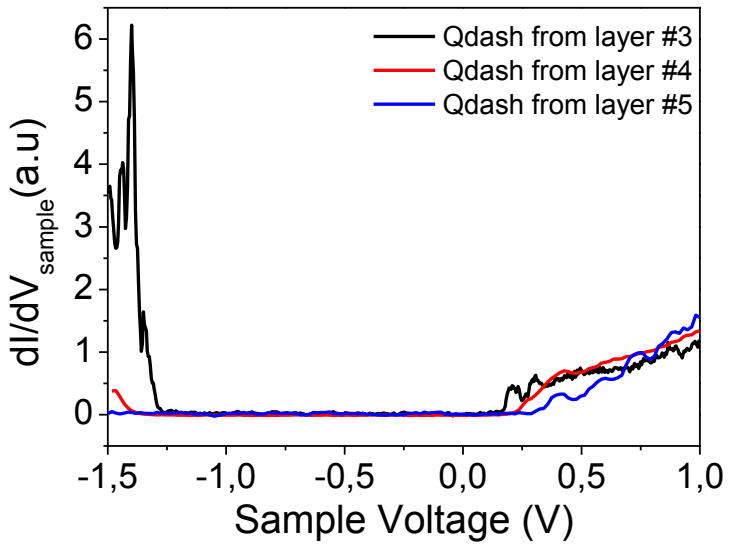

Figure A.2.1. Individual STS spectra taken on Qdashes from layers # 3, 4, 5. The valence band edge shifts towards negative values due to the TIBB effect. The effect is much stronger in magnitude for p-doped semiconductor material than for n-doped.

It has been mentioned in the main manuscript that most of the investigated Qdashes exhibited two confined transversal eigenstates (subbands), while few Qdashes with larger physical dimensions exhibited three eigenstates. STS spectra taken on Qdashes with two sharp peaks have been demonstrated in Figure 1.6b of the main manuscript. For completeness, two examples of spectra taken on Qdashes with three confined eigenstates are depicted in Figure A.2.2. These Qdashes were positioned in layers #4 and #9 respectively.

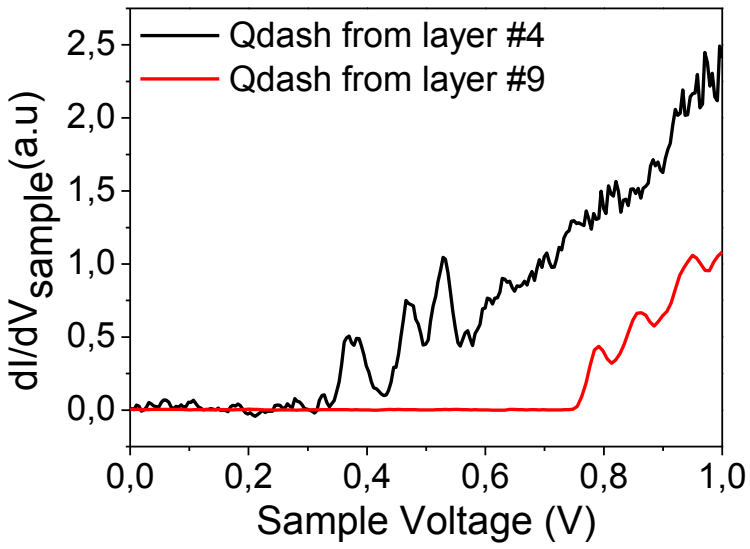

Figure A.2.2. Example individual STS spectra taken on Qdashes with a relatively larger lateral size (Qdash width ~27-28 nm), revealing three sharp peaks.

Appendix C: Broad area lasers for InSb quantum dots on InAs substrate

In addition to the Qdash material optimization which has been the main purpose of this work, we have developed an additional process in order to help our partners within the PROPHET network evaluate their material growth. The University of Lancaster aimed at developing a growth technique for testing weather a novel material using InSb QD's on InAs substrate might be suitable for gas sensing applications in the 3.5 μm wavelength range, which may not be covered using InP based material. Our efforts resulted in adapting the process described in section 4.1. The best possible results for vertical etching, were achieved using a two-step etching process to remove the p+ contact layer, which in this case was binary InAs. The first step consisted of a $H_3PO_4/H_2O_2/H_2O$ bath (ratio 1:1:1), having an etching rate of 0.7μm/min, while in the second step a bath of $H_2SO_4/H_2O_2/H_2O$ (ration 1:8:80) with an

Function	Material	Thickness (nm)	Comment
Contact	InAs	1500	n^{++}-doped
Barrier	InAs	400	X10
QD	InSb	1	X10 (PL at 3.5 μm)
Barrier	InAs	400	
Buffer	InAs	1000	p^{+}-doped
Substrate	InAs		p^{+}-doped

Table A.3.1 – Sample 1, including InSb QD's on InAs substrate, PL at 3.5 μm.

Function	Material	Thickness (nm)	Comment
Contact	InAs	1500	n^{++}-doped
Barrier	InAs	150	X10
QD	InSb	1	X10 (PL at 3.5 μm)
Barrier	InAs	150	
IMF	AlSb	10	
Buffer	InAs	1000	p^{+}-doped
Substrate	InAs		p^{+}-doped

Table A.3.2 – Sample 2, including InSb QD's on InAs substrate, PL at 3.5 μm The results of the developed etching process are shown in Figure A.3.1.

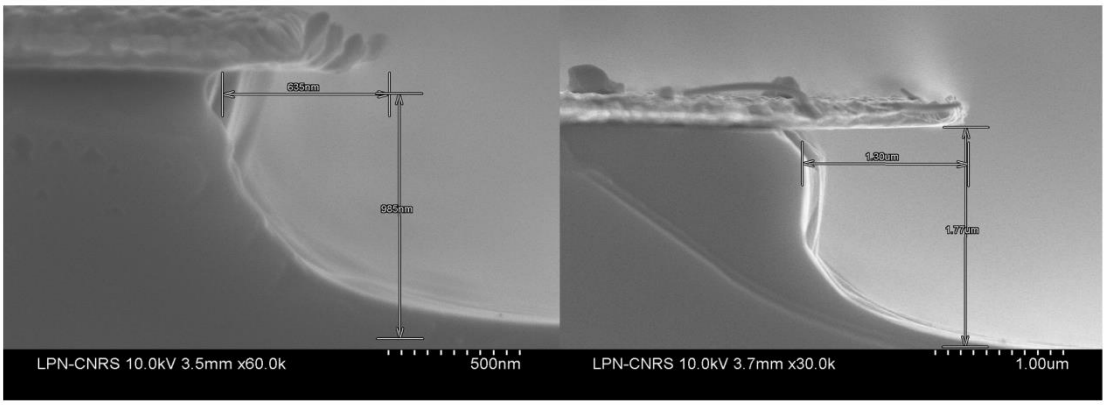

Figure A.3.1 – Etching profile after our two-step etching process: Left: after the first step, Right: second the second step.

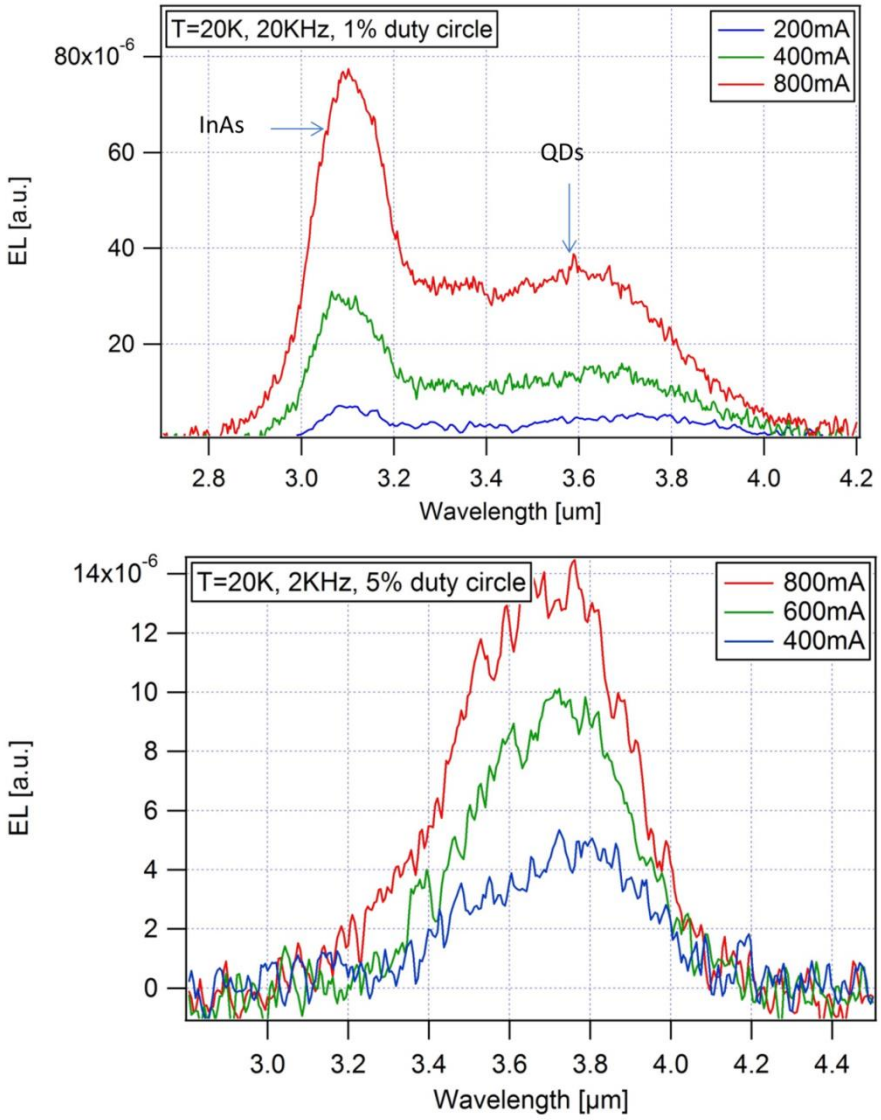

Figure A.3.2 – Electroluminescence of the two InSb based QD's studied samples: Top: Sample 1 ; Bottom: Sample 2.

etching rate of 0.42μm/min was used. This part was critical in this process, since the contact layer was 1.5 μm thick and therefore a fairly vertical etching was highly desirable. In addition, the native oxide removal step was performed using HCl in replacement of the HF acid since it would have attacked the InAs substrate. The epitaxial structures of the studied samples are summarized in tables A.3.1 and A.3.2. Characterization of these samples was subsequently performed at the University of Lancaster and based on these preliminary results they concluded on how to proceed with their subsequent growth campaigns, targeting at long wavelength gas sensing applications. In fact, after investigating several alternative approaches, they have concluded that shifting to GaAs substrates would be preferable for the emission wavelengths they were targeting at, as QD's of better quality and thus more promising liminescence performances could be grown using this material system [127]. Electroluminescence results obtained from the processed samples, using the epitaxial structurs of tables A.3.1 and A.3.2 are shown in Figure A.3.2.

List of publications

Journal Contributions

K. Papatryfonos, G. Rodary, C. David, F. Lelarge, A. Ramdane, and J.C. Girard, "One-Dimensional Nature of InAs/InP Quantum Dashes Revealed by Scanning Tunneling Spectroscopy," Nano Lett. **2015** 15 (7), 4488-4497; DOI: 10.1021/acs.nanolett.5b00963.

K. Papatryfonos, D. Saladukha, S. Joshi, K. Merghem, S. Bouchoule, S. Guilet, L. Le Gratiet, F. Lelarge, T. Ochalski, G. Huyet, A. Martinez, A. Ramdane, "Quantum dash based laterally-coupled distributed feedback lasers emitting at 2 μm using high-duty-cycle etched semiconductor gratings," to be submitted in Appl. Phys. Lett.

International Conferences

K. Papatryfonos, S. Joshi, K. Merghem, S. Bouchoule, S. Guilet, L. Le Gratiet, A. Martinez, A. Ramdane, "Quantum dash lasers for 1.6 - 2 μm," PROPHET Conference, 26-27 June 2014, Cork, Ireland (Oral)

Q. Lu, **K. Papatryfonos,** D. Saladukha, K. Klos, "Photonics enabling environment applications," PROPHET Conference, 26-27 June 2014, Cork, Ireland

K. Papatryfonos, S. Joshi, K. Merghem, S. Bouchoule, S. Guilet, L. Le Gratiet, A. Martinez, A. Ramdane, "Quantum dash based lasers for gas sensing," The 26th International Conference on Indium Phosphide and Related Materials (IPRM 2014), 11-15 May 2014, Montpellier, France

K. Papatryfonos, S. Joshi, K. Merghem, S. Bouchoule, S. Guilet, L. Le Gratiet, A. Martinez, A. Ramdane, "Long wavelength quantum dash based lasers for gas sensing: A novel laterally-coupled DFB/DBR laser design," European Semiconductor Laser Workshop (ESLW 2013), 27-28 September 2013, Bristol, United Kingdom (Oral)

K. Papatryfonos, S. Joshi, K. Merghem, S. Bouchoule, S. Guilet, L. Le Gratiet, A. Martinez, A. Ramdane, "Quantum dash based lasers for gas sensing," International Nano-Optoelectronics Workshop 2013, 19-30 August 2013, Cargese, France

K. Papatryfonos, K. Merghem, S. Joshi, A. Martinez, A. Ramdane, "Long wavelength quantum dash based lasers for gas sensing," International Nano-Optoelectronics Workshop 2012, 07-15 August 2012, Berkelay and Stanford, USA

Résumé

Ce travail de thèse a porté sur l'étude des propriétés fondamentales de bâtonnets quantiques InAs/InP formant la zone active de diodes lasers, à l'aide de microscopie et spectroscopie à effet tunnel à balayage. Nous avons pu étudier la nature de la dimensionnalité de ces nanostructures, mesurer la structure électronique de bâtonnets uniques en fonction de leur position dans la jonction PIN et également établir la cartographie de leur fonction d'onde à l'aide de mesures de conductivité différentielle. Nous avons de plus étudié le potentiel de ces bâtonnets quantiques comme milieu à gain de diodes lasers pour applications en détection de gaz. Nous avons optimisé des structures actives qui ont permis une émission laser en continu jusqu'à 2 µm et nos résultats expérimentaux et de modélisation montrent que cette longueur d'onde d'émission peut être étendue encore plus vers le MIR. De plus nous avons conçu et développé un procédé de fabrication de lasers DFB à couplage latéral à base de réseau de Bragg à fort rapport cyclique qui a permis d'améliorer de façon significative le coefficient de couplage (>40 cm^{-1}). Ce procédé ne nécessitant pas de reprise d'épitaxie est très simple et à bas coût dans sa réalisation. Les valeurs élevées du coefficient de couplage sont d'autre part obtenues sans recourir à des réseaux de Bragg métalliques, comme c'est généralement le cas dans la littérature, qui introduisent des pertes de propagation non négligeables. Cette nouvelle approche a été mise en œuvre pour la réalisation d'un laser monofréquence émettant à 1,986 µm, avec une puissance de sortie par face de 4,5 mW , un courant de seuil de 65 mA et un taux de suppression des modes latéraux > 37 dB. Ces paramètres sont parfaitement adaptés à la détection e.g. de NH_3, ce qui est très important pour des applications industrielles. Ce type de laser DFB à couplage latéral (LC-DFB), à fort κ et faibles pertes de propagation constitue une brique de base pour la réalisation future de composants à deux sections présentant une gamme élevée d'accordabilité en continu pour des applications aussi bien en détection de gaz qu'en télécommunications optiques.

1.6-2.5 µm Quantum Dash based lasers for Gas Sensing

Abstract :

During this work, we first investigated the fundamental properties of single Qdashes, embedded in a diode-laser structure configuration, using cross-sectional scanning tunneling microscopy and spectroscopy. The main results included addressing the open question of the Qdash dimensionality nature, probing the electronic structure of individual nanostructures in respect to their precise location in the p-i-n junction and imaging of the Qdash electronic squared wavefunctions by high-stability differential conductivity mapping. In addition, we have investigated Qdashes as the active material of semiconductor lasers in respect to the gas sensing application. We optimized Qdash based material demonstrating CW lasing up to 2 µm emission wavelength with high performances, while our experimental and simulation results show to be promising for further pushing the emission wavelength out towards longer wavelengths in the future using the same material system. Furthermore, a novel process has been developed, for the fabrication of laterally-coupled DFB lasers using the concept of high-duty-cycle semiconductor gratings, which significantly improved the coupling coefficient (>40 cm^{-1}). This process does not introduce any regrowth step over corrugated substrates, maintaining a very simple and thus low-cost process, while the high coupling coefficient value is achieved without using the conventional highly absorbing metal gratings, which introduce significant additional losses. We implemented this approach on our optimized epi-

wafer and demonstrated high SMSR (>37dB) LC-DFB lasers emitting at 1.986 μm, with output power per facet up to 4.5 mW and I_{th} down to 65 mA for a 630 μm cavity length, suitable for detection of the NH_3 gas, which is important for industrial applications. Such high-κ, low loss, LC-DFB lasers achieved using etched gratings are a preliminary result which is compatible with the fabrication of a two-section LC-DBR laser using the same technology in the future. Such a laser, would combine a significantly simplified process, with sufficient feedback, continuous wide range tunability, and negligible grating-induced losses, finding potential applications both in sensing and telecommunications applications.

References

1) Y. Arakawa and H. Sakaki, Appl. Phys. Lett., vol. 40, pp. 939-941, (1982).

2) M. Asada, Y. Miyamoto, and Y. Suematsu, IEEE J. Quantum Electron., 22, 1915-1921, (1986).

3) G. T. Liu, A. Stintz, H. Li, K.J. Malloy and L.F. Lester, Electron. Lett. 35 1163–1165, (1999).

4) K. Mukai, Y. Nakata, K. Otsubo, M. Sugawara, N. Yokoyama and H. Ishikawa, IEEE J. Quantum. Electron. 36, 472–478, (2000).

5) J.P Reithmaier, A. Somers, S. Deubert, R. Schwertberger, W. Kaiser, A. Forchel, M. Galligaro, P. Resneau, O. Parillaud, S. Bansropun, M. Krakowski, R. Alizon, D. Hadass, A. Bilenca, H. Dery, V. Mikhelashvili, G. Eisenstein, M. Gioannini, I. Montrosset, T.W. Berg, M. van der Poel, J. Mork, B.J. Tromborg, J. Phys. D 2005, 38, 2088-2102., J. Phys. D, 38, 2088–2102, (2005).

6) K. Papatryfonos, S. Joshi, K. Merghem, S. Bouchoule, S. Guilet, L. Le Gratiet, A. Martinez, A. Ramdane, Indium Phosphide and Related Materials (IPRM), 26th International Conference on, 10.1109/ICIPRM.2014.6880538, 1-2 (2014).

7) W.Zeller, M. Legge, A. Somers, W. Kaisser, J. Koeth and A. Forchel, Electron. Lett. 44, 5 (2008).

8) F. Lelarge, B. Dagens, J. Renaudier, R. Brenot, A. Accard, F. Dijk, D. Make, O. L. Gouezigou, J.-G. Provost, F. Poingt, J. Landreau, O. Drisse, E. Derouin, B. Rousseau, F. Pommereau, and G.-H. Duan, IEEE J. Sel. Top. Quantum Electron. 13(1), 111–124 (2007).

9) R. Rosales, S. G. Murdoch, R. T. Watts, K. Merghem, A. Martinez, F. Lelarge, A. Accard, L. P. Barry, and A.Ramdane, Opt. Express 20(8), 8649–8657 (2012).

10) H. Dery, E. Benisty, A. Epstein, R. Alizon, V. Mikhelashvili, G. Eisenstein, R. Schwertberger, D. Gold, J. P. Reithmaier, and A. Forchel, J. Appl. Phys. 95(11), 6103–6110 (2004).

11) M. Gioannini, IEEE J. Quantum Electron. 40(4), 364–373 (2004).

12) S.C. Heck, S. Osborne, S.B. Healy, E.P. O'Reilly, F. Lelarge, F. Poingt, O. le Gouezigou, and A. Accard, IEEE J. Quantum Electron. 45, 12, (2009).

13) H. Saito, K. Nishi, and S. Sugou, Appl. Phys. Lett. 78, 267 (2001).

14) C. Ni. Allen, P. J. Poole, P. Marshall, J. Fraser, S. Raymond, and S. Fafard, Appl. Phys. Lett. 80, 3629 (2002).

15) K. Klaime, C. Calò, R. Piron, C. Paranthoen, D. Thiam, T. Batte, O. Dehaese, J. Le Pouliquen, S. Loualiche, A. Le Corre, K. Merghem, A. Martinez, and A. Ramdane, Optics Express, 21, 23, 29000-29005 (2013).

16) A. Lenz, H. Eisele, R. Timm, L. Ivanova, R.L. Sellin, H.-Y. Liu, M. Hopkinson, U.W. Pohl, D. Bimberg and M. Dähne, Phys. Status Solidi B 246, 717, (2009).

17) A. Lenz, F. Genz, H. Eisele, L. Ivanova, R. Timm, D. Franke, H. Künzel, U. W. Pohl, and M. Dähne, Appl. Phys. Lett. 95, 203105, (2009).

18) F. Genz, A. Lenz, H. Eisele, L. Ivanova, R. Timm, U. W. Pohl, M. Dähne, D. Franke, and H. Künzel, Journal of Vacuum Science & Technology B 28, C5E1 (2010).

19) A. Musiał, P. Kaczmarkiewicz, G. Sęk, P. Podemski, P. Machnikowski, J. Misiewicz, S. Hein, S. Höfling, A. Forchel, Phys. Rev. B 85, 035314 (2012).

20) P. Kaczmarkiewicz and P. Machnikowski, Semicond. Sci. Technol. 27, 105012 (2012).

21) M. Gioannini, IEEE J. Quantum Electron. 42, 3 (2006).

22) J. P. Reithmaier, G. Eisenstein, and A. Forchel, Proc. IEEE 95, 1779 (2007).

23) T. Mensing, L. Worschech, R. Schwertberger, J. P. Reithmaier, and A. Forchel, Appl. Phys. Lett. 82, 2799 (2003).

24) B. Salem, N. Chauvin, T. Benyattou, G. Guillot, C. Bru-Chevallier, G. Bremond, C.Monat, P. Rojo-Romeo, and M. Gendry, Nanotechnology 16, 444 (2005).

25) N. Chauvin, B. Salem, G. Bremond, G. Guillot, C. Bru-Chevallier, and M. Gendry, J. Appl. Phys. 100, 073702 (2006).

26) M. Z. M. Khan, T. K. Ng, U. Schwingenschlogl, P. Bhattacharya and B.S. Ooi, Optics Express, 19, 14, (2011).

27) M. Z. M. Khan , T. K. Ng , C.-S. Lee , P. Bhattacharya and B. S. Ooi, IEEE Photon. J. 5, 4, 1501308 -1501308, (2013).

28) L. Dusanowski, A. Musiał, A. Maryński, P. Mrowiński, J. Andrzejewski, P. Machnikowski, J. Misiewicz, A. Somers, S. Höfling, J.P. Reithmaier, G. Sęk, Phys. Rev. B 90, 125424, (2014).

29) K. Suzuki, K. Kanisawaa, S. Perraud, M. Ueki, K. Takashina, Y. Hirayama, J. Cryst. Growth, 301–302, 97–100, (2007).

30) A. Bera, S. Dey, A.J. Pal, Nano Lett. 14, 2000−2005, (2014).

31) B. Fain, I. Robert-Philip, A. Beveratos, C. David, Z. Z. Wang, I. Sagnes, and J. C. Girard, Phys. Rev. Lett. 108, 126808 (2012).

32) nextnano: General Purpose 3-D Simulations, S. Birner, T. Zibold, T. Andlauer, T. Kubis, M. Sabathil, A. Trellakis, P. Vogl, IEEE Trans. Electron Devices 54, 2137 (2007).

33) J. C. Girard, A. Lemaıtre, A. Miard, C. David, and Z. Wang, J. Vac. Sci. Technol. B 27, 891 (2009).

34) B. Fain, J. C. Girard, D. Elvira, C. David, G. Beaudoin, A. Beveratos, I. Robert-Philip, I. Sagnes, and Z. Z. Wang, Appl. Phys. Lett. 97, 171903 (2010).

35) B. Fain, Ph.D. Thesis, Ecole Polytechnique, Palaiseau, France, September 2012 pp. 46–51

36) R M Feenstra, Y Dong, M P Semtsiv and W T Masselink, Nanotechnology 18, 044015, (2007).

37) A.C. Ford, S.B. Kumar, R. Kapadia, J. Guo, and A. Javey, Nano Lett. 12, 1340−1343, (2012).

38) H. Lin, J. Lagoute, V. Repain, C. Chacon, Y. Girard, J.-S. Lauret, F. Ducastelle, A. Loiseau and S. Rousset, Nature Mater. 9, 235 (2010).

39) S. Perraud, K. Kanisawa, Z.Z. Wang and Y. Hirayama, J. Phys.: Conf. Ser. 61 926, (2007)

40) G. Sęk, M. Motyka, K. Ryczko, J. Andrzejewski, R. Kudrawiec, J. Misiewicz, F. Lelarge, B. Rousseau, G. Patriarche, Proc. SPIE 6481, 64810D, 1-7, (2007).

41) B. Dagens, A. Markus, J.X. Chen, J.-G. Provost, D. Make, O. Le Gouezigou, J. Landreau, A. Fiore and B. Thedrez, Electron. Lett. 41, 323 (2005).

42) P. Boucaud and S. Sauvage, C. R. Phys. 4 1133 (2003).

43) M. Grundmann, O. Stier, and D. Bimberg, Phys. Rev. B, 52, 16, 11969–11981, (1995).

44) G. Maruccio, M. Janson, A. Schramm, C. Meyer, T. Matsui, C. Heyn, W. Hansen, R. Wiesendanger, M. Rontani, and E. Molinari, Nano Lett. 7, 2701 (2007).

45) M.U. Gonzalez, L. Gonzalez, J.M. Garcia, Y. Gonzalez, J.P. Silveira, F. Briones, Microelectron. J. 35, 13 (2004).

46) J. M. Ulloa, S. Anantathanasarn, P. J. van Veldhoven, P. M. Koenraad, and R. Nötzel, Appl. Phys. Lett. 92, 083103 (2008).

47) D. Bimberg, M. Grundmann, and N. N. Ledenstov, Chichester, U.K.: Wiley, (1999)

48) E. U. Rafailov, M. A. Cataluna, and W. Sibbett, Nat. Photonics 1 (7), 395-401 (2007).

49) G. Moreau S. Azouigui, D.-Y. Cong, K. Merghem, A. Martinez, F. Lelarge, B. Rousseau, B. Dagens, F. Poingt, A. Accard, and F. Pommereau G. Patriarche, and A. Ramdane, Appl. Phys. Lett. 89, 241123, (2006).

50) D. Zhou, R. Piron, M. Dontabactouny, E. Homeyer, O. Dehaese, T. Batte, M. Gicquel, F. Grillot, K. Tavernier, J. Even, and S. Loualiche Phys. Status Solidi C, 1–5 (2009).

51) D. Deppe, H. Huang, and O. Shchekin, IEEE J. Quantum Electron. 38(12), 1587–1593 (2002).

52) D. Bimberg, N. Kirstaedter, N. N. Ledentsov, Z. I. Alferov, P. S. Kop'ev, and V. M. Ustinov, IEEE J. Sel. Top. Quantum Electron. 3, 2, 196 –205, (1997).

53) M. Willatzen, T. Tanaka, Y. Arakawa, and J. Singh, IEEE J. Quantum Electron. 30, 3, 640 –653, (1994).

54) S. M. Kim, Y. Wang, M. Keever, and J. S. Harris, IEEE Photon. Technol. Lett. 16, 2, 377 –379, (2004).

55) P. Borri, W. Langbein, J. Mørk, J. Hvam, F. Heinrichsdorff, M.-H. Mao, and D. Bimberg, Phys. Rev. B 60, 11, 7784–7787, (1999).

56) S. Birudavolu, N. Nuntawong, G. Balakrishnan, Y. C. Xin, S. Huang, S. C. Lee, S. R. J. Brueck, C. P. Hains, and D. L. Huffaker, App. Phys. Lett. 85, 2337-2339, (2004).

57) K. Ogai, Y. Kimura, and R. Shimizu, Appl. Phys. Lett. 66, 1560-1562, (1995).

58) V. B. Verma and J. J. Coleman, App. Phys. Lett. 93, 111117 (2008).

59) V. B. Verma U. Reddy, N. L. Dias, K. P. Bassett, X. Li and J. J. Coleman, IEEE J. Quantum Electron. 46, 12 (2010).

60) K. Kash, R. Bhat, D. D. Mahoney, P. S. D. Lin, A. Scherer, J. M. Worlock, B. P. Van der Gaag, M. Koza, and P. Grabbe, Appl. Phys. Lett. 55, 681-683, (1989).

61) T. Fukui, S. Ando, and Y. Tokura, Appl. Phys. Lett. 58, 2018-2020, (1991).

62) L. Goldstein, F. Glas, J.Y. Marzin, M.N. Charasse, G. Le Roux, Appl. Phys. Lett. 47, 1099, (1985).

63) D. Leonard, M. Krishnamurthy, C.M. Reaves, S.P. Denbaars, P.M. Petroff, Appl. Phys. Lett. 63, 3203, (1993)

64) J.M. Moison, F. Houzay, F. Barthe, L. Leprince, E. Andre, O. Vatel, Appl. Phys. Lett. 64, 196, (1994).

65) J.M. Gerard, J.B. Genin, J. Lefebvre, J.M. Moison, N. Lebouche, F. Barthe, J. Cryst. Growth 150, 351, (1995).

66) D. Franke, M. Moehrle, J. Boettcher, P. Harde, A. Sigmund and H. Kuenzel, Appl. Phys. Lett., 91, 081117, (2007).

67) Z.G. Lu, J.R. Liu, S. Raymond, P.J. Poole, P.J. Barrios, and D. Poitras, Opt Express, 16, 14, 10835–10840, (2008).

68) P. Caroff, N. Bertru, A. Le Corre, O. Dehaese, T. Rohel, I. Alghoraibi, H. Folliot and S. Loualiche, Jpn. J. Appl. Phys. 44, 1069-1071, (2005).

69) D. Zhou, R. Piron M. Dontabactouny O. Dehaese, F. Grillot, T. Batte, K. Tavernier, J. Even and S. Loualiche, Appl. Phys. Lett. 93, 161104 (2008).

70) B. Broberg and T. Lindgren, J. Appl. Phys. 55, 3376 (1984).

71) J. Dong, A. Ubukata and K. Matsumoto, IEEE Photon. Technol. Lett., 10, 4, 513-515, (1998).

72) S. Fathpour, Z. Mi, A. R. Kovsh, S. S. Mikhrin, I. L. Krestnikov, A. V. Kozhukhov, N. N. Ledentsov and P. Bhattacharya, Appl. Phys. Lett. 85, 22, (2004).

73) I.P. Marco, A.D. Andreev, A.R. Adams, R. Krebs, J. P. Reithmaier, and A. Forchel, IEEE J. Sel. Top. Quantum Electron., 9,5, 1300-1307, (2003)

74) I.P. Marko, A. Adams, S. J. Sweeney, D. Mowbray, Maurice S. Skolnick, Huiyan Y. Liu, and Kristian M. Groom, IEEE J. Sel. Top. Quantum Electron. 11, 5, (2005).

75) I.P, Marko, S.J. Sweeney, A.R. Adams, S.R. Jin, B.N. Murdin, R. Schwertberger, A. Somers, J.P, Reithmaier, and A. Forchel, Phys. Status Solidi B 241: 3427–3431, (2004).

76) S. Forouhar, R.M. Briggs, C. Frez, K.J. Franz, and A. Ksendzov, Appl. Phys. Lett. 100, 031107, (2012).

77) S. Tomonari, M. Mitsuhara, N. Nunoya, IEEE Photon. Technol Lett. 20, 12, (2008).

78) S. Tomonari, M. Mitsuhara and Y Kondo, NTT Technical Review, 7,1, (2009).

79) S. Sprengel, A. Andrejew, K. Vizbaras, T. Gruendl, K. Geiger, G. Boehm, C. Grasse, and M.C. Amann, Appl. Phys. Lett. 100, 041109, (2012).

80) S. Sprengel, C. Grasse, K. Vizbaras, T. Gruendl, and M.C. Amann, Appl. Phys. Lett. 99, 221109, (2011).

81) S. Belahsene, L. Naehle, M. Fischer, J. Koeth, G. Boissier, P. Grech, G. Narcy, A. Vicet, and Y. Rouillard. IEEE Photon. Technol. Lett. 22, 15, (2010).

82) L. Naehle, C. Zimmermann, S. Belahsene, M. Fischer, G. Boissier, P. Grech, G. Narcy, S. Lundqvist, Y. Rouillard, J. Koeth, M. Kamp and L. Worschech, Electron. Lett. 47, 1092, (2011).

83) D. Bimberg and U.W. Pohl, Mater. Today 14, 388, (2011).

84) R.E. Nahory, M.A. Pollack, W.D. Johnston Jr., and R.L. Barns, Appl. Phys. Lett. 33, 659, (1978).

85) J. Dong, A. Ubukata and K. Matsumoto, IEEE Photon. Technol. Lett., 10, 4, 513-515, (1998).

86) M. Ochiai, H. Temkin, S. Forouhar, and S.A. Logan, IEEE Photon. Technol. Lett., 7, 8, 825-827, (1993).

87) M. Oishi, M. Yamamoto, and K. Kasaya, IEEE Photon. Technol. Lett., 9, 4, 431-433, (1997).

88) H. Kogelnik and C.V Shank, Journ. of Appl. Phys. 43, 2327-2335, (1972).

89) A. Yariv, IEEE J. Quantum Electron., 9, 919-933, (1973).

90) A. Othonos and K. Kalli, "Fiber Bragg gratings: fundamentals and applications in telecommunications and sensing", Artech House, (1999)

91) H. Kogelnik and C.V. Shank, App. Phys. Lett., 18, 152-154, (1971).

92) H. Kogelnik, "Theory of optical waveguides," in Guided-Wave Optoelectronics, T. Tamir, Ed. New York: Springer-Verlag, (1990).

93) T. Erdogan, J. of Lightwave Technol. 15, 8, 1277-1294, (1997).

94) D.K.W. Lam, and B.K. Garside, Applied Optics, 20, 440-445, (1981).

95) M. Yamada and K. Sakuda, Appl. Opt. 26, 3474–3478, (1987).

96) K. David, G. Morthier, P. Vankwikelberge, R. G. Baets, T. Wolf and B. Borchert, IEEE J. Quantum Electron., 27, 1714-1722, (1991).

97) H. Soda, Y. Kotaki, H. Sudo, H. Ishikawa, S. Yamakoshi, and H. Imai, IEEE J. Quantum Electron. 23, 804-814, (1987).

98) J. E. A. Whiteaway, G. H. B. Thompson, C. J. Armistead, A. J. Collar, S. J. Clements and M. Gibbon, Proc. 11_{th} IEEE Int. Semiconductor Laser Conf., Boston, MA, Sept. (1988).

99) C. Kaden, U. Griesinger, H. Schweizer, and M. H. Pilkuhn, J. Vac. Sci. Technol. 10, 6, (1992).

100) G.P Agrawal and N.K. Dutta (Van Nostrand Reinhold, New York) (1968).

101) W.-Y. Choi, J.C. Chen, C.G. Fonstad, Jpn. J. Appl. Phys., 25, 4654-4659 (1996).

102) J. Wiedmann, H-C. Kim, K. Ebihara, B. chen, M. Ohta, S. Tamura, J-I. Shim and S.Arai, Jpn. J. Appl. Phys. 40, 6845-6851, (2001).

103) A. Rast and A. Zach, Electron. Lett. 27, 808-809, (1991).

104) T.W. Johannes, A. Rast, W. Harth and J. Rieger, Electron. Lett. 31, 370-371, (1995).

105) M.L. Osowski, R. Panepucci, I. Adesida and J.J. Coleman, IEEE Photon. Technol. Lett., 9, 422-424, (1997).

106) L.M. Miller, J.T. Verdeyen, J.J. Coleman, R.P. Bryan, J.J. Alwan, K.J. Beernink, J.S. Hughes and T.M. Cockerill, IEEE Photon. Technol. Lett. 3, 6-8, (1991).

107) V.V. Wong, W-Y. Choi, J.M. Carter, C.G. Fonstad, H.I. Smith, Y. Chung and N. Dagli, J. Vac. Sci. Technol. B 11, 2621–2624, (1993).

108) R.D. Martin, S. Forouhar, S. Keo, R.J. Lang, R.G. Hunsperger, R.C. Tiberio and P.F. Chapman, IEEE Photon. Technol. Lett. 7, 244-246, (1995).

109) Y. Watanabe, N. Chen, K. Takei, K. Chikuma, N. Futakuchi and Y. Nakano, IEEE Photon. Technol. Lett. 10, 1688-1690, (1998).

110) M. Kamp, J. Hofmann, F. Schafer, M. Reinhard, M. Fischer, T. Bleuel, J. P. Reithmaier and A. Forchel, Opt. Mater. 17, 19-25, (2001).

111) M. Kamp, J. Hofmann, A. Forchel, F. Schäfer and J. P. Reithmaier, Appl. Phys. Lett. 74, 483-485, (1999).

112) H. Konig, S. Rennon, J.P. Reithmaier, A. Forchel, J.L. Gentner and L. Goldstein, Appl. Phys. Lett. 75, 1491-1493, (1999).

113) M. Legge, G. Bacher, A. Forchel, M. Klude, M. Fehrer and D. Hommel, Electron. Lett. 35, 636-637, (1999).

114) M. Reinhardt, M. Fischer, M. Kamp, J. Hofmann and A. Forchel, IEEE Photon. Technl. Lett. 12, 239-241, (2000).

115) R. Werner, T. Bleuel, J. Hofmann, M. Brockhaus and A. Forchel, IEEE Photon. Technol. Lett. 12, 966-968, (2000).

116) L. Zhang, R. Wang, Z. Zou, A. Gray, L. Olana, T. Newell, D. Webb, P. Varangis and L. Lester, Optical Fiber Communication Conf., Atlanta, 2, 678- 679, (2003).

117) J.W Zimmerman, R.K. Prince, U. Reddy, N.L. Dias, and J.J. Coleman, IEEE J. Sel. Top. Quantum Electron. 19, 4, 1503712, (2013).

118) M. Muller, M. Kamp, A. Forchel, and J.-L. Gentner, Appl. Phys. Lett., 79, 2684, (2001).

119) N. Koslowski, A. Heger, K. Roessner, M. Legge, J. Koeth, L. Hildebrandt, Proc SPIE 8640, 864008, (2013).

120) S. Slivken, N. Bandyopadhyay, S. Tsao, S. Nida, Y. Bai, Q. Y. Lu and M. Razeghi Appl. Phys. Lett 100, 261112 (2012).

121) M. Muller, T. Lehnhardt, K. Rößner, and A. Forchel, Appl. Phys. Lett. 93, 081117, (2008).

122) L.Mahler, A. Tredicucci, F. Beltram, C. Walther, J. Faist, H.E. Beere, D.A. Ritchie, D.S. Wiersma, Nat. Photon. 4, 165-169, (2010).

123) R. Blanchard, S. Menzel, C. Pflügl, L. Diehl, C. Wang, Y. Huang, J.-H. Ryou, R. D. Dupuis, L. Dal Negro, and F. Capasso, New Journal of Physics 13, 113023, (2011).

124) S. Rennon, L. Bach, J.P. Reithmaier and A. Forchel, IEEE J. Sel. Top. Quantum Electron. 7(2), 306–311, (2001).

125) L. Bach, S. Rennon, J. P. Reithmaier, A. Forchel, J. L. Gentner, and L. Goldstein IEEE Photon. Technol. Lett. 14, 7, 1037-1039, (2002).

126) L. Bach, W. Kaiser, J. P. Reithmaier, A. Forchel, M. Gioannini, V. Feies, and I. Montrosset, IEEE Photon. Technol. Lett. 16, 1, 18-20, (2004).

127) Lu, Q., Zhuang, Q., Marshall, A., Kesaria, M., Beanland, R. & Krier, A. Semiconductor Science and Technology. 29, 7, 8 p.075011 (2014).

128) K. Papatryfonos, G. Rodary, C. David, F. Lelarge, A. Ramdane, and J.C. Girard, Nano Lett. 15, 7, 4488–4497, (2015).